Final Report

Title: Advanced Analysis, Validation and Optimization of Virtual Cement and Concrete Testing

Submitted to:

The Florida Department of Transportation Research Center
FDOT Research Center research.center@dot.state.fl.us
605 Suwannee Street, MS 30 Tallahassee, FL 32399

c/o Dr. Harvey DeFord, Ph.D.
Structures Materials Research Specialist
State Materials Office

Submitted by:

Christopher C. Ferraro PhD, PE(ferraro@ce.ufl.edu) (Principal Investigator)
Forrest Masters PhD, PE (Co Principal Investigators)
Benjamin Watts, PhD.
Chengcheng Tao, PhD.
Engineering School of Sustainable Infrastructure and Environment
University of Florida
Gainesville, Florida 32611

May, 2018
Department of Civil Engineering
Engineering School of Sustainable Infrastructure and Environment
College of Engineering
University of Florida
Gainesville, Florida 32611

Disclaimer

The opinions, findings, and conclusions expressed in this publication are those of the authors and not necessarily those of the State of Florida Department of Transportation or the U.S. Department of Transportation.

Prepared in cooperation with the State of Florida Department of Transportation and the U.S. Department of Transportation.

Approximate Conversions to SI Units (from FHWA)

Symbol	When You Know	Multiply By	To Find	Symbol
Length				
in	inches	25.4	millimeters	mm
ft	feet	0.305	meters	m
yd	yards	0.914	meters	m
mi	miles	1.61	kilometers	km
Area				
in^2	square inches	645.2	square millimeters	mm^2
ft^2	square feet	0.093	square meters	m^2
yd^2	square yard	0.836	square meters	m^2
mi^2	square miles	2.59	square kilometers	km^2
Volume				
fl oz	fluid ounces	29.57	milliliters	mL
gal	gallons	3.785	liters	L
ft^3	cubic feet	0.028	cubic meters	m^3
yd^3	cubic yards	0.765	cubic meters	m^3
NOTE: volumes greater than 1000 L shall be shown in m^3				
Mass				
oz	ounces	28.35	grams	g
lb	pounds	0.454	kilograms	kg
Temperature (exact degrees)				
°F	Fahrenheit	5 (F-32)/9 or (F-32)/1.8	Celsius	°C
Illumination				
fc	foot-candles	10.76	lux	lx
fl	foot-Lamberts	3.426	candela/m^2	cd/m^2
Force and Pressure or Stress				
lbf	pound-force	4.45	newtons	N
lbf/in^2	pound-force per square inch	6.89	kilopascals	kPa

1. Report No.	2. Government Accession No.	3. Recipient's Catalog No.
4. Title and Subtitle Advanced Analysis, Validation and Optimization of Virtual Cement and Concrete Testing		5. Report Date December 2017
		6. Performing Organization Code
7. Author(s) Christopher C. Ferraro, Benjamin Watts, Chengcheng Tao, Forrest Masters		8. Performing Organization Report No.
9. Performing Organization Name and Address Department of Civil and Coastal Engineering Engineering School of Sustainable Infrastructure & Environment University of Florida 365 Weil Hall – P.O. Box 116580 Gainesville, FL 32611-6580		10. Work Unit No.
		11. Contract or Grant No. BDV31-977-06
12. Sponsoring Agency Name and Address Florida Department of Transportation 605 Suwannee Street, MS 30 Tallahassee, FL 32399		13. Type of Report and Period Covered Final Report 5/14-12/17
		14. Sponsoring Agency Code
15. Supplementary Notes None		

16. Abstract

Computational models that predict the behavior of cement and concrete seek to reduce industry reliance on predictive empirical relationships through simulation of the micro-scale chemical and thermal phenomena of cement hydration and their influence on macro-scale material properties. Models such as the Virtual Cement and Concrete Testing Laboratory (VCCTL) provide a deterministic link between measurable characteristics of aggregate Computational models that predict the behavior of cement and concrete seek to reduce industry reliance on predictive empirical relationships through simulation of the micro-scale chemical and thermal phenomena of cement hydration and their influence on macro-scale material properties. Models such as the Virtual Cement and Concrete Testing Laboratory (VCCTL) provide a deterministic link between measurable characteristics of aggregate and mineral binders, the temperature and moisture of the curing environment, and the evolving properties of paste, mortar, and concrete. The following report summarizes efforts to explore the as-delivered capabilities of the VCCTL, and identify and rectify its limitations.

17. Keywords.	18. Distribution Statement		
Concrete; Virtual Testing VCCTL; Computer Modeling, Virtual Microstructure	No restrictions.		
19. Security Classif. (of this report) Unclassified	20. Security Classif. (of this page) Unclassified	21. Pages	22. Price

EXECUTIVE SUMMARY

Background

Traditional predictive relationships between the behavior of portland cement concrete and the properties of its constituent materials are largely derived from physical, empirical testing programs. Physical testing of concrete for quality assurance or experimental research requires substantial time and labor, and empirical relationships derived from the resulting data become less precise when applied to materials not included in the original experiment. Models which simulate the hydration of portland cement aim to provide a direct link between measured material characteristics and concrete performance metrics without resource intensive testing programs. A number of models exist [1]; however, the Virtual Cement and Concrete Testing Laboratory (VCCTL) possesses the ability to predict the results of common quality control tests for cement, mortar, and concrete, making it readily applicable to real problems in concrete mixture design.

The VCCTL is capable of simulating the physical properties of cementitious materials, including early-age properties such as heat of hydration, temperature rise, and time of setting. Additionally, the model simulates the physical and mechanical properties such as compressive strength and modulus of elasticity, and values of bulk diffusion and conductivity to estimate durability. Virtual simulations of 28-day properties typically require less than two hours to complete. The VCCTL requires different input properties for the material constituents of cement paste, mortar, and concrete. Chemical and physical properties are required for cementitious binders, mechanical properties for aggregate, and the relative proportions of each determined based on the mixture design. The ability to quickly and accurately predict properties of concrete that would normally require significant labor and extended periods of time to obtain has a number of potential benefits. The cost and risk associated with development of new mixture designs would fall, incentivizing performance-based mixture design. Increased confidence in the performance of concrete would allow for a reduction in overdesign, while potentially enabling a reduction in the amount of cement required for a given mix, improving the sustainability of the mixture by minimizing the CO_2 emissions.

Research Objectives

The objectives of the research detailed in this report were diverse; however, the overall goals of the project related to investigation of the capabilities and limitations of the model with respect to practical implementation, as well as implementation of new computational techniques to improve or expand the capabilities of the VCCTL. These goals included the following specific initiatives

- Validate the VCCTL in the context of Cement and Concrete Reference Laboratory (CCRL) proficiency testing
- Integrate the VCCTL with finite element modeling of temperature rise in mass concrete structures
- Investigate performance when modeling chemical and mineral admixtures
- Develop improvements for modeling chemical and mineral admixtures

- Develop applications integrating the VCCTL with high performance computing resources at the University of Florida
- Apply advanced optimization techniques to analyze the behavior of the VCCTL and select optimal cement chemistries and mixture proportions
- Investigate applications of machine learning for partial replacement of VCCTL functionality
- Investigate the applications of the VCCTL to prediction of durability parameters

Main Findings

The main findings of this study are summarized as follows:

- It is feasible for FDOT to use the VCCTL to participate in the CCRL proficiency sample program without performing heat of hydration testing or mortar compressive strength testing. The results of this research indicate that if this was implemented, virtual laboratory scores would exceed those of a majority of participating labs.
- The accelerating or retarding effects of admixtures can be simulated to a limited degree with the VCCTL by calibrating the time scale of simulations using heat of hydration curves obtained from pastes incorporating those admixtures
- VCCTL simulations of adiabatic temperature rise for portland cement concrete can be used as input for finite element thermal modeling of mass concrete structures
- VCCTL predictions of properties related to durability correlate well with measured results of surface resistivity, and generally obey trends expected based on observations reported in literature
- The implementation of VCCTL in a high performance computing environment enabled comprehensive evaluation of the behavior of the model with respect to ordinary portland cements and binary mixtures through enumeration of more than 500,000 unique simulations
- Multi-objective optimization techniques developed using enumerated simulation data enable rapid determination of ideal cement chemistries when user-specified constraints on elastic modulus, time of set, and CO_2 emissions are provided
- The default capabilities of the VCCTL with respect to pozzolanic materials do not accurately predict compressive strength for binary mortars; however, by implementing and training machine learning algorithms using enumerated data, it is possible to predict compressive strength with high accuracy

Recommendations

Based upon the findings from this study, the following recommendations are suggested:

- Implement a virtual cement proficiency testing program side by side with existing physical testing programs
- Develop Virtual Testing Specifications for virtual ASTM C109 mortar testing and virtual ASTM C1702 heat of hydration testing based on the procedures detailed in Chapter 3
- Conduct Virtual Testing in parallel with FDOT mixture qualification testing, using only X-ray Fluorescence and Laser Particle Size Analysis data for cementitious material inputs

TABLE OF CONTENTS

Contents Page

LIST OF TABLES

LIST OF FIGURES

Figure page

1. INTRODUCTION

1.1. Background

The Virtual Cement and Concrete Testing Laboratory (VCCTL) is a computer modeling tool intended to develop and integrate state-of-the-art computational materials science tools into a user-friendly software interface used to model concrete at the microstructural level. The significance of computer modeling of the concrete microstructure is intended to eliminate much of the time and labor associated with the development and testing of new mixture designs in the laboratory setting.

The potential for the VCCTL to be used as a time and labor saving tool is considerable; however, the capabilities and limitations of its functionality remained largely unexplored until recently due to the complex sample preparation and analysis procedures required to obtain model input data for portland cement. A recent exploratory research program (FDOT Project No. BDK-75-977-73) at the University of Florida has developed and refined these cement characterization techniques, improving upon those originally developed by the National Institute of Standards and Technology (NIST), and provided insight into the current capabilities and limitations of the VCCTL. This research focused on the core functionality of the program; several of the more advanced features have yet to be investigated, and as the details of the program's functionality became clearer, possible applications that were not originally considered emerged.

There also exists the potential to integrate the programming underlying the VCCTL into a broader optimization program, which could potentially optimize multiple desirable characteristics of concrete (cost vs. strength, early-age strength vs. long-term durability, cement content vs. heat release, etc.). This would require computational resources capable of running many simultaneous simulations.

While the current practicality of the VCCTL is somewhat limited, there is potential, with continued research and development, to dramatically increase its effectiveness at tailoring properties through intelligent mix design, developing performance-based specifications, and predicting durability. Since most of the work can be done virtually by the VCCTL software, considerable time and effort in the laboratory would be saved.

1.2. Research Objectives

The research project will utilize materials that have been previously studied (to verify the validity of the VCCTL software), as well as materials specific to Florida, and material used in FDOT-specified mixture designs. The proposed research will investigate the use of the VCCTL software with respect to the analysis and prediction of behavior of cementitious concrete materials. The main objective is, using VCCTL, to develop methods, precision, and limitations relating to intelligent portland cement concrete mix design, using raw materials typically used in Florida Department of Transportation mix designs. Efforts will be made to incorporate the development of performance-based specifications and durability predictions.

2. LITERATURE REVIEW

2.1. Introduction

Hydration of portland cement is an exothermic chemical reaction between the cement particles and water which involves the liberation of heat during the hardening process. When portland cement is mixed with water, the constitute compounds undergo a series of chemical (hydraulic) reactions responsible for the eventual hardening of concrete. The rate of hydration and resulting products are governed largely by the relative concentrations of the four major constituents of portland cement: alite (C_3S), belite (C_2S), aluminate (C_3A), and ferrite (C_4AF). For strength development, the calcium silicates provide most of the strength in the first three to four weeks though, both C_3A and C_2S contribute equally to ultimate strength [2]. Several methods are available to evaluate the progress of cement and hydration in hardened concrete such as measuring the heat of hydration, degree of hydration, compressive strength, etc. In regards to the formation of the calcium silicate hydrate (C-S-H) structure, which constitutes the hardened cement paste, the major constituents of portland cement, C_2S hydrates in a similar manner to C_3S; however, C_2S hydrates at a slower rate. Consequently, the amount of heat liberated by the hydration of C_2S is also lower than the amount of heat liberated by C_3S [3]. In consideration of the portland cement constituents and the hydration of cement, a considerable amount of energy is spent in the manufacturing processes. In order to limit the greenhouse gases emission into the atmosphere and reduce costs of materials, conservation of energy becomes important. For sustainability purposes, the embodied energy or the energy consumed by all of the processes associated with the production of a material becomes an important factor. This is due to the direct relationship between the embodied energy and carbon content [4,5].

In summary, each of the cement compounds have different roles to play in the hydration process. By changing the proportion of each constituent compound and adjusting other factors such as grain size, it is possible to make different types of cement suitable for various construction and environment needs.

VCCTL uses data from real materials to create a virtual cement and concrete model, from which physical (thermal, electrical, diffusional, and mechanical) properties can be obtained using finite difference, finite element, and random walker algorithms. In general, three steps are conducted inside the software to achieve the material properties [6]. The model first creates a 3D microstructure of a portland cement paste input data including material and environmental properties. Among all the data, volume and surface area fractions of the four major cement phases (alite, belite, aluminate and ferrite) are obtained via X-ray powder diffraction, scanning electron microscopy and multispectral image analysis [7]. Then VCCTL simulates the process of hydration by applying rules obtained from the observed hydration kinetics and thermodynamics of portland cement. Once the hydration is complete, physical properties are calculated based on finite element analysis of the microstructure [7].

2.2. VCCTL Structure and Function

The process of creating, hydrating and analyzing a cementitious microstructure using the VCCTL involves multiple discrete executables, invoked by an overarching user interface. The VCCTL interface serves the primary function of allowing the user to conveniently run individual simulations, and provides simple functionality to perform the following tasks:

1. The definition, selection, and modification of virtual materials and their essential properties
2. Specification of the proportions of mixtures (cement, mortar, and concrete) and spatial properties (dispersion, flocculation, real particle shapes, size) of the virtual microstructure
3. Creating and viewing the initial, unhydrated virtual microstructure
4. Definition of the characteristics of the virtual environment (curing conditions, thermal environment), data output schedule, and length for the virtual hydration
5. Simple plotting of virtual hydration results (heat evolved, setting phenomena, degree of hydration)
6. Analysis of mechanical (elastic modulus) and transport (bulk conductivity) properties of hydrated microstructure

The tasks enumerated above can be broken simply into two categories: defining of inputs, as well as the parsing and displaying of outputs. The user interface provides a simple way to accomplish these tasks; however, the computational work required to build, hydrate and analyze virtual microstructures is executed independently of the interface itself. The tasks of initial microstructure creation, microstructure hydration, measurement of elastic properties, and measurement of transport properties are each performed by a separate executable. The input-output structure of the executables is outlined in a flow chart, Figure 2-1, followed by detailed explanations of each phase of simulation and the relevant inputs and outputs.

2.3. Initial Microstructure Creation

The task of building an initial, unhydrated virtual microstructure, outlined in the first column of the flow chart in Figure 2-1, is performed by the executable genmic.exe [8]This program uses measured, physical and chemical properties of the real cement being simulated as well as user defined inputs that change how the microstructure is virtually constructed from measured properties. The two types of inputs are defined, for the purposes of this research, as material property inputs, and process control inputs.

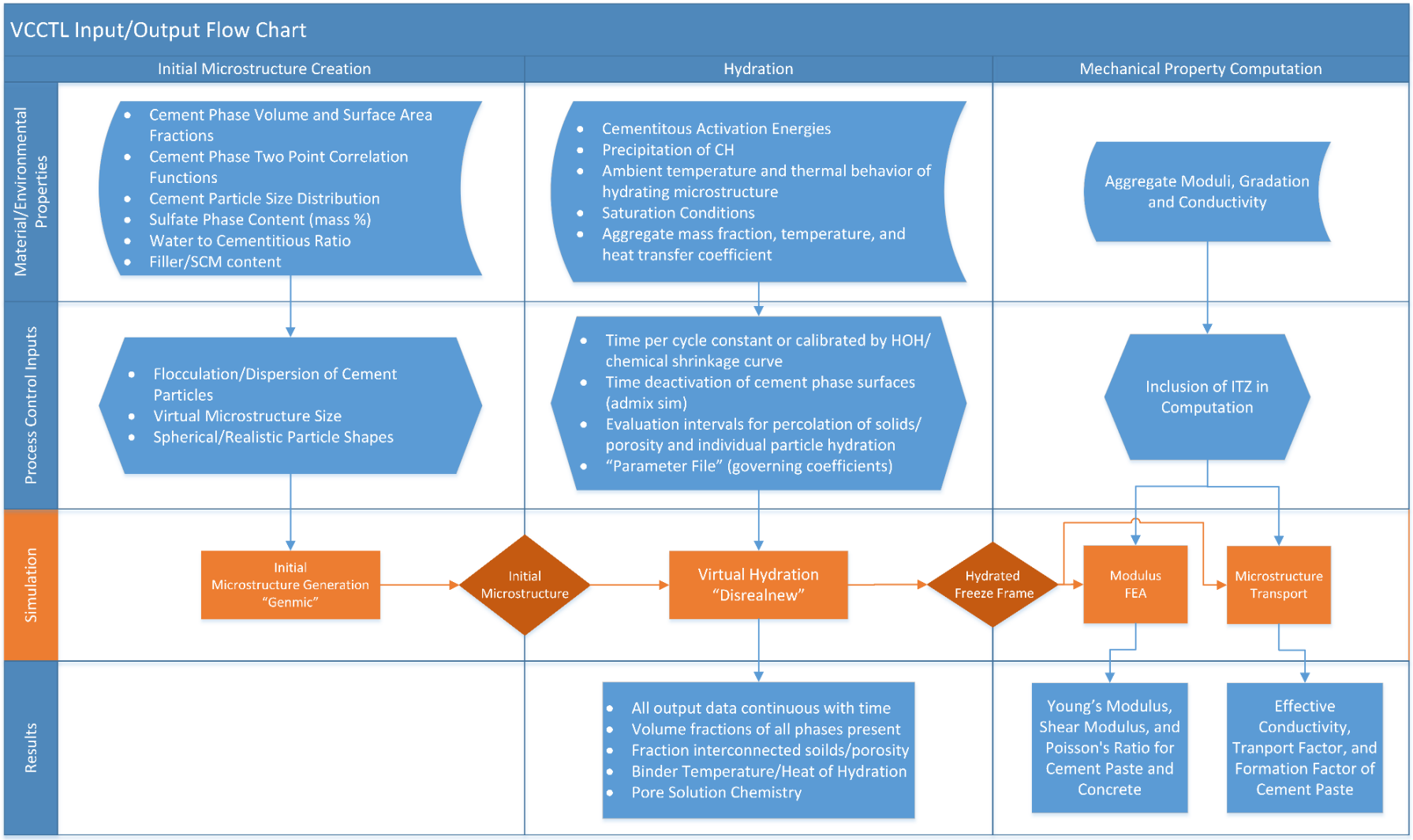

Figure 2-1. VCCTL Structure Flow Chart

2.3.1. Material/Environmental Property Inputs

Cement Composition Inputs

The most important input parameters required by the VCCTL software are the volume and surface area fractions of the four major chemical phases of portland cement, which include alite (C_3S), belite (C_2S), aluminate (C_3A), and ferrite (C_4AF), as well as the alkali and sulfate phases. The volume fractions can be obtained via powder x-ray diffraction; however, acquisition of surface area fraction data is more intensive, involving scanning electron microscopy and multispectral image analysis. The process ultimately results in a false color phase map, from which the volume and surface area fractions of each phase are measured using the MicroChar utility published by NIST [9].

The segmented phase map used to measure phase volume and surface area fractions also provides a representation of the spatial distribution of the different clinker phases. This information is characterized by measuring the isotropic two-point correlation function for each phase, which describes the probability that two given pixels will be of the same phase over a range of distances. This information enables the virtual microstructure to emulate the spatial distribution of clinker phases in the characterized cement.

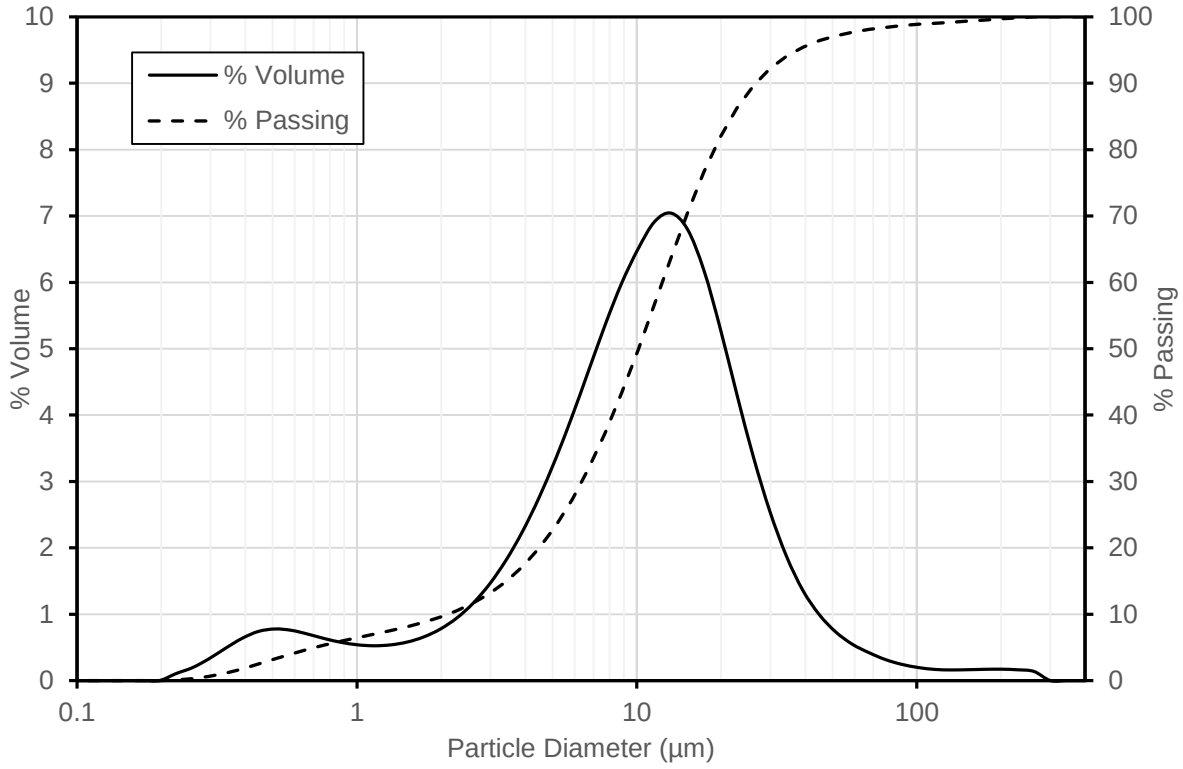

Figure 2-2: Cement Particle Size Distribution

The particle size distribution of the cement is measured using laser particle size analysis, and is required by GENMIC to accurately reproduce the range of particle sizes present in the cement being simulated. This technique measures the diffraction of light scattered by particles as they pass through a laser beam [10]. Particles are measured until the size distribution no longer changes. A typical particle size distribution is shown in Figure 2-2.

Gypsum Phase Mass Fractions

Calcium sulfate in the form gypsum is interground with cement clinker to produce portland cement, which is done to prevent the flash set of C_3A during hydration. A portion of gypsum converts to anhydrite and hemihydrate due to residual heat during the grinding process [11]. All three of the calcium sulfate phases influence the early-age behavior of cement; the relative mass fraction of each is critical for accurate simulations [8]ASTM 1365 provides a procedure for acquiring mass fraction data via X-Ray diffraction for all crystalline components of portland cement including the calcium sulfate phases [12].

Cement Paste Properties

In addition to the material properties of the cementitious materials , the specific characteristics of the cementitious paste are required by GENMIC. The most important of these is the water to cementitious materials ratio; however, there are also options to add other materials including pozzolans and fillers such as limestone or quartz.

Process Control Inputs

The process control inputs for initial microstructure creation are optional, and responsible for performing certain operations on the microstructure that are intended to result in more realistic simulations. These options include provisions to use more realistic particle shapes than the default spherical option, as well as ways to account for the stearic effects of different types of admixture. The size of the microstructure image being created is a process control option as well, with the voxel resolution set at one cubic micron per voxel.

Cement Particle Shape Data

The VCCTL software builds the digital microstructure using spherical particles, though it also has provisions for the use of real cement particle shapes. These particle shapes are obtained using x-ray computed microtomography scans of real cement particles, which are then individually modeled using a spherical harmonic analysis of the particle surface. This process is effectively the application of Fourier decomposition to a spherical polar coordinate system, and characterizes the aggregate surface as a set of line segments with varying radii, emanating from the center of mass at angles θ and φ [13]. The spherical harmonic characterization of the particle can then be used to reconstruct the particle virtually with arbitrary size and orientation [14]. A database of shape data for several different cements is included with the VCCTL.

Cement Particle Dispersion

The VCCTL software provides the option to create a simulation that considers dispersed cement particles as it composes the virtual microstructure. This option is provided to simulate the mutual repulsion of cement particles that occurs [15] when water-reducing admixtures are present. The functional effect of this is that space between particles is more uniform, which can result in more accurate simulation of hydration and a corresponding increase in strength [16]. The dispersion of particles can be set to 0, 1, or 2, with the values indicating the minimum number of pixels separating each particle in the virtual microstructure. This is accomplished by surrounding each particle with a false layer of voxels of the same thickness as the specified dispersion distance [17]. Following placement of the particle, the false layer of voxels is removed.

2.3.2. Microstructure Creation (genmic.exe)

Microstructure creation using GENMIC begins with a number of text input files created by the VCCTL, most of which simply contain the data described above in its raw format. One exception is the particle size distribution. Most portland cements have a significant size fraction that is smaller than one micron in diameter. To overcome the one micron resolution limit of the VCCTL, a dissolution bias value is calculated, which allows for the placement of one voxel particles that dissolve as though they were clusters of smaller particles. The number of one voxel particles is calculated to be equivalent to the total volume of particles under one micron in size, while the bias is calculated as the ratio of the total surface area of these particles to their total volume [11]. This calculation is performed by the VCCTL interface and reported in *.bias file, which is one of the text files required by GENMIC.

The microstructure is created within GENMIC by first defining the microstructure size, volume fraction of binder, and volume fraction of water. The program calculates from this how many total voxels are available for binder. The user then specifies the numeric index of the phase to be placed, as well as the fraction of the binder to be assigned to that phase. There is then a prompt for the number of size bins for the current phase, after which the diameter of the class and phase volume fraction residing in that class are input for all size classes. All phases are input using their corresponding phase identifier, and all size classes in this stage must be 1 micron or larger. Notably, clinker is a single phase at this point; the distinction of the clinker into different clinker phases occurs later.

After the definition of the phase size fractions the program calculates how many particles of each phase to place based on the number of available binder voxels (Figure 2-3). Particles are then placed randomly. Particles are not allowed to overlap when placed; another location is tried if a new particle impinges upon one that exists. When particle placement is finished, the two point correlation functions for the clinker phases are used to separate the “clinker” particles into their four constituent phases.

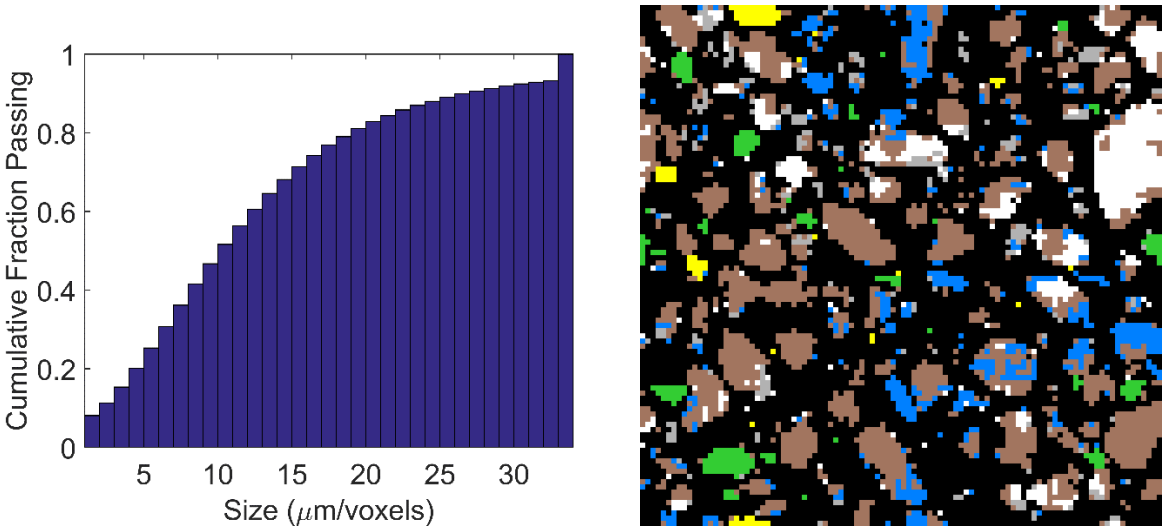

Figure 2-3. Virtual microstructure cross-section with corresponding discretized cumulative particle size distribution, used to determine volume fraction for each size of placed particle

The microstructure is then altered to match the volume and surface area fractions exactly by changing particle phases to match volume fractions, and moving particles to match surface area fractions. Particles are moved based on an analysis of local curvature, which essentially looks at the fraction of voxels in the current voxel's local neighborhood (typically some regularly sized cube or sphere) that are porosity [12]. This measure of curvature allows particles of a specific phase to be moved to areas of higher or lower curvature to enforce the proper surface area fractions. The final step is the placement of the one pixel particles using the file created by the VCCTL user interface. The finished microstructure can then be named and saved in a user defined directory.

Output Results

The only tangible result of the initial microstructure creation phase is the three-dimensional image (Figure 2-4) produced by genmic.exe. The image can be measured to verify that the cement volume and surface area fractions were replicated accurately using a small utility called stat3d.exe, which is included with the VCCTL. This utility may be useful for evaluating the level of phase concentration variability inherent to the microstructure creation process.

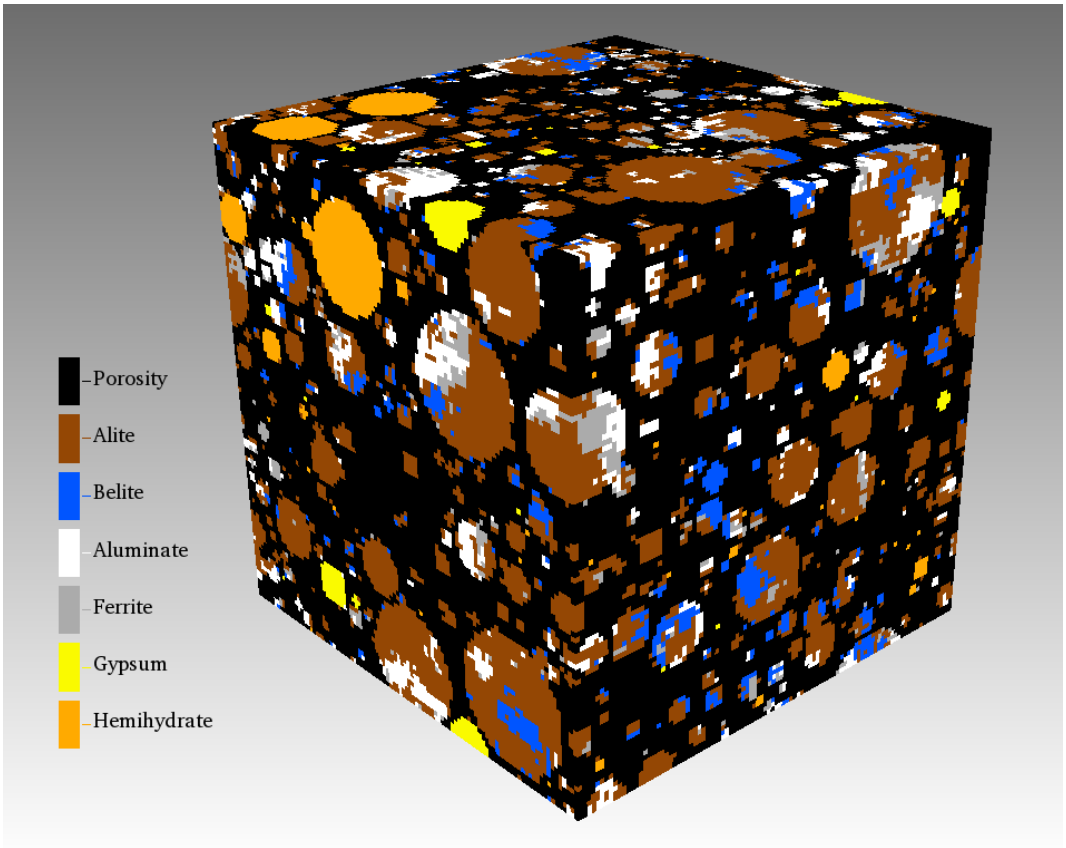

Figure 2-4. Microstructure image generated by genmic.exe

2.4. Hydration Simulation

The execution of the virtual hydration of the initial microstructure begins with the microstructure created by GENMIC, with the different phases of cement, gypsum, and other materials that may be present represented as clusters of voxels suspended in voxels of porosity, which in this case represent water. The model performs operations on the microstructure using rules that are derived from observed behavior of cementitious systems as well as the known volume stoichiometry of the portland cement hydration, which is summarized in Figure 2-5. These rules are implemented via a cellular-automata algorithm; this type of algorithm operates on a two dimensional or three dimensional lattice, and iteratively changes sites in the lattice based on their current values as well as the values of neighboring sites [12].

Silicate Reactions

$$C_3S + 5.3H \rightarrow C_{1.7}SH_4 + 1.3CH$$
$$1 \quad 1.34 \quad 1.521 \quad 0.61$$

$$C_2S + 4.3H \rightarrow C_{1.7}SH_4 + 0.3CH$$
$$1 \quad 1.49 \quad 2.077 \quad 0.191$$

Aluminate and Ferrite Reactions

$$C_3A + 6H \rightarrow C_3AH_6$$
$$1 \quad 1.21 \quad 1.69$$

$$C_3A + 3C\bar{S}H_2 + 26H \rightarrow C_6A\bar{S}_3H_{32}$$
$$0.4 \quad 1 \quad 2.1 \quad 3.3$$

$$2C_3A + C_6A\bar{S}_3H_{32} + 4H \rightarrow 3C_4A\bar{S}H_{12}$$
$$0.2424 \quad 1 \quad 0.098 \quad 1.278$$

$$C_4AF + 3C\bar{S}H_2 + 30H \rightarrow C_6A\bar{S}_3H_{32} + CH + FH_3$$
$$0.575 \quad 1 \quad 2.426 \quad 3.3 \quad 0.15 \quad 0.31$$

$$2C_4AF + C_6A\bar{S}_3H_{32} + 12H \rightarrow 3C_4A\bar{S}H_{12} + 2CH + 2FH_3$$
$$0.348 \quad 1 \quad 0.294 \quad 1.278 \quad 0.09 \quad 0.19$$

$$C_4AF + 10H \rightarrow C_3AH_6 + CH + FH_3$$
$$1 \quad 1.41 \quad 1.17 \quad 0.26 \quad 0.545$$

Figure 2-5. Cement phase reactions and volume stoichiometries used as governing parameters for cellular automata hydration in the VCCTL [18]

The initial step in the hydration is dissolution, wherein the microstructure is scanned to identify those voxels which are adjacent to porosity, and thus potentially eligible to enter into solution. Whether each eligible voxel actually dissolves is determined by two parameters, which are unique to each phase. A Boolean solubility flag simply indicates whether the voxel is actually eligible to dissolve, and a dissolution probability with a value between 0 and 1. A second pass through the microstructure allows all surface voxels to take a one step random walk. If the resulting location of the walk lands the voxel in porosity, and the dissolution of the voxel is determined to be probable, the voxel enters into solution. A voxel in solution represents a

collection of all the ions created by the dissolution of one voxel of the original phase. If the resulting location of the random walk is not in porosity, the voxel remains in its original position. The voxels of dissolved ions then walk randomly through the porosity, and can interact with other voxels in specified ways. The reaction rules are summarized in Figure 2-6, where "dis" represents a dissolution reaction, "col" represents a collision with another phase, "nuc" represents nucleation of a crystal, and an asterisk indicates a dissolved phase [12].

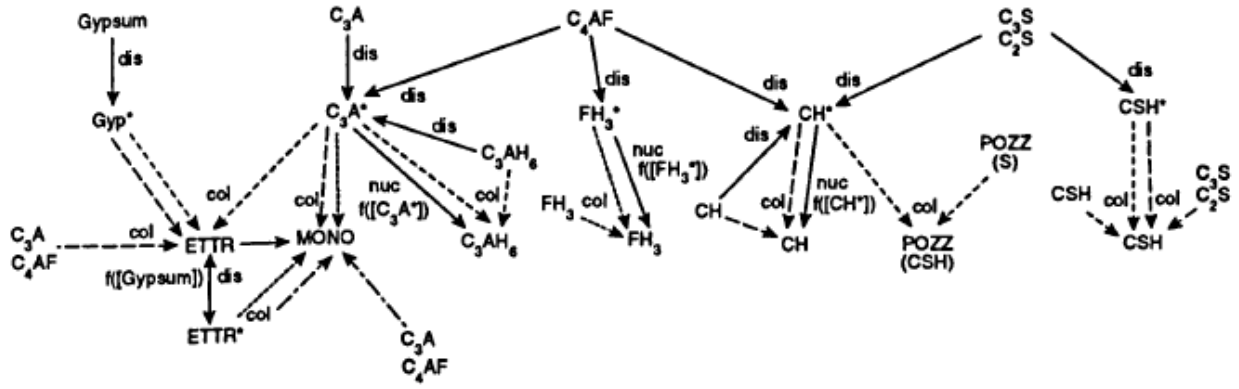

Figure 2-6. Phase Reaction Rules [12]

Following the random walk of the dissolved voxels and prior to the next dissolution operation (the next cycle) the number of each pixels of each solid phase present is measured. This allows for the calculation of the heat released and chemical shrinkage based on the heat of formation and total system volume change respectively. Other measurements, such as the percolation of solids or porosity in the microstructure, are calculated at the user specified intervals specified in the input to disrealnew.exe. Snapshots of the hydrating microstructure are saved to files similar to the initial microstructure GENMIC for analysis to determine mechanical properties.

2.4.1. Hydration Material/Environmental Property Inputs

Curing Conditions

The majority of the inputs required for virtual hydration are intended to curing conditions of the hydration being simulated. The majority of the options provided define the thermal relationship between the hydrating virtual microstructure and the surrounding environment, with three different scenarios. In each case an initial temperature of the binder system is required, while certain options also need a defined ambient temperature. The initial temperature of aggregate, if present, can be defined to simulate the initial effects of a heated or chilled aggregate [19]. An isothermal option is provided in which the model keeps the temperature of the system at the defined initial temperature indefinitely. There is also a semi-adiabatic option, in which a heat transfer coefficient can be defined that regulates the rate of flow of heat out of the virtual microstructure. An adiabatic thermal condition is available, in which all heat generated during hydration is retained within the virtual microstructure. Lastly, it is possible to specify a time-

temperature history for the hydration to follow. This option, however, is present in the command line execution of disrealnew.exe but not in the VCCTL user interface. This history is defined by a time at a certain temperature, followed by a time to ramp to a new temperature and time at that new temperature. This format can be specified for many rate steps.

Additional curing options simulate the effects of water availability for the hydration simulation. In the saturated state, the model allows consumed water voxels to be replenished as long as their locations have a free path to the borders of the virtual microstructure. This allows the hydration to progress with infinite available water until the percolation threshold is reached, after which the flow of additional water into the microstructure is not possible [19]. In the sealed condition, the model simply does not replenish water voxels as they are consumed, limiting the available water to that present in the initial microstructure. As the hydration progresses water is consumed staring with the regions of largest capillary porosity.

Hydration Behavior

The behavior of the microstructure over time is dependent largely upon the characteristics of the virtual cement. Most of these properties are defined as part of the initial creation of the microstructure; one exception to this is the activation energy of the cementitious materials being simulated. The model takes activation energies for cement, slag, and fly ash as inputs for the virtual hydration process. These values can be particularly influential in situations in which the temperature of the model is not constant, as the calculated heat released is updated every cycle using a version of the Arrhenius equation [19]:

$$k = e^{-\left[\frac{E_A}{8.314}\left(\frac{1}{T_c+273.15}+\frac{1}{298.15}\right)\right]} \qquad 2\text{-}1$$

where k is the rate constant, E_A is the activation energy of the cement, and T_c is the current temperature

2.4.2. Hydration Process Control Inputs

Many of the inputs required for the hydration process are not related to the properties of the simulation itself, but are instead options given to the user that control how exactly the hydration occurs. These options are typically intended to provide additional realism.

Model Time Calibration

One of the inherent limitations of the VCCTL is that no information is provided to define the specific length of each computational cycle and thus simulate the time domain of the model [20]. Each cycle is either set to be a specific fixed length of time, or the time scale of the simulation is calibrated based on experimental heat of hydration or chemical shrinkage data. The following relationship is used to fit the time of each cycle to experimental data:

$$t = \beta \times n^2 \qquad 2\text{-}2$$

Where β is a scaling factor calculated to best fit the experimental data, t is time, and n is the number of cycles. The heat of hydration data used to calibrate the time scale does not need to extend the entire length of the simulation being performed; a quadratic extrapolation of the heat release curve if computed when the time domain extends beyond that of the provided data. Previous research by Sant et al. as well as Watts & Ferraro has indicated that this input can be critical to providing accurate results for simulation of early-age properties [21,22], and may provide the ability to simulate the early-age effects of certain classes of admixture.

Surface Deactivation

The surface of the virtual cement particles can be deactivated during the early stages of hydration. The model requires inputs for the phase of the particles to be deactivated, the percentage of the total surface area of those particles to deactivate, the length of time for which they will be deactivated, and the length of time to bring the particles back to full activity. This option is provided as a method for directly simulating the effects of certain types of water reducing and retarding admixtures, which in many cases are adsorbed onto the surfaces of cement particles, reducing the area available for reaction. While this provides a theoretically accurate method for simulating the behavior of admixtures, the direct action of most water reducers and retarders is not known to the degree of specificity required by the model.

Data Output Settings

Much of the useful data produced by the VCCTL is a product of the virtual hydration, and while many properties are recorded continuously as hydration progresses, some are calculated at user specified intervals. The computation of age specific mechanical properties such as bulk conductivity or elastic modulus requires snapshots of the hydrating microstructure. The frequency with which these snapshots are created are defined in this step. The amount of time to hydrate the microstructure for is also defined in this step, which has implications for the time required depending upon whether early-age properties or late-age results are the desired outputs.

2.4.3. Hydration Output Data

In addition to the microstructure snapshots output at specific times during hydration, 64 different characteristics of the hydrating microstructure are measured and recorded continuously and provided as a tab-delineated text file with the suffix *.data. Of these parameters, 34 describe the volume fractions of the cement and hydration products that make up virtual microstructure and are reported on a per cycle basis. The other 30 outputs include solution concentrations and activities for sodium, potassium, calcium and sulfate, total porosity, fraction porosity, three-dimensional connectivity of solids, average fraction porosity, pH and conductivity of the pore solution, non-evaporable water content, gel/space ratio, temperature of the binder, heat release, degrees of hydration for cement and fly ash, and the number of simulation cycles run.

Fraction Interconnected Solids

The fraction solids connected value quantifies the transition of a portland cement paste from a viscous suspension of particles to a rigid interconnected matrix, which is the fundamental description of the phenomenon of "set". Prediction of this property is useful for estimating the required time for different construction techniques, and several critical operations on young concrete are scheduled based on the occurrence of setting. Experimental tests for the setting time of cement typically adopt arbitrary limits to define "initial set" and "final set." As described in ASTM C403, time of set is determined by the resistance of a mortar to the penetration of a needle with a specific cross sectional area, and defines initial set as a resistance of 500 pounds per square inch, and final set as 4000 pounds per square inch. By comparing the times of initial and final set to the fraction solids connected curve the relationship may be calibrated to develop solids connected values that approximate initial and final set.

Heat Release

The heat release calculated during hydration is calculated on a per cycle basis using enthalpies of hydration obtained from literature for the different hydrating phases. This information can be calculated based on the known remaining volume of a specific phase [18]. When a heat of hydration curve is used to calibrate the time scale of the model, the resulting output curve will be identical to the input curve. When a fixed per-cycle time constant is used; however, the calculated heat release can be a useful parameter for evaluating the accuracy of the model, particularly combined with other hydration output parameters.

Chemical Shrinkage

Chemical shrinkage is computed by the VCCTL using the known volume fractions of all initial and hydrated phases combined with the differences in specific gravity between those phases. Both autogenous and chemical shrinkage can be simulated by simply changing the curing conditions of the virtual microstructure. Like heat release, a measured chemical shrinkage curve can be used to calibrate the time scale of the model by comparing the calculated and measured values every cycle and altering the time constant such that the calculated curve follows the experimental data. In the absence of this data or when heat of hydration data is used for time calibration, chemical shrinkage as predicted by the model provides another benchmark for evaluating the accuracy of the simulation.

2.5. Mechanical And Transport Properties

Measurements of paste elastic modulus are calculated from snapshots of the virtual microstructure captured at critical ages using finite element analysis [23]. Each voxel in the hydrated microstructure image is a trilinear element, with bulk and shear moduli that are defined based on phase [24]. The algorithm operates by applying a uniform engineering strain of 0.10 to the microstructure in the xx, yy, zz, xz, yz, and xy directions, then uses the conjugate gradient algorithm to minimize the elastic energy equation:

$$E_n = \frac{1}{2}uAu + bu + C \qquad 2\text{-}3$$

where A is the hessian matrix comprising the stiffness matrices for each element, b is a constant vector, C is a constant calculated based on the applied strain and periodic boundary conditions, and u is a vector containing all displacements.

When the paste microstructure is generated for a mortar or concrete, an invisible barrier (Figure 2-7) is placed in the center of the microstructure along the yz plane. This simulates single-sided growth of hydration products against an aggregate surface and replicates the mechanisms responsible for the formation of the interfacial transition zone (ITZ) [25].

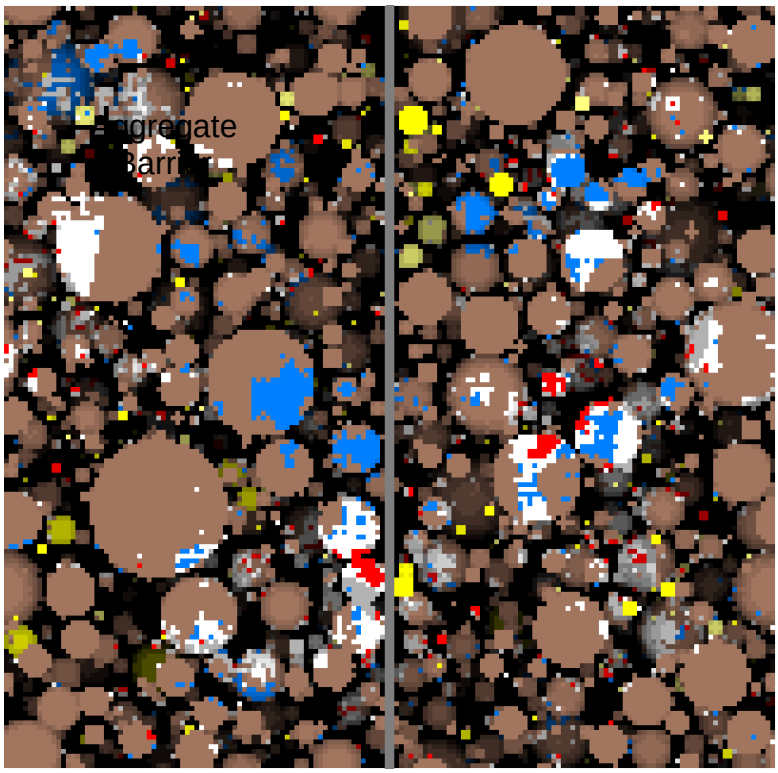

Figure 2-7. Example VCCTL microstructure with representation of aggregate barrier shown in gray

To calculate the modulus of the ITZ, its width is first set as equal to the median cement particle size [26]. The bulk and shear moduli of each slice of the hydrated microstructure within this distance of either side of the aggregate barrier are then averaged to determine the ITZ modulus.

Further calculation of mortar or concrete elastic modulus requires the bulk moduli, shear moduli, volume fractions, and gradations of the coarse and fine aggregates. The aggregate properties are combined with the modulus of the paste to compute the elastic modulus of the

composite material, using differential effective medium theory (D-EMT). This technique is used to calculate the elastic properties of a composite matrix with spherical inclusions, wherein the inclusions are surrounded by a shell with elastic properties differing from both their own and those of the matrix. This method is used to approximate aggregate surrounded by ITZ, suspended in a matrix of cement paste. The calculations performed are detailed by Garboczi and Berryman [27], and involve calculating the effective diameters and moduli for each aggregate size, computing the new effective aggregate size distribution and total effective aggregate fraction, and finally the implementation of a fourth order Runge-Kutta algorithm to solve coupled differential equations 2-4 and 2-5

$$\frac{dK}{d\varphi} = -kK/\varphi \qquad 2\text{-}4$$

$$\frac{dG}{d\varphi} = -gG/\varphi \qquad 2\text{-}5$$

Where k and g are the dilute limit slopes [28], φ is the matrix volume fraction, and K and G are the bulk and shear moduli of the composite material.

Strength is then calculated from the composite moduli through empirical relationships; the equation used depends upon the shape of the simulated specimen (cube or cylinder) and whether the material is mortar or concrete.

Prediction of strength by the VCCTL has been implemented using two different techniques as the model has evolved. The original method for calculation of compressive strength utilized an equation derived by Mindess [28] which incorporates published data in combination with a defined relationship between the gel-space ratio and the degree of hydration was originally published by Powers, as presented in Equation 2-6 [29]:

$$X = \frac{0.68\alpha}{0.32\alpha + \frac{w}{c}} \qquad 2\text{-}6$$

where α is the degree of hydration, and w/c is the water to cement ratio of the cement paste. The degree of hydration output from the VCCTL was used to compute the gel-space ratio over time; strength could then be calculated from the gel space ratio for a specific age [19,30,31] per the equation 2-7 :

$$\sigma_c(t) = \sigma_A X(t)^n \qquad 2\text{-}7$$

where σ_A is the intrinsic strength of the cement and n varies between 2.6 and 3.0 based on the cement in question [28]. This method relies on an experimentally measured 3-day mortar strength to first solve for σ_A assuming a value of 2.6 for n [19,30,31]; the evolution of compressive strength over time was then calculated per Eq. (2-6).

The second and current method for prediction of compressive strength in the VCCTL is based on the computed elastic modulus of the paste, mortar or concrete. Strength is calculated from modulus using an empirical relationship [21,31] based on equations described by Neville [32]. As of software version 9.5.3 the equation in the source code [33] used for the prediction of compressive strength of mortar cubes is as follows:

$$f'_c = (5.0 * 10^{-4})E^{3.18577} \qquad 2\text{-}8$$

where E is the elastic modulus of the mortar in gigapascals. Another, similar relationship was developed based on measurements of elastic modulus of mortar prisms and compressive strength mortar cubes [34];

$$f'_c = (3.79 * 10^{-3})E^{2.6} \qquad 2\text{-}9$$

This relationship was used to calculate the compressive strength of mortars from elastic moduli predicted by the VCCTL, with very good agreement for the mortars considered in the referenced study.

3. SIMULATION OF ADMIXTURE SET TIME EFFECTS USING ISOTHERMAL HEAT OF HYDRATION CURVES

3.1. Introduction

This chapter explores a method for modeling the influence of chemical admixtures on the set behavior of portland cement mortar using the Virtual Cement and Concrete Testing Laboratory (VCCTL). The VCCTL is capable of translating characteristic heat evolution behavior into virtual measurements of setting time. Previous research has attempted to directly relate the setting time of cement with changes in the rate of power generation using isothermal calorimetry [29]; however, these types of correlations do not reliably apply to all mixture designs [30]. This is likely because setting of portland cement is not exclusively regulated by the thermal progress of hydration, and is dependent upon a number of other physical and chemical material properties. The VCCTL provides a computation mechanism to relate the thermal behavior of paste and stiffening behavior of mortar, by using a measured heat generation curve to regulate the hydration of a virtual microstructure, while accounting for the mixture proportions and evolving thermal conditions of a mortar set-time test specimen.

Several studies [31–34] have focused on validation of the set prediction capabilities of the VCCTL, typically by comparing the predictions of the model to measured set times of paste using the Vicat method. The ability of the VCCTL to regulate hydration using external data has also been evaluated with regards to the detection of setting [21]; however, a chemical shrinkage curve was used for input instead of heat evolution data. These studies correlated the measured set time of ordinary paste with the VCCTL computed percentage of interconnected particles in the virtual microstructure, and found that the time of initial setting corresponded to a sharp increase in the percentage of interconnected particles in simulations. This study was performed to test the relationship between the VCCTL interconnected solids value and setting time of mortars containing different types of admixtures, and with compositions similar to that of mortar sieved from concrete. The potential environmental and economic benefits of cement hydration modeling are significant; however, widespread adoption will necessitate the ability to simulate the effects of common chemical admixtures.

3.2. Setting and the VCCTL

The early-age hydration of portland cement is characterized by dissolution and reprecipitation of cement phases and hydration products. The primary early-age contributor to strength development, C_3S, dissolves and combines with water to form calcium-silicate-hydrate (C-S-H) and portlandite or calcium hydroxide (CH) [35]. These hydration products precipitate on the surface of cement particles and grow outward. As this growth progresses, the particles connect and become rigidly bonded together [36].This process occurs on a continuous basis; however, the primary practical concern is the limit of workability, or the time at which the mixture is no longer plastic and cannot be properly finished [35]. This is commonly referred to as initial set.

The time required for the cement particles in suspension to become interconnected is a function of the physical characteristics of the suspension and the rate at which the hydration reaction progresses. The water-to-cement ratio (w/c) has the greatest effect; as the amount of water is reduced, the distance between particles and the time required for them to become interconnected declines [21].The size of the particles also influences the rate at which dissolution-reprecipitation occurs; a finer average particle size increases the available surface area for reaction to occur, thus, accelerating set [35]. The particles in unmodified portland cement paste also have a tendency to flocculate into clumps, which can reduce the free water in suspension and contribute to faster setting [37]. Flocculation is driven by weak and reversible electrostatic attraction between the cement particles; most water-reducing admixtures operate by negating this attraction, with a resultant increase in free water [35].

The setting of a portland cement is chemically regulated by the addition of calcium sulfate as gypsum. The proper amount of gypsum delays the otherwise extremely rapid hydration of C_3A, consequently, preventing immediate stiffening and providing a period of workability [38]. An overdose of sulfate can result in a different phenomenon, known as "false set" in cements with little or no C_3A , in which the mixture appears to set, but can be made fluid again with sufficient mixing [37].

Setting is also influenced by any environmental or chemical conditions which regulate hydration in general. Hot or cold temperatures accelerate or retard hydration, and in turn accelerate or delay set. The presence of certain types of admixtures can also accelerate or retard set, either as a direct result of their method of action, or as a side effect of their primary function.

3.3. Experimental Design

3.3.1. Admixture Selection

Chemical admixtures are commonly used in cement-based mixtures to reduce water demand, increase working time, or accelerate strength development. These additions frequently modify the hydration behavior of portland cement, and can impact the setting time of the mixture. Water reducers induce an electrostatic or stearic repulsion between cement particles by coating them with negatively-charged, long-chain polymers [39]. This disperses the particles evenly in solution, effectively increasing the free water and reducing the suspension viscosity [36]. Because these polymers are adsorbed onto the surfaces of cement particles, they limit hydration as long as they are active. This effect, combined with the increased distance between the particles due to dispersion, results in an increase in the time required for set to occur. Due to this phenomenon, many water reducing admixtures are also classified as retarding admixtures even though other methods of set retardation exist.

Retarding admixtures operate by reducing the solubility of the calcium silicate phases, typically by coating particles in a barrier that hinders the dissolution of calcium ions [39]. This coating can have a water reducing effect as well, but classes of admixtures that do not alter the workability of the mix exist, notably those based on soluble phosphates. In addition to a set retarding effect, the use of retarding admixtures in mass concrete structures can prevent thermal

cracking by reducing the rate of heat generation and the corresponding differential thermal stresses [36].

Accelerating admixtures based on soluble inorganic salts operate by shortening the induction period and accelerating the hydration of silicates [40], increasing the rate at which C-S-H forms [41], quickening set and hydration in general. A historically common and effective accelerator is calcium chloride, though alternatives such as calcium nitrite are used in reinforced concrete systems to eliminate corrosion caused by chloride ions in close proximity to steel. Calcium nitrite admixtures are frequently marketed as both accelerating and corrosion inhibiting admixtures for this reason.

Commercially available and ASTM C494 [42] compliant admixtures were selected for this study, and included a lignosulfonate-based type D water reducer and retarder, a polycarboxylate-based type F high range water reducer, a calcium chloride type E accelerator and water reducer, as well as a calcium nitrite-based type C accelerator, which also meets the ASTM C1582 [43] standard for corrosion inhibiting admixtures. The selection of admixtures for this study was intentionally broad; all four have different classes of active chemical species and different intended usages. Low, moderate, and high dosage rates were selected for each admixture based on the manufacturer's recommended dosage range; admixture types and dosages are detailed in Table 3-1.

Table 3-1. Admixture Types and Dosage

Admixture Type	Formulation	Dosage Range	Composition
Type D	Type D	3-10 oz/cwt	Lignosulfonate
Type F	Type F	2-10 oz/cwt	Polyacrylate
Type E	Type E	8-40 oz/cwt	Calcium Chloride
Type C	Type C/Corrosion Inhibitor	2-6 gal/yd^3	Calcium Nitrite

3.3.2. Isothermal Conduction Calorimetry

Isothermal conduction calorimetry was used to obtain heat of hydration curves for each admixture-dosage combination. The procedures for specimen preparation outlined in ASTM C1702 were adhered to. The total specimen mass was calculated to be approximately 6 g to facilitate internal mixing. Admixtures were incorporated by preparation of a dilute solution for each dosage rate. Special care was taken to ensure exacting thermal mass balance between specimen and reference vials, with the masses of the vials themselves accounted for in addition to the mass of specimen. Samples were allowed to reach thermal equilibrium overnight before the addition of the water-admixture solution, after which heat evolution was logged for 48 hours.

3.3.3. Time of Set Testing

For each admixture type and dosage, a mortar was prepared and tested according to ASTM C403. The use of the Vicat Needle [44] apparatus for time of set testing was initially considered; however, the requirement that the paste have a specific "normal" consistency (per ASTM C187) was incompatible with the viscosity modifying effects of certain admixtures and the water-to-cement ratio chosen for the study. All mortar prepared for this research had the same ratio of cement to sand, which was chosen to be representative of the mortar that would be sieved from a concrete mix. The mortar was mixed using a stand mixer (Figure 3-1), and the initial temperature was recorded, along with the ambient conditions during the test.

Figure 3-1. Hobart A120 Commercial Stand Mixer

3.3.4. Simulation Input and Parameters

The cement used for this research was characterized as part of previous research, using SEM/EDS microanalysis and a multi-step image processing procedure detailed in Appendix A. The volume and surface area fraction data obtained for that research is shown in Table 3-2, and was used to simulate the cement used in this study.

Table 3-2. Cement Mineral Phase Composition

Phase	Mass % (XRD)	Volume %	Surface Area %
C_3S	59.95	66.14	58.44
C_2S	13.67	15.72	20.37
C_4AF	13.49	12.04	4.07
C_3A – Cubic	4.30	5.74	17.12
C_3A – Orthorhombic	0.59	-	-
$CaCO_3$ (Limestone)	4.29	-	-
$CaSO_4*2H_2O$ (Gypsum)	1.80	-	-
$CaSO_4*0.5H_2O$ (Hemihydrate)	0.70	-	-
$CaSO_4$ (Anhydrite)	0.16	-	-

The cement used for this study contained approximately 4.3% limestone. The percent by mass of the limestone and the different sulfate phases were obtained via XRD (Table 3-2) combined with automated Rietveld refinement, and incorporated into all microstructures used in this study. The particle size distribution for the cement to be simulated is also required as input to the VCCTL. The particle size distribution and cumulative size distribution found for this cement are exhibited in Figure 3-2.

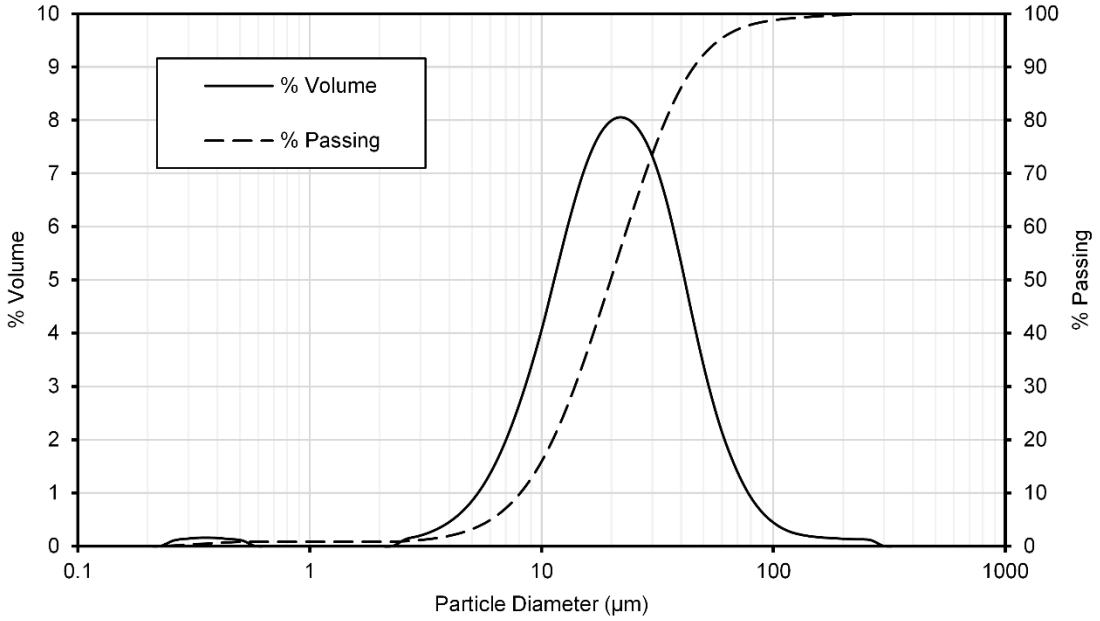

Figure 3-2. Cement Particle Size Distribution

The primary goal when choosing the initial state and environmental conditions for the model is to accurately simulate actual conditions. The generation of the initial microstructure requires several inputs that are intended to simulate surface-specific phenomena. The degree-of-dispersion setting in the VCCTL allows for the specification of the minimum number of pixels of water between each particle, with options for zero, one, and two pixels available. For mixtures with no water reducer present, the dispersion was set to zero pixels, while mid-range water reducers were set to 1 pixel, and high-range water reducers were set to 2 pixels. Realistic particle shapes were used in the generation of all microstructures.

During initial trial testing for time of set, it was noted that a significant amount of heat developed as the test neared final set, to the point where the specimen was warm to the touch relative to ambient conditions. Because time of setting tends to decrease with higher temperatures [45,46], the semi-adiabatic thermal condition was chosen for simulating the time of set in this study. This allows for the specification of a heat transfer coefficient out of the virtual microstructure, which combined with the initial binder temperature and the temperature of the ambient environment enables the approximate simulation of any temperature rise. This technique is limited in that the actual thermal environment of the test specimen is more complex than a single, constant heat transfer coefficient. To determine the optimal temperature coefficient, the temperature of a control specimen was logged for 12 hours. For simulations of the mortar used in the study, priority was placed on matching the experimental temperature curve during the period up to final setting. The resultant heat transfer coefficient chosen for simulations was 0.4 W/K, which produced a simulated temperature profile exhibited in Figure 3-3. This heat transfer

coefficient was used for all simulations; all time of set testing was performed in the same controlled environment with the same equipment and procedures.

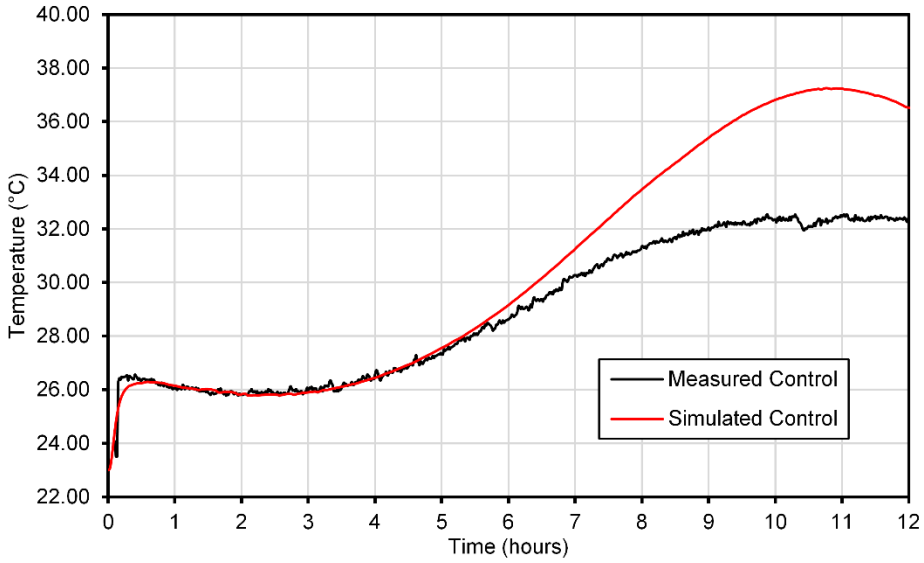

Figure 3-3. Simulated and measured specimen temperature rise

While there is some deviation of the simulated temperature rise curve after 5 hours elapse, the final set time for the control mix precedes this age. This deviation is expected; it is unlikely that the thermal conditions of a setting time specimen can be fully captured using a single heat transfer coefficient; however, this method is more realistic than simply assuming the conditions of the test specimen are isothermal.

For each hydration simulation, the temperature was set to the initial recorded temperature of the paste during the time of set test, the thermal state was set to isothermal, and the curing conditions were saturated. The specific heat of hydration curve for each admixture type and dosage was used to calibrate the time scale of the model. Each admixture-dosage combination was simulated with two independent hydrations of the same initial microstructure. Because the hydration process is simulated with an element of randomness, the results of two simulations with identical starting conditions are expected to show a small amount of variability.

3.4. Results

3.4.1. Isothermal Conduction Calorimetry

The power and total heat evolution curves obtained via conduction calorimetry and used as inputs for the VCCTL are presented in the following figures. The figures presented in the following pages observe certain conventions; all are presented with the control specimen as obtained from a plain portland cement at 0.45 w/c.

3.4.2. Type D Admixture

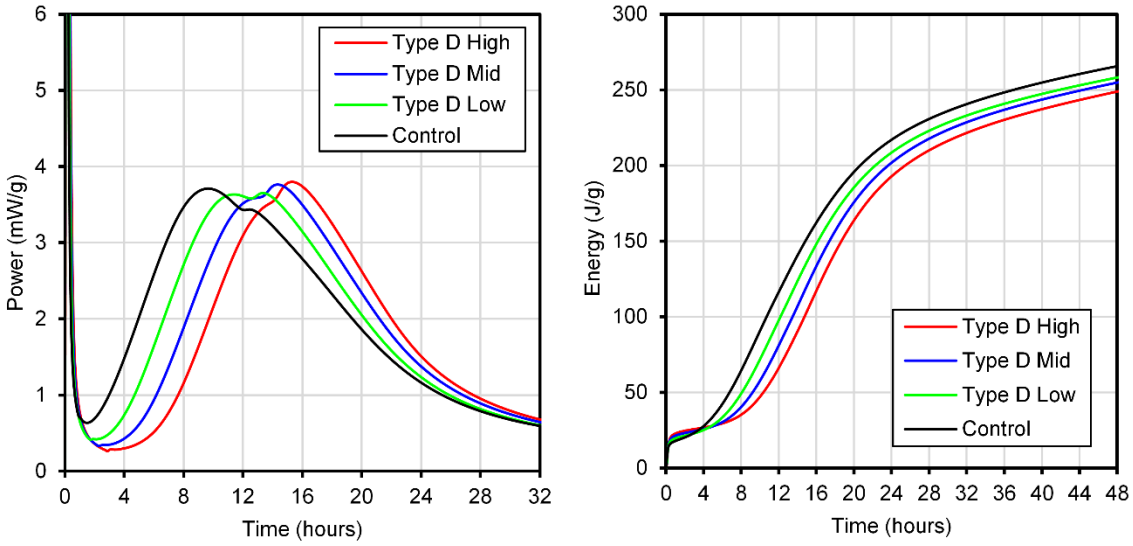

Figure 3-4. Type D Admixture Power and Energy with Time

The results from calorimetry of the type D and F admixtures are presented in Figure 3-4. The type D admixture exhibited significant retardation, with a delay of approximately two hours from the control at each increasing dose. The power curve also shows a shift in the prominence of the first (usually referred to as the main or C_3S hydration peak) and second (usually referred to as the aluminate peak) peaks in the bulk hydration phase. The first peak is higher than the secondary for the control curve, and as the dosage rate increases the first peak falls slightly and the second peak rises. It is possible that this corresponds to an increase in the rate of formation of ettringite, the commonly attributed source of the second peak during the bulk hydration phase [47]. The total energy curves for each dosage reflect the successive delay present in the power curves; the slope of the total heat curves appear to be unchanged from the control after the conclusion of the beginning of the bulk hydration phase.

3.4.3. Type F Admixture

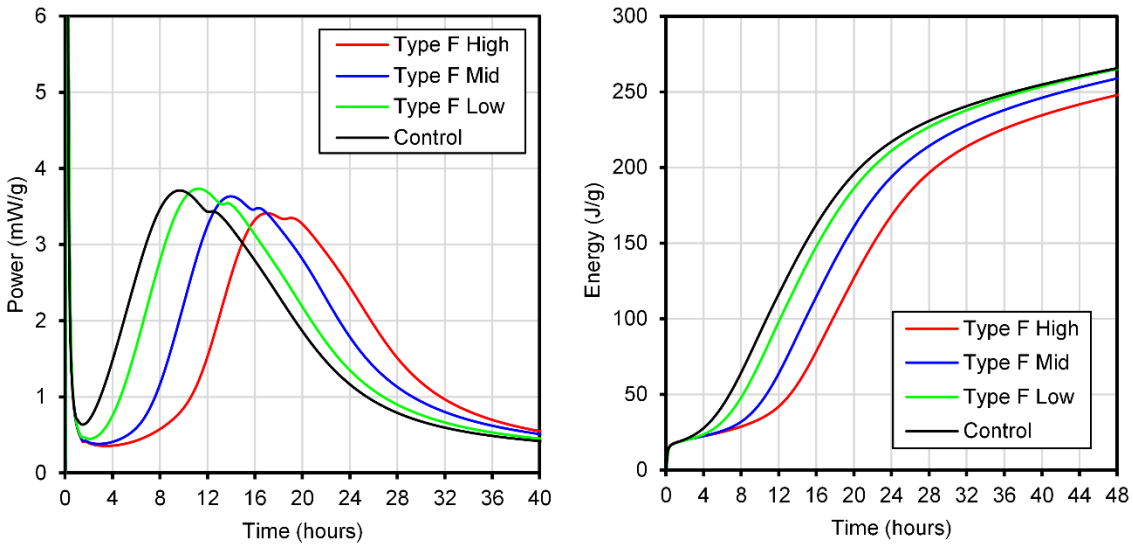

Figure 3-5. Type F Admixture Power and Energy with Time

The type F admixture (Figure 3-5) induced a high degree of retardation, with a slight retardation from the control at the lowest dosage, and approximately three additional hours of retardation with each successive dose. The retardation of heat release at the highest dosage rate is such that peak heat does not occur until approximately 17 hours, which is roughly 2 hours later than the highest dosage of the type D admixture. The relative prominences of the first and second peaks in the bulk hydration phase exhibit less of a shift than with the type D admixture, with the first peak falling slightly relative to the second with each increase in dosage. The peak power generation also falls slightly with the moderate and high dosages of the type F admixture. The energy curves exhibit a steeper slope at the 48 hour mark when the type F admixture is present. This effect is pronounced enough that the lowest dosage has approximately the same 48 hour energy as the control, despite an initial delay in heat generation.

3.4.4. Type E Admixture

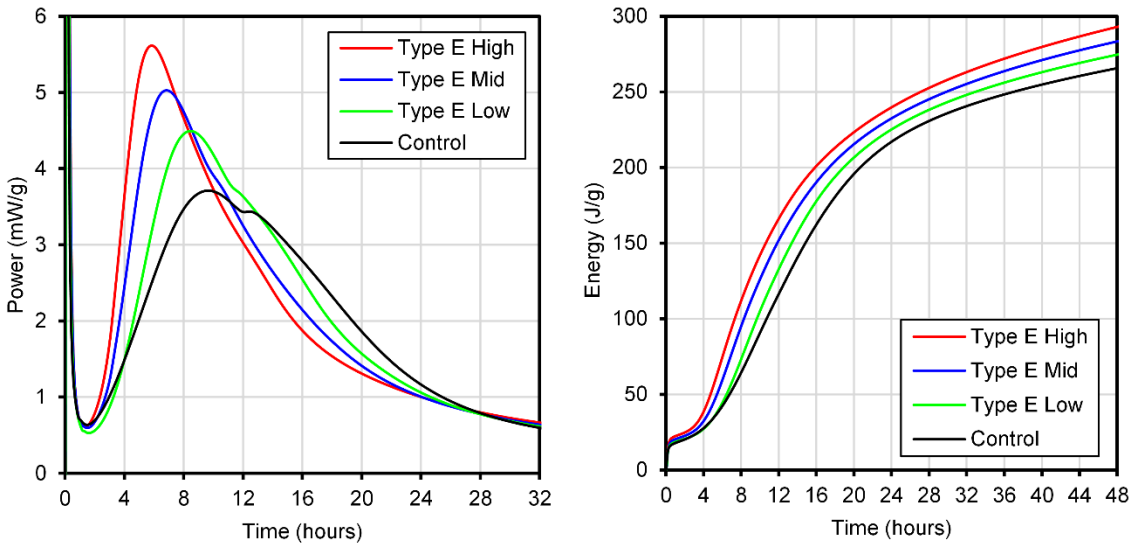

Figure 3-6. Type E Admixture Power and Energy with Time

The power and energy curves obtained from the type E accelerating admixture (Figure 3-6) exhibit sharp contrast to those of the water-reducing and retarding admixtures. While the type D and type F admixtures showed slight changes in the shape of the bulk hydration peaks, their primary effect was that of a shift; the ultimate changes in the shapes of the peaks and the peak heat output were slight in comparison. The type E admixture exhibits substantial alteration of the shape of the bulk hydration power curve. The height and time of the first peak shifts up and to the left with each successive dosage increase; the highest dosage reaches a peak heat value approximately 50% higher and 4 hours earlier than the control. There is still a second peak associated with renewed formation of ettringite; however, the shift is less substantial. The height of this second peak is slightly diminished as the dosage increases, and no apparent shift in the time at which it occurs is visible. The magnitude of the primary peak does make the secondary peak difficult to distinguish at high dosage rates; however, it is still present, occurring at approximately 13 hours.

The energy curves exhibit a less pronounced increase in shape in comparison to the power curves for the Type E admixture; they do show the accelerating effect of increased dosages, and there is a gradual change in the curvature to a more rounded shape. The slope of the energy curves at 48 hours also increases slightly at the higher dosage rates. Type E admixtures are both accelerators and water reducers; it is possible this effect is again due to more thorough hydration resulting from a more uniform microstructure due to dispersion of cement particles.

3.4.5. Type C Admixture

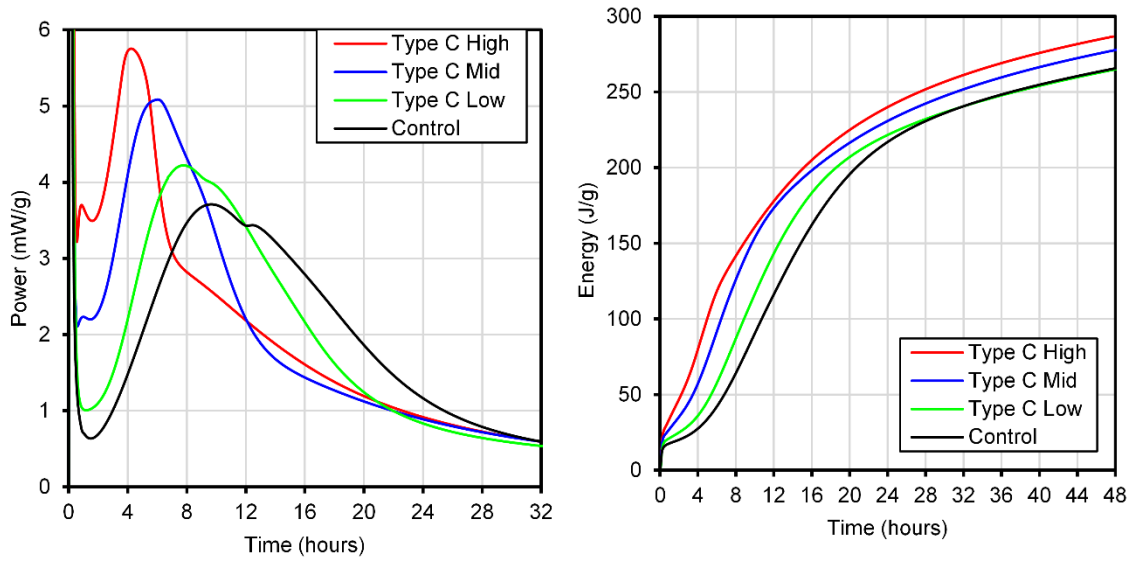

Figure 3-7. Type C/Corrosion Inhibiting Admixture Power and Energy with Time

The power and energy curves obtained for the different dosage rates of the type C admixture (Figure 3-7) exhibit a dramatic change both in the time to reach peak values and the general shapes of the curves. Each successive increase in dosage results an increase in peak height and decrease in time to peak, and an increase in the power generated by the reaction during the "dormant" phase. The highest dosage rate exhibits a "dormant" power generation equal to that of peak power generated by the control. A small peak prior to the bulk phase also appears immediately after the initial peak that corresponds with the addition of water and initial mixing. The type C admixture used for this experiment was calcium nitrite-based; prior work has attributed the increase in peak height to increased ettringite formation [48] in admixtures of this type, though the shape of the peaks observed was not similar to those seen in Figure 3-7.

3.5. Set Simulation Study

Each of the energy curves obtained from different admixture-dosage combinations were used as inputs for hydration simulations. The same combinations were prepared as mortars and tested, adhering to the procedure defined in ASTM C 403. Comparison of the results of the simulations with the measured penetration resistance values requires the definition of equivalent values to provide consistent comparisons for each of the combinations. These equivalent values were developed using the control simulations and penetration resistance testing.

3.5.1. Control Specimen and Calibration

The fraction-solids-connected value computed by the VCCTL and the penetration resistance measurements obtained per ASTM C403 both provide methods to quantify the degree to which the cementitious matrix has become rigid. They do not, however, provide the same types of

measurements. Penetration resistance is a measurement related to the yield stress of the hydrating material, while the solids-connected value provides a direct quantification of the phenomena underlying the behavior of set. These measurements are not directly comparable without some type of calibration. Because the accuracy of the VCCTL with respect to admixture simulation is being called into question by this study, the calibration of the two types of measurements was developed using the controls.

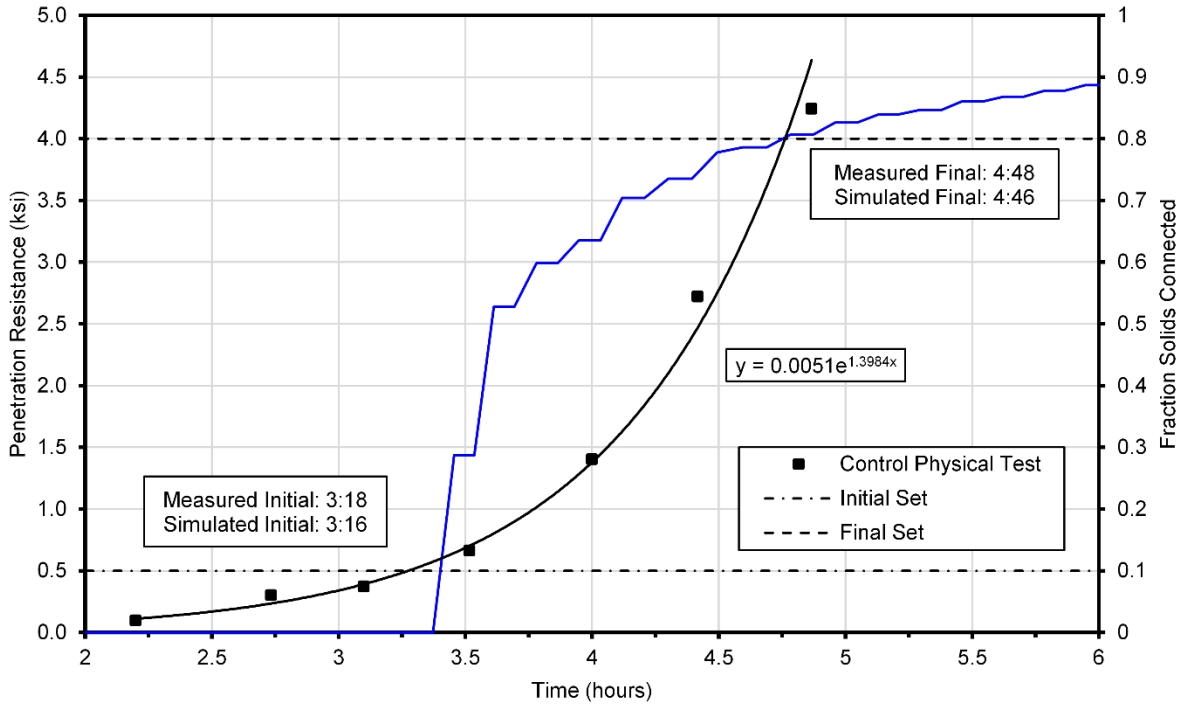

Figure 3-8. Control Simulation and Set Time Test

Figure 3-8 exhibits the penetration resistance development of the mortar on the left axis, with the corresponding values of initial and final set denoted by thin black horizontal lines at the standard locations. The right axis corresponds to the solids-connected values for the two simulation trials. The scales for the vertical axes are set such that every 500 psi of penetration resistance corresponds to a 10% increase in solids connected. This results in the crossover points of the penetration resistance curves and the simulated solids connected values occurring concurrently with initial and final set. Extrapolating from this, the solids connected values that correspond to initial and final set are 0.1 and 0.8 respectively. Regardless of the relative scaling of the y axes, the development of penetration resistance and fraction solids connected values both occur within the same 1-hour window. The equivalent values developed using the controls were used to gauge the effectiveness of all the admixture-dosage combinations examined in this study.

3.5.2. Type D Admixture

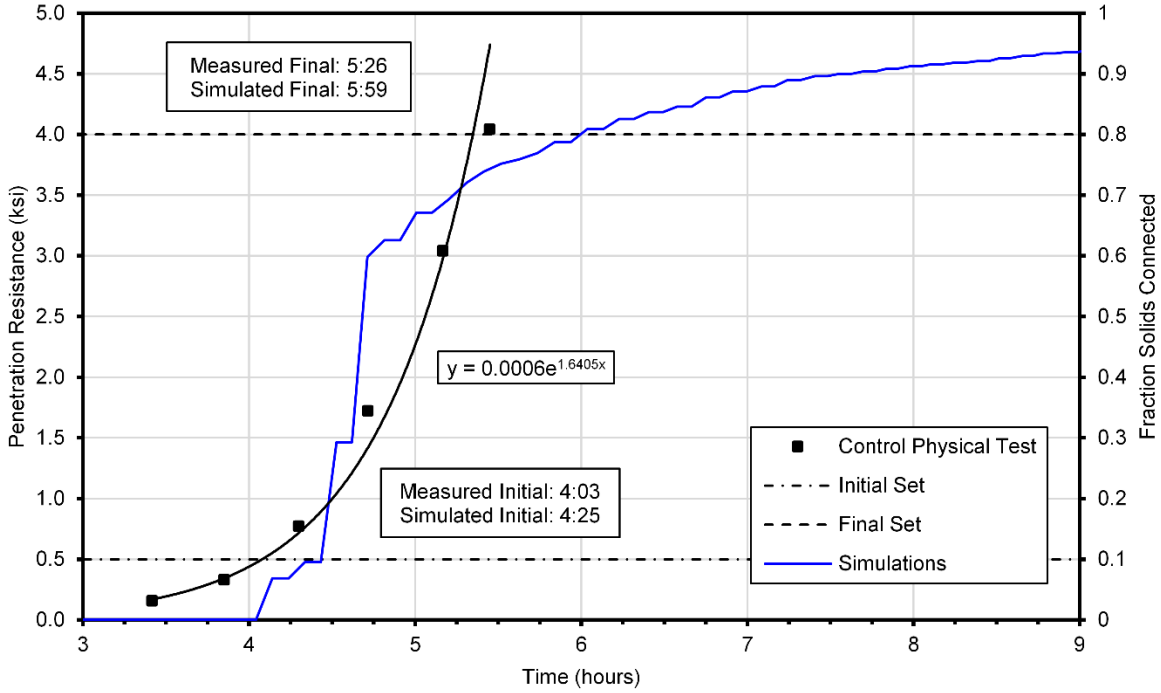

Figure 3-9. Type D low dosage simulation results

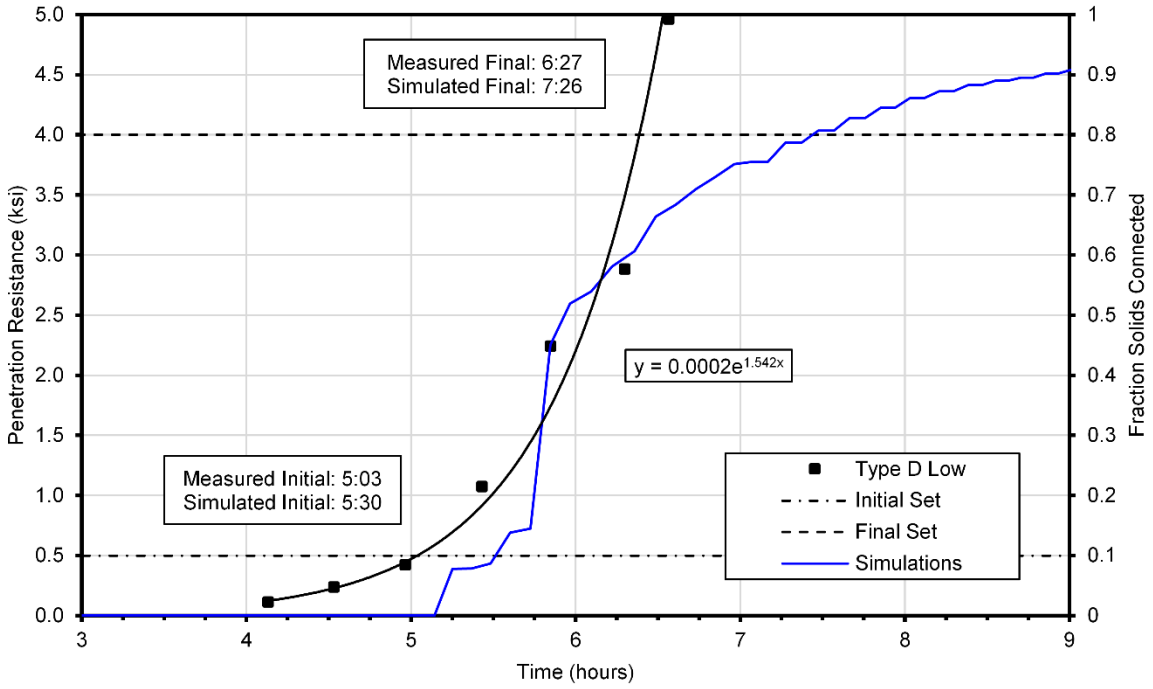

Figure 3-10. Type D middle dosage simulation results

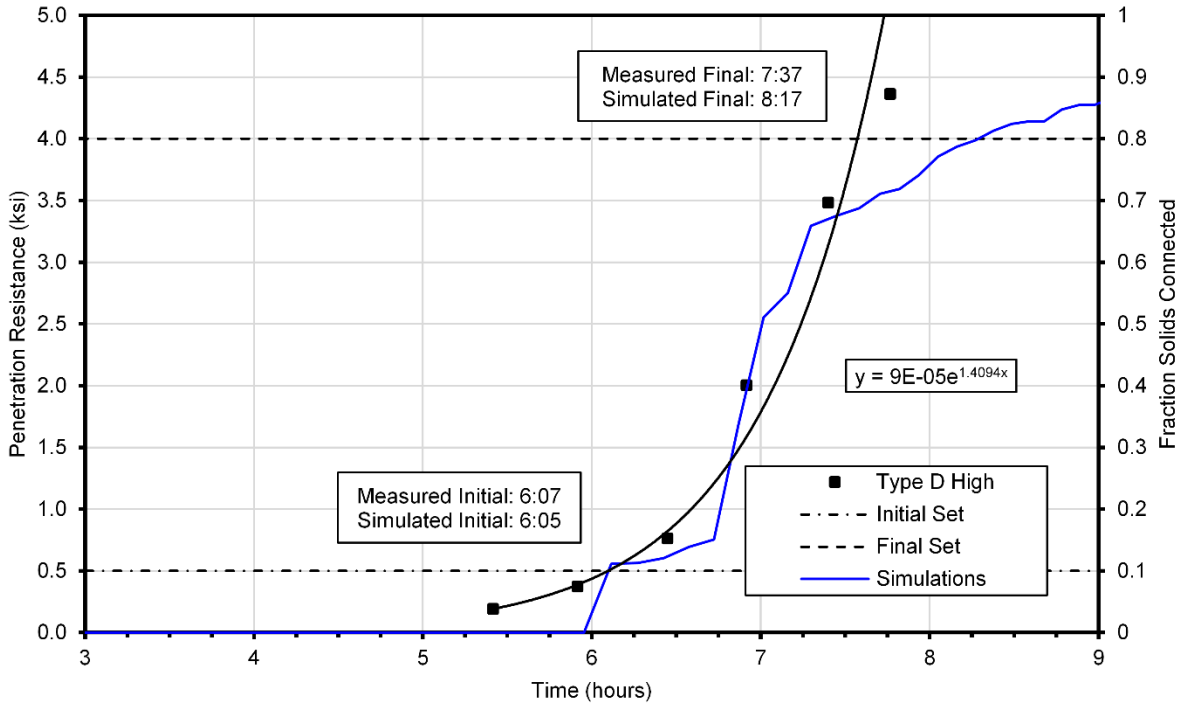

Figure 3-11. Type D high dosage simulation results

Measured initial set times for the type D specimens (Figures 3-9 to 3-11) ranged from 4 hours to 6 hours, while measured final set times ranged from 5.5 to 7.5 hours. The time from initial to final set was approximately 1.5 hours for all dosage rates. The simulated set times generally overestimated time of set by one hour or less. There was no discernable change in the degree of overestimation as dosage increased.

3.5.3. Type F Admixture

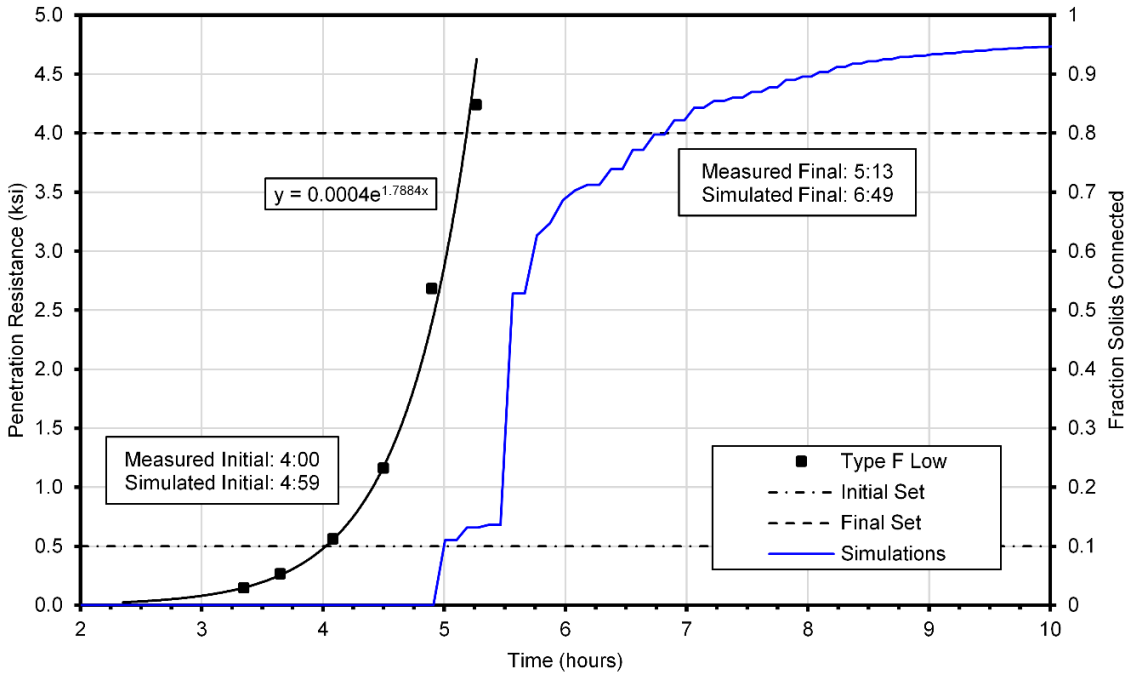

Figure 3-12. Type F low dosage simulation results

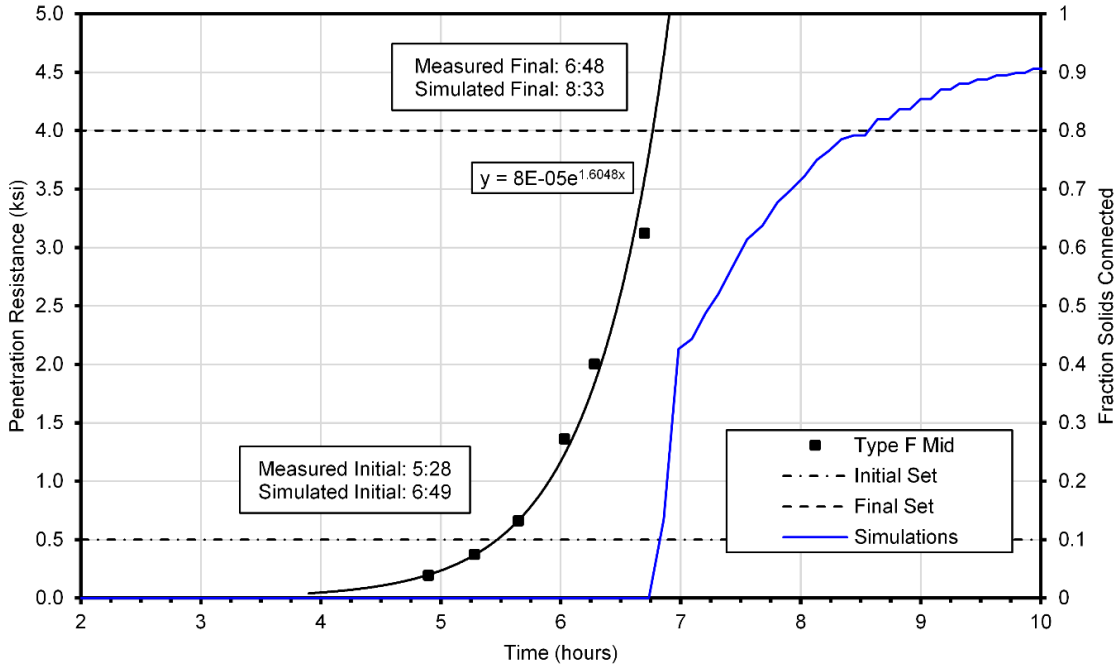

Figure 3-13. Type F middle dosage simulation results

The specimens containing type F admixtures (Figures 3-12 and 3-13) reached initial set at approximately 4 hours for the lowest dose, and 5.5 hours for the moderate dose. Final set occurred just over one hour after initial set in both cases. A larger discrepancy between simulated and measured set times resulted with the type F specimens, with an overestimation of more than one hour for initial set and nearly two hours for final set. As with the type D admixture, no trend was observed with admixture dosage. The highest dosage of type F admixture is notably absent from the simulations; the combination of the relatively high water-to-cement ratio of 0.45 and a maximum dosage of type F admixture resulted in a mixture with excessive segregation, rendering the sample unsuitable for penetration resistance measurements.

3.5.4. Type E Admixture

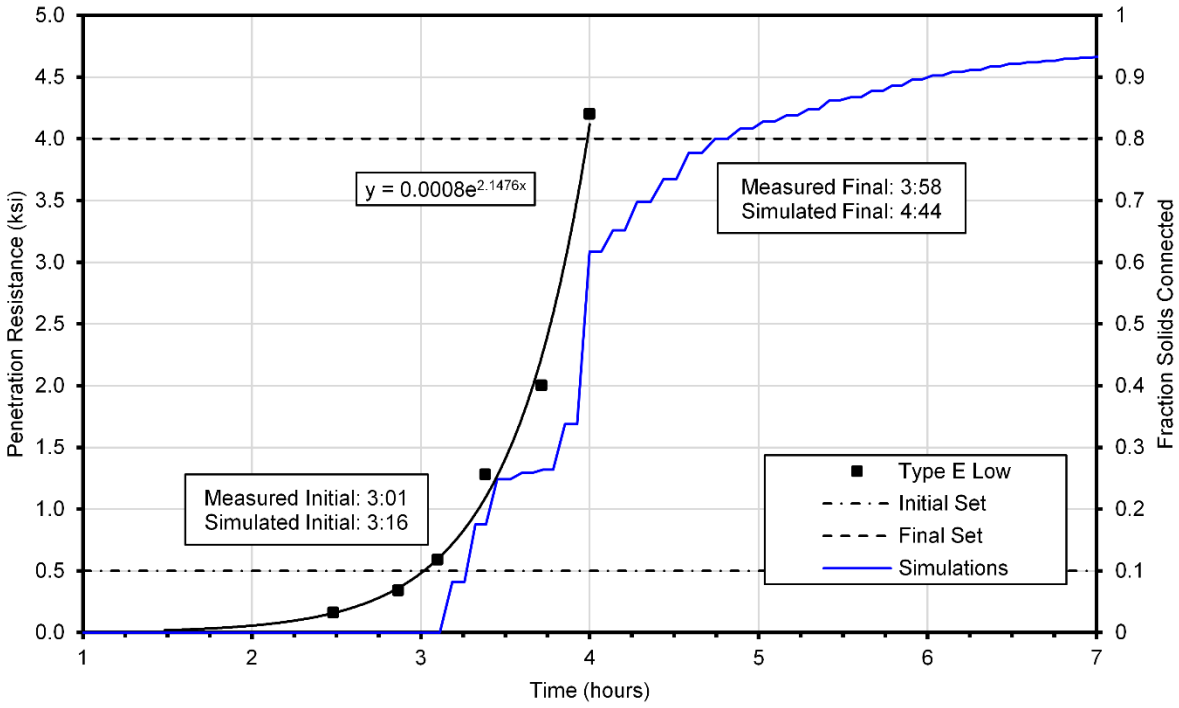

Figure 3-14. Type E low dosage simulation results

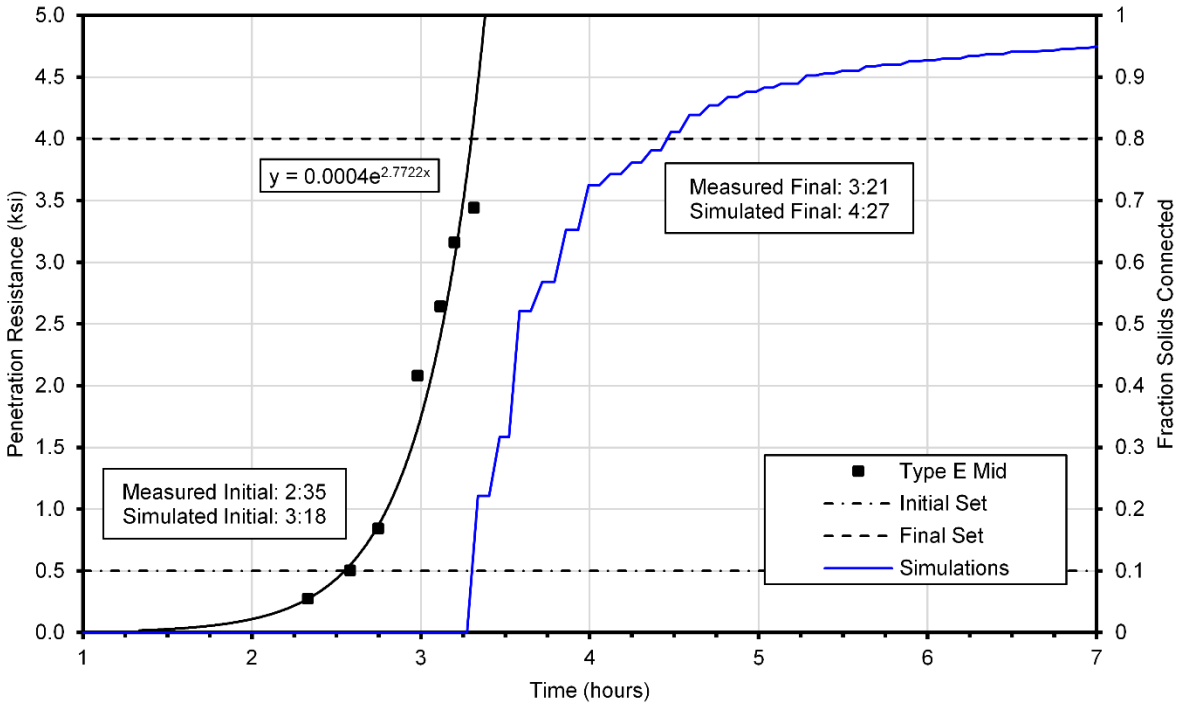

Figure 3-15. Type E middle dosage simulation results

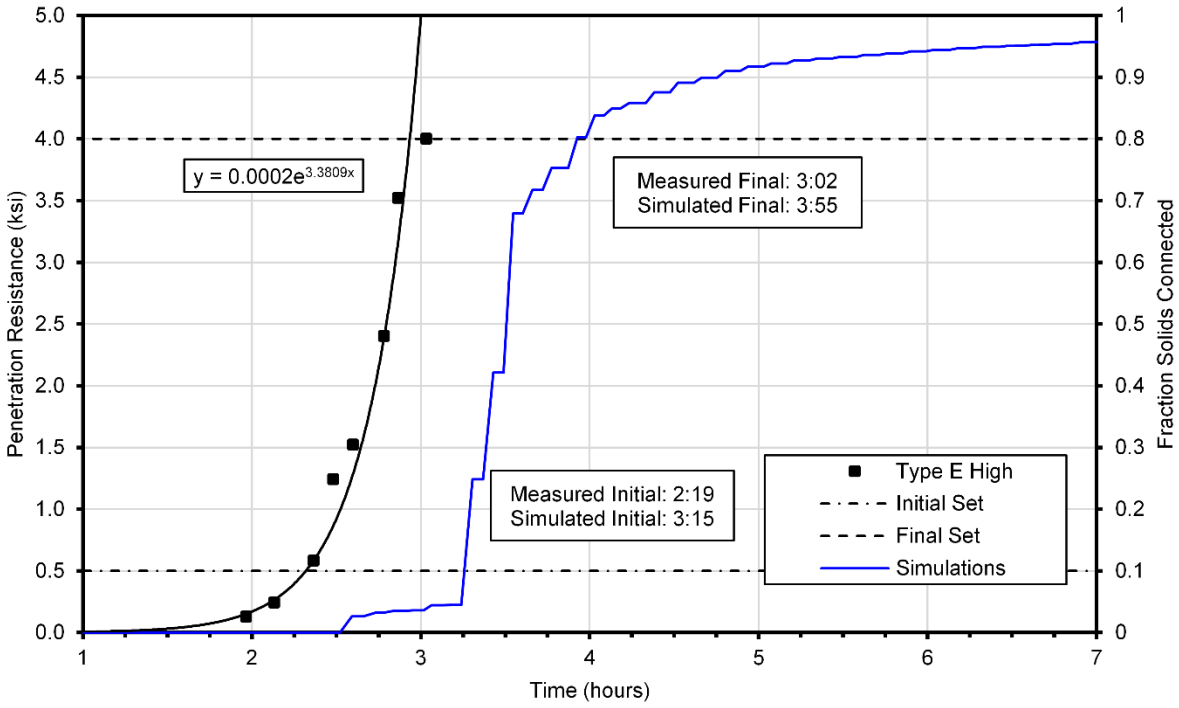

Figure 3-16. Type E high dosage simulation results

Measured initial set times for the specimens containing type E admixture (Figure 3-14 to 3-16) decreased with increasing dosage, ranging between 3 hours and 2.25 hours, while final set occurred between 1 hour and 0.5 hours after initial. The development of penetration resistance was more rapid as the admixtures dosage increased. Simulated initial and final set occurred later than measured results for all dosages, with an increase in error as dosage rose.

3.5.5. Type C Admixture

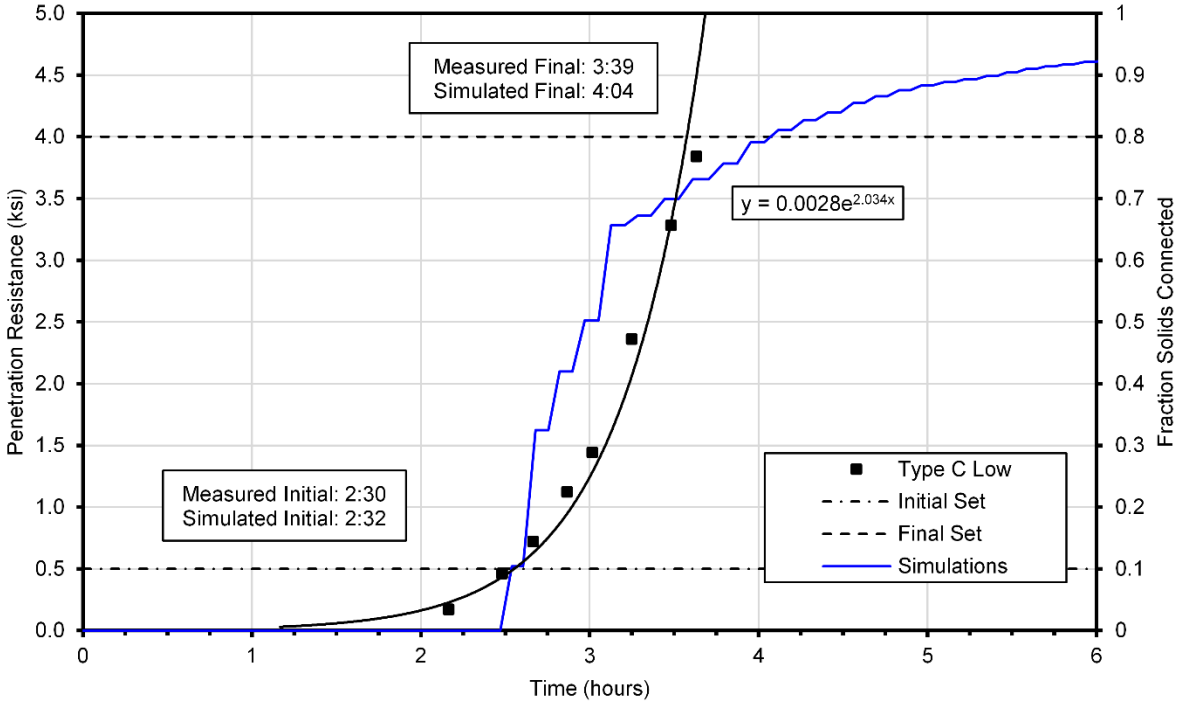

Figure 3-17. Type C low dosage simulation results

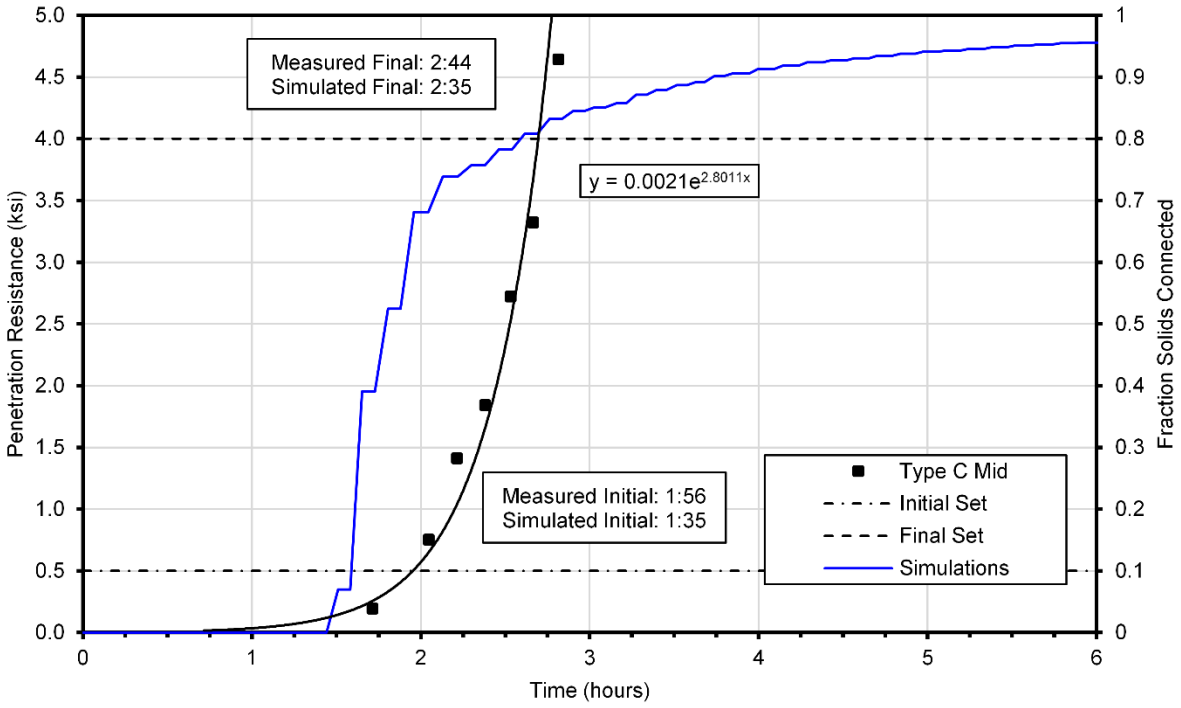

Figure 3-18. Type C middle dosage simulation results

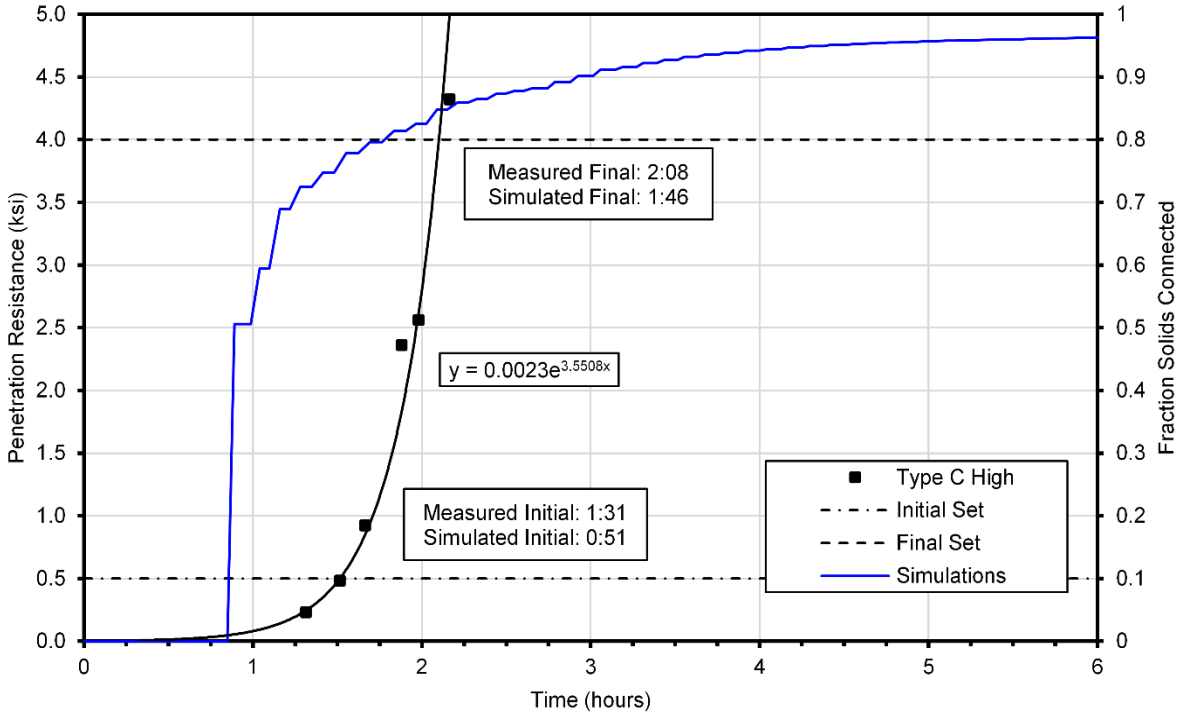

Figure 3-19. Type C high dosage simulation results

Initial set for the type C specimens (Figure 3-17 to 3-19) occurred at approximately 2.5 hours for the low dosage, 2 hours for the moderate dosage, and 1.5 hours for the high dosage. Time to final set occurred approximately 1 hour to 30 minutes later, decreasing as dosage increased. Simulated set times agreed with measured values at the lowest dosage, and began to underestimate set time, particularly initial set, as dosage increased.

3.6. Discussion and Conclusions

Table 3-3. Summary of Measured and Simulated Set Times

Admixture		**Type D**			**Type F**		**Type E**			**Type C**		
Dosage	Control	Low	Mid	High	Low	Mid	Low	Mid	High	Low	Mid	High
Measured Initial	03:18	04:03	05:03	06:07	04:00	05:28	03:01	02:35	02:19	02:30	01:56	01:31
Simulated Initial	03:16	04:25	05:30	06:05	04:59	06:49	03:16	03:18	03:15	02:32	01:35	00:51
Measured Final	04:48	05:26	06:27	07:37	05:13	06:48	03:58	03:21	03:02	03:39	02:44	02:08
Simulated Final	04:46	05:59	07:26	08:17	06:49	08:33	04:44	04:27	03:55	04:04	02:35	01:46
Initial Set Error (m)	00:02	00:22	00:27	00:02	00:59	01:21	00:15	00:43	00:56	00:02	00:21	00:40
Final Set Error (m)	00:01	00:33	00:59	00:40	01:36	01:45	00:46	01:06	00:53	00:25	00:09	00:22

The addition of early-age heat of hydration data to VCCTL produces very accurate results when predicting the set time for unmodified mortar. The results of the initial and final set predictions for the control specimen agree with the measured results via penetration resistance to within less than 10 minutes. A convenient metric for evaluation of the viability of the predicted set times can be found within ASTM C403. This standard specifies maximum multi-operator precision values for initial and final set of 19.4 minutes and 28.7 minutes respectively; the simulated set time values for the control are well within these limits. The accuracy of the results for the control specimen supports the methodology of maximum realism when selecting parameters for simulations.

For certain types of admixtures, the incorporation of heat of hydration data into the VCCTL allows for useful prediction of time of set. Simulations for type D water reducer were slightly higher than the multi-operator precision values for initial setting at low and moderate dosages, and within two minutes at the highest dose. The final setting projections for the low dosage was also slightly higher than the values specified in ASTM C 403. For type C admixtures, predictions for all dosage rates were within multi-operator precision with the exception of initial set at the moderate and high dosages.

The type F admixture used in this study exhibited the largest discrepancies between the simulated and measured values. Farrington [49] observed significant differences between the setting and heat release behavior of paste and mortar with polycarboxylate admixtures; both the induction period and setting time for pastes were found to occur several hours after those of prepared or sieved mortars. The discrepancy was attributed to a combination of factors including greater cement dispersion in mortars, differences in mixing shear, and a larger amount of surface area for admixture adsorption. Regardless of the mechanism underlying the discrepancies between mortar and paste containing polycarboxylates, the experiments performed in this study confirm that the difference is significant, and is likely the reason behind the inaccurate setting times from the VCCTL for type F admixtures. It is possible that similar effects are responsible for the poor predictions of setting for the type C admixture; however, further investigation is required.

Generally speaking, the accuracy for predictions of mixtures containing admixtures decreased as the dosage of the respective admixture increased. The deviation of the predictions from reality with increasing dosage is likely a reflection of the nature of the hydration simulation. To some extent, supplying a characteristic heat of hydration curve for each admixture does compensate for the resulting change in setting time; however, the simulations do not take into account any possible changes to the chemistry of the hydrating specimen. As dosage increases, the chemical discrepancies between the behavior of the virtual and physical hydrations become more extreme. It is likely that the thermal behavior of admixtures in concrete is only part of the information required to accurately simulate early-age properties.

Several conclusions can be drawn directly from the results presented in this study:

1. The VCCTL can be used to accurately predict the time of set in mortar incorporating specific admixtures based on the techniques developed herein.

2. For all admixtures, the incorporation of specific heat of hydration data improves predictions when compared to the control simulation; for the type D and type C admixtures these predictions approach or exceed the level of precision specified by ASTM C403.

3. The VCCTL predicts initial and final set of plain portland cement paste to within an accuracy of 5 minutes when calibrated with a heat of hydration curve.

4. For setting tests that are performed using standardized equipment in consistent environmental conditions, the temperature rise in mortar can be accurately approximated by the VCCTL using the semi-adiabatic thermal condition.

5. Predictions using the technique presented herein did not produce accurate results for mortar mixtures which contain type F water reducing admixtures. This can be attributed to differences in the setting and heat release behavior of pastes and mortars containing polycarboxylate admixtures.

4. VCCTL PROFICIENCY ANALYSIS FOR MORTAR COMPRESSIVE STRENGTH AND CEMENT HEAT OF HYDRATION

4.1. Background

The virtual cement and concrete testing laboratory is a portland cement hydration modeling package active development, with the ultimate goal of supplementing and potentially replacing resource intensive physical testing and certification. An important part of the development process for any model is validation; small scale validations of the VCCTL have been performed; however, to consider this model a true "virtual laboratory" it should be evaluated using the same metrics applied to real cement testing and qualification laboratories. The cement and concrete reference laboratory (CCRL) curates a proficiency sample program (PSP), that enables participating laboratories to gauge the precision and accuracy of their testing programs against the pool of participating labs. As many as 1100 laboratories participate in this program, and the resulting data is publicly available.

A large number of simulations would be required to perform a virtual proficiency analysis using the data available from CCRL as input to the VCCTL. Integration of the model with the UF HiperGator computing cluster has enabled retroactive participation in the proficiency sample program through simulation of approximately 11,000 virtual cements. Approximately 150 measured cement compositions for each of 20 reference cements were simulated; two sets of simulations were performed for each cement, with different approaches to the adaptation of available CCRL data to the required VCCTL inputs. The simulated results for heat of hydration and mortar compressive strength were ranked using metrics defined by CCRL, and compared to measured results from the proficiency sample program.

4.2. Introduction

The Virtual Cement and Concrete Testing Laboratory (VCCTL) is a cement hydration modeling package intended to supplement physical testing and qualification of portland cement-based materials. As the VCCTL and its predecessor, Cemhyd3d, have been developed, validations of predictive accuracy have been performed. Past studies [34,50] have compared simulated results to the plastic and hardened properties of reference cements. Inputs for these simulations were the product of a single characterization for each cement, using procedures outlined by Stutzman & Bentz (1994) to measure the phase specific volume and surface area fractions for the cement, combined with laser particle size analysis (LPA) to obtain a particle size distribution. These procedures provide all of the input data required by the VCCTL; however, simulation results are completely dependent upon one measurement of the cement properties.

The cements utilized for these validations were sourced from the Cement and Concrete Reference Laboratory (CCRL), which distributes reference cements to participating laboratories on a biannual basis. These laboratories perform a number of standard tests to characterize the properties of the raw material along with plastic and hardened properties. Laboratories report results to CCRL, which compiles and publishes reports summarizing the data collected. Samples are distributed and tested in pairs, to enable the identification of laboratory bias [51], and

statistics for each set of test results are calculated to provide an indication of the precision of the test method [52].

Several of the tests performed as part of the CCRL program characterize properties of the raw cement required for input to the VCCTL, including composition via XRF (ASTM C114) and the Bogue equations, as well as specific surface area via Blaine fineness (ASTM C204). For these tests there are generally more than 150 reported measurements per reference cement. The use of each measurement of composition and fineness as input for the VCCTL would allow the precision of these measurements to be captured, and enable direct comparison of the precision and accuracy of simulated outputs to their corresponding experimental values. To implement this type of comparison each cement composition requires an individual simulation, and some assumptions must be made use the CCRL data as input to the VCCTL.

The VCCTL is generally used on an ordinary desktop workstation, where a 28-day simulation takes one to two hours to complete using modern hardware, depending on input options selected and outputs required. Because the software is open source, it can be compiled and run in a large scale UNIX compute cluster; in many cases such clusters have thousands of cores available for simulation. For this study, the VCCTL was run in the University of Florida's HiperGator compute cluster, with 500 cores dedicated to running simulations. This eliminated the time penalty associated with running more than 150 unique compositions for 22 reference cements. Batch generation of simulation input files and batch processing of output files was handled using custom Matlab scripts.

4.3. Experimental Methodology

4.3.1. Composition and Fineness Inputs

The execution of simulations using the composition and fineness data provided by the CCRL requires a number of assumptions to be made, as the data available provides less information than that obtained using the methods developed for use with the VCCTL. The composition data reported to CCRL only provides mass percentages for the four clinker phases, and while the specific surface area measurement obtained via air permeability serves as a useful quality control measurement, it simply does not provide enough information to create a particle size distribution.

For the composition inputs required by the VCCTL, the mass fractions reported for each cement were used as is and simply converted to volume fractions using density values for each phase [53]. The surface area fractions were assumed to be equal to the volume fractions for each phase. This assumption is unlikely to be strictly accurate; however, literature indicates that there is no definable relationship between surface area and volume fractions [54,55]. The sulfate mass fractions required by the VCCTL were supplied using the SO_3 oxide compositions measured via XRF; the mass fraction of sulfate was assumed to be entirely dihydrate (gypsum).

To provide the needed particle size distribution data using available measurements of specific surface area, the database of particle size distributions included in the VCCTL was utilized. Each of the cement compositions reported in the CCRL database had an associated measurement of specific surface area; each particle size distribution present in the VCCTL

database has a corresponding specific surface area measurement. Because it is impossible to generate a particle size distribution using only a specific surface area measurement, a particle size distribution was instead selected from one of six taken from the VCCTL database, with specific surface area values ranging from 250-500 m^2/kg in 50 m^2/kg increments. This approach in no way attempts to match the particle size distribution of the CCRL cement, it merely ensures that the distribution used for simulation has a similar specific surface area to that measured via Blaine fineness.

In addition to approximate method of selecting a PSD from the VCCTL database using Blaine number, physical specimens for as many CCRL cements as possible were obtained. Their particle size distribution was measured using a laser particle size analyzer. Cement samples were dispersed in ethanol for measurement; a refractive index with a real component of 1.7 and an imaginary component of 1.0 was used. In total 22 reference cements were analyzed; the resulting particle size distributions (Figure 4-1) were used for each set of composition measurements for a given cement. Though the use of the same particle size distribution for all samples of a particular cement reduces the variability of the model inputs, it provides a more direct measurement of particle size than picking an approximate distribution based on Blaine number.

Standard test methods were used to define required simulation inputs beyond raw cement properties. Simulations for measurement of compressive strength used water to cement and sand to cement ratios of 0.485 and 2.75, respectively, as specified in ASTM C109. Because this standard specifies moist curing conditions for the duration of specimen storage, saturated curing conditions were used in the simulations. Testing for compressive strength of mortar cubes requires the use of a sand with a standard gradation as defined in ASTM C33, this gradation was used as required for prediction of elastic modulus and compressive strength. These predictions also require bulk and shear moduli for the aggregates; in this case values of 36.4 GPa and 31.1 GPa were used, consistent with the bulk and shear moduli for quartz (reference). For heat of hydration tests, ASTM C1702 requires the water to cement ratio to be no less than 0.4, and stipulates that additional water may be needed to obtain good mixing. The virtual water to cement ratio was set at 0.5, and the curing conditions were defined as sealed, to replicate the lack of additional water in an isothermal calorimeter cell. It is important to note that the selection of model inputs using the relevant test standards assumes that laboratories participating in the CCRL proficiency program followed the standards exactly.

Several other inputs required for virtual testing were selected based on default values or assumptions. The value for the time/cycle^2 constant, β, was left at the default value of 0.00035, and held constant for all simulations performed as part of this study. Because of the large number of simulations performed, the virtual microstructures were constructed with spherical particles. No particle shape data was available for the specific cements considered in this study, and microstructure generation with realistic particle shapes takes approximately twice as long as with spherical particles.

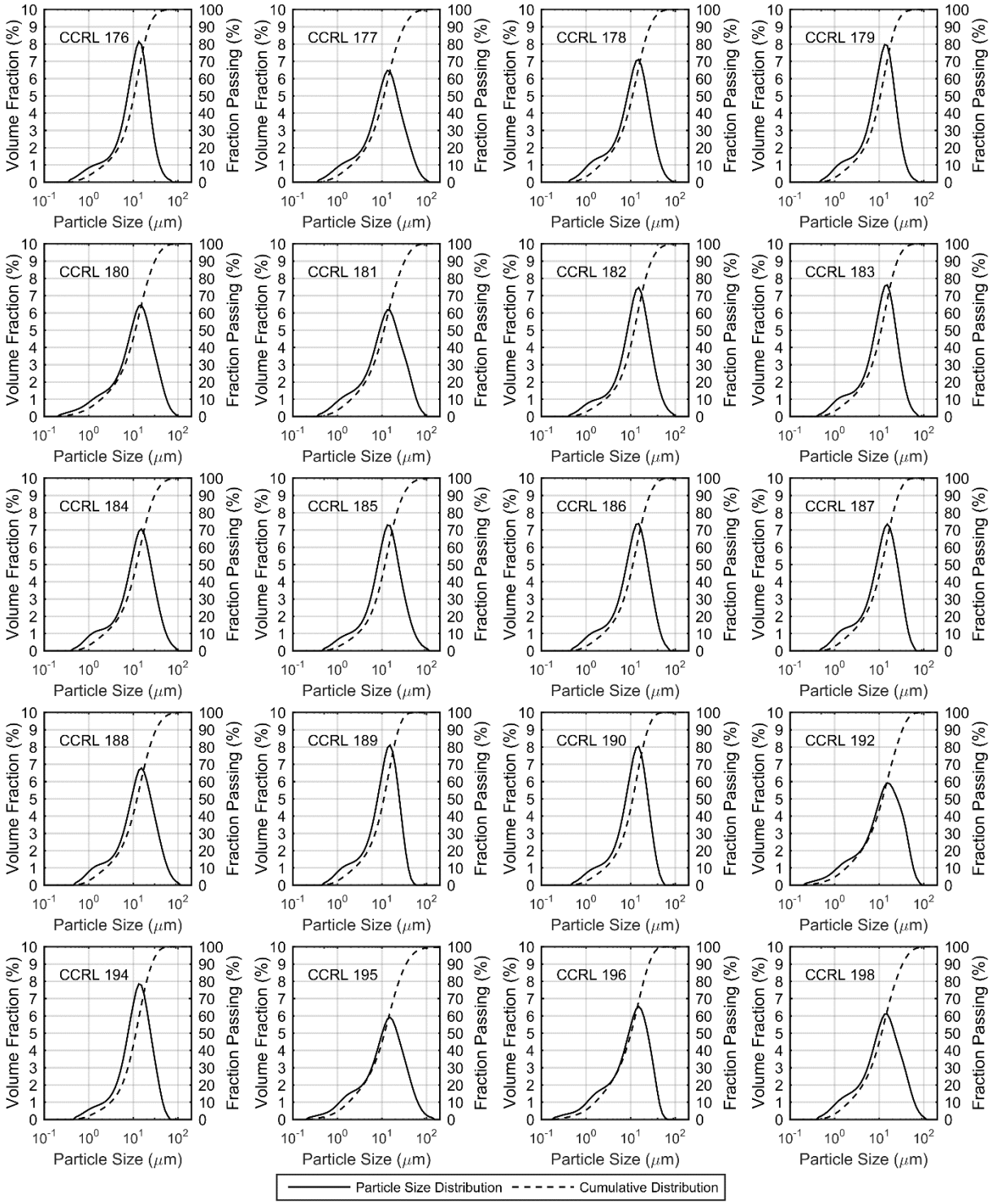

Figure 4-1. Cumulative and particle size distributions for type I, II, and III cements considered in this study

The thermal conditions for virtual heat of hydration and compressive strength tests were both defined as isothermal; for heat of hydration testing the real conditions are isothermal, and it was assumed that any temperature rise in the mortar cubes was negligible, due to the small size of the specimens. For calculations of mortar elastic modulus performed as part of virtual strength testing, the option to omit the ITZ calculations exists; however, for this study the effects of the ITZ were included.

4.3.2. Comparison of Simulations to Experimental Data

The simulated mortar and heat of hydration results were compared directly to the experimental results using the two methods for particle size input. Heat of hydration simulations were performed out to three and seven days, and compared to results obtained via ASTM C1702. Heat of hydration data via ASTM C186 was also available for comparison to the results of seven-day simulations. Simulations for compressive strength were measured at both three and seven days, and compared directly to the corresponding CCRL measurements.

The purpose of the laboratory proficiency program is ultimately to provide feedback to laboratories on the accuracy of the standard tests they run. A simple ranking system is applied by CCRL to provide a metric for individual laboratory performance; laboratories are assigned a numeric rank from five to one for each different test, based on the number of standard deviations between their respective measurement and the mean of the measurements reported. A rank of five is assigned to all laboratories whose measurements fall within one standard deviation of the mean; the rank decreases by one for each additional half standard deviation. Any laboratory whose measurement falls more than 2.5 standard deviations from the mean is assigned a rank of 1. The intent of this study is to evaluate the VCCTL in the same manner as any other laboratory participating in the proficiency sample program, so the ranking system used by CCRL has been applied to the predictions for a given cement. While the lowest ranking assigned to a laboratory by CCRL is a 1, any reported values that fall more than three standard deviations away from the mean are typically eliminated from the dataset. To reflect this, any of the virtual test results that were more than three standard deviations away from the mean was assigned a rank of zero. Unlike a normal laboratory participating in the PSP, each virtual test consisted of one prediction for each cement composition simulated. The rank of the prediction was instead calculated as the difference between the means of the CCRL reported and simulated data sets. Each pair of CCRL cements considered in this study has a corresponding sample report, which includes information about the origin of the cements, their type per ASTM C150, and a summary of any anomalous behavior observed during the testing program. The cements considered included samples 176 through 198; samples 191 and 197 were eliminated from consideration due to reported false setting tendencies, while sample 193 was eliminated due to its classification as a type V cement per ASTM C 150.

4.4. Results

4.4.1. Virtual Strength Testing

The virtual compressive strength results (Figure 4-2) at three days of age were generally lower than the experimental data. The average rank for the approximate PSD method was 1.8,

while the measured PSD inputs resulted in an average rank of 1.0. These ranking indicate that both methods were more than 2.0 standard deviations away from the mean of the experimental data. The seven-day compressive strength results (Figure 4-3) exhibited a similar trend of under prediction, with average rankings of 2.95 and 1.35 for the approximate and measured PSDs respectively.

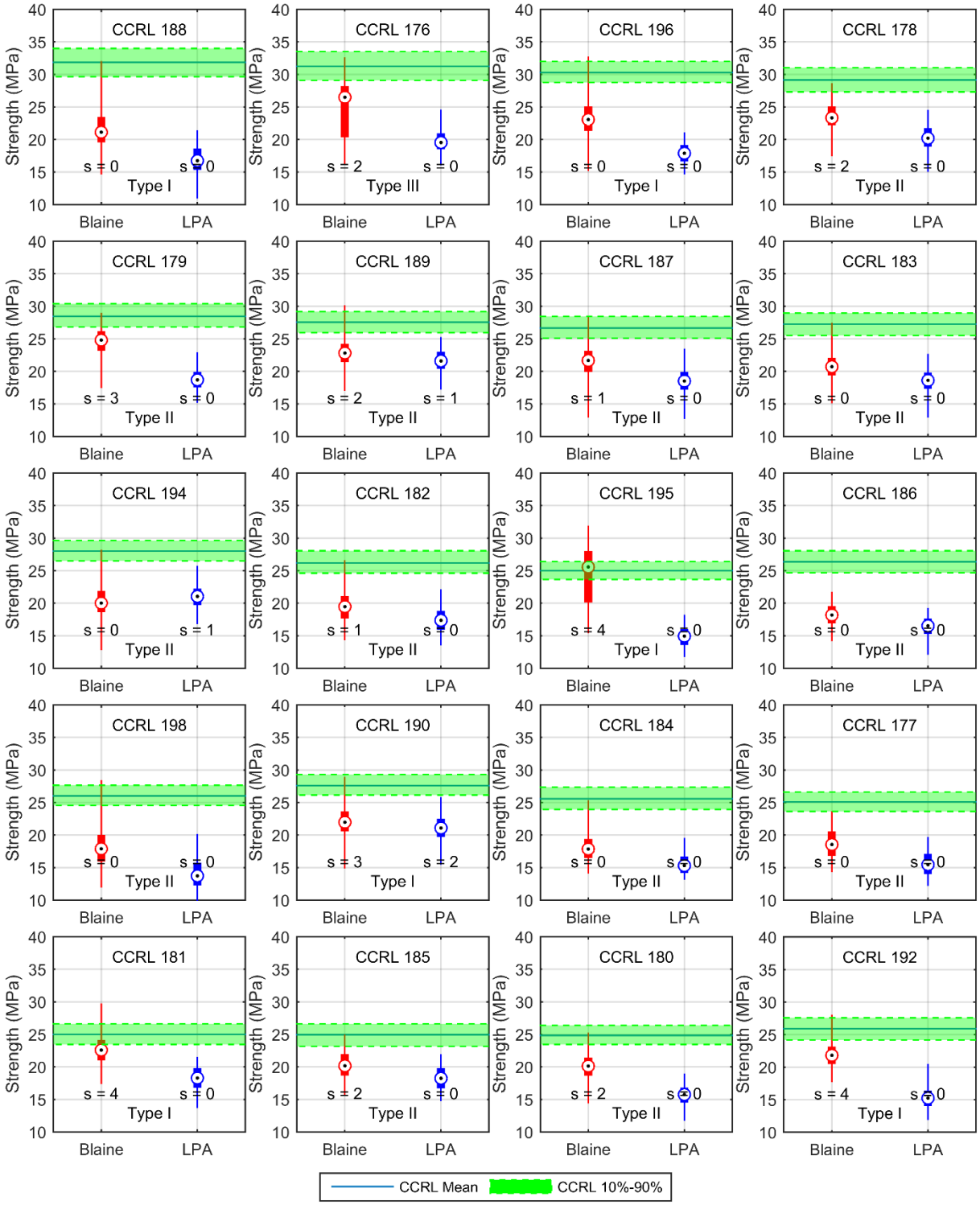

Figure 4-2. Comparison of predicted three-day compressive strength using two methods for particle size input to the experimental results measured according to ASTM C109

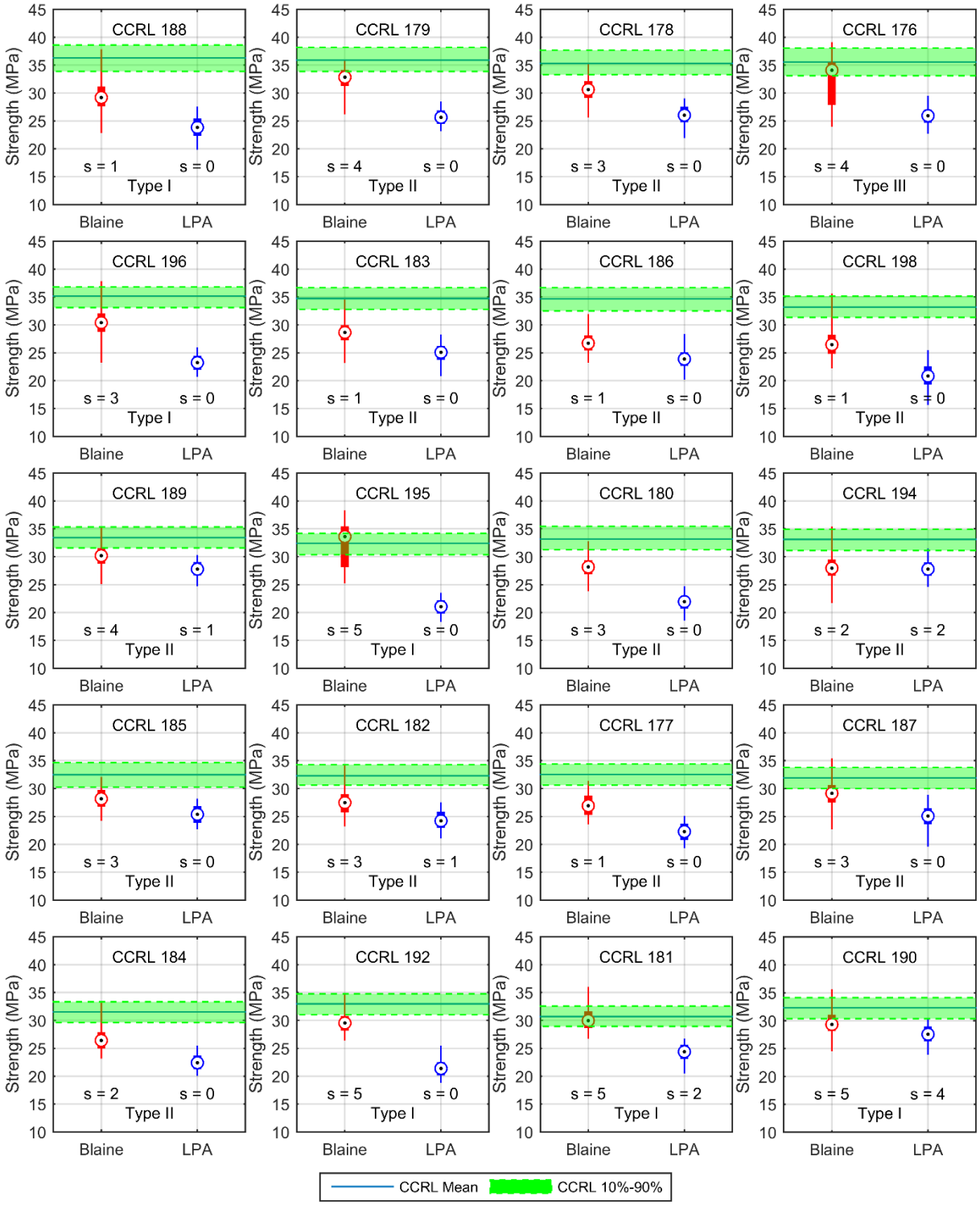

Figure 4-3. Comparison of predicted seven-day compressive strength using two methods for particle size input to the experimental results measured according to ASTM C109

4.4.2. Virtual Heat of Hydration Testing

The results of three-day heat of hydration simulations (Figure 4-4) generally agree with the experimental data, though there is variability in the laboratory rank assigned to the predictions. Variation in the spread of the experimental data appears to influence the rank independently of the proximity of the prediction to the experimental mean. This variation in spread may be the result of the limited number of experimental measurements available for this test. The difference between the use of Blaine-approximated PSDs and the experimentally measured PSDs can be seen in the average laboratory rank across all cements; the approximate method had an average ranking of 3.2, while the experimentally measured PSDs resulted in an average rank of 3.8. Based on these rankings, the predictions for the virtual laboratory were within an average of 2 standard deviations away from the mean.

Predictions for 7-day heat of hydration per ASTM C1702 (Figure 4-5) also show good agreement with experimental data. Variability in the spread of the experimental data still exists; however, fewer low ranking predictions are present. The average rank for the approximate approach was 4.4, while the predictions using measured PSDs had an average rank of 4.8. This places the average predictions for both methods within 1.5 standard deviations of the mean for seven-day heat of hydration. The virtual measurements are comparably accurate when compared to the 7-day heat of hydration values per ASTM C186 (Figure 4-6) with average rankings of 5.0 and 4.8 for the approximate and experimentally measured PSDs respectively. The comparison of virtual test results to the heat of hydration results per ASTM C186 was the only case for which the simulations using measured PSDs performed worse than those with approximated PSDs.

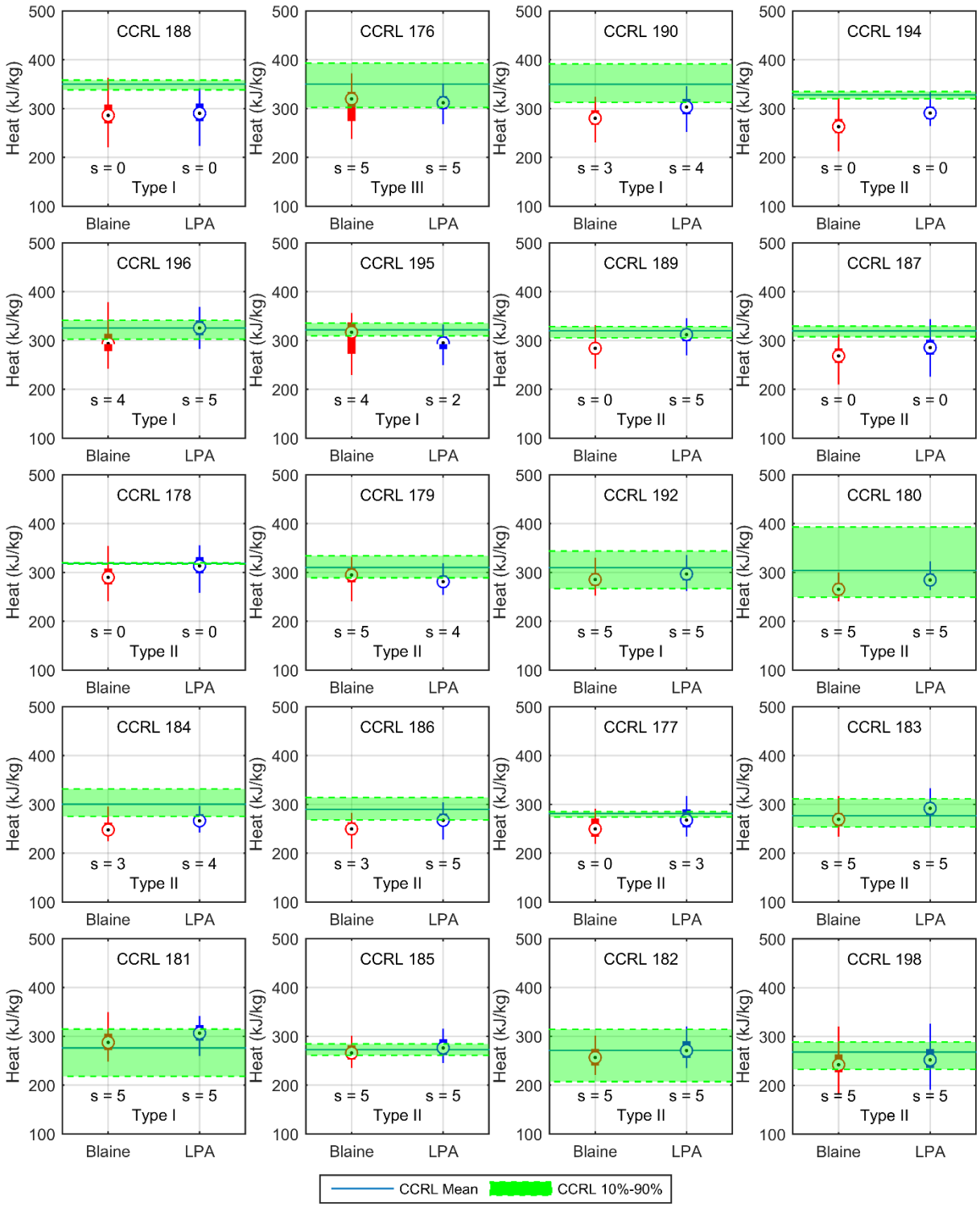

Figure 4-4. Comparison of predicted three-day heat of hydration using two methods for particle size input to the experimental results measured according to ASTM C1702

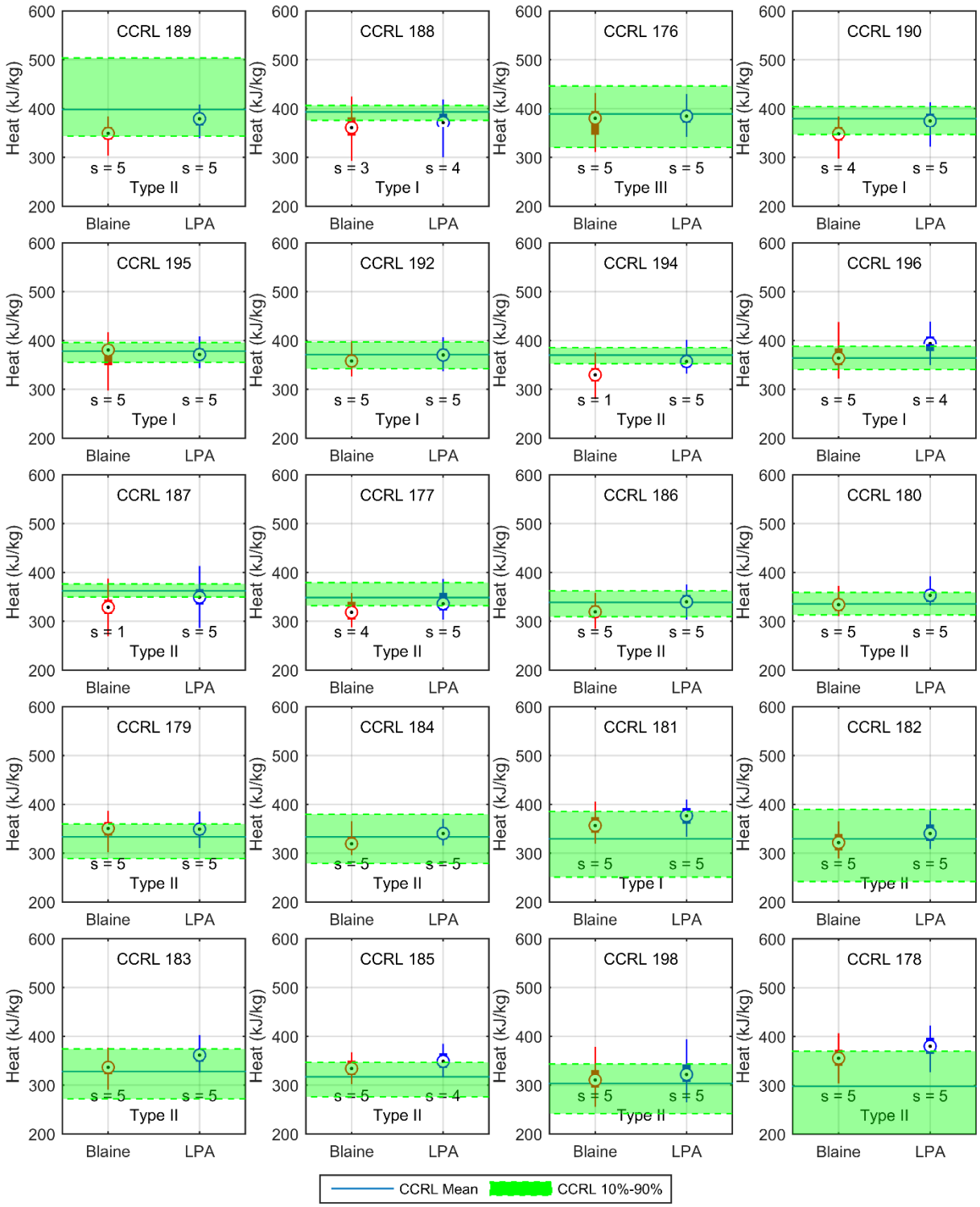

Figure 4-5. Comparison of predicted seven-day heat of hydration using two methods for particle size input to the experimental results measured according to ASTM C1702

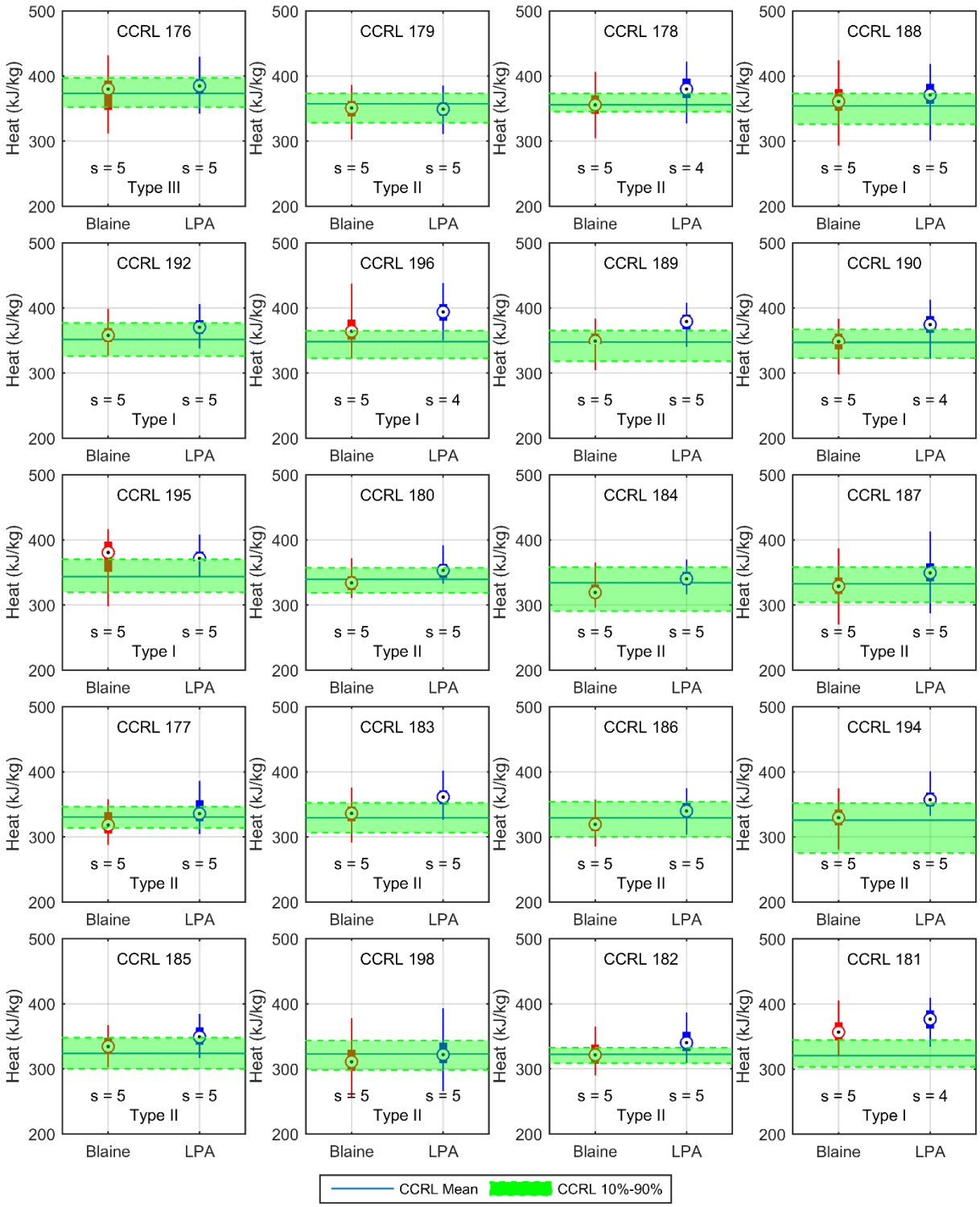

Figure 4-6. Comparison of predicted seven-day heat of hydration using two methods for particle size input to the experimental results measured according to ASTM C186

4.5. Discussion

4.5.1. Heat of Hydration Prediction

The overall results for heat of hydration prediction were favorable, with the 7-day results outperforming the 3-day results regardless of the fineness input used. An important consideration when evaluating the performance of the virtual laboratory is the significance of the ranking system used by CCRL. While any laboratory whose measurement deviates by more than 2.5 standard deviations from the mean of the reported values is assigned a rank of one, reported values that fall further than 3 standard deviations away from the mean are generally eliminated from the reported results. The seven-day predictions for both particle size input methods had no measurements rejected, and the average ranking for seven-day predictions indicates that the virtual laboratory consistently predicts heat of hydration to within 1.5 standard deviations of the experimental mean.

4.5.2. Modified Strength Predictions

To understand the generally poor predictions of mortar compressive strength, a more detailed overview of prediction methodologies may be useful. Prediction of strength by the VCCTL has been implemented in two different ways as the model has evolved. The original method for calculation of compressive strength utilized an equation derived by Mindess [35] using published data in combination with a defined relationship between the gel-space ratio and the degree of hydration [56]. The resulting equation is as follows:

$$X = \frac{0.68\alpha}{0.32\alpha + \frac{w}{c}} \qquad (4\text{-}1)$$

where α is the degree of hydration, and w/c is the water to cement ratio of the cement paste. The degree of hydration output from the VCCTL was used to compute the gel-space ratio over time; strength could then be calculated from the gel space ratio for a specific age [18,33,57] per the following relationship:

$$\sigma_c(t) = \sigma_A X(t)^n \qquad (4\text{-}2)$$

where σ_A is the intrinsic strength of the cement and n varies between 2.6 and 3.0 based on the cement in question [35]. This method relied on an experimentally measured 3-day mortar strength to first solve for σ_A assuming a value of 2.6 for n [18,33,57]; the evolution of compressive strength over time was then calculated per Eq. (4-2).

The second and current method for prediction of compressive strength in the VCCTL is based on the computed elastic modulus of the paste, mortar or concrete. Strength is then calculated using an empirical relationship [19,33] based on equations described by Neville [36]. As of software version 9.5.3, the equation in the source code [24] used for the prediction of compressive strength of mortar cubes is as follows:

$$f'_c = (5.0 * 10^{-4}) E^{3.18577} \qquad (4\text{-}3)$$

where E is the elastic modulus of the mortar in gigapascals. A limited number of other relationships between the compressive strength and modulus of mortar can be found in literature. Kosaka and Tanigawa [58] proposed eqn. 4-4;

$$f'_c = e^{\left[\frac{\frac{E}{1000}+5.5}{7.7}\right]} \qquad (4\text{-}4)$$

while Valentini et. al [59] developed a relationship (eqn. 4-5) similar to that used in the VCCTL based on measurements of elastic modulus of mortar prisms and compressive strength mortar cubes

$$f'_c = (3.79 * 10^{-3})E^{2.6} \qquad (4\text{-}5)$$

This relationship was used to calculate the compressive strength of mortars from elastic moduli predicted by the VCCTL, with very good agreement for the mortars considered in the study.

A bisquare weights power fit of the CCRL compressive strength data to the elastic modulus values simulated with measured PSDs (Figure 4-7) produces a relationship (4-6) similar in format to equations 3 and .

$$f'_c = 0.08221E^{1.77} \quad (4\text{-}6)$$

The new equation for prediction of compressive strength was developed using the virtual results computed with measured particle size distributions based on the performance of that method in heat of hydration predictions. For both three- and seven-day measurements of isothermal heat of hydration this method performed better than the approximate PSDs based on the average laboratory ranking, and though the virtual laboratory ranking average using measured PSDs was slightly lower for the heat of solution data, this approach produced consistently higher rankings across test methods and ages.

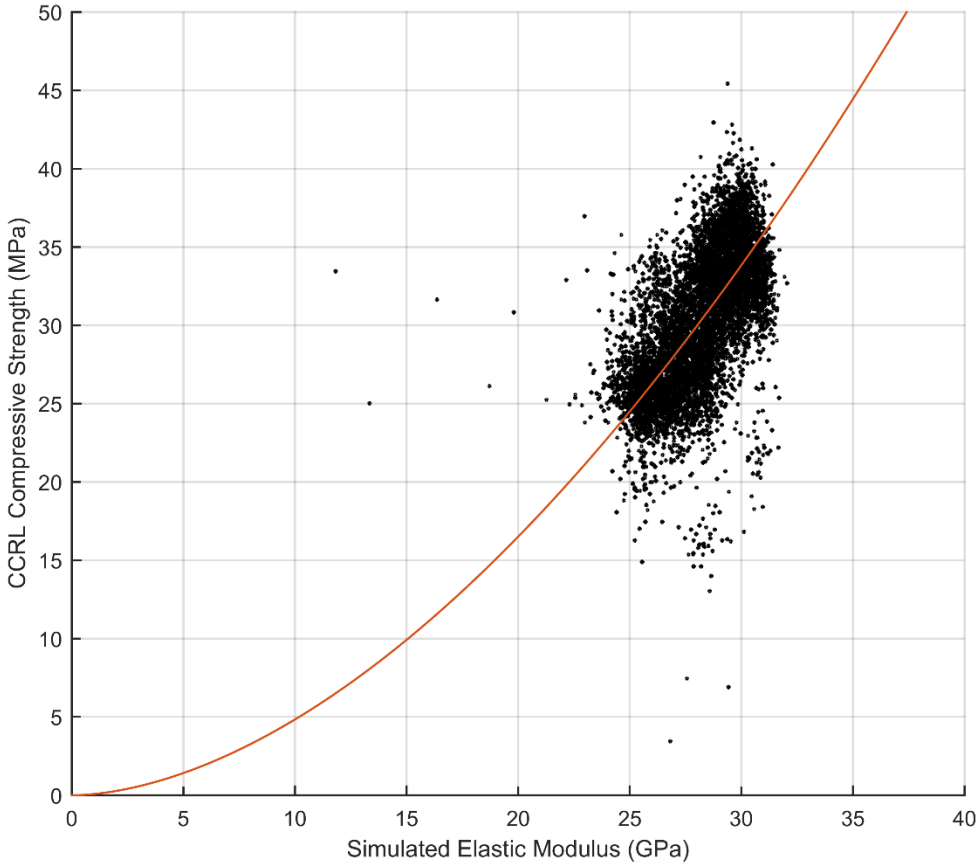

Figure 4-7. Power fit of CCRL measured compressive strength to simulated mortar elastic modulus

The need to develop a new empirical strength prediction equation for this study highlights a general lack of consensus in literature as to the specific nature of the modulus-compressive strength relationship. Because of this, potential alternative methods for computation of compressive strength from other VCCTL outputs were explored. Bentz et al. [60] found that the relationship between heat of hydration per ASTM C186 and mortar compressive strength for 7- and 28-day measurements was linear for mortars prepared according to ASTM C109. A linear fit of the three- and seven-day mortar strengths to the simulated heat of hydration measurements (Figure 4-8) resulted in the following equation:

$$f'_c = 0.075 * heat + 5.901 \qquad (4\text{-}7)$$

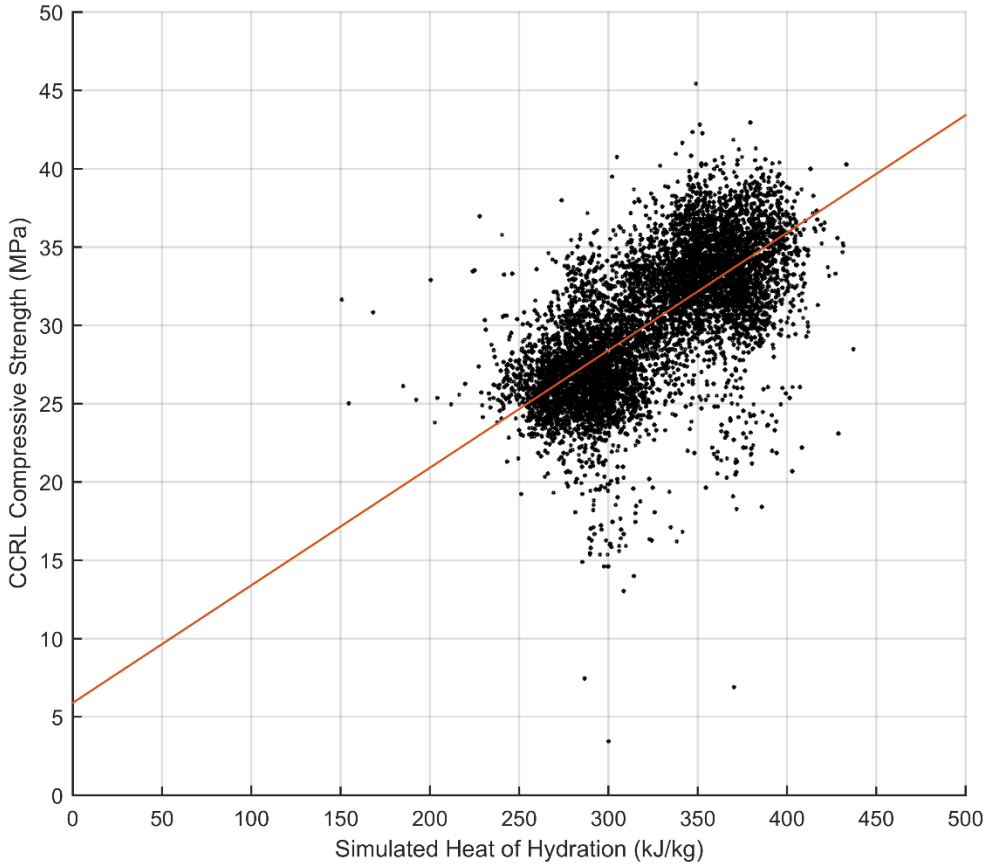

Figure 4-8. Linear fit of CCRL measured compressive strength to simulated cement heat of hydration

Figures 4-9 and 4-10 present a comparison of the 3- and 7-day virtual strengths calculated using four different methods: the default relationship used by the VCCTL as described in Eqn. 4-3, the relationship proposed by Valentini et al. (Eqn. 4-5), the fit of the experimental strength data to the virtual modulus results (Eqn. 4-7) and the relationship developed for mortar strength and virtual heat of hydration (Eqn. 4-8) based on the work of Bentz et al. For the three-day compressive strength results (Figure 4-9), the average rankings using the default, V14, power fit, and B12 equations were 0.3, 0.65, 4.45, and 4.75 respectively. The average rankings for virtual seven-day compressive strength results were better than the three-day results, with rankings of 0.55, 0.7, 4.6, and 4.75 for the default, V14, power fit, and B12 relationships respectively.

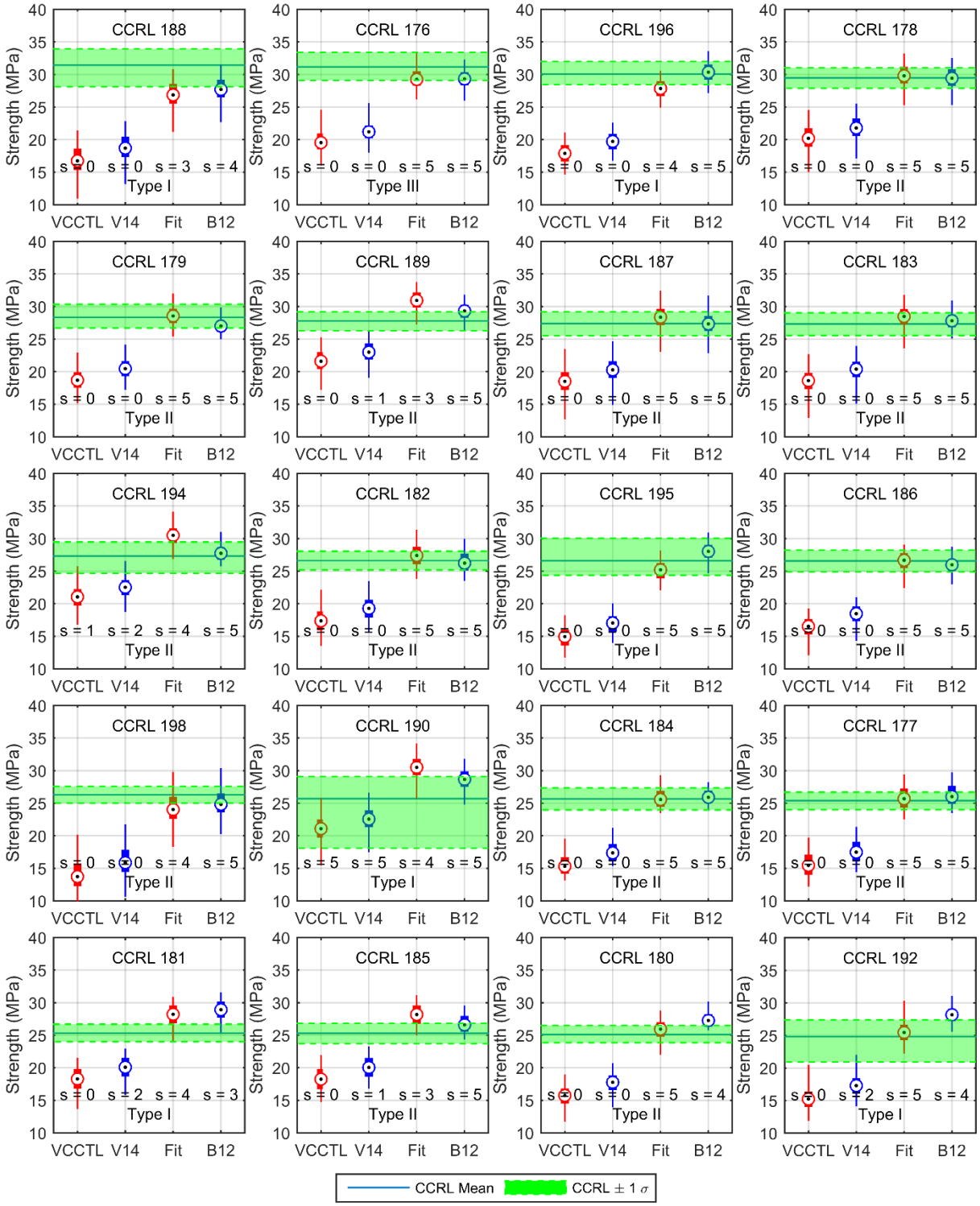

Figure 4-9. Comparison of three-day strength predictions using different methods

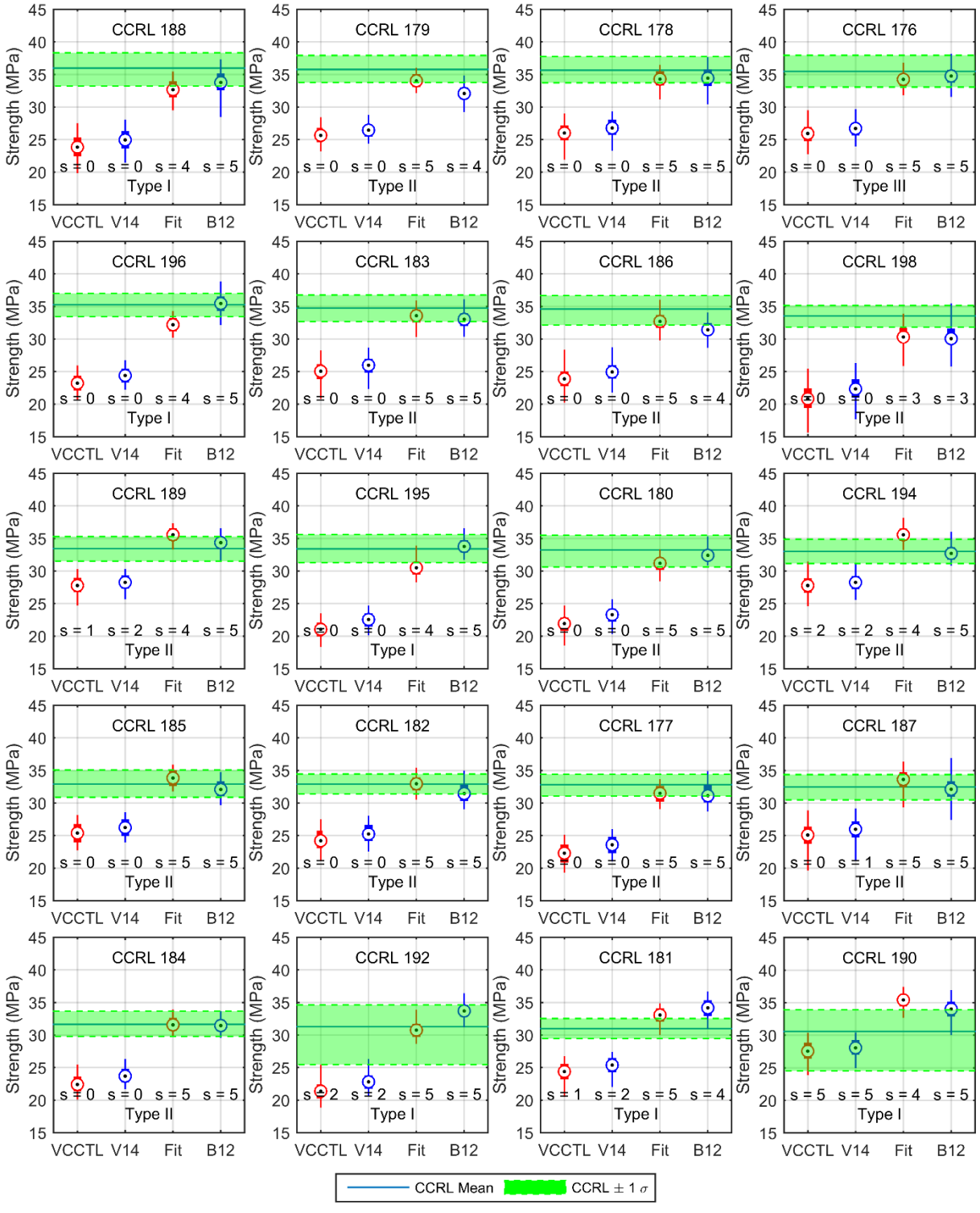

Figure 4-10. Comparison of seven-day strength predictions using different methods

While the equation developed directly from the data used in this study performed better for predictions of strength than the default equation or ACI 318, it is important to acknowledge that a relationship developed using an inherently limited dataset may not apply to other data. It is also notable that the default mortar strength prediction used by the VCCTL, the empirical equation developed by Valentini et al. [59] for use with the VCCTL, and the relationship developed for this study do not share any similarity other than the general power equation format. It is likely that more research is required, specifically with regards to the relationship between the compressive strength of mortar cubes and elastic modulus of mortar, to determine if empirical prediction of strength from elastic modulus is adequate for all potential virtual mortars.

4.6. Conclusions

1. Using a simplified set of virtual material properties, it is possible to emulate a physical laboratory using the VCCTL and retroactively participate in the CCRL proficiency sample program, while producing virtual test results that fall within the limits of acceptability specified by CCRL.
2. The VCCTL is capable of virtually measuring the compressive strength for ASTM C109 mortars made with 20 different cements to within 1.5 standard deviations of the experimental values.
3. The VCCTL can virtually measure the heat of hydration for a set of 20 different cements, and produce results that are within an average of two standard deviations away from the experimental mean.
4. For ASTM C109 mortars, empirical predictions of compressive strength are more accurate when based on simulated heat of hydration than when based on simulated elastic modulus.
5. It is not necessary to calibrate the VCCTL time/cycle^2 factor for individual cements. The results obtained in this study used the default value of 0.00035 time/cycle^2 for each of the cements used in this study.

5. ADVANCED VALIDATION AND APPLICATIONS

5.1. Introduction

The virtual cement and concrete testing laboratory (VCCTL) is nominally capable of predicting a broad array of material properties under varying thermal and envrionmental conditions; however, the accuracy of predictions for many properties has not been validated. To explore the most practical applications of the VCCTL's capabilites researchers chose to:

- Investigate the performance of the model when predicting hydration progress measurements such as heat of hydration, chemical shrinkage, and pH
- Demonstrate potential applications of the VCCTL to thermal simulation of mass concrete

These efforts necessitated thorough characterization of the input properties required by the VCCTL, including SEM/EDS analysis of the portland cements to acquire volume and surface area fractions for the primary mineral phases, isothermal calorimetry for heat of hydration measurements, and measurements of chemical shrinkage using the buoyancy method.

5.2. Materials Characterization

5.2.1. Characterization of Volume and Surface area fractions

The procedure followed for acquisition and analysis of the portland cements considered in this study has been detailed in Appendix A; however, for this task some changes were incorporated improve the analysis technique. The most difficult aspect of segmenting the EDS phase maps for calcium, silicon, alumium, sulfur, potassium and sodium into the four primary cement mineral phases and alkali sulfates has been distinguishing the alite and belite phases. These phases have the same elemental components, and only differ in the ratio of calcium to silicon. This contrast is typically visible in the silicon and backscatter electron maps; however, even when the contrast from these maps is compounded, the noise present in the silicon map makes segementation difficult. This has been resolved through the development of a filter that averages the grey values of the silicon map on a region specific basis, taking advantage of the morphologicial differences between the alite and belite phases. This filter is applied to the silicon map, which generally exhibits the most obvious differences in brighness between the two phases. An example of the map before and after this filter is shown in Figure 5-1, while the final segmentaion of alite and belite is shown in Figure 5-2, with the alite in brown and the belite in blue.

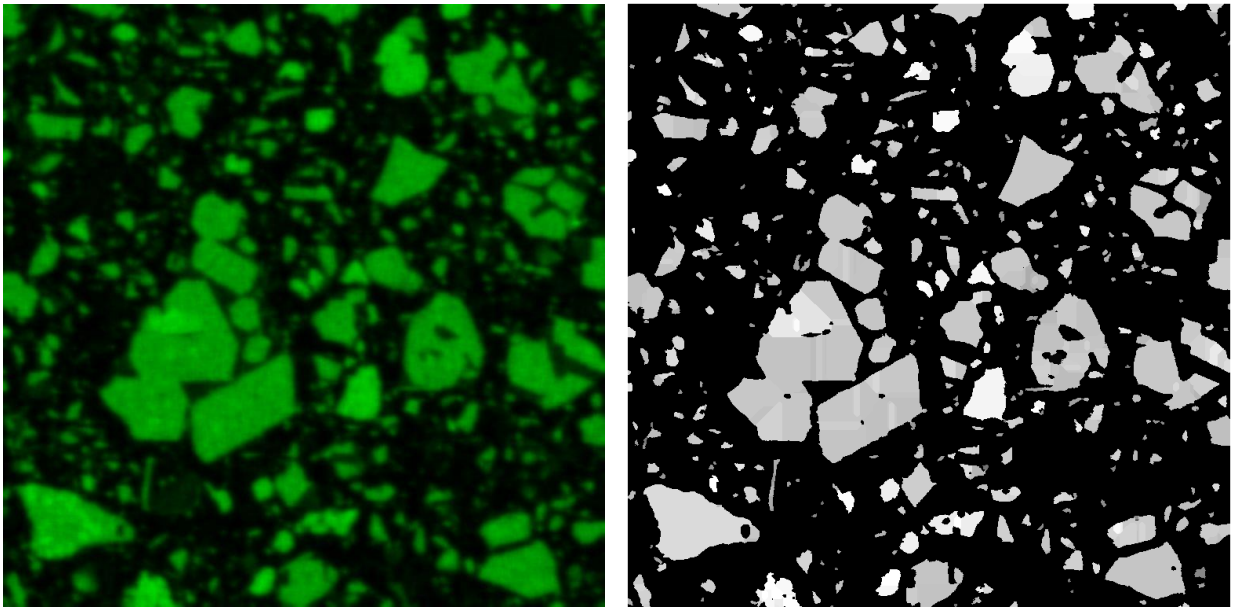

Figure 5-1. Silicon map before and after filtering

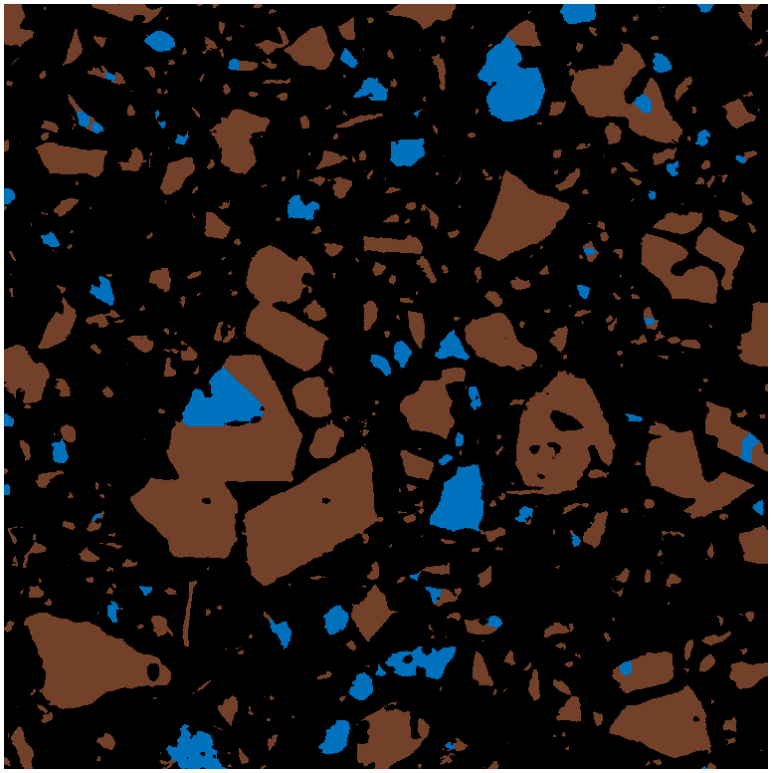

Figure 5-2. Segmentation of alite and belite

Two cements were analyzed for the volume and surface area fraction inputs required by the VCCTL, one type I/II cement produced locally (Cement A), and one type I/II cement from

Illinois (Cement B). The computed mass and surface area fractions for these cements are shown in Table 1, along with mass fractions of minor phases obtained from quantitative XRD.

Table 5-1. Cement phase inputs

	Cement A		Cement B	
Phase	Mass %	Surface Area %	Mass %	Surface Area %
C_3S	59.99	62.8	70.55	72.19
C_2S	14.5	11.6	8.73	5.21
C_4AF	11.01	5.35	13.24	7.11
C_3A	6.96	10.44	5.89	13.22
K_2SO_4 (Arcanite)	1.72	1.54	1.29	2.27
$CaCO_3$ (Limestone)	3.45	-	-	-
$CaSO_4*2H_2O$ (Gypsum)	1.73	-	2.0	-
$CaSO_4*0.5H_2O$ (Hemihydrate)	0.70	-	2.0	-
$CaSO_4$ (Anhydrite)	0.54	-	-	-

5.2.2. Cement Particle Size Distributions

The VCCTL requires a measured particle size distribution for cements being simulated. This is typically acquired using laser particle size analysis performed using the wet method, with ethanol as the dispersing medium. The measured distributions acquired using this technique and used as inputs for the simulations performed in this study are shown in Figures 5-3 and 5-4.

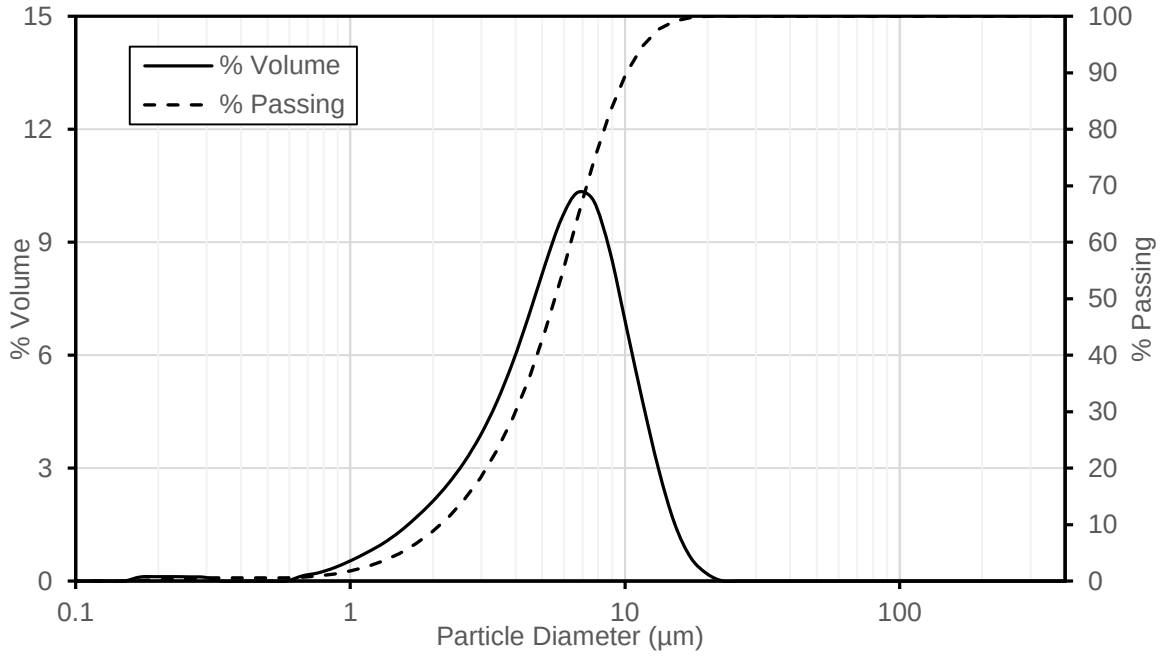

Figure 5-3. Volume and Cumulative particle size distribution for Cement A, acquired using Laser Particle Size Analysis

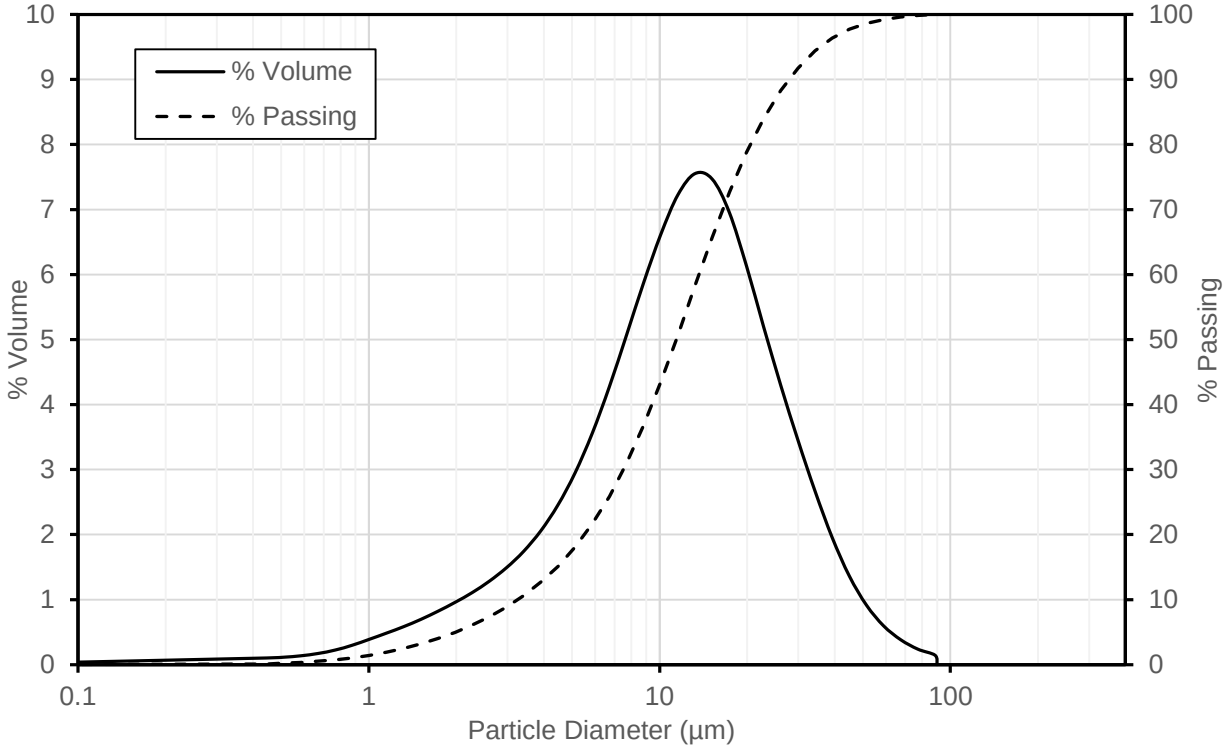

Figure 5-4. Volume and Cumulative particle size distribution for Cement B, acquired using Laser Particle Size Analysis

5.2.3. Secondary Cement Inputs

The cement compositional data and particle size distributions are the primary inputs required by the VCCTL, and are the only inputs mandatory for executing simulations. There are secondary inputs; however, that potentially can improve the accuracy of simulations, particularly when early-age properties are a priority. The computation of elapsed time in the VCCTL by default follows equation 5-1

$$t = \beta \times n^2 \quad (5\text{-}1)$$

where β is a user-defined constant and n is the number of computation cycles performed. When greater accuracy is required, the elapsed time calculation can instead be computed based on a user-supplied heat of hydration curve. At the conclusion of each computational cycle, the model evaluates the amount of heat generated, and compares that to the supplied heat of hydration curve. The elapsed time is then set to be the time on the input curve where the heats are the same [19]. This can also be performed using a chemical shrinkage curve, instead of a heat of hydration curve.

Heat of hydration and chemical shrinkage are both properties that can be predicted by the VCCTL or used as inputs to the VCCTL. For this study the heats of hydration

for the two cements were measured and used as inputs, at a w/c of 0.5 for cement A, and at w/c values of 0.4 and 0.55 for cement B. The resulting measurements are exhibited in Figure 5-5.

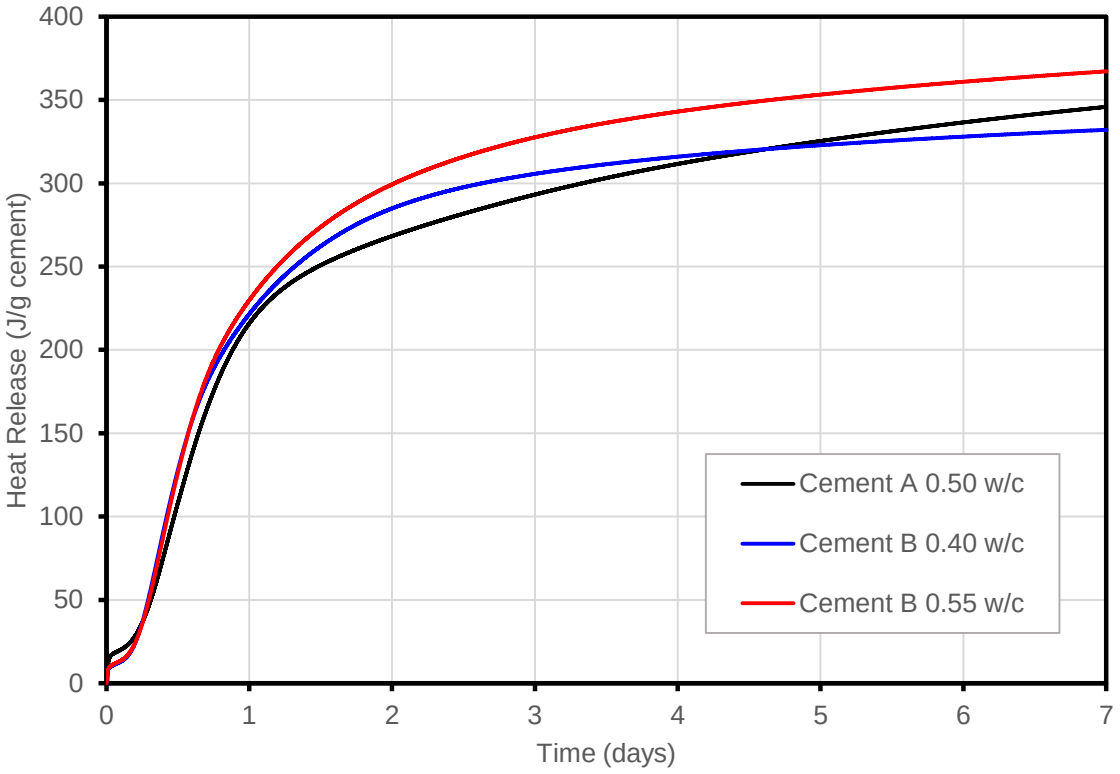

Figure 5-5. Measured heat of hydration curves for the cement and w/c combinations examined in this study

The three curves in Figure 5-5 were used both as time calibration inputs for the VCCTL, as well as references for evaulating uncalibrated VCCTL simulations of heat of hydration. The three input/refrence curves were similar in magnitude, with differences in slope and ultimate magnitude that likely stem both from differences in chemistry as well as w/c. Cement B exhibited more rapid heat evolution at water to cement ratios higher and lower than that of cement A from approximately 0.25 to 4.25 days of age.

5.3. Chemical Shrinkage

5.3.1. Chemical shrinkage Testing Methodology

The chemical shrinkage of portland cement paste is defined as the volume change that occurs at early ages due to hydration in a saturated condition [37]. Measurement of the volume change for the purposes of this experiment was performed using the buoyancy method, which is described in detail by Sant et al. [61]. The test operates on the principle that as a sample immersed in a fluid changes in volume, the amount of fluid displaced by the sample also changes by the same amount, producing a corresponding change in the buoyant mass of the sample. This change can be measured by suspending the sample in a fluid bath from the underhook of an appropriately sensitive analytical balance. The change in volume can be calculated simply by dividing the change in mass by the density of the fluid. This test was performed using an apparatus very similar to that shown in Figure 5-6.

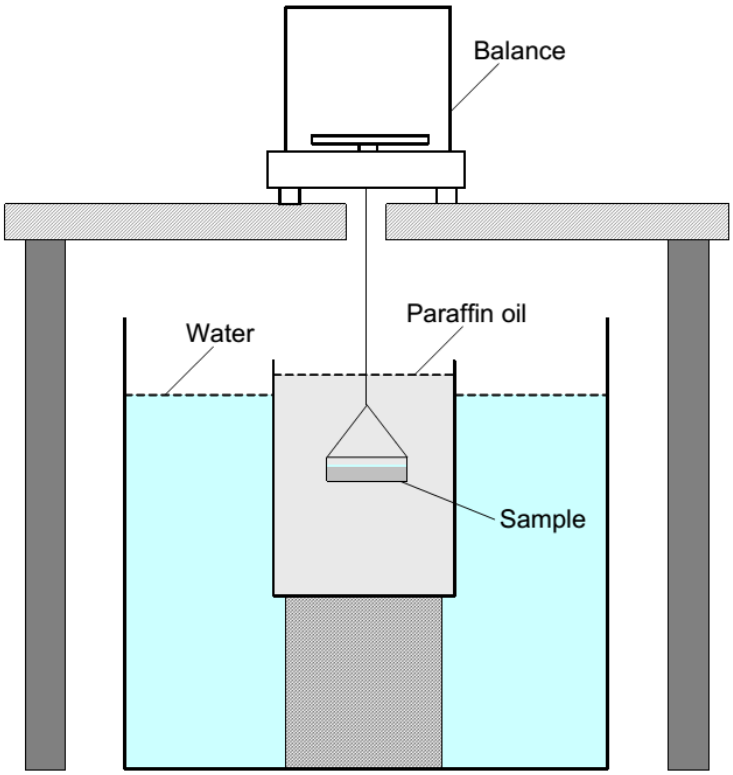

Figure 5-6. Buoyant Shrinkage Apparatus [61]

The only discrepancies between the referenced procedure and that performed as part of this study are in the sample preparation procedure. It is critical that samples prepared for this testing procedure are free of air bubbles, as when they are immersed in the paraffin bath any bubbles that escape will be measured as sudden and discontinuous changes in mass. This is

accomplished in the referenced procedure by mixing pastes in a vibratory paint shaker under vacuum. For this experiment samples were prepared using a small Pyrex bowl with a removable vacuum manifold. The desired proportions of cement and water were weighed into the bowl, typically with approximately 100 g of total material to facilitate uniform mixing. Prior to the attachment of the vacuum manifold, a magnetic stirring bar was deposited in the mixing bowl. The vacuum manifold was then attached, and the bowl was evacuated to approximately 26 inches of mercury. The sample was mixed for 2 minutes using an external magnet to manipulate the magnetic stirring bar inside the bowl, followed by 30 seconds of consolidation on a vibrating table. This cycle was repeated three times before returning the sample to atmospheric pressure.

Following mixing, the sample was deposited into a crystallization dish 70 mm in diameter and 50 mm tall. Care was taken to prevent the inclusion of air, and after 25 g of paste had been placed in the dish, it was rapped sharply against the table to remove any additional bubbles. To provide additional water for curing and create a barrier between the paraffin oil and cement paste, 9 mL of water was carefully deposited over the paste, taking care to prevent mixing. The sample was then suspended using very fine polyester thread attached to two small binder clips, which were clamped to the rim of the crystallization dish at a slight angle to prevent the entrapment of bubbles. The sample was carefully lowered into the paraffin bath, and gently swayed from side to side to eliminate bubbles trapped under the dish or in the binder clips. This procedure, from the addition of water to cement to the beginning of measurements, required approximately 20 minutes to complete.

5.3.2. Chemical Shrinkage Results

As with isothermal calorimetry, chemical shrinkage can be both a time calibration input for the VCCTL, or a simulated hydration measurement. Chemical shrinkage was measured for the same three combinations of cement and water-to-cement ratio as used for isothermal calorimetry. For each combination, at least two measurements of shrinkage were recorded to capture any variability present in the test; typically readings were taken for 48 hours. The two measured shrinkage curves were then averaged. The results for the three cases are shown in Figures 5-7, 5-8, and 5-9.

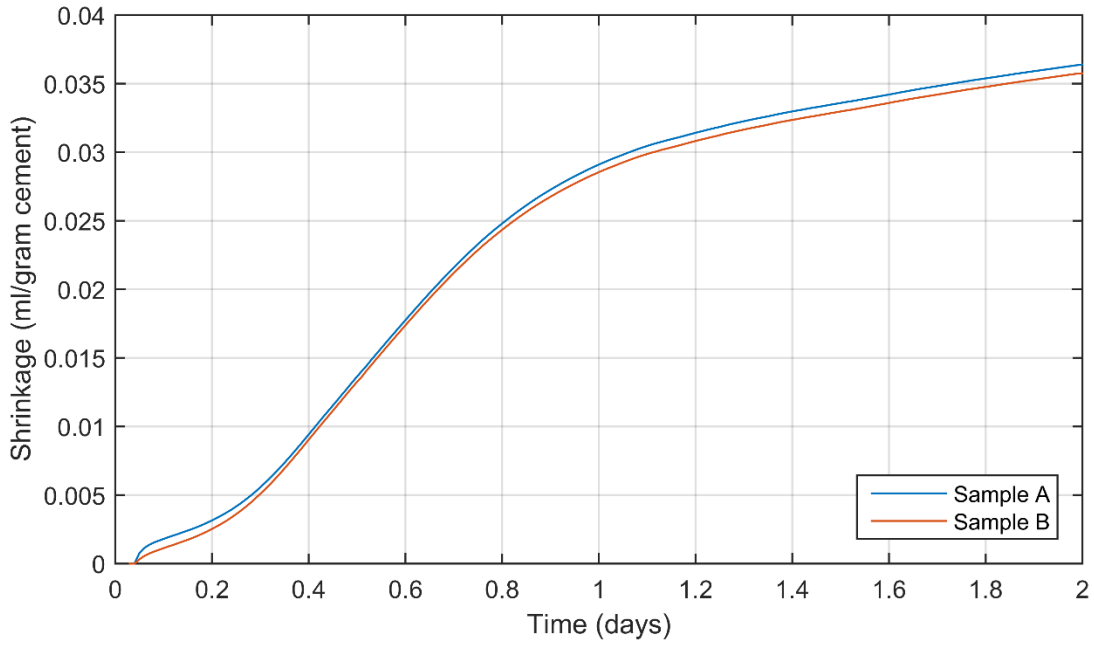

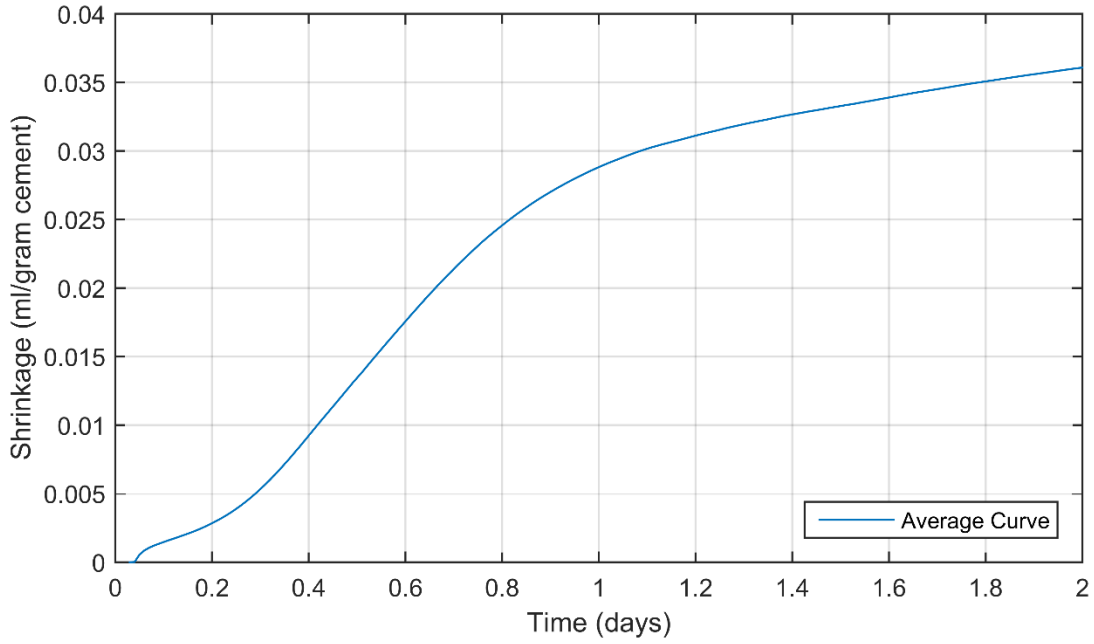

Figure 5-7. Raw and averaged chemical shrinkage measurements for Cement A with a 0.50 w/c

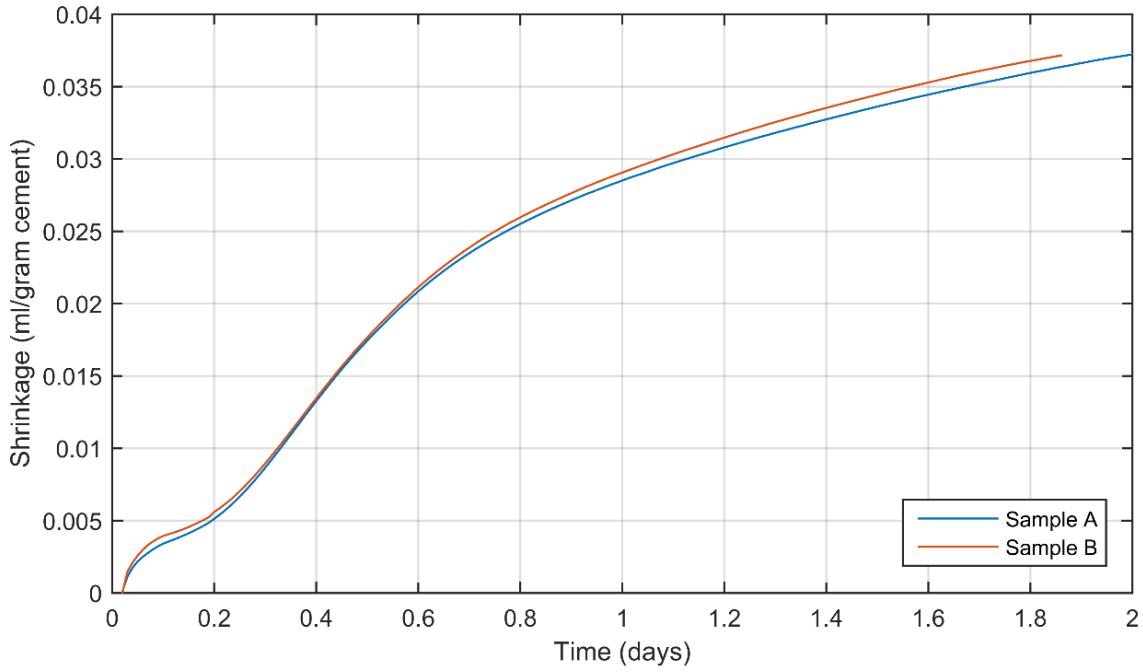

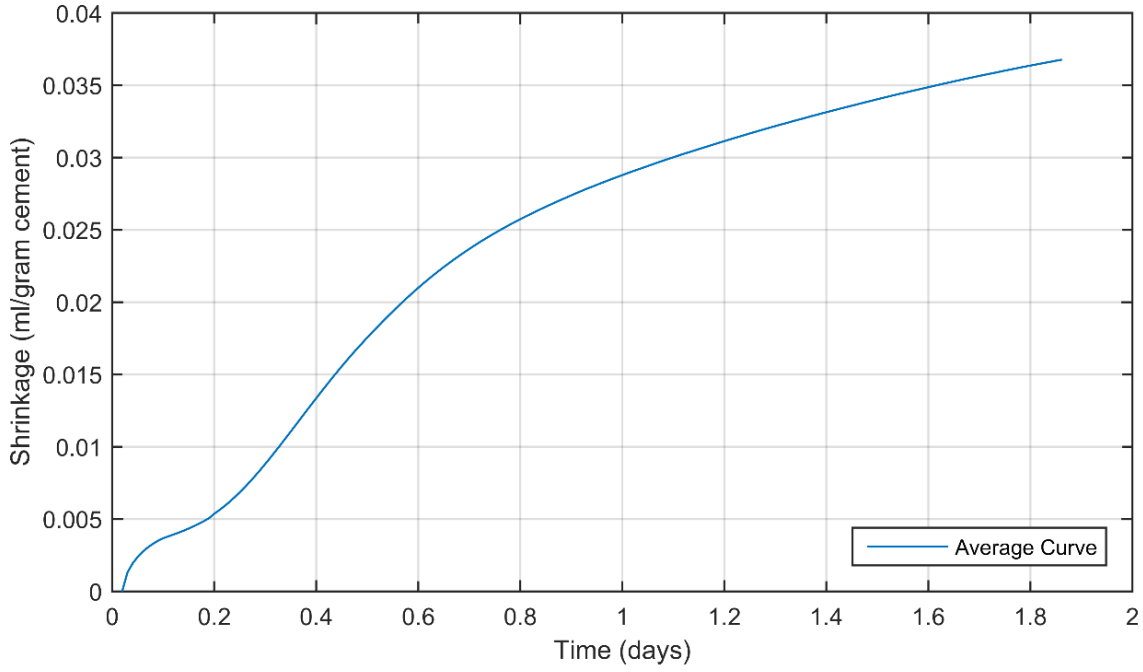

Figure 5-8. Raw and averaged chemical shrinkage measurements for Cement B with a 0.40 w/c

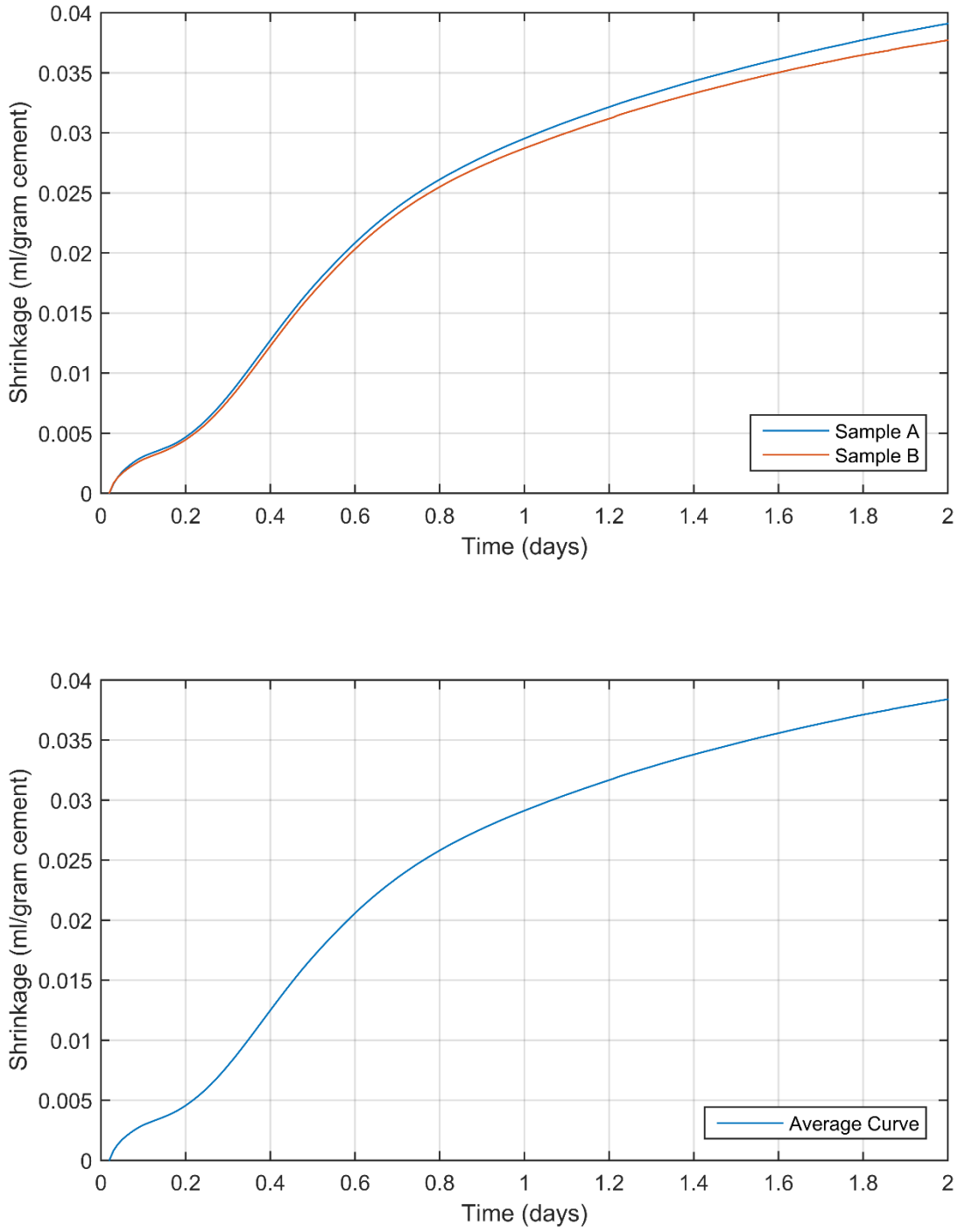

Figure 5-9. Raw and averaged chemical shrinkage measurements for Cement B with a 0.55 w/c

Figures 5-7, 5-8, and 5-9 show that the chemical shrinkage at 48 hours for each of the three cases was quite similar, falling between 0.036 mL per gram of cement and 0.038 mL per

gram of cement. This stands in contrast to the results of the isothermal calorimetry testing, likely due to differing moisture conditions of the two test methods. The isothermal calorimetry tests were performed in internally mixed, sealed vials, where the only water available for hydration was that present at initial mixing. The chemical shrinkage tests were performed in a saturated condition, where the relatively thin layer of paste was able to access additional water throughout the duration of the test. While the ultimate magnitude of shrinkage across all three cases was similar, there were some differences in the early-age behavior of the samples. The initial rate of shrinkage for cement B at both water-to-cement ratios was higher than that of cement A until approximately 18 hours of age, which to some degree parallels the more rapid heat evolution observed for cement B in isothermal calorimetry testing.

5.4. Simulation of Heat of Hydration and Chemical Shrinkage

5.4.1. Uncalibrated Heat of hydration Simulations

The ability of the VCCTL to calibrate the timing of a simulation using a heat of hydration curve is not necessarily required, and the time and labor required to acquire this data for any potential combination of cement and w/c is not insignificant. It is possible to simulate heat of hydration directly; Figures 5-10, 5-11, and 5-12 exhibit the results of directly simulating the three cases considered in this study. Simulation environmental parameters were set to mimic the conditions of the isothermal test: the curing condition was set as sealed, the thermal environment set to be isothermal, and the temperature set to be 23° C.

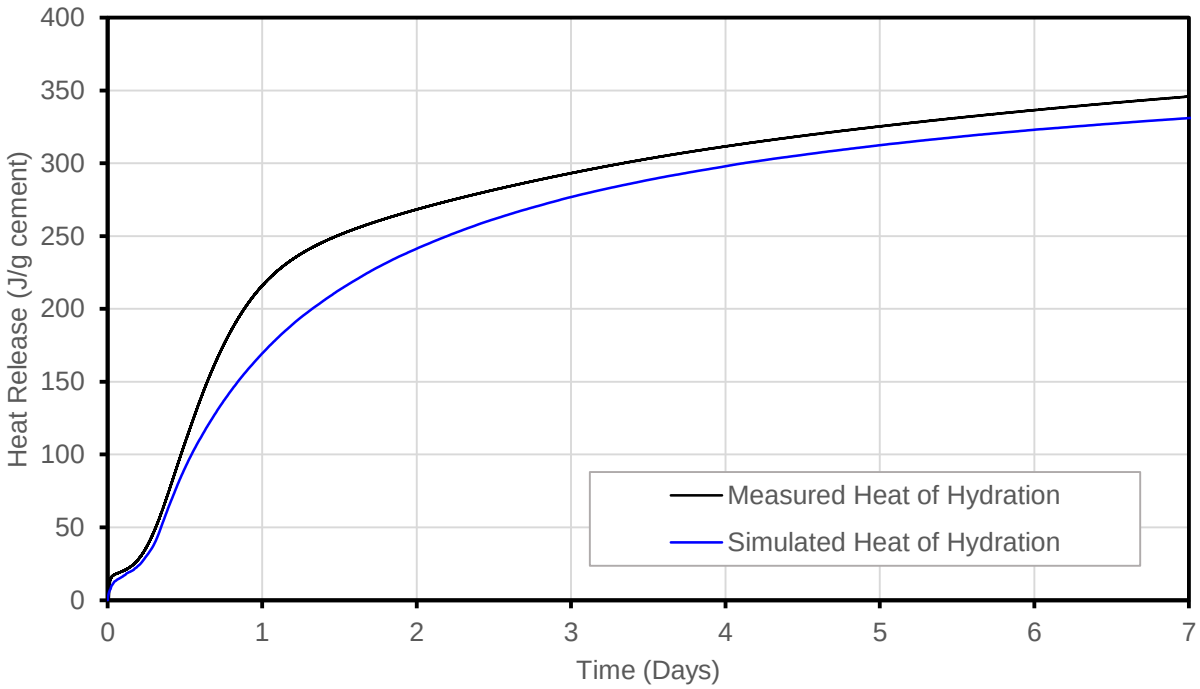

Figure 5-10. Simulated and measured 7-day heat of hydration for cement A at w/c 0.50

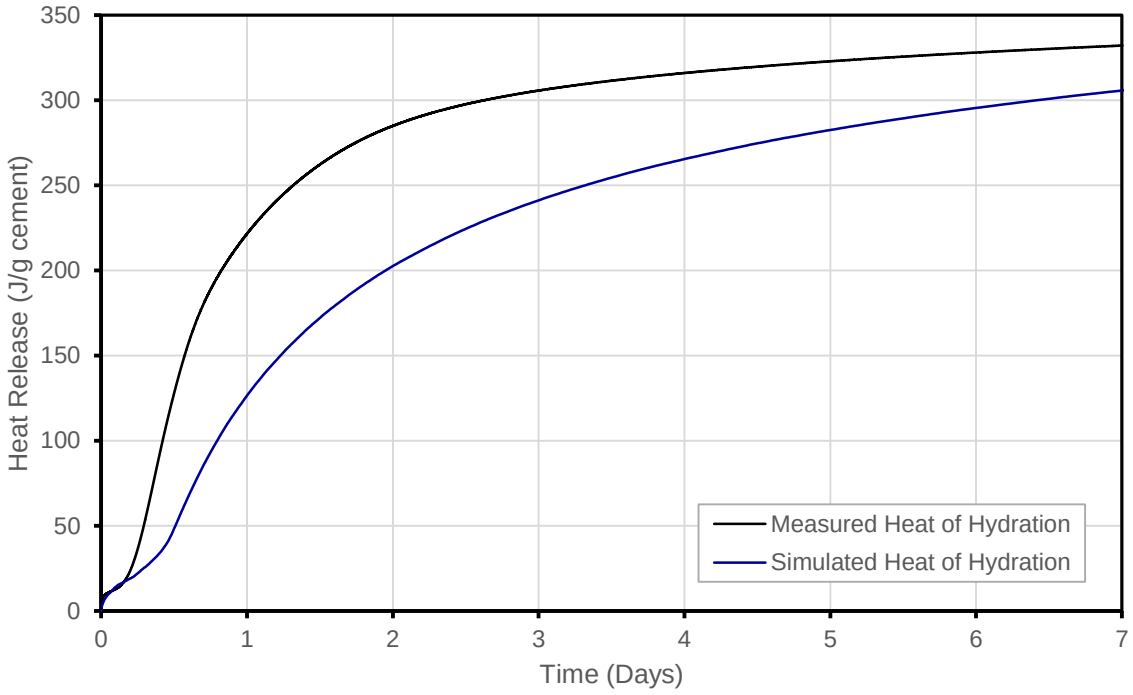

Figure 5-11. Simulated and measured heats of hydration for cement B at w/c 0.40

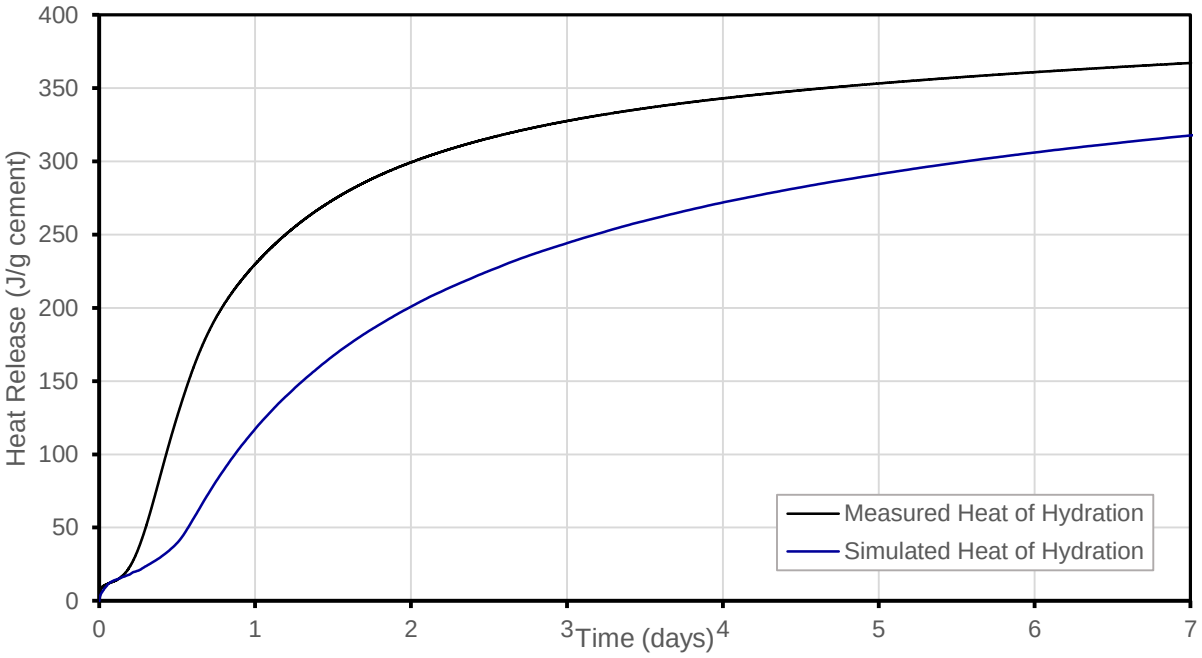

Figure 5-12. Simulated and measured heat of hydration for cement B at w/c 0.55

The results of the uncalibrated simulations for the three cases were mixed. For cement A at a 0.5 w/c (Figure 5-13) the simulated heat of hydration at 7 days agreed with the experimental value to within 15 J/g or approximately 5%, though the discrepancy was larger between 0.5 and 2.5 days, with the simulation underestimating the heat released by almost 50 J/g at 1.5 days of age. For cement B the results showed a similar trend but the underestimation of heat release was more dramatic. The 7-day heat of hydration for cement B at 0.40 w/c was within 30 J/g or approximately 10%; however, the largest discrepancy, occurring at the same time as that of cement A, was approximately 100 J/g. The results for the 0.55 w/c case for cement B are very similar to the 0.40 w/c case. The generally poor results for both simulations involving cement B may be related to the early-age behavior of the simulations; in both cases there is a significant delay to the start of the steepest portion of the curve typically attributed to the end of the induction period [36]. This effectively offsets the simulated heat release to the right.

5.4.2. Chemical Shrinkage Simulation

The simulation of chemical shrinkage was evaluated using both calibrated simulations, in which the measured heat of hydration curve for a given case was used to provide time information to the VCCTL, and uncalibrated simulations, wherein the default time constant was used just as in the uncalibrated heat of hydration simulations. The heat of hydration results for the calibrated simulations are not shown, as the method used by the VCCTL to follow the heat evolution curve produces a simulated curve that is identical to the measured curve. The results for the three cases are presented in Figures 5-13, 5-14, and 5-15.

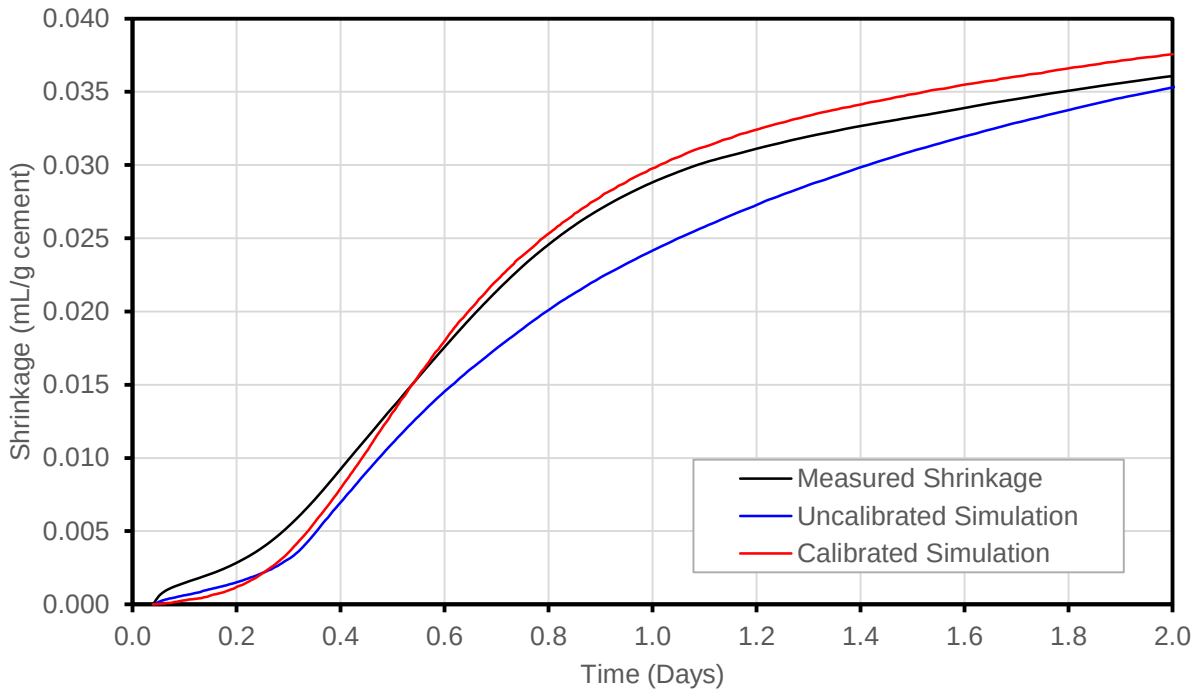

Figure 5-13. Calibrated and uncalibrated shrinkage simulation results for cement A at 0.50 w/c

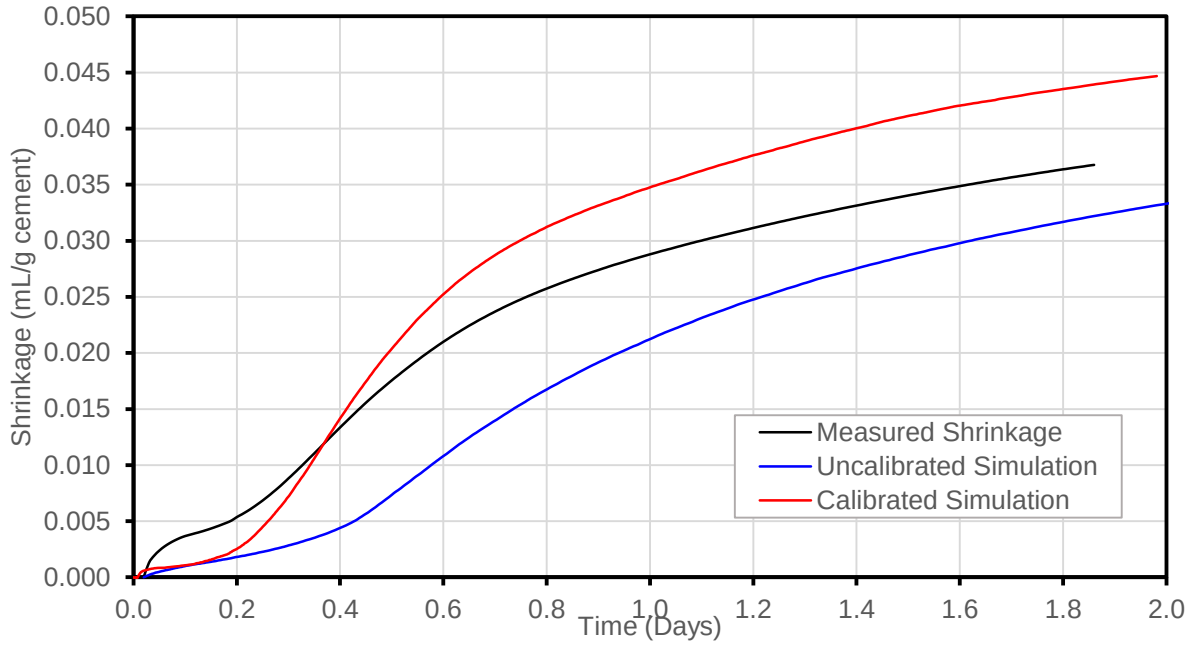

Figure 5-14.Calibrated and uncalibrated shrinkage simulation results for cement B at 0.40 w/c

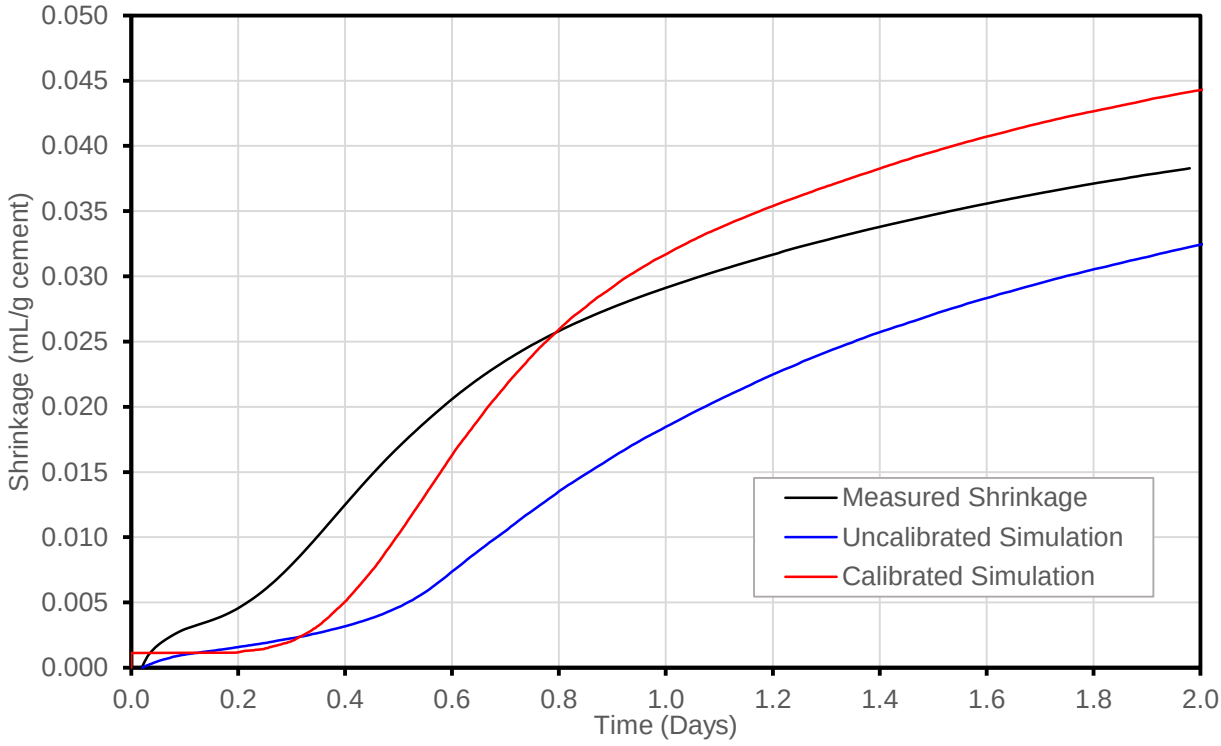

Figure 5-15. Calibrated and uncalibrated shrinkage simulation results for cement B at 0.55 w/c

The uncalibrated shrinkage results for all three cases behaved in a manner similar to the uncalibrated heat of hydration curves. The 0.50 w/c cement A underestimated the shrinkage slightly through the duration of the test, with the largest discrepancy of 0.005 mL/g cement occurring at approximately 1 day. Both cases for cement B underestimated the shrinkage more dramatically, and exhibited the same delay in the end of the induction period.

Calibration of the shrinkage simulations distinctly altered their results. For cement A at 0.50 w/c there was a noticeable improvement. The differences at early and later ages are similar to the uncalibrated simulations, if not slightly larger; however, the general shape of the shrinkage curve more closely matches that of the measured data. The time that formerly exhibited the largest discrepancy now agrees to within 0.0005 mL/g. The simulated curve also crosses the measured curve, shifting from slight underestimation before 12 hours to slight overestimation after. The calibrated shrinkage simulations for cement B exhibit similar changes in shape to those for cement A but the discrepancies are larger.

5.4.3. Discussion

The results of the heat of hydration and shrinkage simulation study show very good behavior with the locally sourced cement A, but generally poor results for the cement sourced from Illinois. The very high measured alite content of this cement may be a contributing factor for its poor behavior in the model; however, further investigation is required to ascertain the reasons behind this behavior. The motivation for examining and validating the heat of hydration and chemical shrinkage behavior of the VCCTL was based on the fundamental nature of these parameters. Shrinkage and heat of hydration are computed continuously throughout the simulation from changes in the mass balance of the initial cement phases and hydration products and their respective specific gravities and heats of formation [62]. These properties represent the most fundamental metrics with which the virtual microstructure can be conveniently compared to the real hydrating cement paste, and provide a good indication of the accuracy of the simulation as a whole.

The time calibration capability of the VCCTL appears to be most effective when the uncalibrated simulation results do not deviate excessively from the measured values. This ability of the VCCTL has demonstrated applicability to problems of set time simulation [63], and produced a distinct improvement in the simulation of shrinkage for cement A; however, it cannot compensate for simulations where the uncalibrated behavior differs distinctly from the measured.

5.5. Investigation of Pore Solution pH Simulation

The VCCTL predicts the evolving pH of the pore solution of the virtual microstructure, based on the mass fraction of alkali sulfates specified in the inputs for portland cement. Details of the calculations used to solve for the chemical equilibrium of the pore solution are outlined by Bentz [64]; these calculations are used to solve for the concentrations of sodium, potassium, calcium, sulfate, and hydroxide (pH) ions, as well as the mass fractions of CH, gypsum, and syngenite.

The pH of the pore solution of cement A was measured at three different ages, following the procedures outlined by Hooton and Thomas [65] for pore solution extraction. Two-inch cylindrical specimens were cast from mortar sieved from a concrete mix with a cement content of 615 lb/yd^3, a 0.417 water-to-cement ratio, and a coarse-to-fine aggregate ratio of 1.3. The specimens were stored in sealed vacuum bags until testing.

To compare the simulated pH to that measured using the above techniques, one mixture was created in the VCCTL with proportions that mimicked the mortar fraction of the concrete mix. The mix was hydrated under sealed conditions, and two hydration simulations were performed, one calibrated with the heat of hydration curve measured from cement A, and one with the default time/cycle relationship used elsewhere in this report. The measured and simulated pH testing results are compared in Figure 5-16.

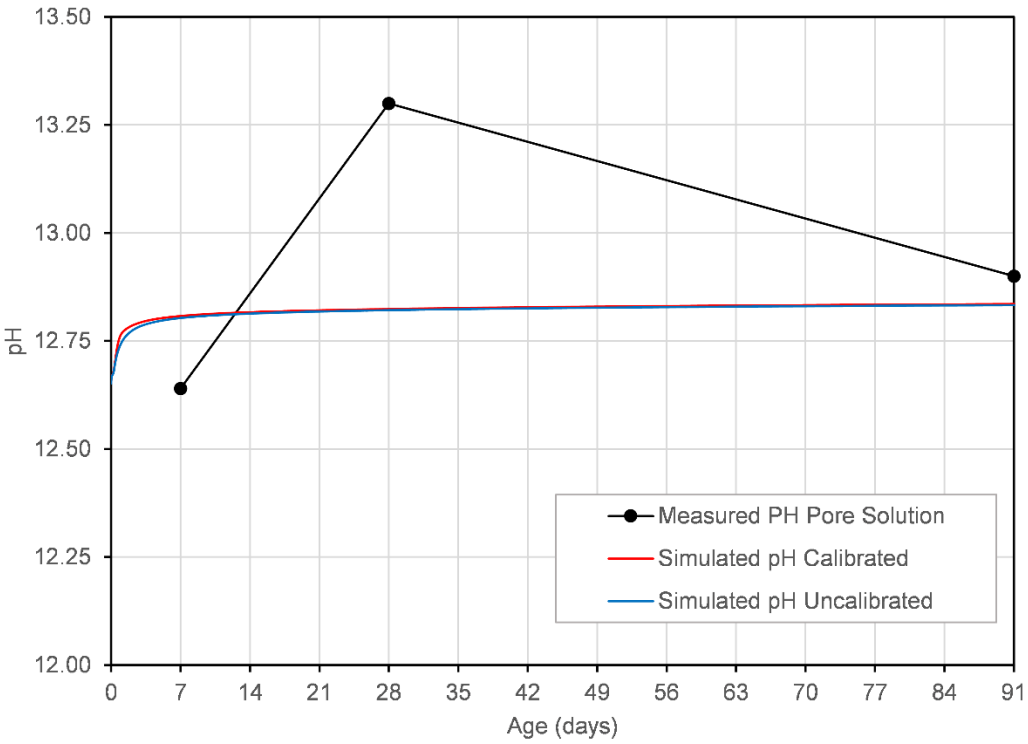

Figure 5-16. Comparison of simulated and measured pore solution pH for cement A

The simulated pore solution pH results acquired from the calibrated and uncalibrated VCCTL simulations differ slightly, with the calibrated values slightly exceeding those of the uncalibrated simulations. The simulations compare favorably to the measured values at both 7 and 91 days of age, falling less than 0.25 points from the measured values, shifting from overestimation at 7 days to under estimation at 91 days. The 28-day pH simulation deviates more substantially from the measured value, underestimating by approximately 0.5 points. This deviation is well outside the accuracy of the pH meter used (± 0.05), assuming the meter was

properly calibrated when the testing was performed. The measured pH values exhibit more variability than the simulated, which remain fairly constant after 28 days of age.

5.5.1. Limitations of VCCTL and Implications for Future work

The decision to investigate the influence of time calibration on the simulations detailed in this report was based on knowledge of a key limitation of the VCCTL: the cycle-wise cellular automata simulation of portland cement hydration has no inherent link to real time [20]. The two current solutions to this problem at this time limit the potential efficacy and applicability of the VCCTL to practical applications in concrete mixture design, either by requiring additional testing of the simulated material, or by limiting accuracy through approximation. There are also uncertainties regarding the consistency of the VCCTL across a range of different cement compositions, which can ultimately be attributed to the static rules used to govern the simulation of hydration. These parameters assign probabilities to events of dissolution, combination, and precipitation in the digital microstructure, and represent properties of the hydrating microstructure that vary continuously with both time and initial chemistry [11].

Work is currently underway to develop modifications to the VCCTL using high performance computational methods, with the goal of fully understanding the model's response to a broad array of different input properties, and implementing a dynamic input preprocessor that will select the optimum set of cellular automata parameters based on input chemistry. This will be accomplished by first enumerating and simulating a set of simulations with incrementally varied governing parameters, then using the resulting dataset to train a neural network model using supervised machine learning. This approach should allow for complete control over the behavior of the model, and will likely be critical to the application of the VCCTL to accurate simulation of mineral admixtures, as well as improvements to the behavior of the model in general.

5.6. Applications of the VCCTL to Mass Concrete Thermal Modeling

The VCCTL is capable of simulating many properties of cement and concrete that can be difficult or impossible to measure, and take into account a wide array of different thermal and environmental parameters. For mass concrete elements above a certain minimum dimension, it is frequently required that a thermal control plan be submitted by the contractor prior to construction; this plan frequently includes the results of finite element thermal simulation using a software package such as TNO DIANA. The simulation results are used to estimate the maximum temperature differential and propose mitigation strategies, such as reduced placement temperature, insulation of formwork and finished surface, and cooling pipes, when absolutely required.

TNO DIANA requires an adiabatic temperature rise curve for the simulation of temperature rise as well as thermal behavior of concrete in a structure. True adiabatic temperature rise measurements are difficult to acquire, and commonly substituted semi-adiabatic tests can produce results that fail to predict potential thermal problems. The VCCTL is capable of simulating adiabatic temperature rise by simply preventing heat from leaving the hydrating

digital microstructure. A common metric for the definition of mass concrete is the specification of a minimum dimension; however, the cement content of a mixture can influence the thermal behavior of a concrete structure significantly. To explore the relationship between element minimum dimension and temperature rise and differential, a series of simulated adiabatic temperature profiles were generated using the VCCTL, and provided as input to several different sizes of structure in TNO Diana.

5.6.1. Simulation of Adiabatic Temperature Rise

The simulation of adiabatic temperature rise in the VCCTL used a standard type I/II cement characterized using the procedures detailed in appendix A. The simulated mixture design used a coarse-to-fine aggregate ratio of 2:1, a water-to-cement ratio of 0.40, and varied the cement content from 250 lb/yd^3 to 1,000 lb/yd^3. An isothermal calorimetry curve measured from the cement was provided to calibrate the simulation, and simulations were executed in the adiabatic thermal condition with a starting temperature of 21° C. The results of the adiabatic simulations are shown in Figure 5-17. The simulations results show the expected increase in ultimate temperature as cement content increases.

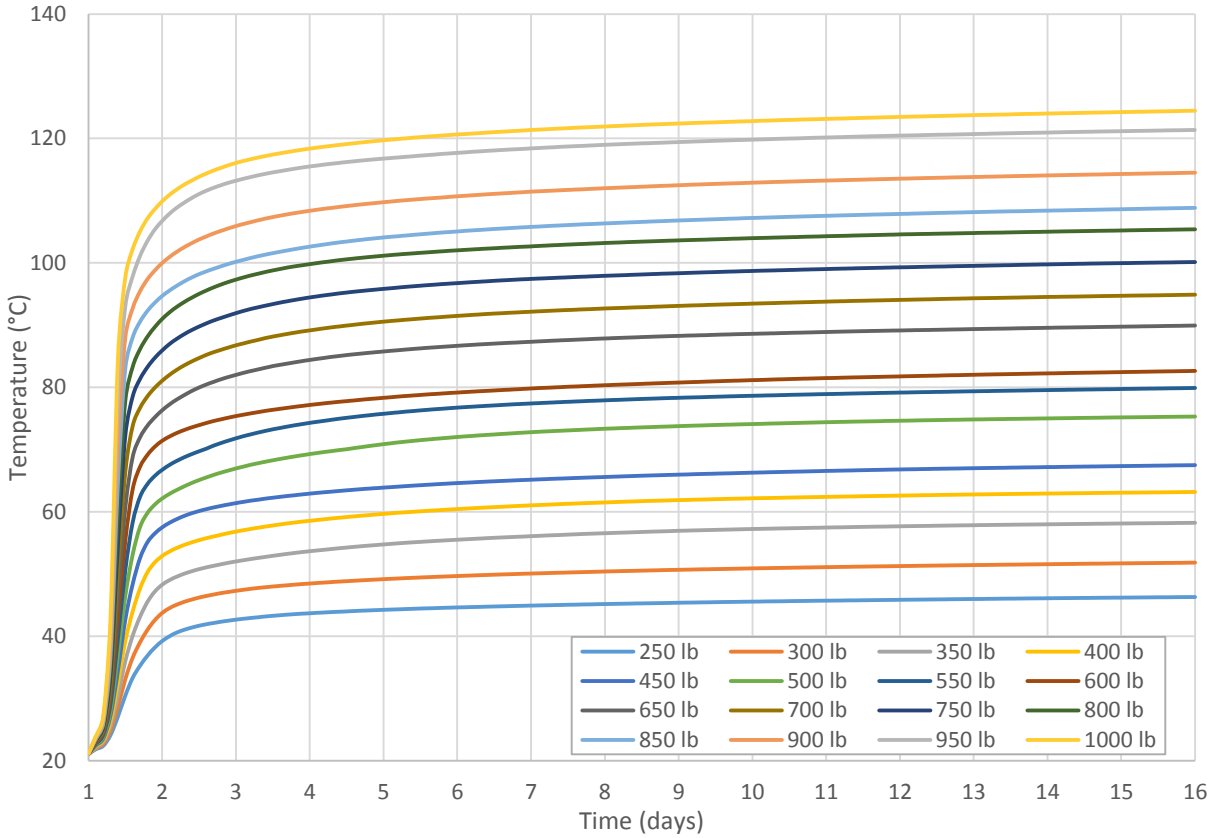

Figure 5-17. VCCTL simulated adiabatic temperature rise for concretes with varying cement content

5.6.2. Thermal Finite element Simulation

To simulate the thermal behavior of a range of minimum structure dimensions, a series of two-dimensional geometries were generated in TNO DIANA. The geometry consisted of a rectangular slab with a length-to-thickness ratio of 10:1, with measurements of temperature recorded from a column of nodes in the center of the element. Half symmetry was utilized to reduce the number of simulation nodes required. The geometry of the model also included a large area of simulated soil below the slab. The geometry of the model was scaled to set the thickness of the slab at 6 inch increments, from 6 inches in thickness up to 10 feet in thickness. Figure 5-18 exhibits an example simulation, showing the temperature distribution at the time of maximum temperature as well as the geometry used for all simulations.

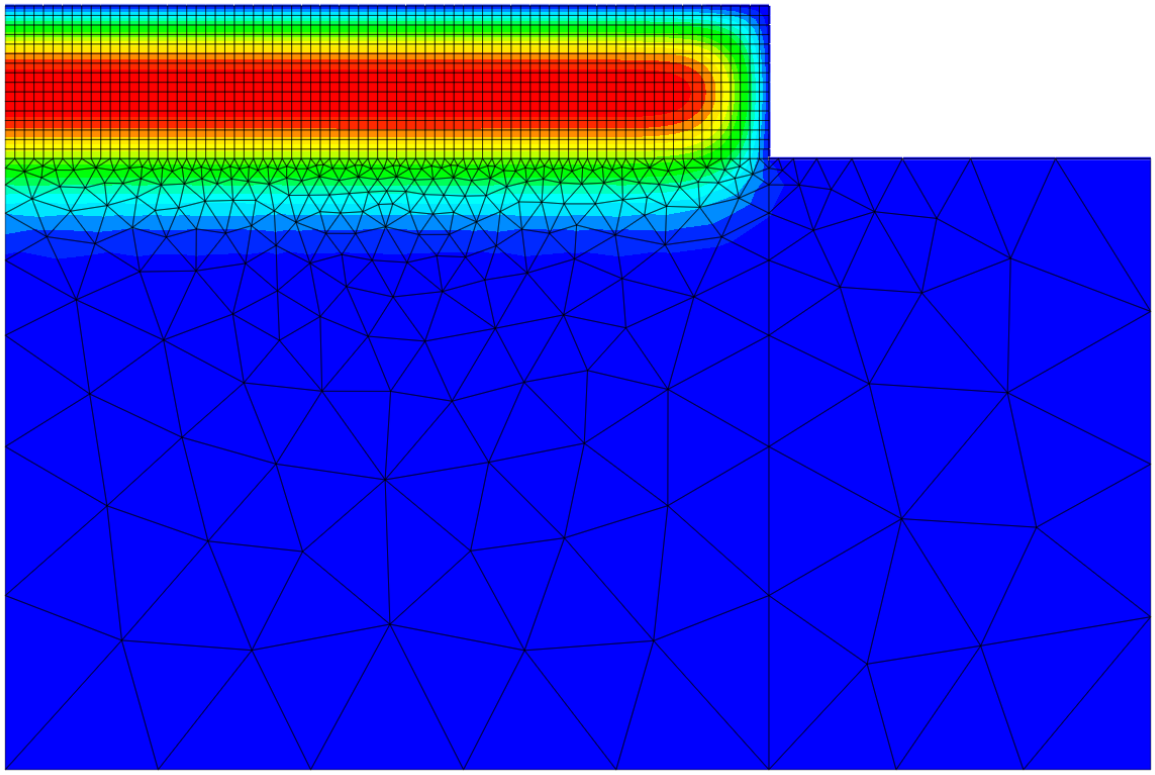

Figure 5-18. Finite element geometry and thermal distribution example

Thermal simulation in TNO Diana also requires boundary conditions and material properties that should be selected to closely replicate the real system. All simulations used the same set of conditions in this study, all initial temperatures were set at 73° F, and the convective heat loss from all surfaces exposed to air was set at an equivalent R value of 0.044. The material properties used for all simulations are summarized in Table 5-2. Simulations were performed for 16 days, with the plywood formwork removed from the slab after 1 day of simulation time. The

ultimate purpose of this exercise was to determine the combinations of cement content and minimum dimension above which additional measures must be provided to mitigate excessive temperature differentials. The default assumption was that no thermal control measures were implemented, to provide the "worst case" scenario, as early removal of formwork/insulation results in higher temperature differentials in mass concrete and increases the potential for thermal cracking. This scenario was used to determine the potential for large temperature differentials and designate minimum dimension and cementitious content as mass concrete.

Table 5-2. Material properties used for thermal simulations

	ρ (lb ft^{-3})	C_P (J g^{-1} K^{-1})	R (in^{-1})
Concrete	145	0.88	0.1
Soil	108	0.8	0.085
Plywood	33.7	1.034	1.5

5.6.3. Thermal Simulation Results

The results of the thermal simulations are summarized in Figure 5-19. The combination of twenty different geometries and sixteen different cement contents produces 320 simulation possibilities. Instead of simulating all possible cases in DIANA, simulations were targeted towards the cases that came closest to the maximum thermal differential of 35°F specified in ACI 207 [46]. This differential was calculated as the maximum difference of either the center point and bottom point or center point and top point along the centerline of the slab. In total 72 simulations were executed to determine the size above which each cement content produced a differential that exceeded the allowable maximum.

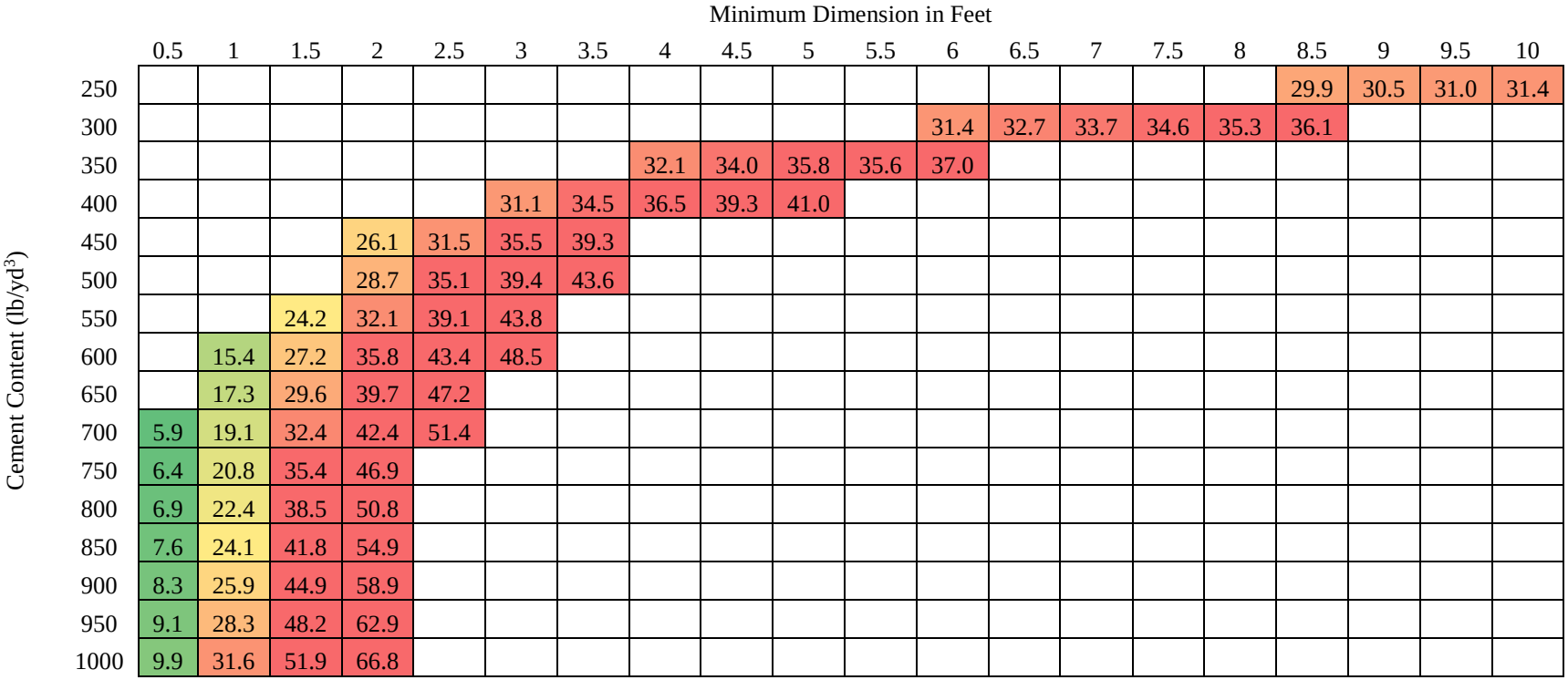

Figure 5-19. Maximum temperature differentials surrounding the cases where the differential exceeds 35°F

6. INVESTIGATION OF VCCTL MODELING FOR SUPPLEMENTARY CEMENTITIOUS MATERIALS

6.1. Introduction

Existing studies and validations using the Virtual Cement and Concrete Testing Laboratory (VCCTL) have focused exclusively on cementitious systems containing only ordinary portland cement [22,50,59,66]. This currently limits the practical implementation of virtual testing to mixtures that do not contain mineral admixtures; however, limited functionality is included with the VCCTL for modeling pozzolanic materials. To evaluate the behavior of the VCCTL in this context, a virtual experiments was developed and implemented. The first compares the performance of the VCCTL to measured mortar compressive strengths of ten binary mixtures. The composition and fineness of the materials used in the binary mixtures as well as measurements of compressive strength and heat of hydration were obtained in collaboration with a separate FDOT investigation of different pozzolanic materials [67]. A separate virtual experiment, similar to that detailed in the Task 9 Deliverable for this project, was also performed to assess the response of the VCCTL simulated binary pozzolanic mixtures to changes in pozzolan chemistry, fineness, and replacement percentage.

6.2. VCCTL Modeling of Pozzolanic Materials

The cellular automata simulation of cementitious materials in the VCCTL (detailed in Task 1 Deliverable) is based on observed reaction stoichiometry for the raw mineral binders and their subsequent hydration products. Calculation of the evolving thermal and mechanical state of the bulk microstructure over time requires known physical properties of the mineral species involved, including density, composition, and heat of formation. The specific reactions and properties used by the VCCTL to simulate the hydration of fly ash are summarized in Figure 6-1 and Table 6-1.

Table 6-1. Physical properties of VCCTL fly ash mineral phases and hydration products [68]

Compound Name	Compound Formula	Density (Mg/m^3)	Molar volume (cm^3/mol)	Heat of formation (kJ/mol)
Silica	S	2.2	27.	-907.5
Aluminosilicate	AS	3.247	49.9	
Stratlingite	C_2ASH_8	1.94	215.63	
Anhydrite	$C\bar{S}$	2.61	52.16	-1424.6
Gypsum	$C\bar{S}H_2$	2.32	74.2	-2022.6
Calcium chloride	$CaCl_2$	2.15	51.62	-795.8
Friedel's salt	$C_3A(CaCl_2)H_{10}$	1.892	296.66	
Calcium Hydroxide	CH	2.24	33.1	-986.1
Calcium silicate hydrate	$C_{1.7}SH_4$	2.12	108.	-3283
Pozzolanic C–S–H	$C_{1.1}SH_{3.9}$	1.69	101.8	-2299.1
Tricalcium aluminate	C_3A	3.03	89.1	-3587.8
Dicalcium aluminosilicate	C_2AS	3.05	90.	
Calcium aluminodisilicate	CAS_2	2.77	100.62	

Pozzolanic C–S–H Formation

$$1.1CH + S + 2.8H \rightarrow C_{1.1}SH_{3.9}$$
$$1.349 \quad 1 \quad 1.867 \quad 3.771$$

$$C_{1.7}SH_4 + 0.5H \rightarrow C_{1.1}SH_{3.9} + 0.6CH$$
$$1 \quad 0.083 \quad 0.943 \quad 0.184$$

Calcium Chloride-Aluminate Reactions

$$C_3A + CaCl_2 + 10H \rightarrow C_3A(CaCl_2)H_{10}$$
$$1.7261 \quad 1 \quad 3.487 \quad 5.747$$

$$C_4AF + CaCl_2 + 14H \rightarrow C_3A(CaCl_2)H_{10} + CH + FH_3$$
$$2.4797 \quad 1 \quad 4.882 \quad 5.747 \quad 0.641 \quad 1.3522$$

Anhydrite to Gypsum Conversion

$$C\bar{S} + 2H \rightarrow C\bar{S}H_2$$
$$1 \quad 0.69 \quad 1.423$$

Stratlingite Formation

$$2CH + AS + 6H \rightarrow C_2ASH_8$$
$$1 \quad 0.7538 \quad 1.631 \quad 3.26$$

$$CAS_2 + C_3A + 16H \rightarrow 2C_2ASH_8$$
$$1 \quad 0.886 \quad 2.862 \quad 4.286$$

$$CAS_2 + C_4AF + 20H \rightarrow 2C_2ASH_8 + CH + FH_3$$
$$0.786 \quad 1 \quad 2.81 \quad 3.37 \quad 0.2586 \quad 0.5453$$

Figure 6-1. VCCTL fly ash hydration reactions, with volume stoichiometries listed below each chemical phase [68]

6.2.1. Simulation Inputs and Limitations

To simulate the influence of supplementary cementitious material on the properties of paste, mortar and concrete, the VCCTL provides methods for inputting the properties of slag and fly ash only. The fly ash input (Figure 6-2) provides the ability to specify the concentrations of three different "glass" phases: aluminosilicate glass (AS), calcium aluminum disilicate (CAS_2) glass, and pure silica (S), as well as C_3A, calcium chloride, and anhydrite.

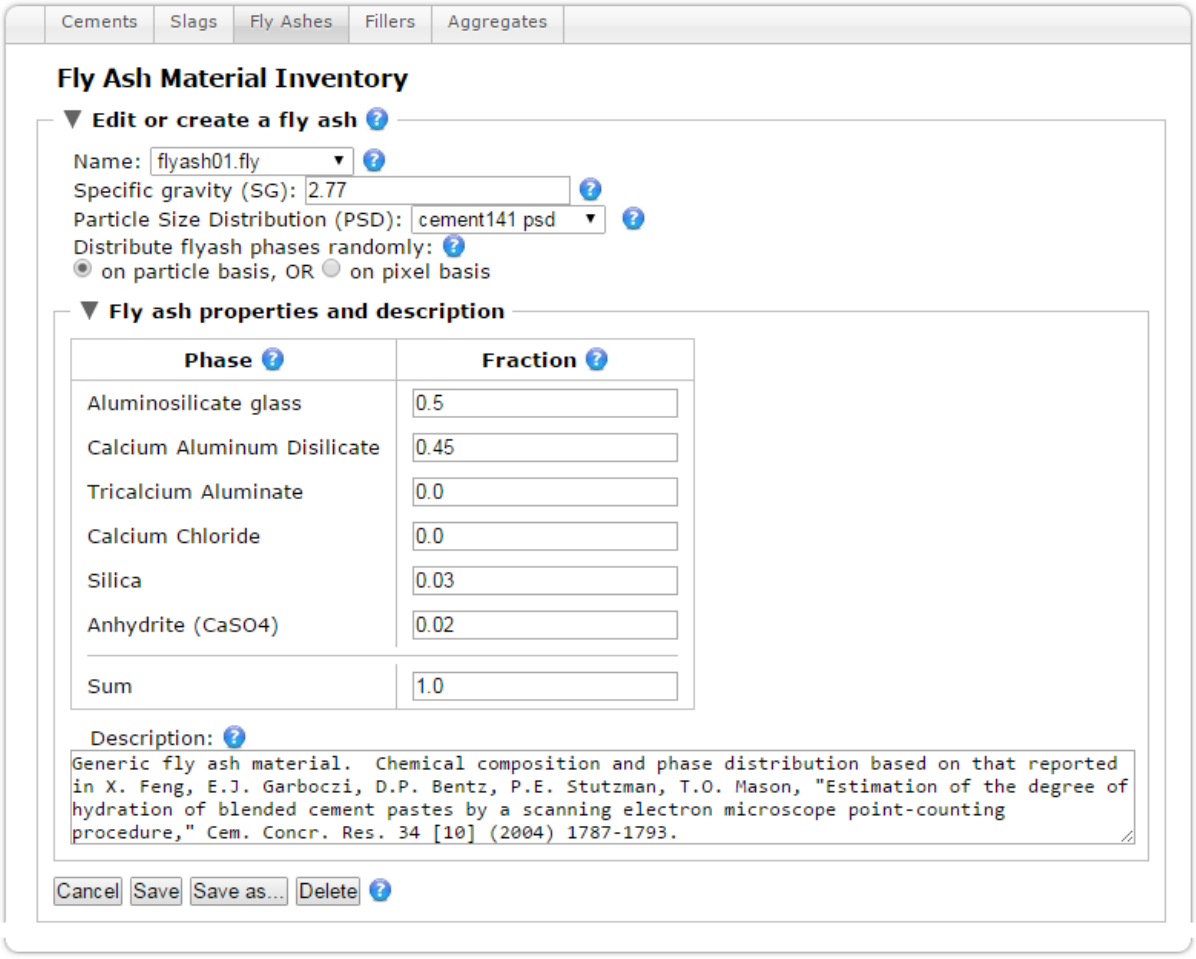

Figure 6-2. VCCTL Fly Ash Input Screen

This allows many supplementary materials such as silica fume and metakaolin to be approximately modeled as "fly ash" regardless of their nominal classification, as long as they are primarily amorphous and comprised of silicon, calcium, and aluminum oxides. It should be noted that the VCCTL does not provide any direct modeling of the differences between amorphous and crystalline materials. The three "glassy" phases provided to model fly ash have reaction stoichiometries and dissolution probabilities that are derived from literature [68], which provide bulk approximations of the real behavior of the materials on the molecular scale. While it is

possible with XRD to quantify the proportions of amorphous material and remaining crystalline phases in many supplementary cementitious materials, different amorphous phases cannot be discerned, and the VCCTL in its current state does not have the ability to model or even distinguish phases that are similar elementally but different in structure. As an example, the VCCTL contains no quartz phase [19]; the only silica phase is that associated with fly ash. The only alternative is to model quartz as a totally inert "filler" phase.

Combining oxide compositional data from XRF with qualitative phase identification through XRD enables mass balance calculations of composition for many supplementary materials as combinations of VCCTL fly ash phases and VCCTL cement phases. VCCTL fly ash inputs were calculated such that the overall mineral oxide proportions of the input phases matched those determined via XRF, while maximizing the contribution of the "glass" VCCTL fly ash phases to the total mass balance. This is accomplished using the following procedure:

1. Calculate the molar fraction for each mineral oxide from XRF data
2. Determine if C_3A is present, or if any crystalline phases containing CaO, Al_2O_3, SiO_2, or MgO are present using XRD (e.g. calcite, periclase, free lime)
3. Increase fraction of VCCTL "glassy" phases iteratively, using CAS_2 to match the XRF CaO content, AS to match the XRF Al_2O_3 content, and S to match the silica content
4. If it is not possible to match the XRF molar fractions with the phases from step 3 alone, add identified crystalline phases to correct the mass balance

For the six materials examined in this experiment, this procedure was able to account for greater than 99% of the mineral oxides reported from XRF. The results of these calculations for the materials considered in this study are summarized in Table 6-2.

Table 6-2. Summary of calculated VCCTL inputs for supplementary materials

		F Ash	C Ash	Micron 3	Metakaolin	RHA	Silica Fume
VCCTL Fly Ash Phases	Aluminosilicate Glass (AS)	62.99	21.46	45.73	99.94	0.11	-
	Calcium Aluminum Disilicate Glass (CAS_2)	6.27	59.21	45.21	-	-	2.32
	Tricalcium Aluminate (C_3A)	-	-	-	-	-	-
	Calcium Chloride	-	-	-	-	-	-
	Silica Glass	30.74	-	9.05	-	99.36	97.22
	Anhydrite	-	-	-	-	-	-
VCCTL Cement Phases	Periclase	-	6.07	-	-	-	-
	Calcite	-	-	-	-	-	-
	Lime	-	13.2	-	-	-	-

VCCTL slag inputs are more limited, and are calculated based on the mass of calcium, silicon, aluminum, magnesium, and sulfur oxides per mole of slag, using an online utility [69]. The hydration of slag in the VCCTL is highly empirical, with all slag being represented by a monolithic phase, and all slag hydration products represented as a slag-CSH phase [70]. The VCCTL slag inputs calculated using the published utility from measured XRF oxide compositions as well as known specific gravity [67] are presented in Table 6-3:

Table 6-3. VCCTL slag input parameters

	Slag	Slag-CSH
Molecular Mass (g/mol)	2984	4526
Specific Gravity (g/cm^3)	2.98	2.35
Molar Volume (cm^3/mol)	1002	1926
Ca/Si molar ratio	1.29	1.35
Si per mol Slag	17	-
H_2O/Si Molar Ratio	-	5.464
C_3A/mol slag	-	-
Base Reactivity	1	-

Any slag or fly ash being simulated also requires a particle size distribution, and while heat of hydration information is not required as an input by the VCCTL, it can be used to benchmark the accuracy of simulations, as well as calibrate the timing of any simulations containing those materials.

6.3. Input Characterization Methods

Based on the above requirements for inputs to the VCCTL, data was collected using four different experimental techniques for a set of common cement replacements, as well as some alternative materials being evaluated for potential use in the state of Florida. These materials included class F fly ash, ultrafine class F fly ash, class C fly ash, silica fume, metakaolin, ground granulated blast furnace slag, and rice husk ash. The following tests were performed:

1. X-ray diffraction was used to determine if any of the crystalline phases considered by the VCCTL were present, such as C_3A, calcium chloride, or anhydrite;
2. Quantitative X-Ray fluorescence was performed to measure the concentration of different elements on an oxide basis;
3. Laser Particle size analysis was used to measure the particle size distributions of the different materials;
4. Isothermal calorimetry was performed to measure the heat of hydration for each material at a range of replacement percentages selected based on the actual use of those materials.

6.3.1. X-ray Diffraction Results

X-ray diffractograms were collected for all materials; Figures 6-3 through 6-8 show the results for materials with identifiable crystalline peaks. The supplementary materials being considered for simulation are largely amorphous; however, amorphous content analysis was not performed, due to the lack of relevant simulation capabilities in the VCCTL as previously detailed. It should be noted that quantity values listed in association with identified peaks in the diffractograms are inaccurate due to difficulties with Rietveld refinement given the large amount of amorphous material present. The only unexpected material present in the diffractograms was the sodium chloride observed in the class C fly ash. Sodium chloride can be found in raw fly ash [71] as a product of flue gas desulfurization processing [72], and it is generally recognized that class C fly ash is more variable in composition than class F ash [73]. The combination of XRF results with XRD results allows for an estimation of the upper limit for certain detected crystalline phases.

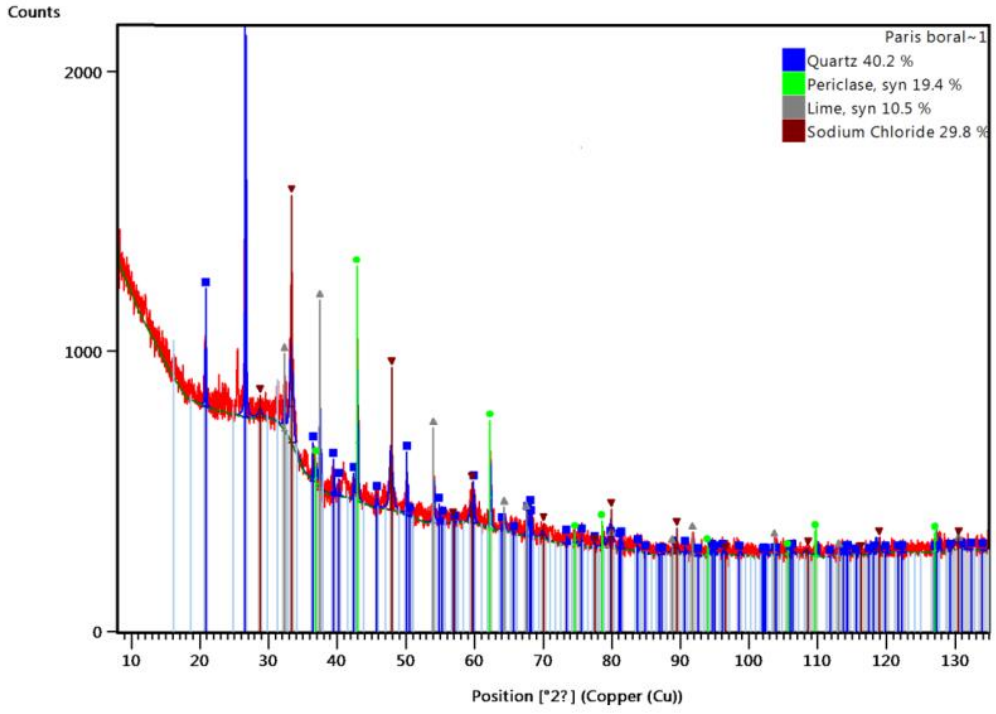

Figure 6-3. X-ray diffraction results for class C fly ash

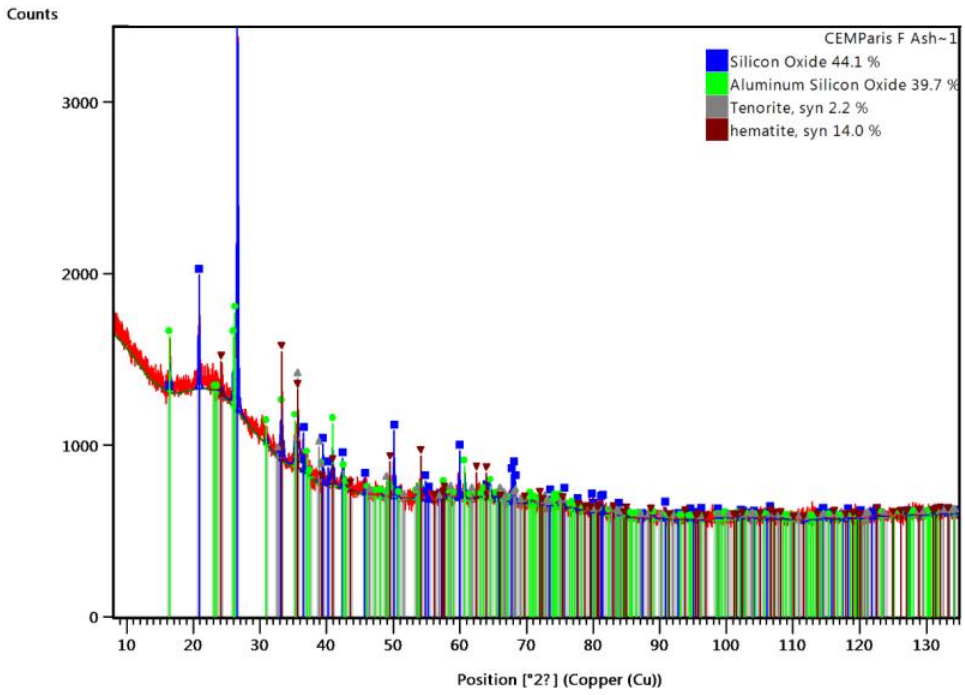

Figure 6-4. X-ray diffraction results for class F fly ash

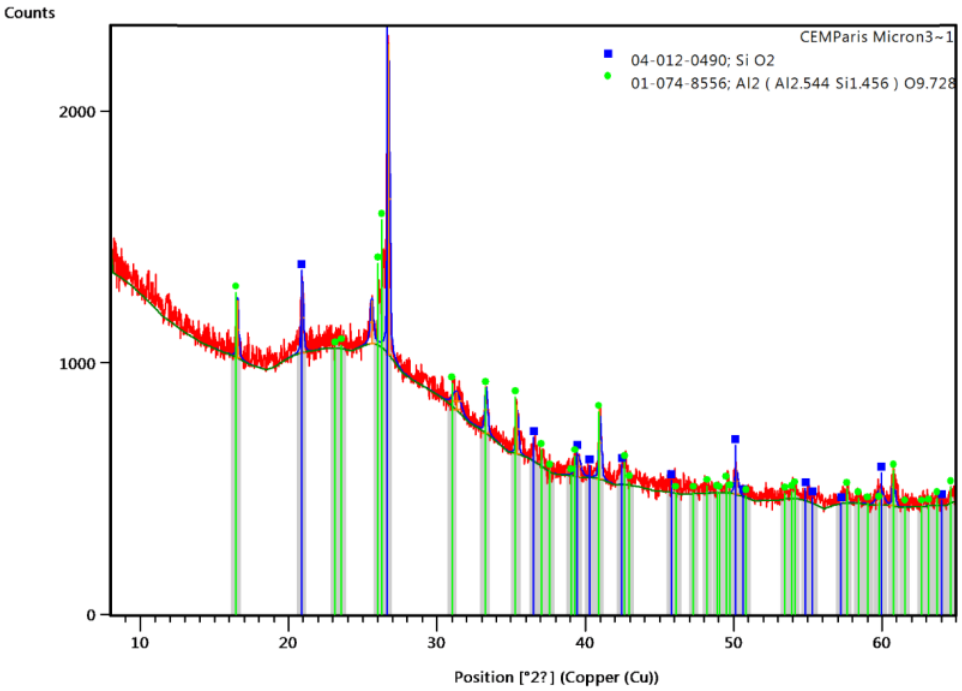

Figure 6-5. X-ray diffraction results for ultrafine class F fly ash

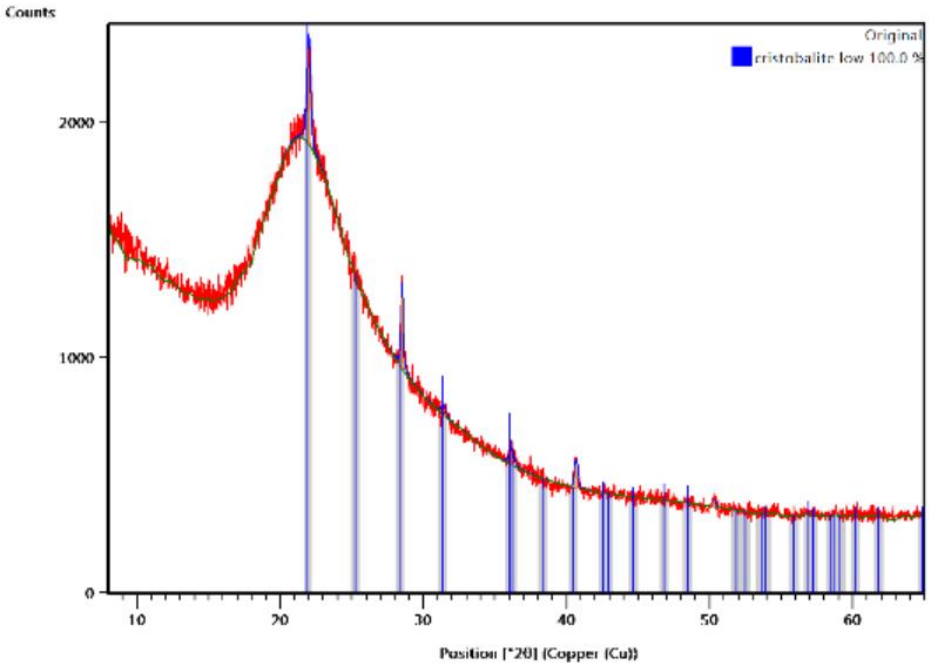

Figure 6-6. X-ray diffraction results for rice husk ash

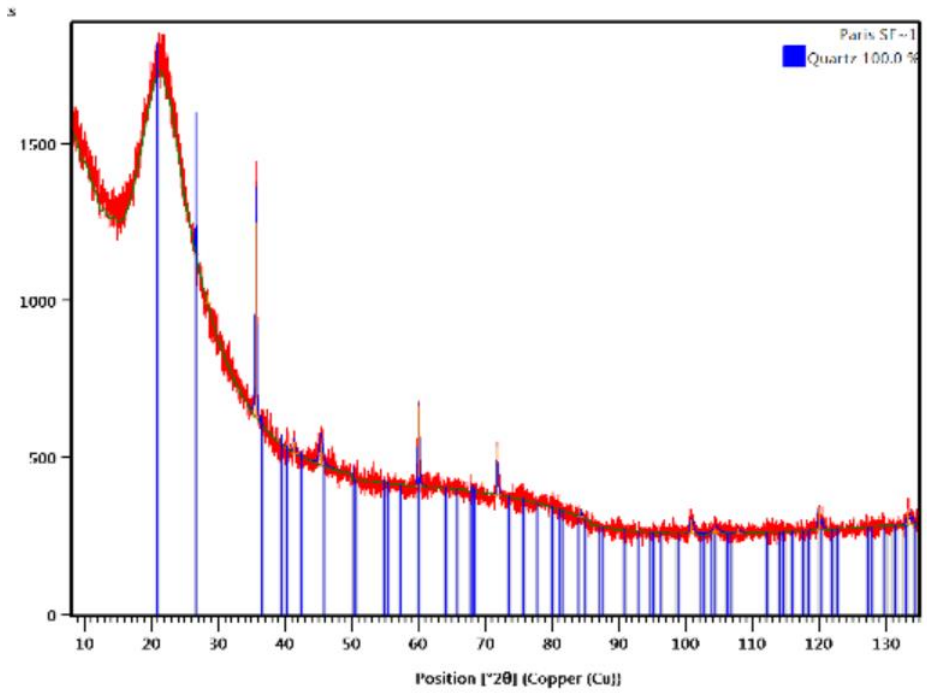

Figure 6-7. X-ray diffraction results for silica fume

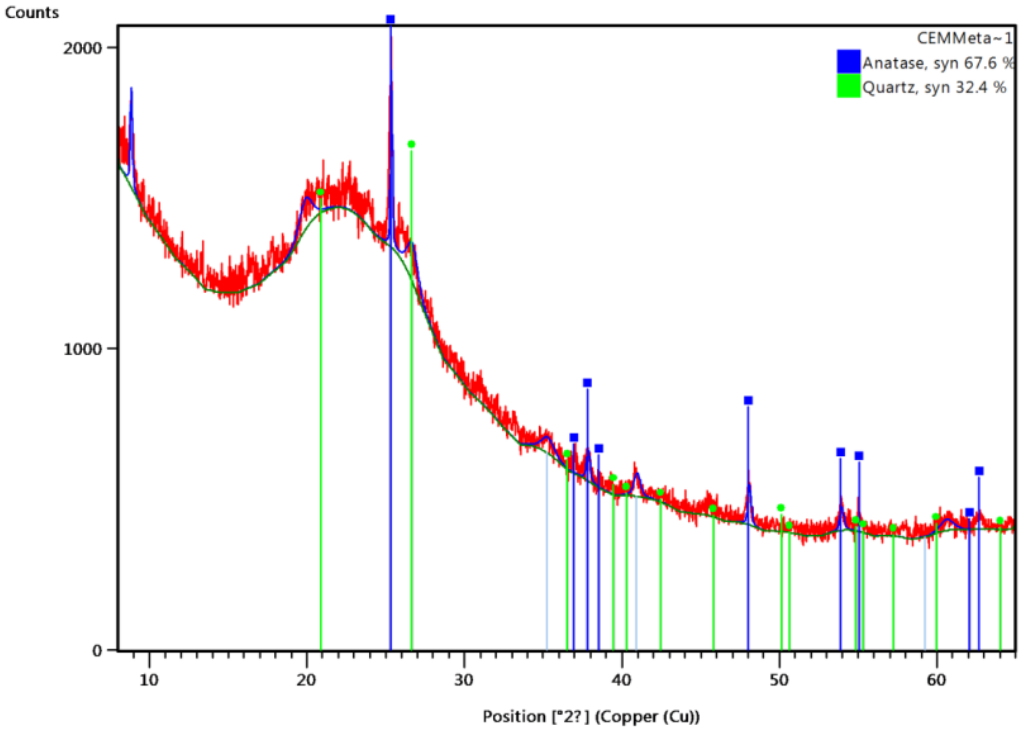

Figure 6-8. X-ray diffraction results for metakaolin

6.3.2. X-Ray Fluorescence Results

Table 6-4 exhibits the mineral oxide compositions of the seven supplementary materials analyzed for this study. Measured compositions fall within established ranges [73–75] for each respective class of material. This information provides the primary compositional input to the VCCTL. The relative concentrations of silicon, calcium, and aluminum are used to compute the combination of VCCTL phases that produce the appropriate mass balance. The XRF data in combination with the XRD data also provides some information about the crystalline phases detected. The class C fly ash (Figure 6-3), for example, contains the crystalline phases periclase (MgO) and sodium chloride;, however, the quantity is unknown based upon the x-ray diffractogram alone. The XRF oxide analysis for class C fly ash identifies periclase (MgO) as 6.36% of the material, and sodium as 1.88%. This allows an upper limit to be established for the relative amounts of the detected crystalline phases. It may also be possible to simulate certain phases, like periclase, as they can be incorporated as part of the portland cement.

Table 6-4. XRF Oxide analysis results

Chemical Oxide	Class F Fly Ash	Class C Fly Ash	Ground Blast Furnace Slag	Silica Fume
SiO_2	57.8	34.7	33.6	90.9
Al_2O_3	21.4	18.5	14.4	0.39
Fe_2O_3	11.8	5.66	0.61	2.14
CaO	1.29	26.4	41.1	0.85
MgO	1.32	6.36	5.88	0.78
SO_3	0.24	1.84	2.56	<0.01
Na_2O	0.90	1.88	0.19	0.20
K_2O	2.52	0.43	0.34	1.07
TiO_2	0.99	1.45	0.53	<0.01
P_2O_5	0.19	0.86	0.02	0.10
Mn_2O_3	0.04	0.04	0.35	0.19
SrO	0.05	0.43	0.07	0.01
Cr_2O_3	0.02	0.01	<0.01	<0.01
ZnO	0.02	0.01	<0.01	0.07
BaO	0.07	0.83	0.06	<0.01

Table 6-4 (continued)

Chemical Oxide	Metakaolin	Rice Husk Ash	Micron[3] ultrafine fly ash
SiO_2	51.5	94.0	51.0
Al_2O_3	43.7	0.03	25.4
Fe_2O_3	0.47	0.07	4.42
CaO	<0.01	0.52	10.2
MgO	0.14	0.45	2.15
SO_3	0.01	0.21	0.72
Na_2O	0.28	0.08	0.49
K_2O	0.25	2.47	1.06
TiO_2	1.35	-	1.45
P_2O_5	0.08	1.49	0.37
Mn_2O_3	<0.01	0.18	0.08
SrO	0.02	-	0.13
Cr_2O_3	0.01	-	0.02
ZnO	<0.01	0.02	0.04
BaO	0.2	-	0.16

6.3.3. Laser Particle Size Analysis Results

The results of laser particle size analysis for the materials considered in this study are presented in Figures 6-9 through 6-15. The distributions were obtained using a laser particle size analyzer (LPA), with the powders suspended in recirculating ethanol to optimize dispersion. An ultrasonic probe in the LPA was activated to break up flocculated particle for multiple successive 1 minute cycles. This was continued until the observed mean particle size changed less than 1 μm between cycles. The resultant distributions are input directly to the VCCTL and require no further analysis or post-processing.

The measured distributions for most of the analyzed materials agreed with typical reported values [73], with the exception of two materials: metakaolin (Figure 6-12) and silica fume (Figure 6-13), which exhibited anomalous, strongly bimodal distributions. The metakaolin distribution has peaks at approximately 0.15 μm and 4.5 μm, with the smaller peak accounting for approximately 20% of the material, and the larger peak comprising the remaining 80%. The distribution's bimodality may be indicative of particle agglomeration that is too strong for the 35W ultrasonic probe to remove;, however, the average particle size is consistent with a range of values reported in literature between 1 μm and 4 μm [76–79]. The measured distribution for silica fume indicates particles much larger than the typically reported average size of 0.15 μm [73,80];, however, silica fume is typically supplied in a densified form as much larger particle clusters. The distribution in Figure 13 is typical of a densified silica fume measured using a LPA with an ultrasonic probe similar in power to that used in this research [81].

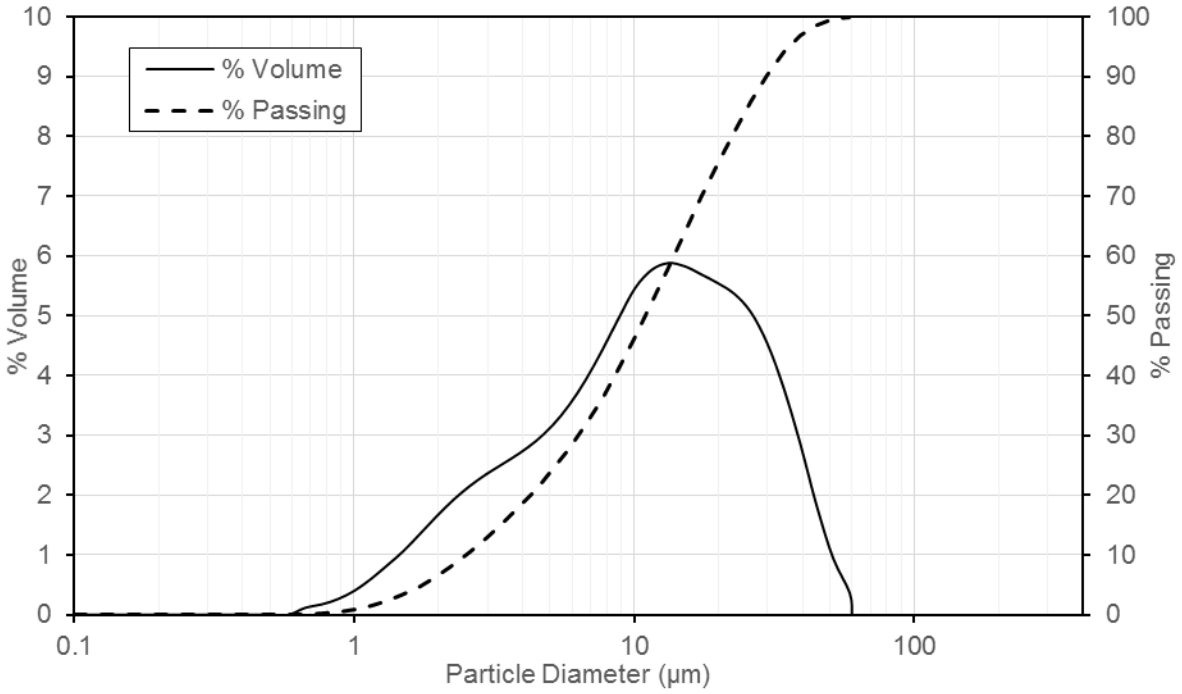

Figure 6-9. Volume and Cumulative Particle Size Distributions for Class F Fly Ash

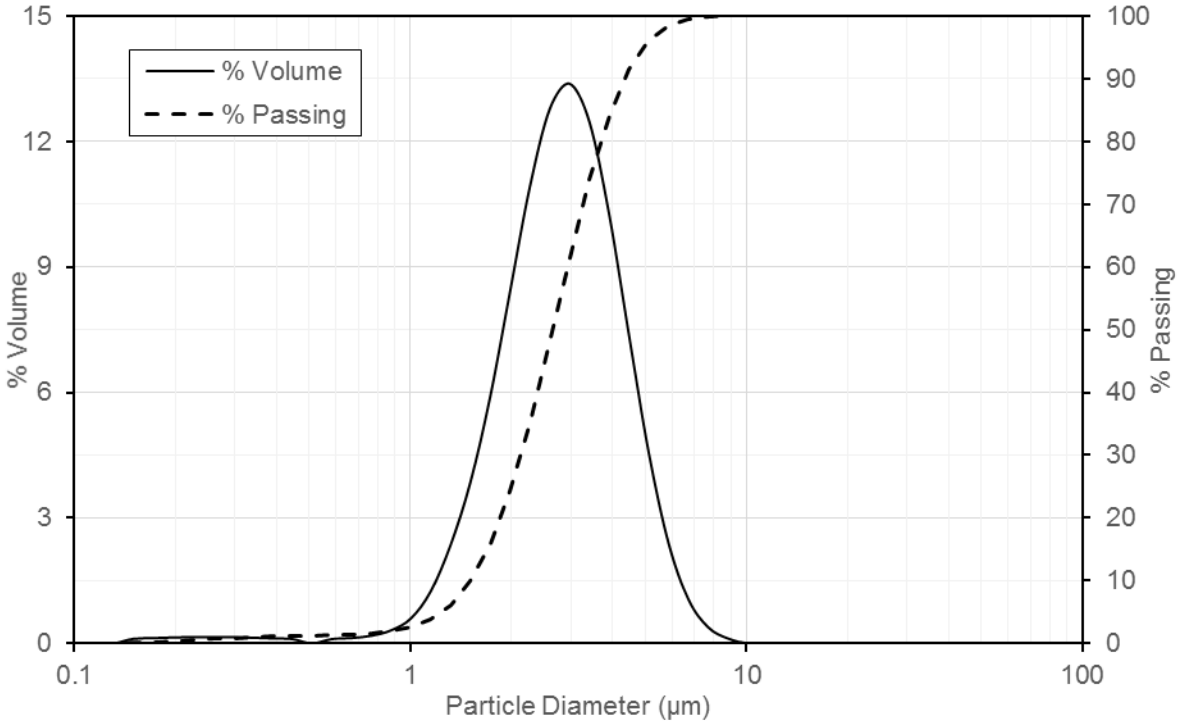

Figure 6-10. Volume and Cumulative Particle Size Distributions for Micron 3 Fly Ash

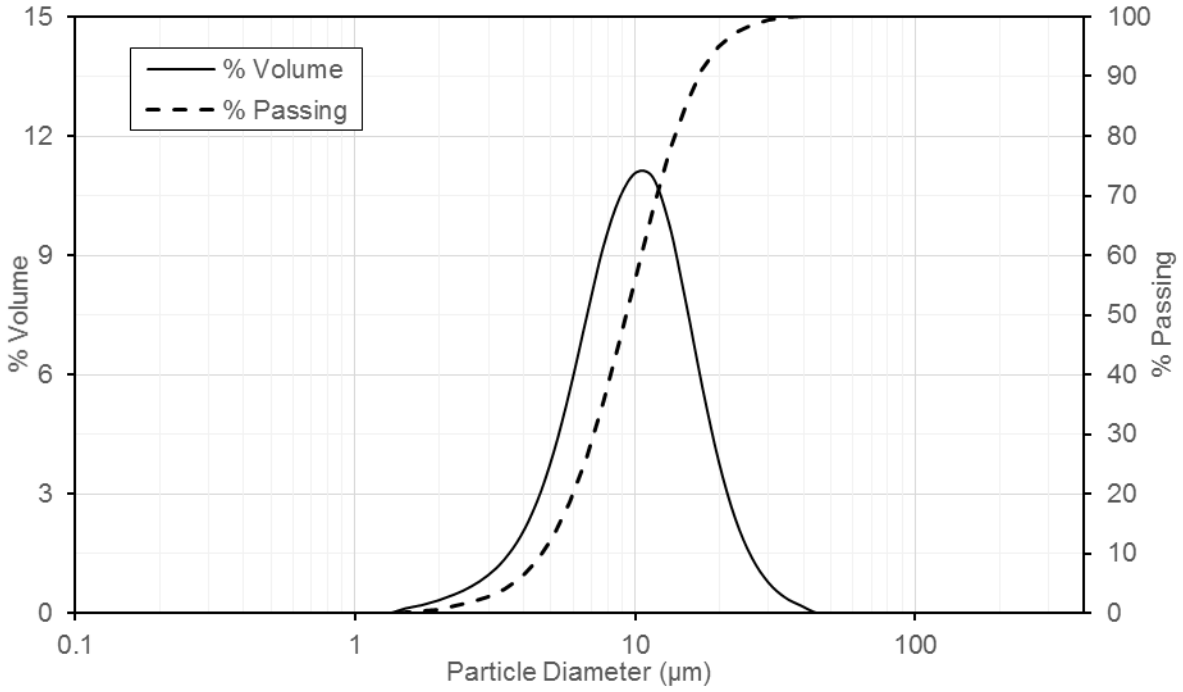

Figure 6-11. Volume and Cumulative Particle Size Distributions for Blast Furnace Slag

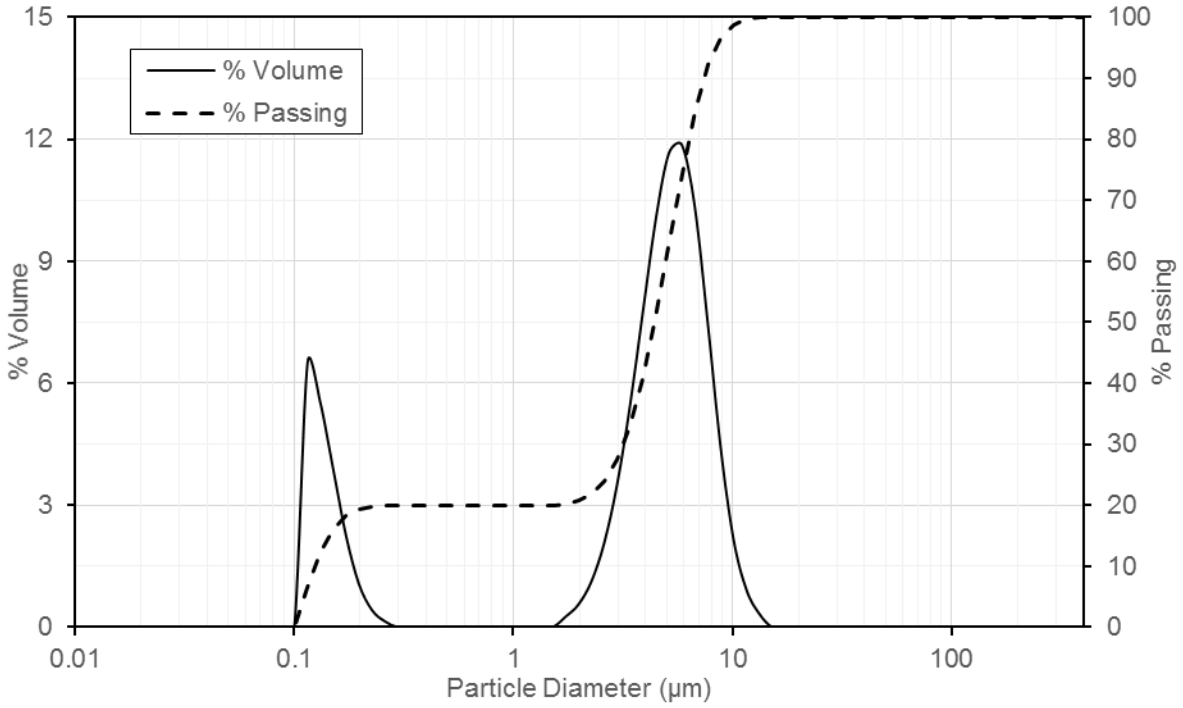

Figure 6-12. Volume and Cumulative Particle Size Distributions for Metakaolin

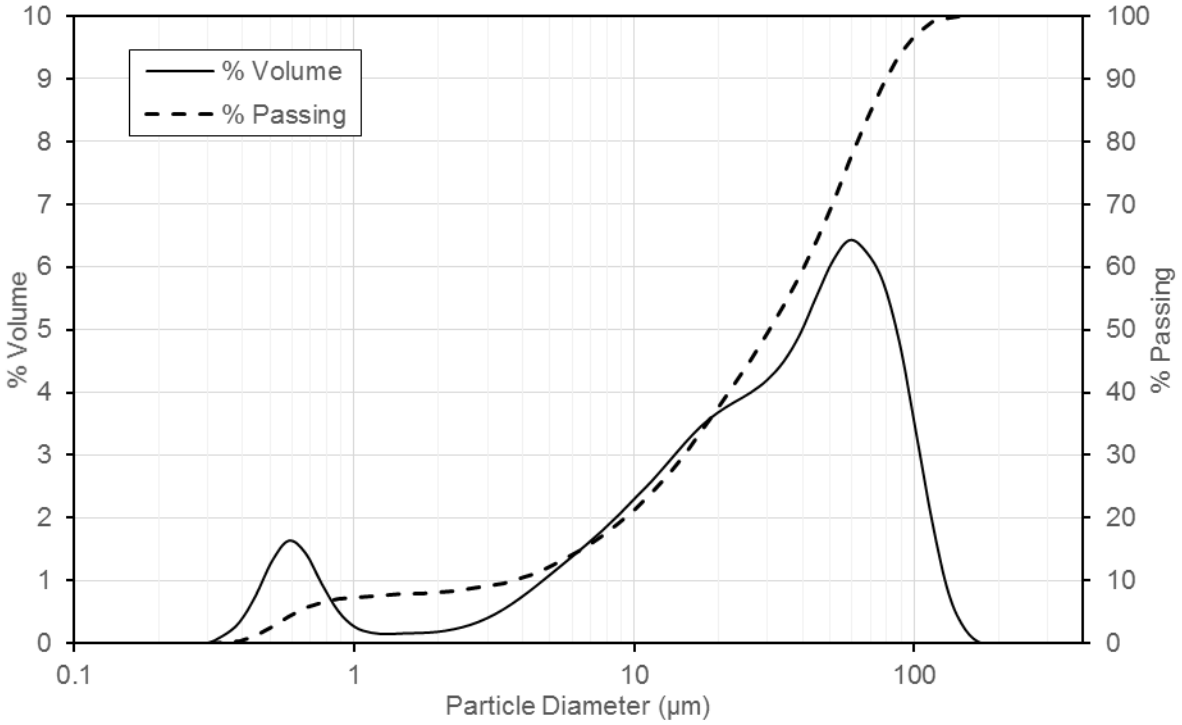

Figure 6-13. Volume and Cumulative Particle Size Distribution for Densified silica fume

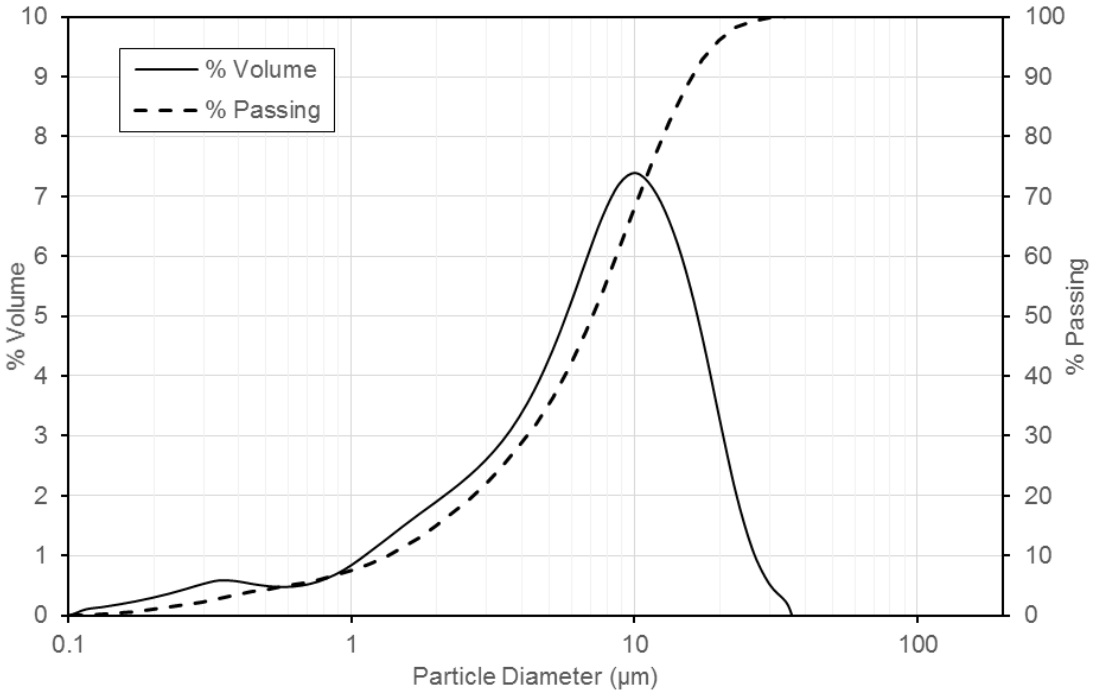

Figure 6-14. Volume and Cumulative Particle Size Distributions for Class C Fly Ash

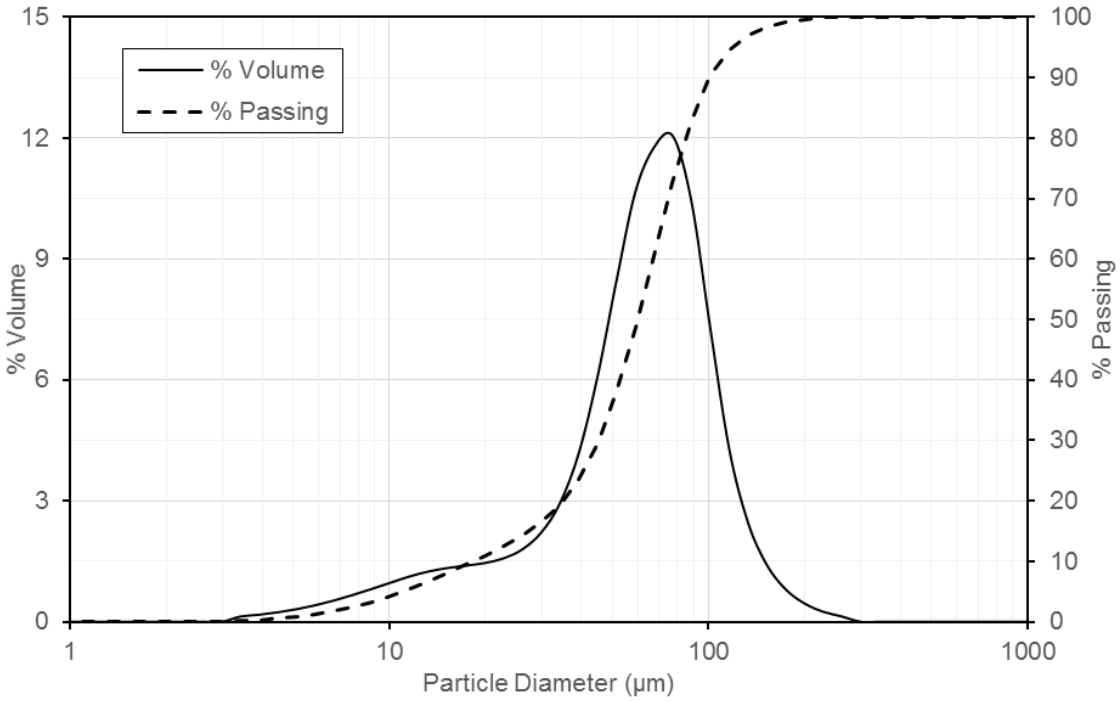

Figure 6-15. Volume and Cumulative Particle Size Distributions for Rice Husk Ash

6.3.4. Isothermal Calorimetry Results

Figures 6-16 through 6-20 show the results of isothermal calorimetry testing for several of the materials being considered, with multiple replacement percentages for each material. Isothermal calorimetry testing was performed in adherence with ASTM C1702 specifications. All speciemens were prepared at a 0.5 w/c, using internally mixed vials. Procedural details were identical to those reported in technical memorandum 2. Isothermal curves are not mandatory inputs for the VCCTL; however, they can be used to calibrate the time domain of simulations containing these materials, and can alternatively be compared to simulation results to gauge the accuracy of the models behavior with different supplementary materials.

With the exception of metakaolin, the analyzed supplementary cementitious materials generally reduce 7-day isothermal heat of hydration when blended with portland cement, with higher replacement percentages typically having a more dramatic effect [73]. The measured heat of hydration curves presented in Figures 6-16 to 16-21 exhibited no anomalous behavior with respect to reported values [79]; material specific differences in the degree of heat reduction as replacement percentage increased were typical of those reported in literature [79] for those materials.

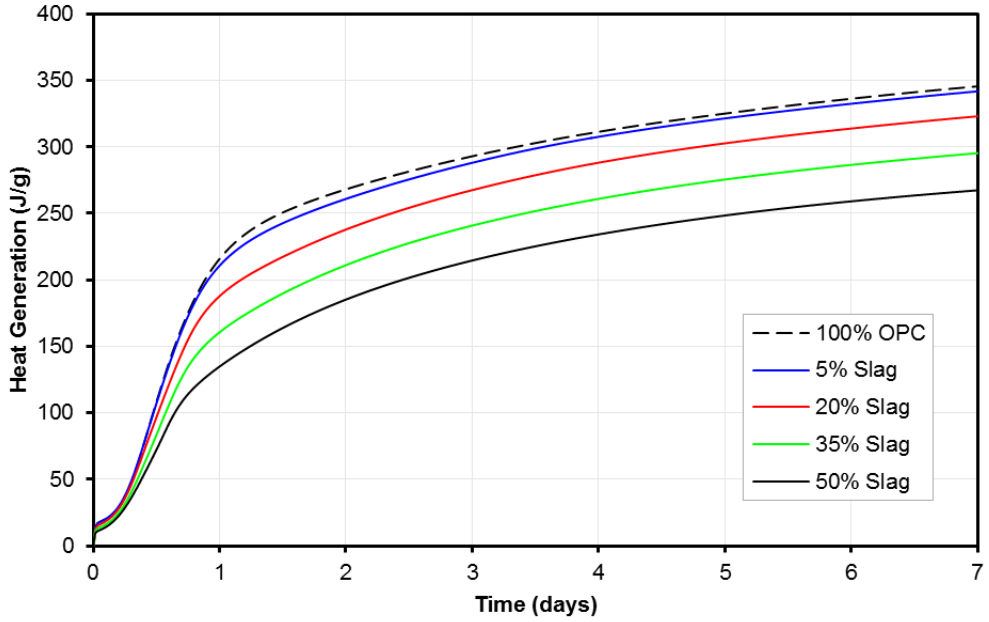

Figure 6-16. Heat of hydration results for ground granulated blast furnace slag

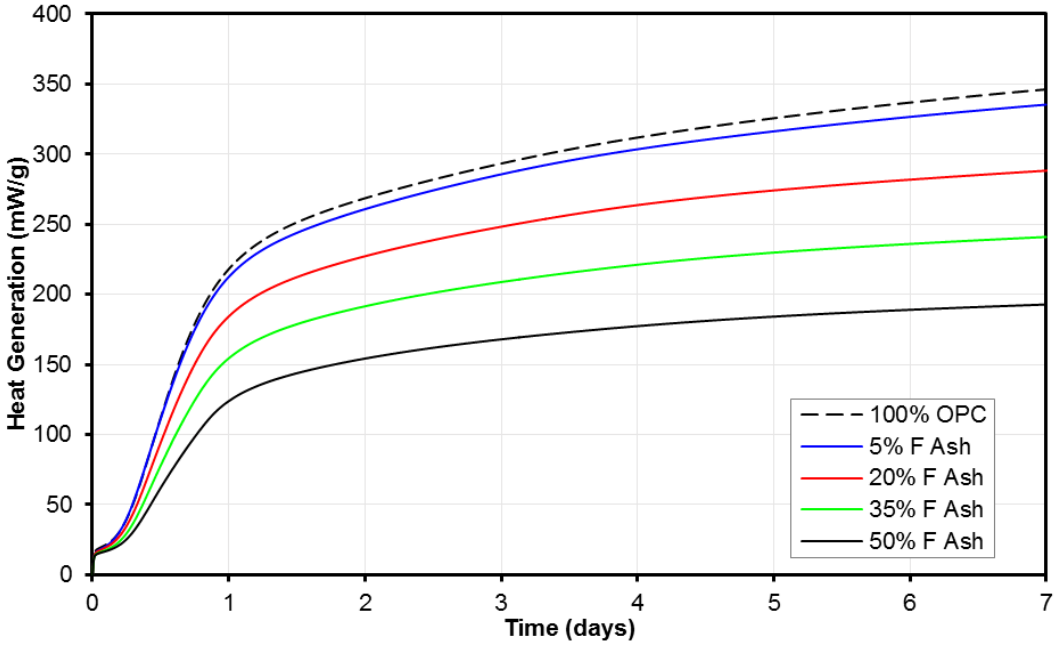

Figure 6-17. Heat of hydration results for class F fly ash

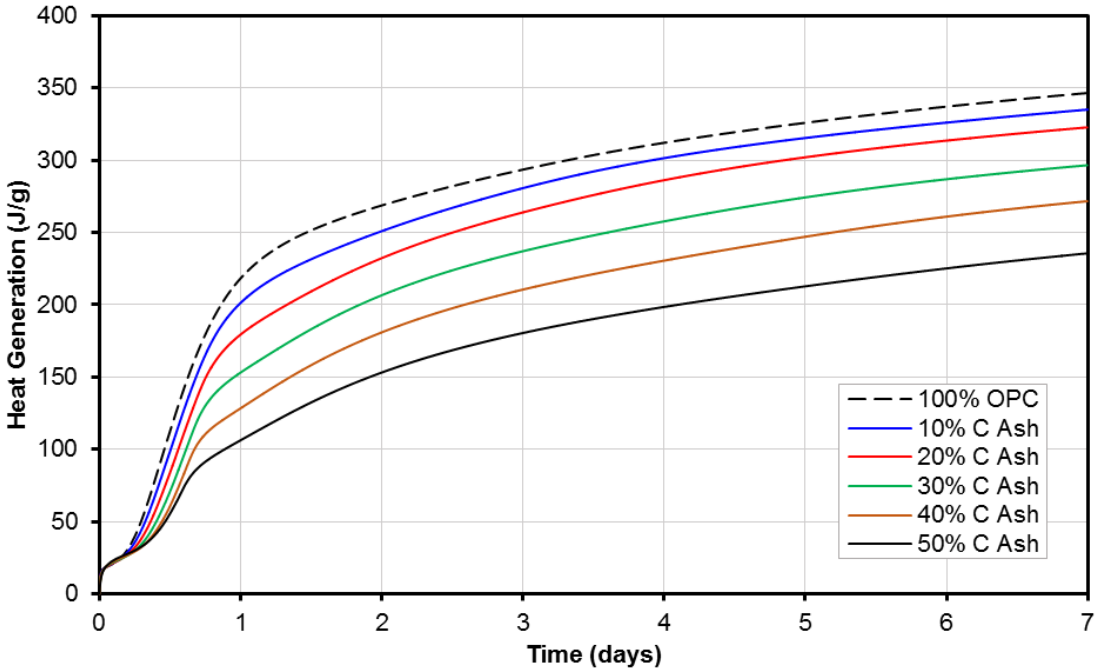

Figure 6-18. Heat of hydration results for class C fly ash

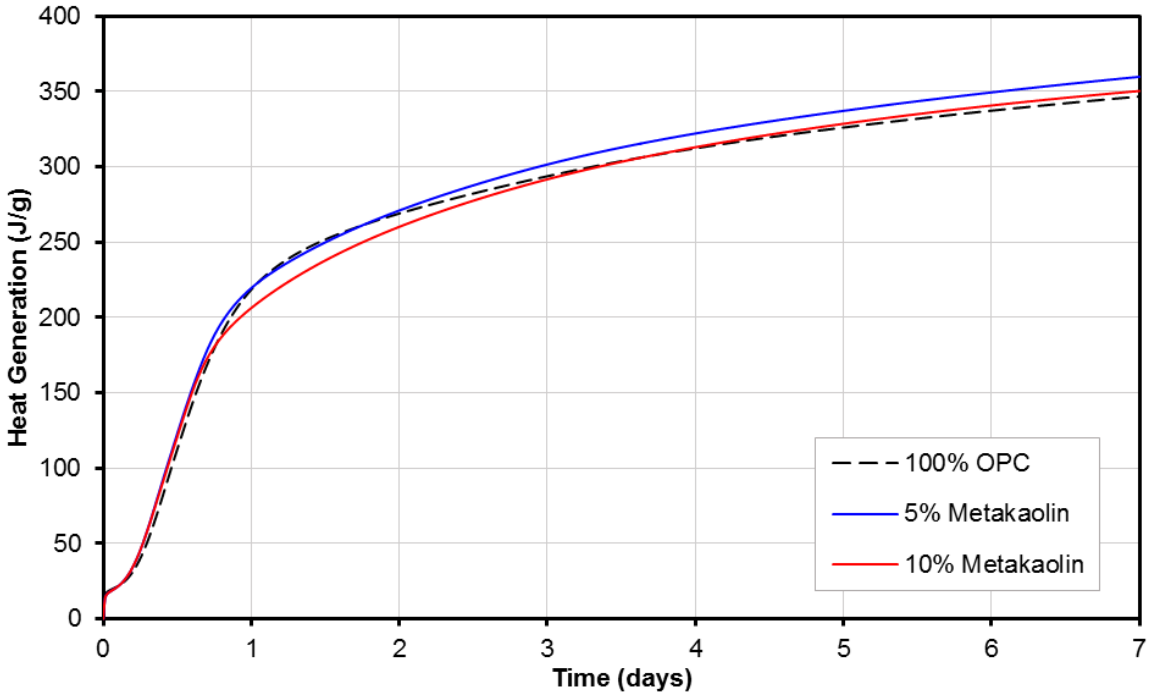

Figure 6-19. Heat of hydration results for metakaolin

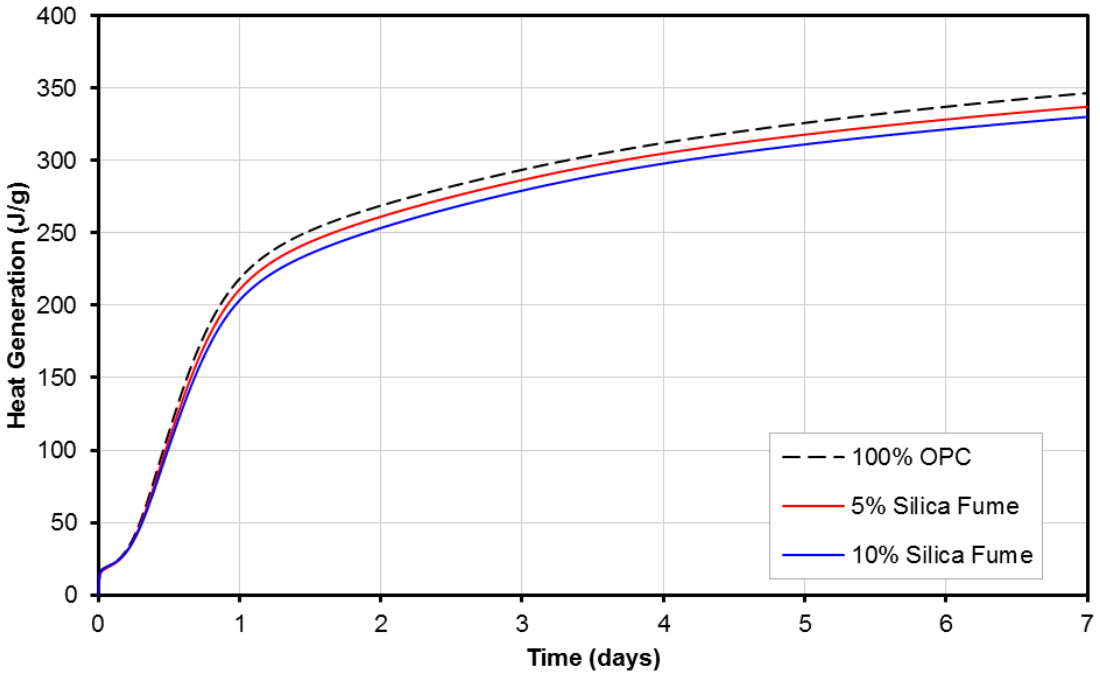

Figure 6-20. Heat of hydration results for silica fume

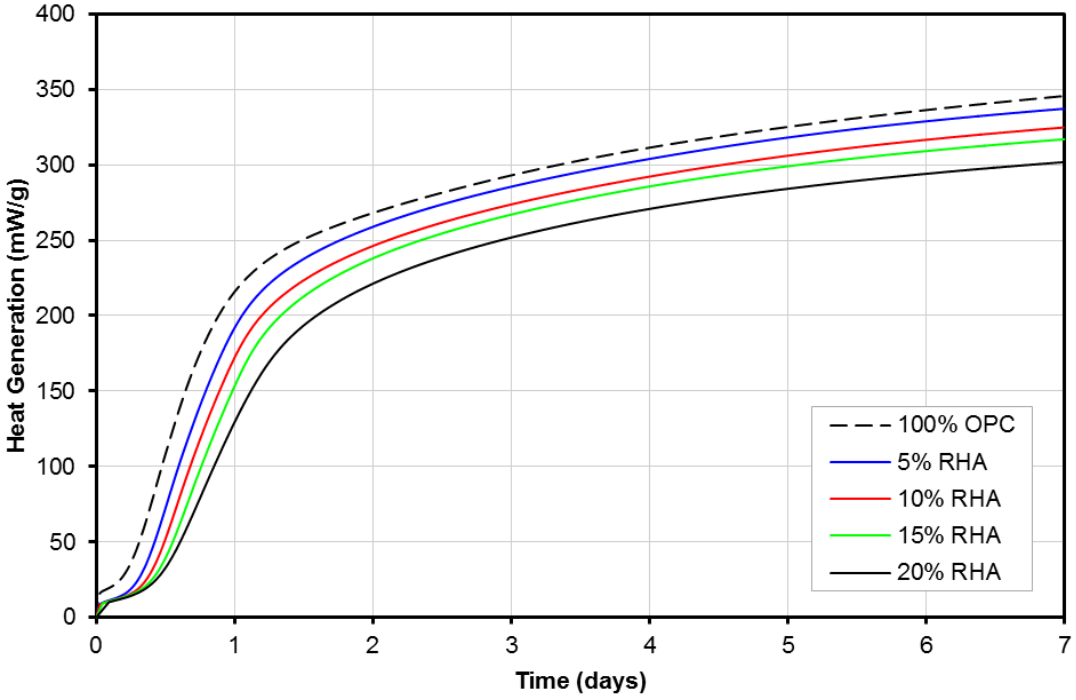

Figure 6-21. Heat of hydration results for rice husk ash

6.4. Evaluation of VCCTL Performance for Binary Mixtures

6.4.1. Experimental Design

The primary goal of this experiment was to determine the accuracy with which the VCCTL can simulate the compressive strength of binary mortars for pozzolanic materials, using the material characterization procedures and data detailed above. Ten binary mixtures were selected and simulated, based on commonly used replacement materials as well as available data for mortar compressive strength and isothermal heat of hydration. Selected mixtures are summarized in Table 6-5. The authors intended to evaluate model performance for mortars containing blast furnace slag in addition to those selected; however, attempts to execute VCCTL simulations with the developed slag inputs failed to hydrate beyond an age of 20 hours, for reasons that could not be determined.

Table 6-5. Selected binary pozzolanic mixtures

Mix ID	Material	Replacement %
1	Class C Fly Ash	10
2	Class C Fly Ash	20
3	Class C Fly Ash	30
4	Class C Fly Ash	50
5	Class F Fly Ash	20
6	Class F Fly Ash	40
7	Metakaolin	5
8	Metakaolin	10
9	Rice Husk Ash	5
10	Rice Husk Ash	10

The composition, fineness, and heat of hydration inputs, as developed in the Task 4 Deliverable, for cement and pozzolans were used for all mortar simulations. Heat of hydration data for each combination of pozzolan and replacement percentage was provided as time calibration input for the VCCTL, in an effort to maximize the fidelity of simulations to measured data, particularly at early ages. Other simulation inputs including mixture proportions, curing conditions, and temperature were set to match the procedures [82] and conditions present during mortar compressive strength testing. Simulation conditions for this experiment were similar to those detailed in chapter 3, excepting the addition of virtual pozzolanic materials.

Simulations were run to 56 days of age, with the VCCTL elastic modulus and compressive strength calculations performed at 1, 3, 7, 14, 28, and 56 days. Strength results were compared to VCCTL predictions, using the default empirical relationship which calculates strength from strength from modulus (eqn. 6-1). This equation was pulled directly from the source code [83], where comments indicate it was fitted from data provided by Siam Cement Group. To the best of the authors' knowledge, the data in question appears to be unpublished.

$$f'_c = (5.0 * 10^{-4})E^{3.18577} \quad (6\text{-}1)$$

Strength results were also compared to two empirical prediction equations developed from in Chapter 3, one of which calculates compressive strength based on simulated heat of hydration (eqn. 6-2),

$$f'_c = 0.075 * heat + 5.901 \quad (6\text{-}2)$$

while the other predicts compressive strength from simulated mortar elastic modulus (eqn. 6-3), and is similar in form to equation 1.

$$f'_c = 0.08221E^{1.77} \quad (6\text{-}3)$$

6.4.2. Results

Class C Fly Ash

Comparisons of the measured mortar compressive strengths for mixtures containing class C fly ash are presented in Figures 6-22 to 6-25. Generally speaking, the accuracy of the VCCTL predictions for class C ash decreases as the measurement age increases and as replacement percentage increases. None of the three empirical prediction equations used to calculate strength showed a consistent advantage across all replacement percentages and ages. The 10% replacement case (Figure 6-22) appears to agree most closely with predicted values; the default prediction equation approximates measured values at 1, 3, and 7 days of age, but begins to deviate at later ages. All prediction equations exhibited the worst performance in the 50% replacement case (Figure 6-25); the default VCCTL relationship predicted strength values less than 50% those measured after 7 days, and while the heat and modulus equations fared slightly better, overall performance remained poor.

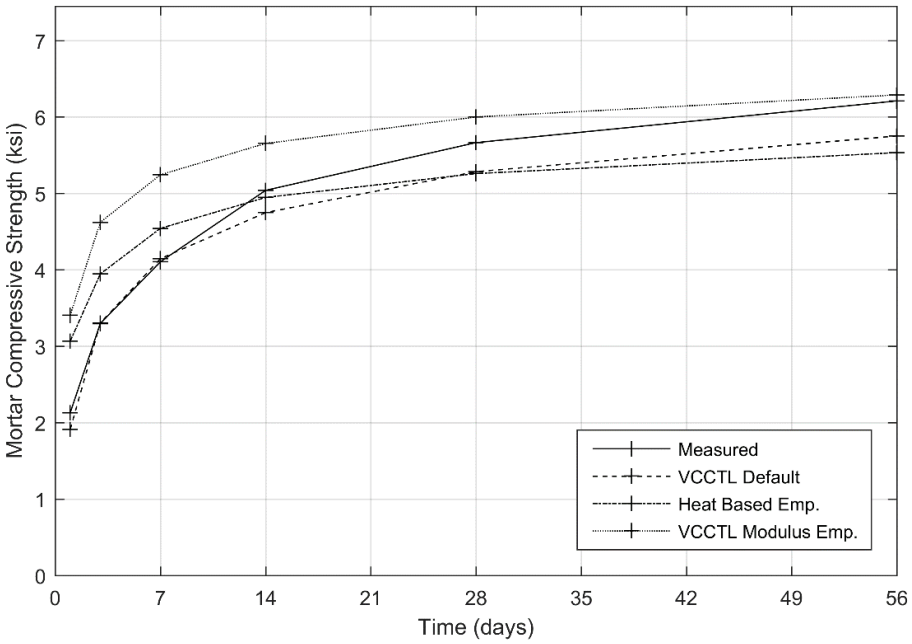

Figure 6-22. Measured compressive strength for mortar with 10% class C fly ash, compared to three VCCTL compressive strength prediction relationships

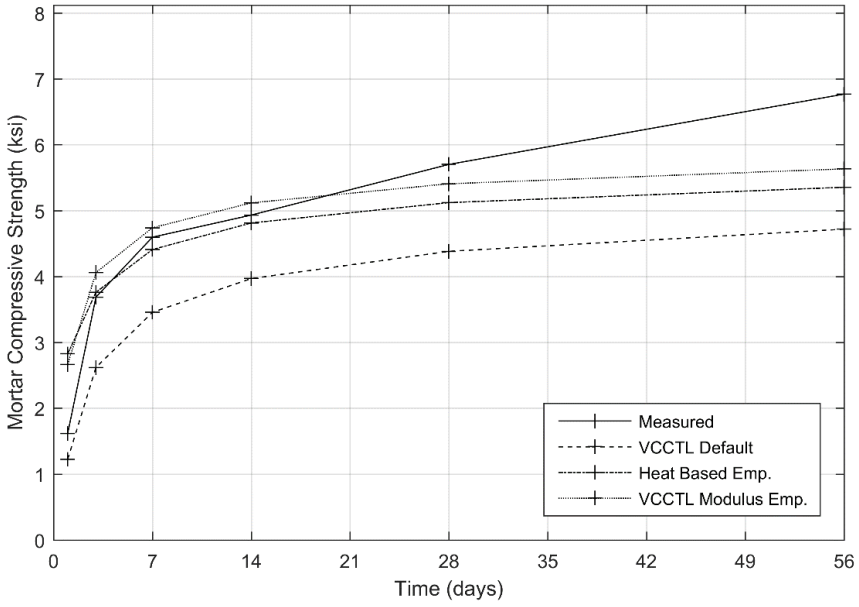

Figure 6-23. Measured compressive strength for mortar with 20% class C fly ash, compared to three VCCTL compressive strength prediction relationships

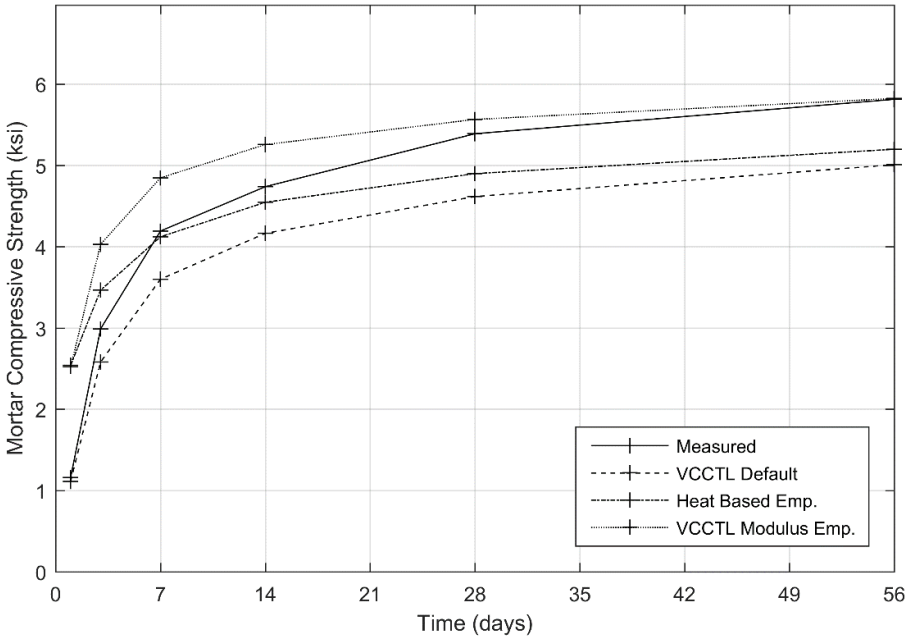

Figure 6-24. Measured compressive strength for mortar with 30% class C fly ash, compared to three VCCTL compressive strength prediction relationships

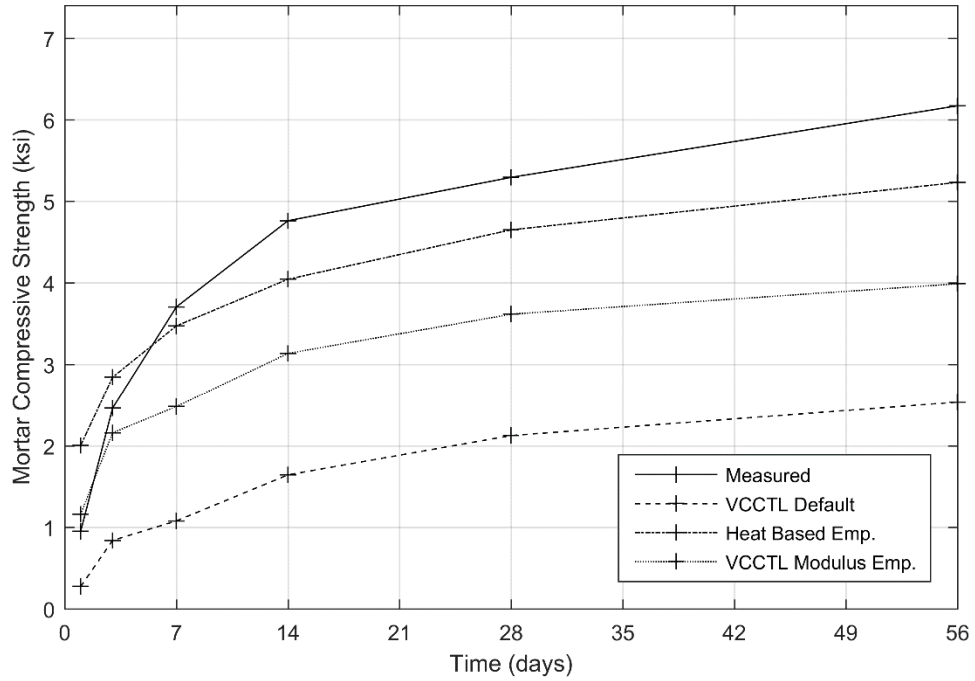

Figure 6-25. Measured compressive strength for mortar with 50% class C fly ash, compared to three VCCTL compressive strength prediction relationships

Class F Fly Ash

Predicted compressive strengths for mixtures containing class F fly ash (Figures 6-26 and 6-27) exhibited similar trends to those observed for class C fly ash; however, the discrepancies were consistently larger than those of class C ash. At both 20% and 40% replacement percentages, the VCCTL predicted significantly less strength development at later ages. The default prediction relationship exhibited the worst performance, under-predicting strength to an increasing degree as specimen age increased. The heat and modulus-based empirical relationships over-predicted at ages earlier than 7 days, and under-predicted thereafter, with the heat-based prediction performing marginally better at later ages.

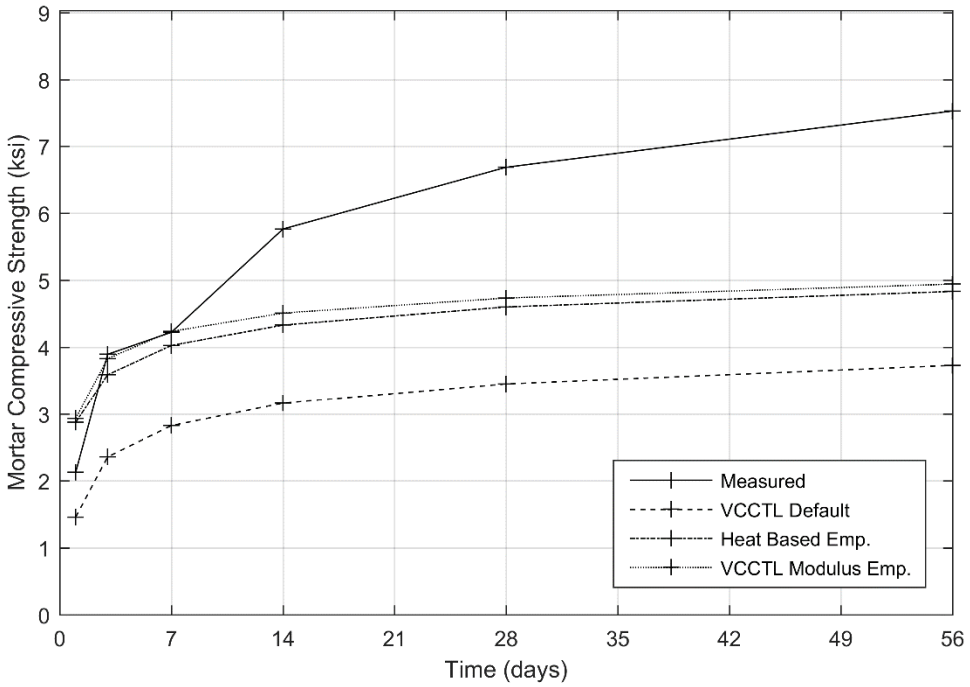

Figure 6-26. Measured compressive strength for mortar with 20% class F fly ash, compared to three VCCTL compressive strength prediction relationships

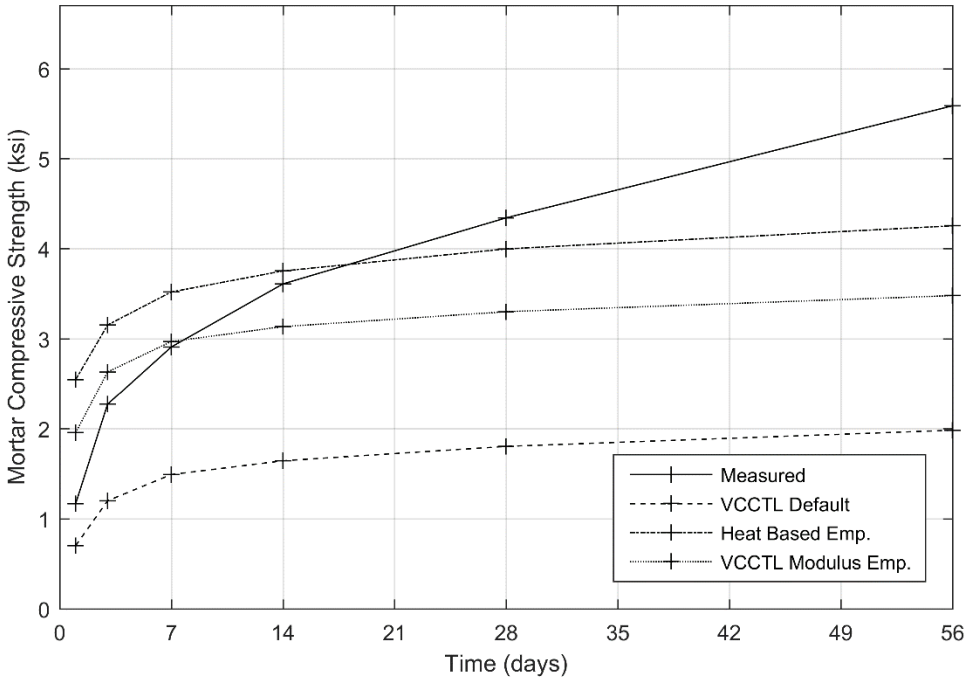

Figure 6-27. Measured compressive strength for mortar with 40% class F fly ash, compared to three VCCTL compressive strength prediction relationships

Metakaolin

The predicted values at the 5% and 10% replacement levels (Figures 6-28 and 6-29) for metakaolin dramatically underestimated the strengths achieved by the physical specimens. As with other replacement materials, higher replacement amounts produced greater deviation from the measured values. The three different VCCTL strength equations did not show any clear advantage in prediction of strength for metakaolin; only the heat-based equation agreed with experimental data at any point, which was at 1 day of age for both replacement percentages.

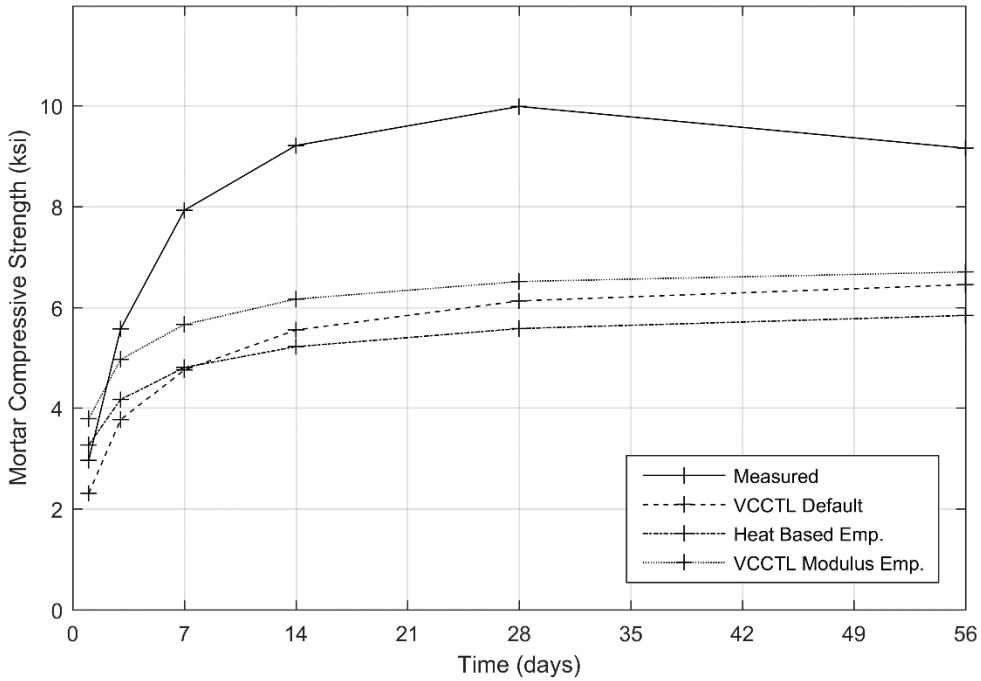

Figure 6-28. Measured compressive strength for mortar with 5% metakaolin, compared to three VCCTL compressive strength prediction relationships

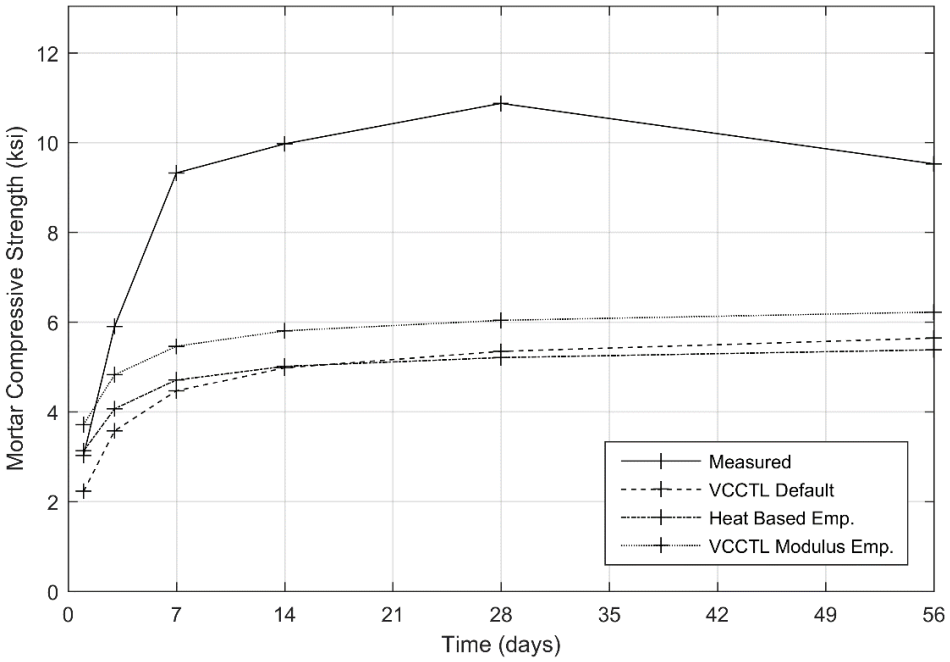

Figure 6-29. Measured compressive strength for mortar with 10% metakaolin, compared to three VCCTL compressive strength prediction relationships

Rice Husk Ash

Compressive strengths of mortars containing 5% and 10% rice husk ash (Figures 6-30 and 6-31) exceeded the values predicted by the three different VCCTL equations, though to a lesser degree than predictions for metakaolin. Measured compressive strengths increased slightly as replacement percentage increased. Only 1-day predictions at the 10% replacement level were approximately close to measured values. The degree to which the measured values were overestimated decreased somewhat between the 5% to 10% replacement amounts. The differences between the three VCCTL prediction equations diminished significantly as replacement percentage increased.

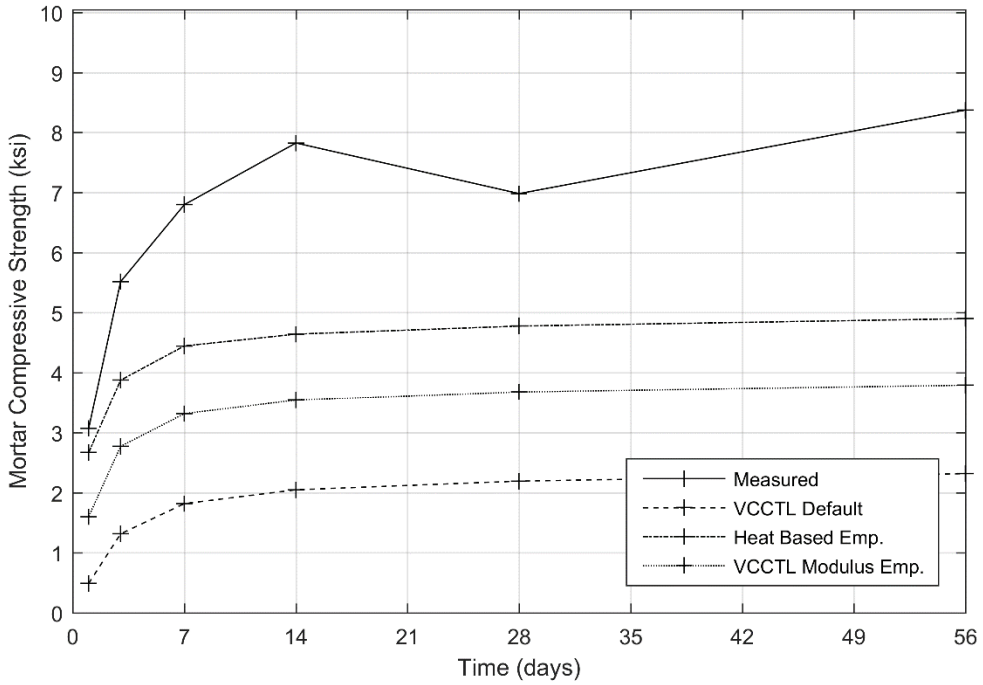

Figure 6-30. Measured compressive strength for mortar with 5% rice husk ash, compared to three VCCTL compressive strength prediction relationships

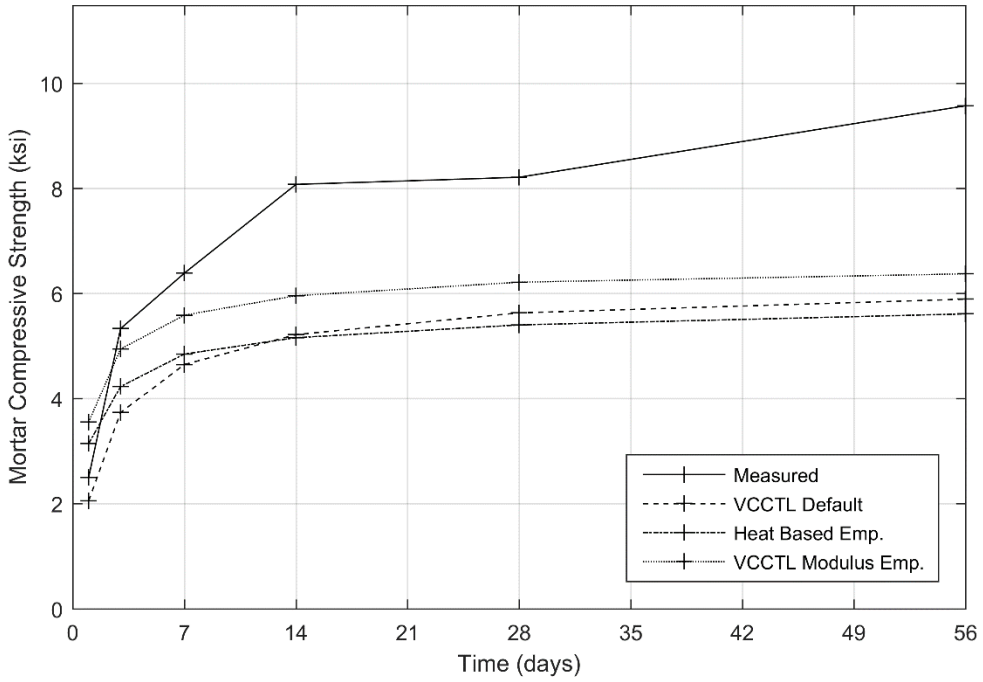

Figure 6-31. Measured compressive strength for mortar with 10% rice husk ash, compared to three VCCTL compressive strength prediction relationships

6.4.3. Discussion

The results comparing VCCTL predictions of compressive strength to measured values indicate that in the as-delivered configuration, the VCCTL does not predict compressive strength of mortars containing supplemental materials with a useful degree of accuracy. The relationships developed from CCRL data to predict compressive strength from heat of hydration and VCCTL mortar elastic modulus do not appear to work with any degree of efficacy for mixtures incorporating supplementary cementitious materials. In the future, these equations should only be applied in the context of quality control testing for ordinary portland cement. Chapter 7 details an alternative method of strength prediction using artificial neural networks (ANN's), which may be applicable to a broader range of cementitious material composition.

6.5. Pareto Optimization of VCCTL Binary Mixtures

6.5.1. Experimental Design

To better understand how the VCCTL responds to changes in pozzolan composition, fineness, and replacement percentage, methods developed and detailed in chapter 9 were applied. A total of 16,000 VCCTL simulations of mortars containing pozzolans were executed on the UF HiperGator high-performance computational cluster, and multi-variate pareto optimization techniques developed in Chapter 9 were applied to elucidate the performance limits associated with a bi-objective optimal performance criterion. In this case, Pareto fronts were computed to

visualize the ideal trade off solutions when maximizing 7-day mortar elastic modulus and minimizing initial setting time or 7-day heat of hydration.

Virtual pozzolans were randomly generated over ranges selected to encompass a broad range of potential compositions. Each virtual pozzolan comprised up to five VCCTL phases. Four of these phases are designated expressly by the VCCTL to simulate pozzolanic materials (aluminosilicate glass (AS), calcium aluminum disilicate (CAS_2) glass, amorphous silica (S), and C_3A from fly ash). Also included were varying amounts of a fifth "inert" phase, intended to simulate minimally reactive materials that are sometimes found in fly ash, e.g. quartz or periclase. A total of 1000 randomly generated pozzolans were simulated, over the ranges shown in Table 2. All simulations were run using the same portland cement characterized as part of the Task 4 Deliverable, with hydration conditions set based on the specified conditions and procedures in ASTM C109 [82].

Table 6-6. Ranges used for random generation of VCCTL Pozzolan Chemistries

Phase	Mass Fraction Range
AS	0 to 1
CAS_2	0 to 0.07
S	0 to 1
C_3A	0 to 0.05
Inert	0 to 0.4

The 1000 randomly generated chemistries were simulated at sixteen different combinations of replacement percentage and average particle size. The four different replacement percentages were chosen as 5%, 20%, 35%, and 50%. Particle size distributions were generated artificially, with mean particle sizes of 12.5 μm, 7.5 μm, 2.5 μm, and 0.5 μm. Generated distributions were lognormal, with standard deviations set at two thirds of the specified average particle size. The cumulative distributions used as inputs to the VCCTL are shown in Figure 6-32.

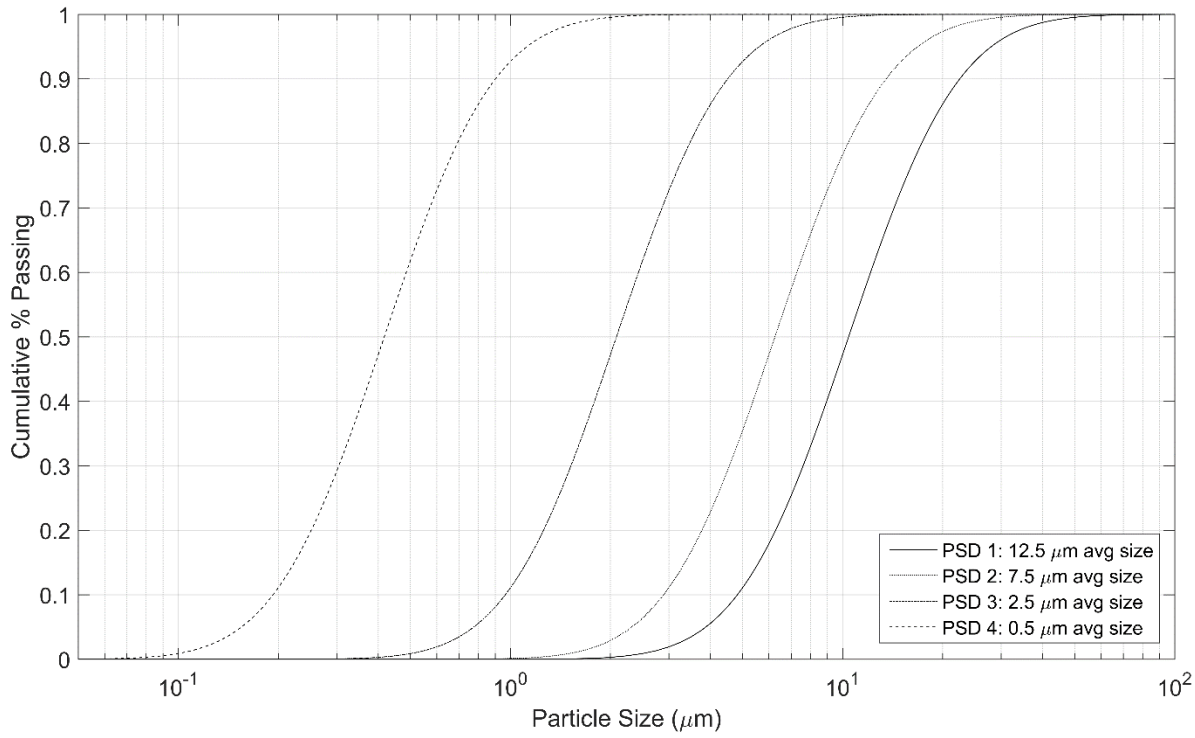

Figure 6-32. Lognormal cumulative distributions used to provide particle size input to the VCCTL

Two bi-objective optimization cases were investigated using pareto analysis, corresponding to different practical performance tradeoffs that are common when using supplementary cementitious materials. The first case maximized 7-day elastic modulus while minimizing 7-day heat of hydration. Pozzolanic materials are commonly used to decrease temperature rise in mass concrete structures; however, it is desirable to mitigate reductions in mechanical performance that commonly occur at high replacement percentages. The second case maximized 7-day elastic modulus while minimizing initial set time. Pozzolanic additions can increase setting times [67], an effect which can be detrimental to the timing and expediency of concrete finishing operations. Setting time in this case was determined as the time at which the fraction-solids-connected value output by the VCCTL reached 0.1; this approach is detailed in Chapter 2.

6.5.2. Results

Maximize 7-day elastic modulus, Minimize 7-day heat of hydration

The results of the min-max pareto optimization for elastic modulus and heat of hydration are presented in Figures 6-33 to 6-36. Each figure shows the performance of the 1000 simulated pozzolan chemistries at a given fineness, while the subplots within each figure illustrate the effects of changing the pozzolan replacement percentage. Generally speaking, the trends

exhibited by the VCCTL, as fineness and replacement percentage change, align with those observed in portland cement systems containing mineral admixtures [84]. At low replacement percentages, the influence of particle size was minimal, but increased as the particle size decreased, likely due to improved particle packing in the initial cement microstructure. The coarsest particle size distribution, shown in Figure 6-33 (12.5 μm average particle size), exhibited the largest changes in elastic modulus as replacement percentage increased. The variation in modulus due to changes in pozzolan chemistry did not significantly change as replacement percentage increased; however, the heat of hydration did, with the range of 7-day heat of hydration increasing in size as replacement percentage increased.

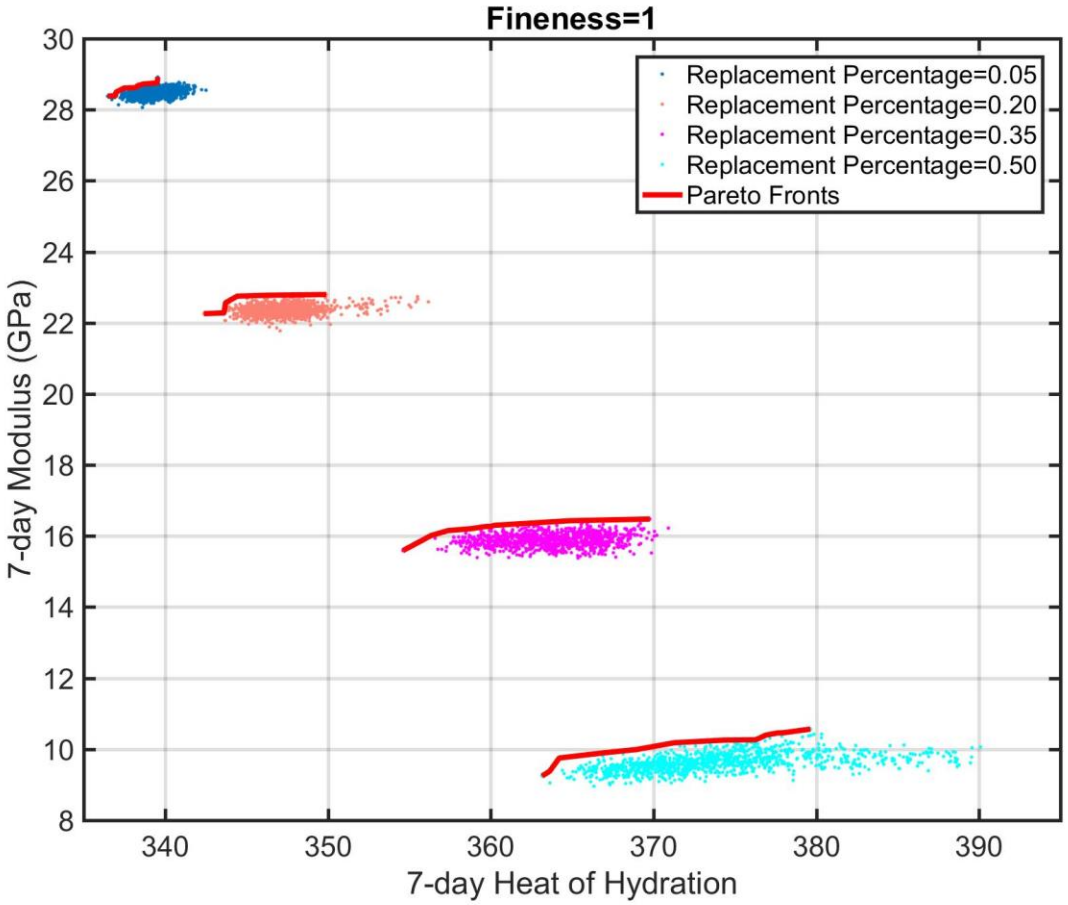

Figure 6-33. Min-max pareto fronts for the 7-day elastic modulus vs. 7-day heat of hydration case for 0.05, 0.20, 0.35, and 0.50 replacement fractions with pozzolans of 12.5 μm average particle size.

As the average particle size of the pozzolans decreased, shown in Figures 6-34 (7.5 μm average), 6-35 (2.5 μm average), and 6-36 (0.5 μm average), the modulus increased at all replacement percentages, and the influence of pozzolan chemistry on both modulus and heat of hydration increased. Pozzolans with the smallest average particle size (Figure 6-36) produced the

lowest reduction in elastic modulus as replacement percentage increased; however, the influence of chemistry with increasing replacement percentage was more pronounced. The min-max pareto front became smaller as fineness decreased and replacement percentage increased; this had the effect of reducing the number of optimal pozzolan chemistries in those cases.

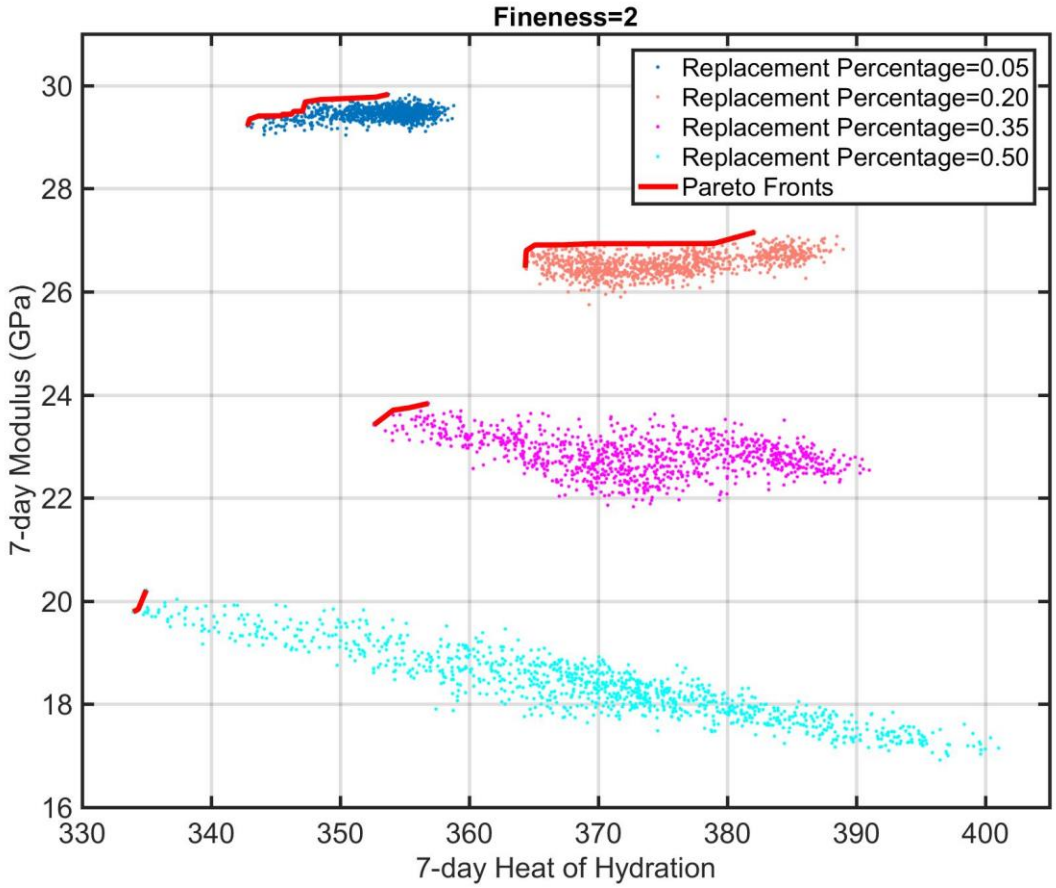

Figure 6-34. Min-max pareto fronts for the 7-day elastic modulus vs. 7-day heat of hydration case for 0.05, 0.20, 0.35, and 0.50 replacement fractions with pozzolans of 7.5 μm average particle size.

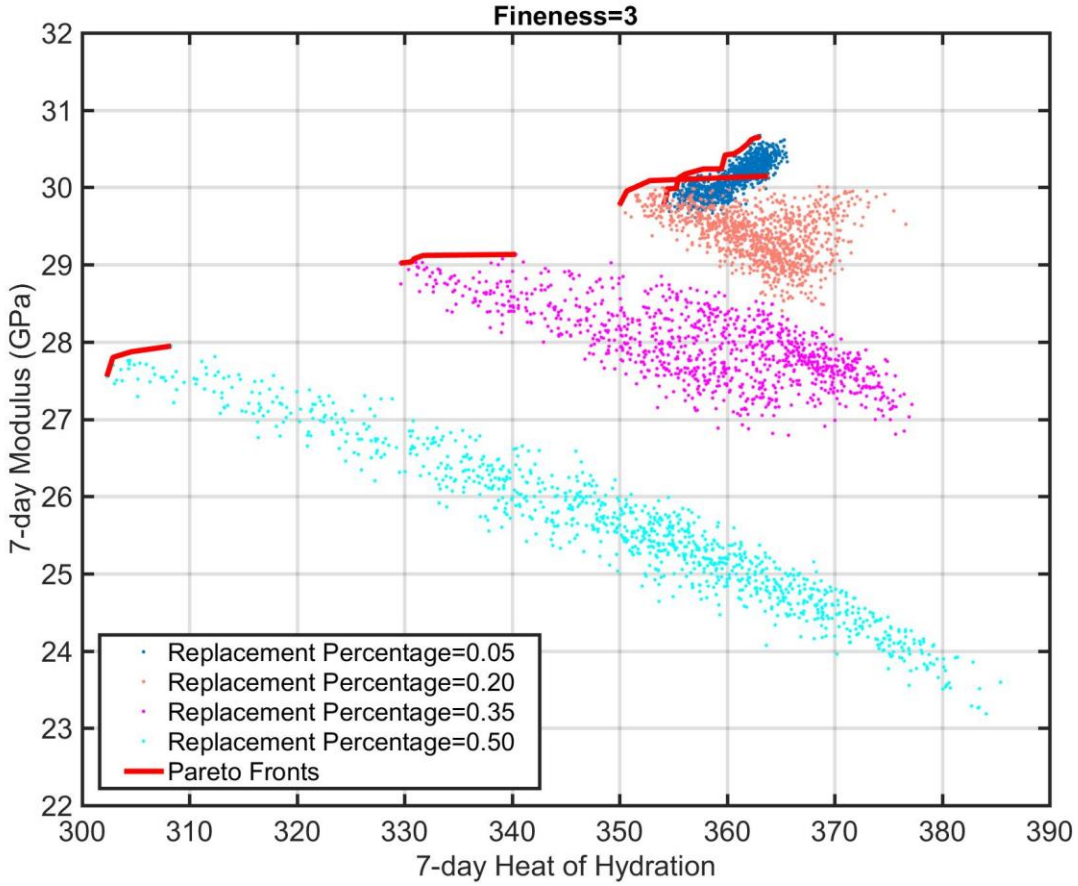

Figure 6-35. Min-max pareto fronts for the 7-day elastic modulus vs. 7-day heat of hydration case for 0.05, 0.20, 0.35, and 0.50 replacement fractions with pozzolans of 2.5 μm average particle size.

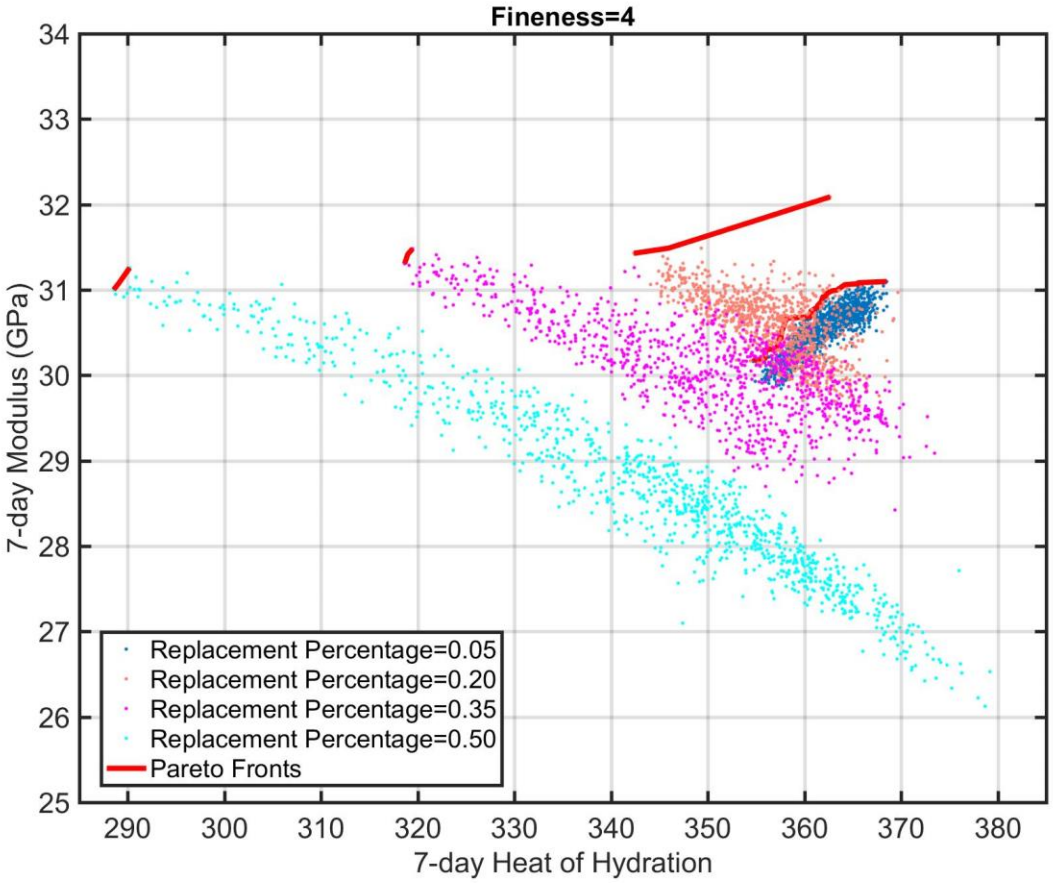

Figure 6-36. Min-max pareto fronts for the 7-day elastic modulus vs. 7-day heat of hydration case for 0.05, 0.20, 0.35, and 0.50 replacement fractions with pozzolans of 0.5 μm average particle size.

Maximize 7-day elastic modulus, Minimize initial setting time

The results of pareto optimization for the min-max elastic modulus and initial setting time case are presented in Figures 6-37 (12.5 μm average particle size), 6-38 (7.5 μm), 6-39 (2.5 μm), and 6-40 (0.5 μm), using the same conventions as used for the elastic modulus – heat of hydration case. In general, the trends observed when minimizing initial setting time were similar to those observed when minimizing heat of hydration; however, some significant differences existed, particularly at a finer average particle size. As with heat of hydration, an increase in replacement percentage at smaller particle sizes increased the effect of pozzolan chemistry on behavior; however, the size of the pareto front exhibited the opposite trend. The range of behavior associated with the trade-off optimal solutions increased with increasing replacement percentage and decreasing average particle size, effectively broadening the range of optimal pozzolan chemistries in those cases.

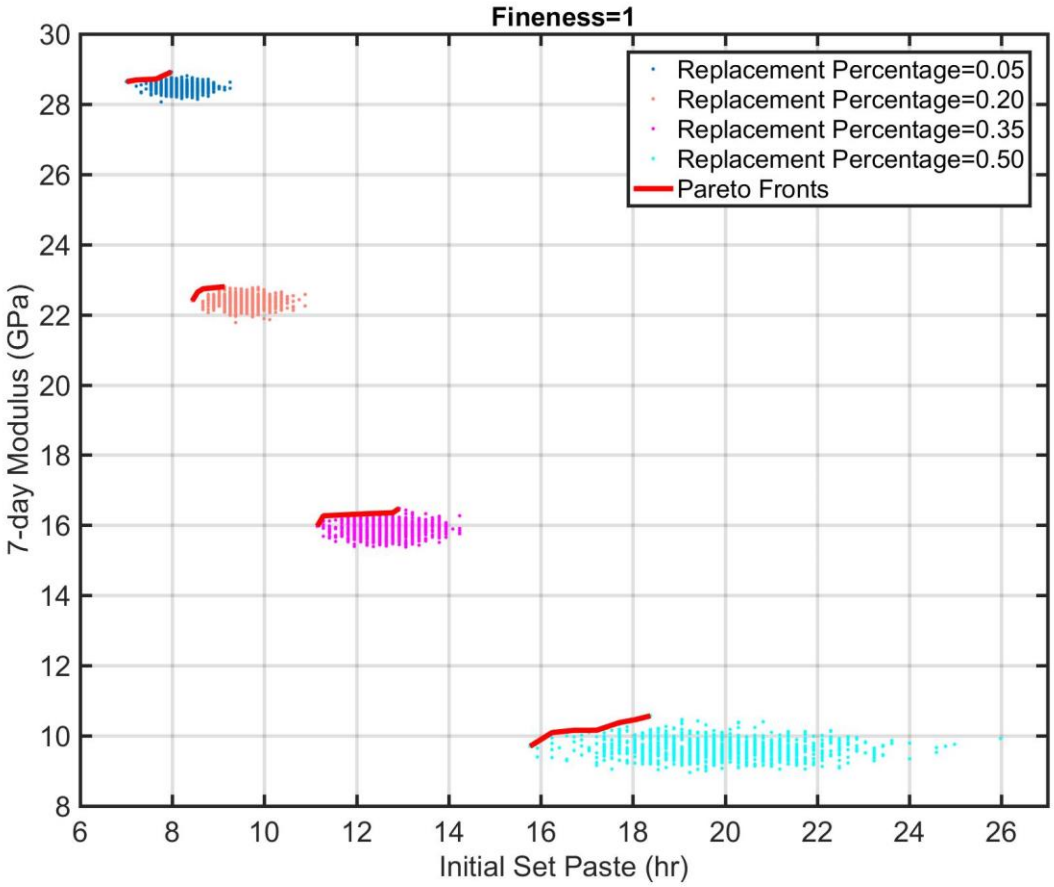

Figure 6-37. Min-max pareto fronts for the 7-day elastic modulus vs. 7-day heat of hydration case for 0.05, 0.20, 0.35, and 0.50 replacement fractions with pozzolans of 12.5 μm average particle size.

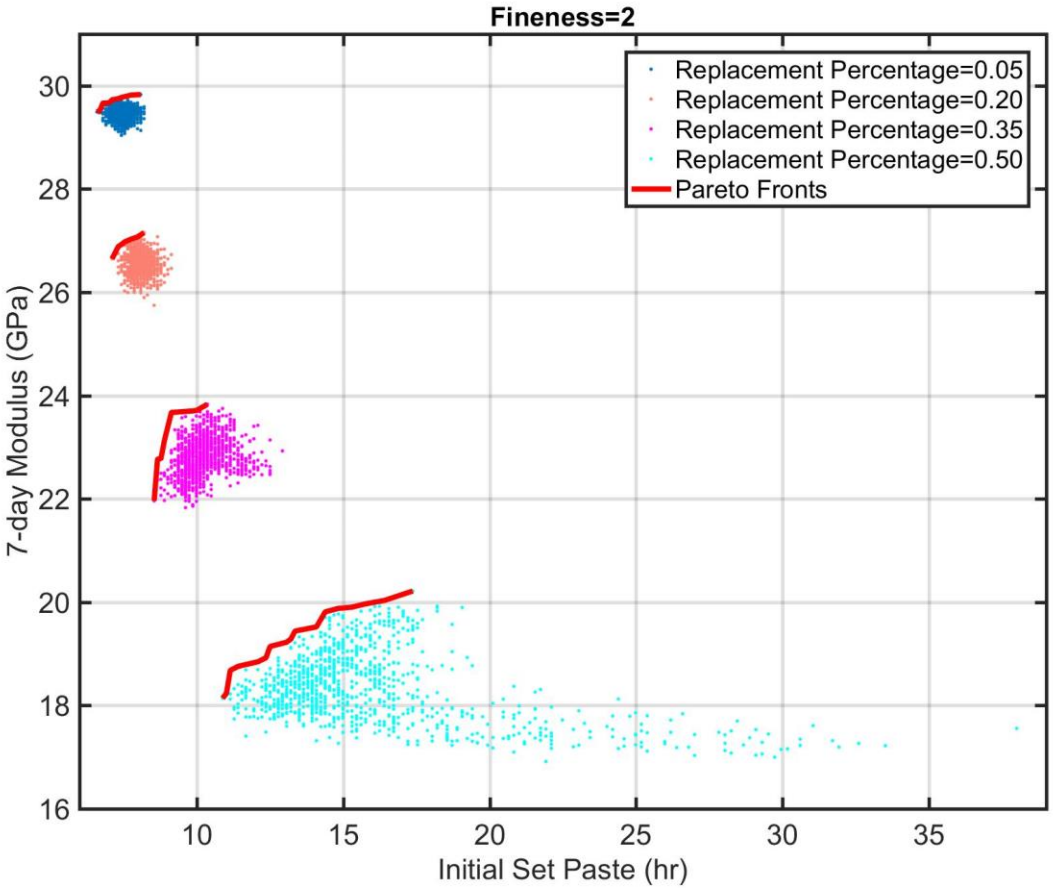

Figure 6-38. Min-max pareto fronts for the 7-day elastic modulus vs. 7-day heat of hydration case for 0.05, 0.20, 0.35, and 0.50 replacement fractions with pozzolans of 7.5 μm average particle size.

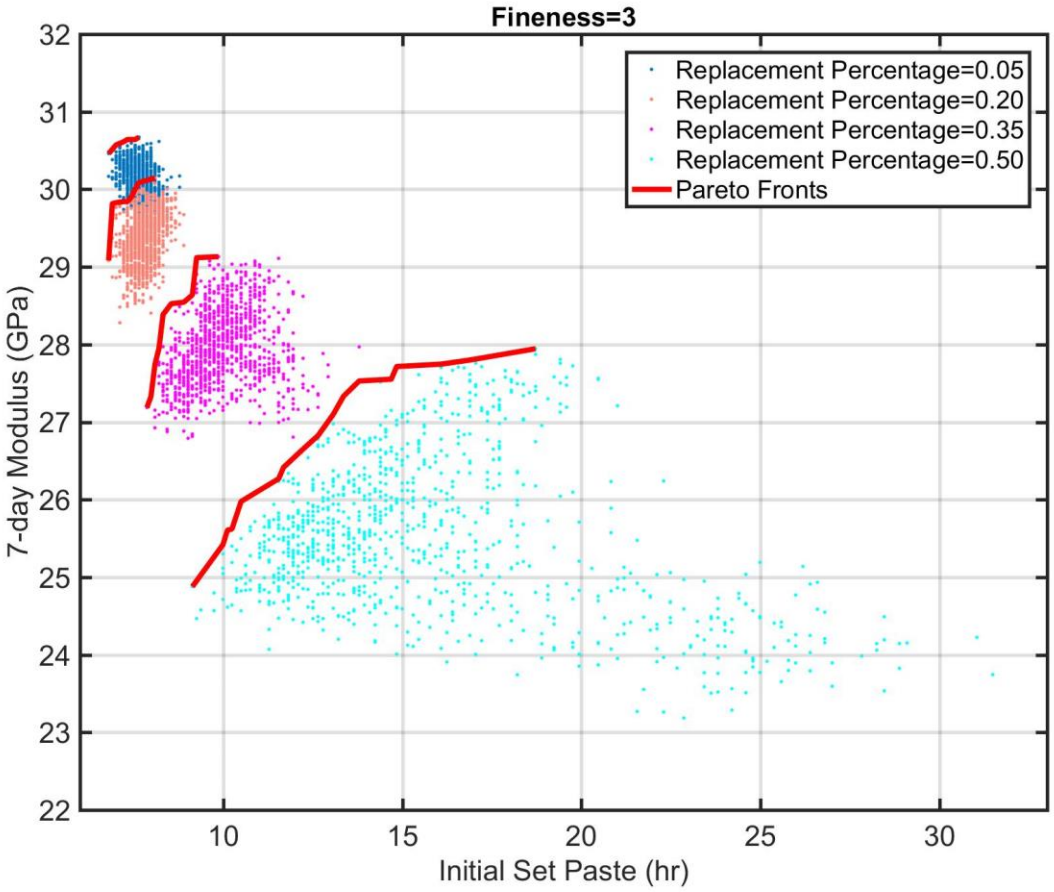

Figure 6-39. Min-max pareto fronts for the 7-day elastic modulus vs. 7-day heat of hydration case for 0.05, 0.20, 0.35, and 0.50 replacement fractions with pozzolans of 2.5 μm average particle size.

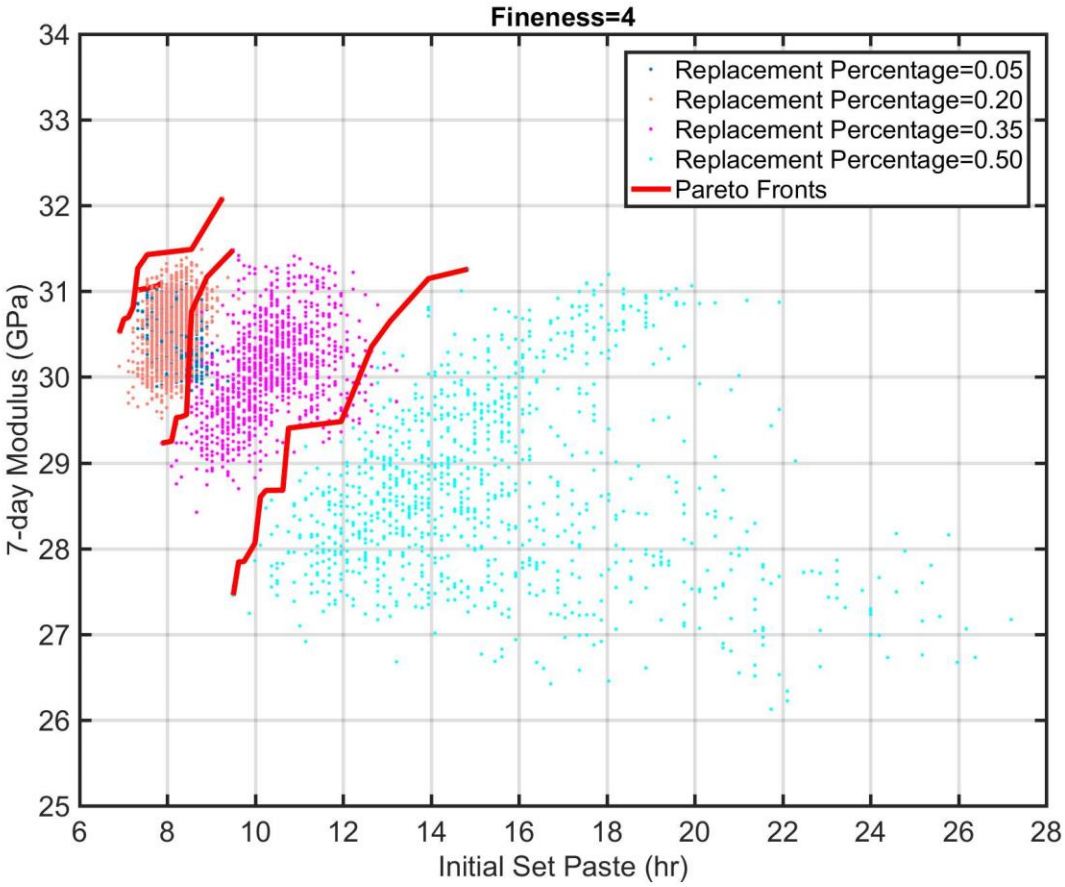

Figure 6-40. Min-max pareto fronts for the 7-day elastic modulus vs. 7-day heat of hydration case for 0.05, 0.20, 0.35, and 0.50 replacement fractions with pozzolans of 0.5 μm average particle size.

6.5.3. Discussion

The pareto analysis of VCCTL performance, with respect to pozzolan chemistry at different average particle sizes and replacement percentages, shows promise as a potential method to assess the performance of the model with respect to generally observed behavior. Generally speaking, the VCCTL qualitatively replicates commonly observed trends associated with changes in pozzolan fineness and replacement percentage. The practical utility of any optimal solutions derived from this technique is contingent upon accurate predictions from the VCCTL; however, this technique has potential value for real data as well, assuming a database of measured performance data for mixtures containing supplementary materials is available. Additionally, no published work evaluating the behavior of the VCCTL in this context exists; the authors of the model generally state that the VCCTL is optimized for portland cement mixtures with type I-II compositions, and qualify the functionality of routines for simulating the hydration of fly ash as experimental [70].

7. IMPROVEMENT OF VCCTL COMPRESSIVE STRENGTH PREDICTIONS

In Chapter 6, a basic assessment of the VCCTL's ability to predict compressive strength for pozzolanic materials using inputs developed from XRF oxide compositions. Performance was compared to measured compressive strength data obtained in collaboration with a separate FDOT investigation of pozzolanic materials [67]. Simulated results were compared to the measured data using three empirical relationships detailed in Chapter 3. Agreement was generally poor; however, modeling of supplementary cementitious materials an acknowledged limitation of the VCCTL and cement hydration models in general [83], due to the broad range of compositions associated with these materials. This task was initially going to investigate altering and improving the underlying code of the VCCTL to improve handling of supplementary materials; however, no working research agreement (CRADA) with NIST was ever established, and the authors believe that making significant alterations to the deeply complex code of the VCCTL without the assistance of NIST personnel is not a feasible course of action.

As an alternative to modifying the code of the VCCTL, it was postulated that specific machine-learning algorithms may be able to replicate the output of the VCCTL given the same inputs, and that these algorithms may be further modified to predict the properties of real materials using VCCTL inputs. This chapter presents an overview of the machine learning methods used to accomplish this task, as well as details of the performance of these algorithms when predicting compressive strength for the same mortars evaluated in Chapter 6.

7.1. Machine Learning and Artificial Neural Networks

7.1.1. Background

The discipline of machine learning encompasses a broad array of models and algorithms that, instead of being explicitly programmed, can be trained using real data to find solutions to specific problems [85]. The approach lends itself to problems for which large amounts of input and output data exist but solution mechanisms are poorly understood or otherwise extremely complex. Some recent successes in solving problems of this type include advances in language translation [86], image captioning [87], and the emulation of simple computer programs through analysis of code [88]. The task of predicting the changing properties of hydrating cement and concrete shares commonalities with some of these examples; the properties of concrete are dependent upon the properties of its constituent materials and environment, but the mechanisms by which these properties evolve are complex and not fully understood. Large repositories of also data exist describing the properties of constituent material and the behavior of the resulting products. Based on these observations, research is underway to apply machine learning techniques to the problem of cement hydration modeling.

7.1.2. Artificial Neural Networks

In the most general sense a neural network is a computational model that relates inputs to outputs using highly connected layers of adaptive parallel computational units [89]. These units are termed artificial neurons, and operate by calculating a nonlinear function of a weighted sum of their inputs. In the case of Figure 7-1, the nodes x_1 through x_4 represent the input values, *j* is

the index of the current node, *j'* is the index of a specific input node, and $w_{jj'}$ is the weight from input node *j'* to node *j*. The value a_j is the incoming activation, while σ is the activation function itself. A variety of activation functions exist for artificial neurons, the most appropriate type depends on the application of the neural network, and it is possible for different layers of a neural network to have different activation functions. Traditional neural networks comprise three layers of artificial neurons, each of which communicates with all of the neurons in previous and subsequent layers, but not with neurons in the current network. This is classified as a feedforward neural network or perceptron, a simplified representation of which is detailed in Figure 7-2.

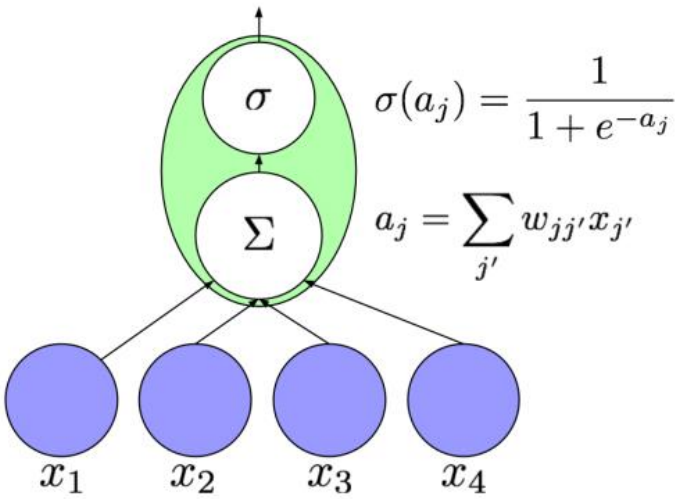

Figure 7-1. Functional diagram of an artificial neuron [90]

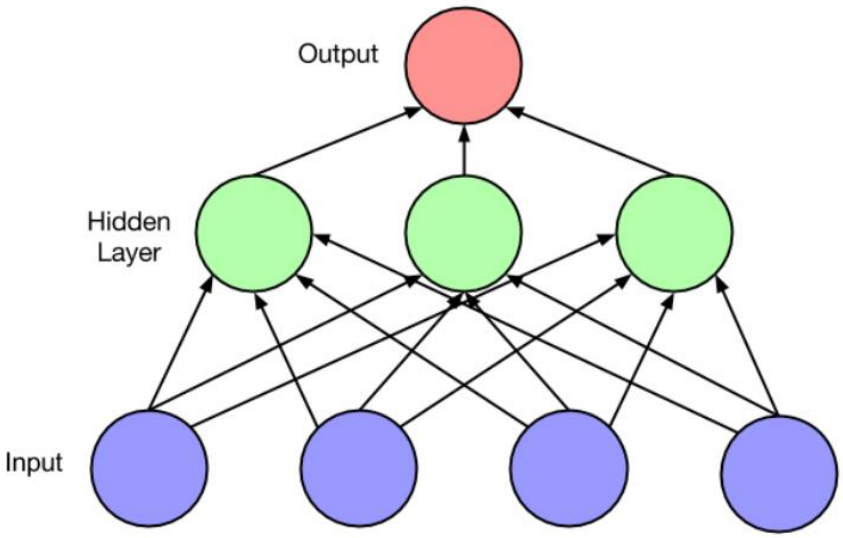

Figure 7-2. Simplified feedforward neural network [90]

The most popular method for training neural networks is backpropagation of error, a technique which iteratively modifies the weights of each connection to produce the best agreement between the expected result and the behavior of the network [91]. This is accomplished by first feeding a set of training cases through the network in a forward pass. The comparison between the values of the output layer and the expected values from the training data is the total error. The partial derivative of the accumulated training error can then be computed with respect to the individual weights of the connections, and gradient descent applied to modify each of the weights iteratively, moving backward through the network. The initial weights of the network are typically randomized to avoid symmetry issues, and with large datasets a smaller mini-batch of cases are often chosen randomly to speed up training.

7.2. VCCTL Replacement

It may be possible to train a specific type of neural network, known as a recurrent neural network (RNN), to accurately emulate the response of the VCCTL over a broad range of inputs. Basic RNNs (Figure 7-3) operate similarly to the feedforward networks discussed previously; however, they operate in time steps, where the input to the next time step is the value of the input nodes combined with the previous values of the hidden layer. These models are Turing-complete [92], or capable of simulating any computational problem [93]. This has been applied to the simulation of simple computer programs, using a recurrent neural network that reads source code [88].

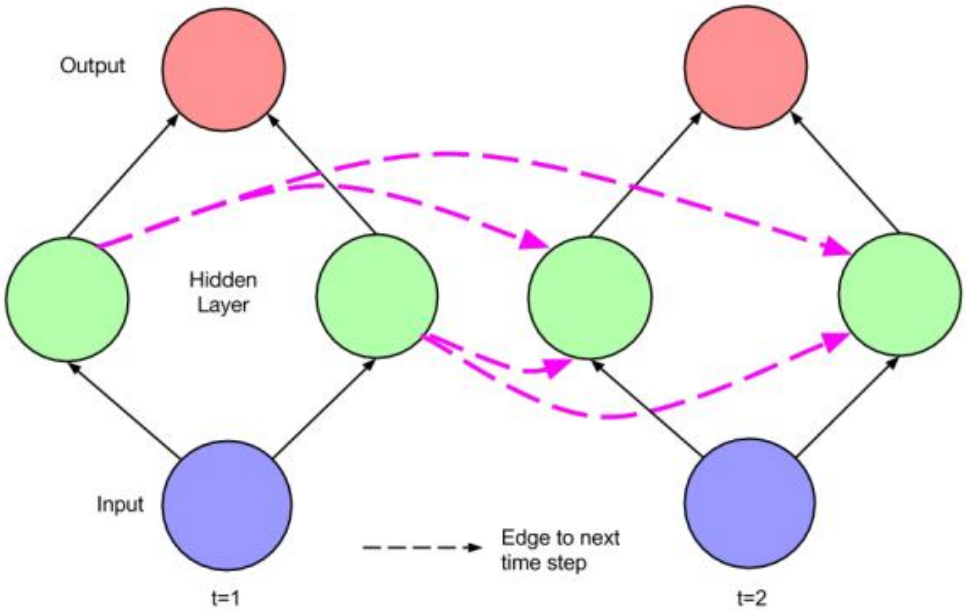

Figure 7-3. Simplified diagram of a recurrent neural network [90]

The predominant architecture for RNNs employs Long Short-Term Memory (LSTM) units in the hidden layer. LSTMs, introduced by Hochreiter and Schmidhuber in 1997 [94], solved a longstanding problem with recurrent neural networks, that of vanishing or exploding gradients. Training of recurrent neural networks typically employs backpropagation of error through time (BPTT), treating the recurrent network as a sequence of networks.

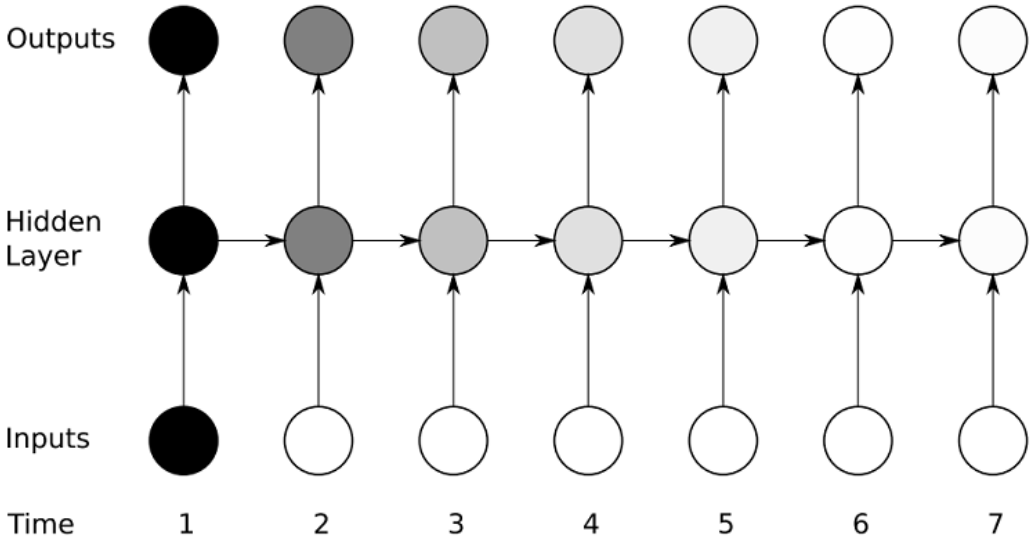

Figure 7-4. Illustration of the vanishing gradient problem with backpropagation of RNNs [95]

Conventional RNNs trained using this method were vulnerable to the problems of vanishing or exploding error (Figure 7-4) as training moved backward across longer time steps. The LSTM network eliminated the issue of vanishing error by integrating a self-connected "error carousel" which remembers the error over time, allowing for much faster training with fewer training cases.

The purpose of the VCCTL is to simulate, given a set of initial conditions, the evolving properties of cementitious materials over time. The virtual microstructure of the VCCTL also acts as a sort of memory between time steps, storing information about the history of the virtual hydration. The parallels between the abilities of RNNs and the VCCTL combined with the capability of enumerating hundreds of thousands of unique simulation cases using HiperGator, has led to the conclusion that it may be possible to replace the VCCTL with a RNN. When properly trained, this RNN would execute much faster than the VCCTL, which currently requires approximately two hours to simulate a single hydration, while retaining the VCCTL's predictive behavior. This would eliminate the need for the computationally intensive cellular automata model, and expedite the process of training the model on measured experimental data.

7.3. RNN Implementation

The RNN architecture for this study is shown in Figure 7-5, with small changes in configuration to accept as input the calculated VCCTL phase volume fractions for all initial VCCTL phases, as well as particle size information for the pozzolanic additions in the form of 10^{th}, 50^{th}, and 90^{th} percentile diameters. Because the physical experiments being replicated for this exercise were obtained from standard mortars with the same aggregate proportions, w/c, curing conditions and mixing procedure, those parameters were not included. The number of input and output nodes for a neural network is determined by the number of input and output values. For the recurrent network used for this experiment a total of 22 input nodes were used, corresponding to the initial VCCTL volume fractions and pozzolan particle size information, while three output nodes predicted heat of hydration, mortar compressive strength, and mortar elastic modulus.

An important consideration when training neural networks is to avoid overfitting, a phenomenon wherein a model has fitted the training set so closely that it captures the noise in the data [96]. Overfitted models may not perform well when applied to data outside of the scope of the initial training data. For this example, overfitting of the neural network was avoided by manually reducing the number of hidden layer neurons such that network predictions were acceptable when compared to specified limits of precision for the test methods being emulated [97]. The number of hidden nodes ultimately chosen was 12, in a single layer.

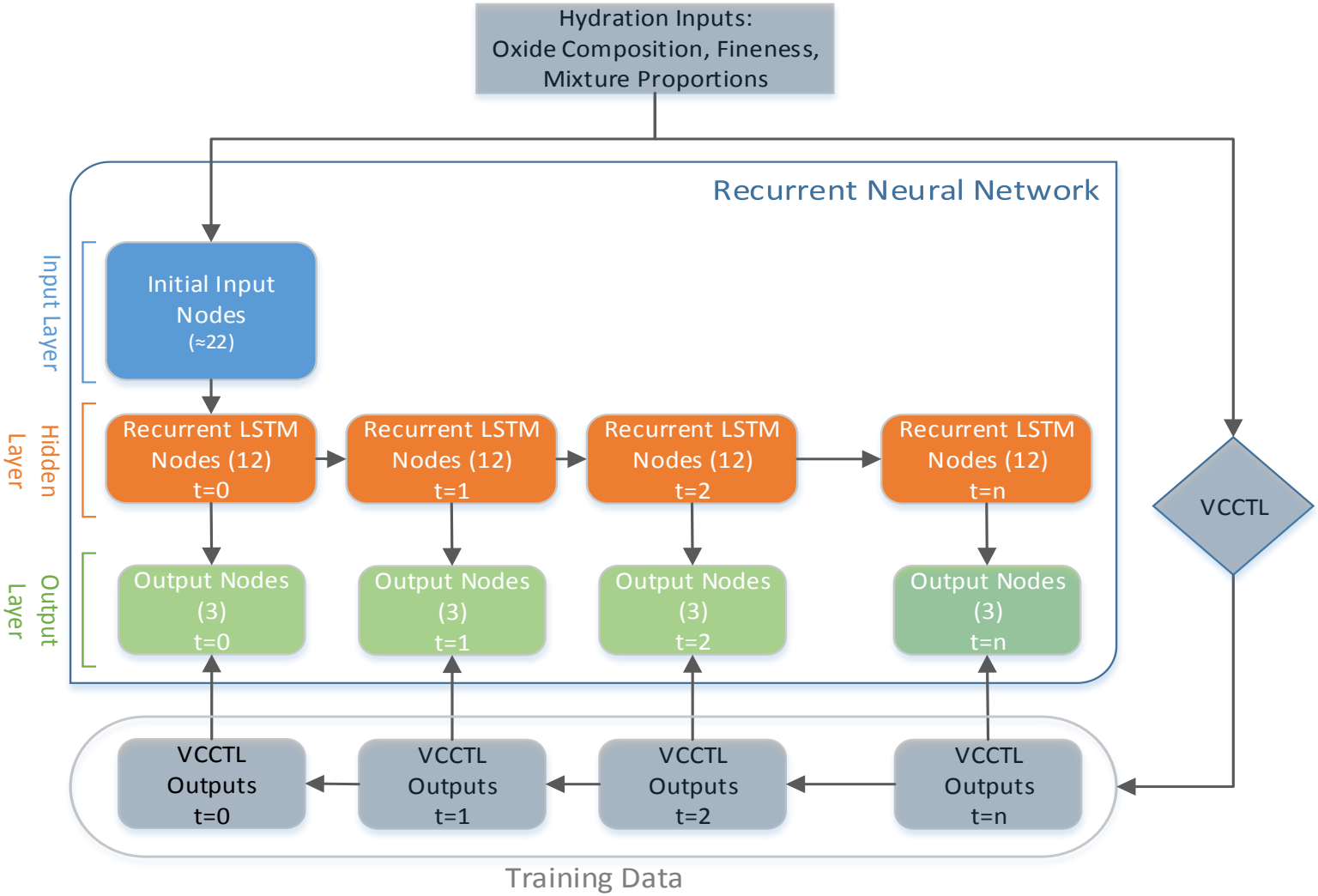

Figure 7-5. Functional diagram of recurrent hydration simulation network, with training data flow illustrated for a single case

Training of the RNN was divided into two stages: general training of the network using the VCCTL generated pozzolan cases detailed in Chapter 6, followed by the application of transfer learning, refitting the resulting network to actual experimental data. This approach has been used with RNN architectures to perform tasks where the acquisition of training data is difficult or resource intensive [98], but simulations of the real system are possible. As in this case, the simulated training data was easier to acquire but less realistic than measured training data. Similarities to other studies [99,100] also exist, in which complex teacher neural networks were used to train a simpler recurrent network; in this case the teaching model is the VCCTL. In this example, the actual experimental data for final training was the same as that used in Chapter 6 for evaluation of VCCTL predictions for binary mortars containing mineral admixtures.

7.4. Results

The results of the compressive strength and heat of hydration predictions from the recurrent neural network replacement are presented in Figures 7-6 through 7-15, and compared to the experimentally measured values for the same 10 binary mixtures evaluated in Chapter 6. The heat of hydration results show the actual measured values out to 7 days of age, while after 7 days the curves are extrapolated by the VCCTL. This functionality of the VCCTL is detailed in chapter 2.

The results of the RNN model for compressive strength agree very well with experimental data for most ages and all binary mixture. For mortars containing metakaolin and rice husk ash, the RNN-predicted values maintain decent agreement while ignoring the irregularities present in the experimental measurements at 28 days. The RNN results appear to increase monotonically even when the experimental results do not. The only significant exception to the above observations is the 1-day value predicted for 40% class F fly ash, which overestimates the compressive strength significantly. RNN predictions for heat of hydration perform similarly to those for compressive strength, generally agreeing quite closely with experimental and VCCTL extrapolated values, with the same exception of 1-day results for class F ash at a 40% replacement value.

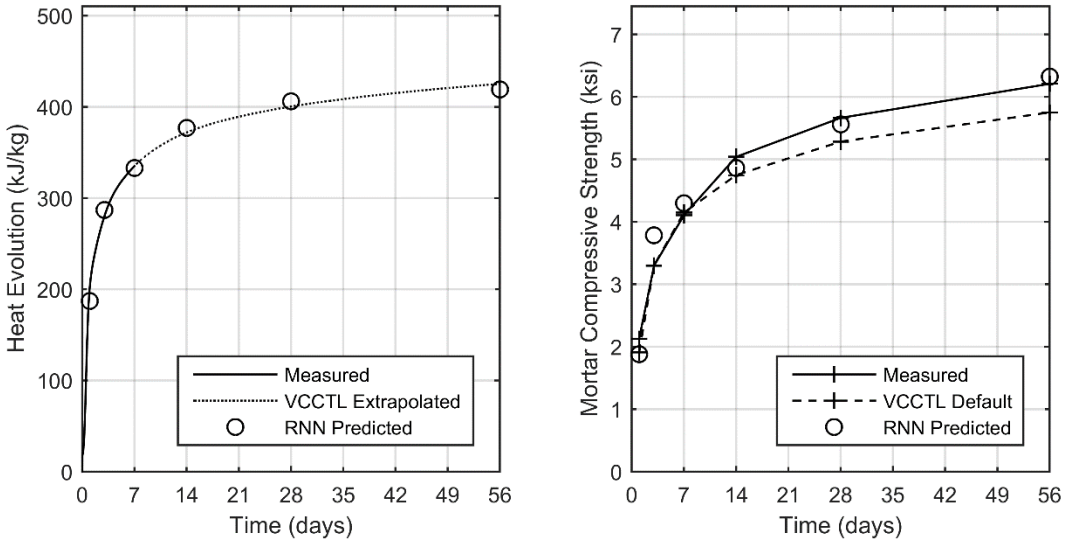

Figure 7-6. Measured heat of hydration and compressive strength for mortars with 10% class C fly ash, compared the default VCCTL compressive strength prediction relationship as well as predictions from the implemented recurrent neural network

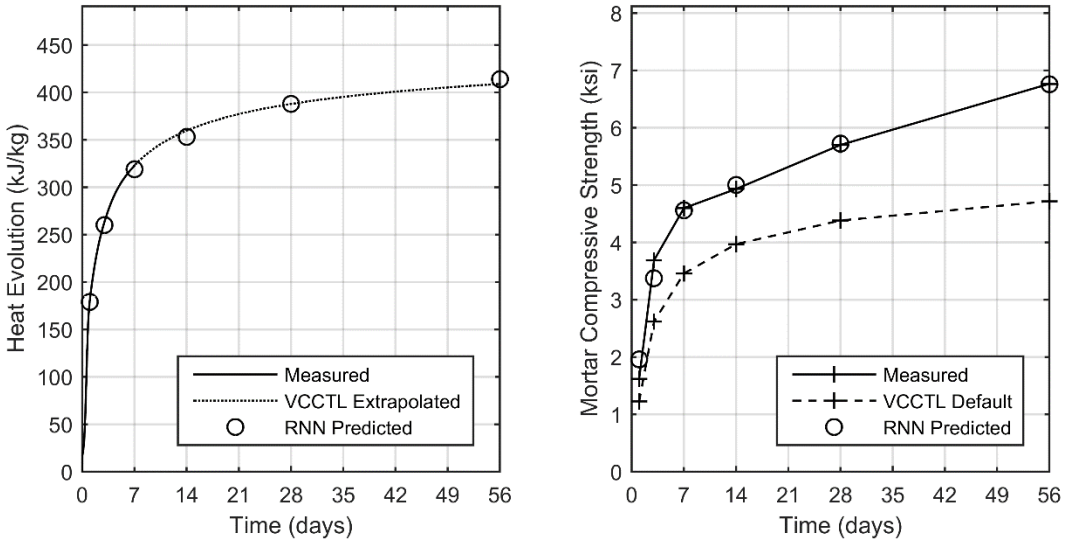

Figure 7-7.Measured heat of hydration and compressive strength for mortars with 20% class C fly ash, compared to the default VCCTL compressive strength prediction relationship as well as predictions from the implemented recurrent neural network

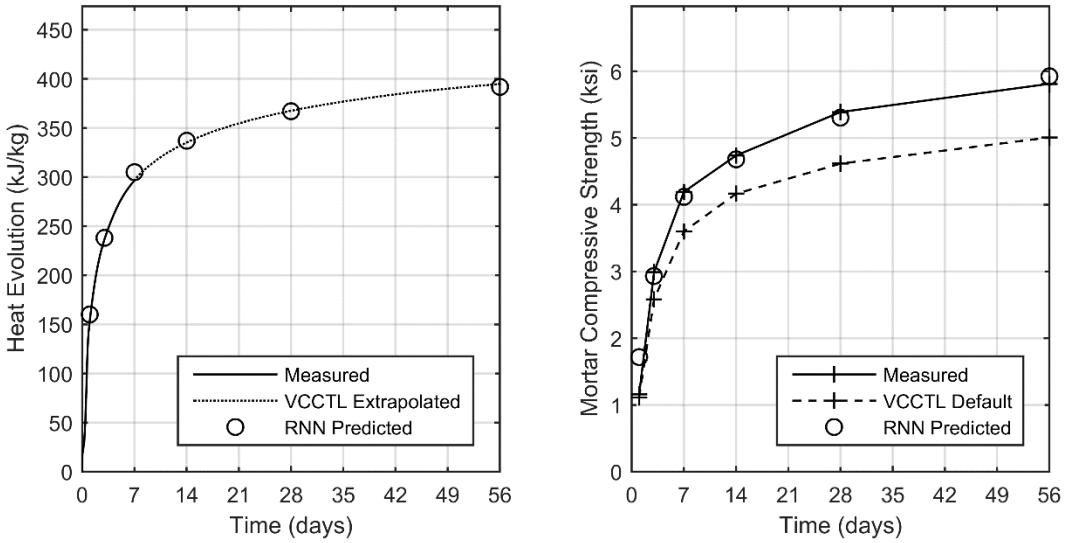

Figure 7-8. Measured heat of hydration and compressive strength for mortars with 30% class C fly ash, compared to the default VCCTL compressive strength prediction relationship as well as predictions from the implemented recurrent neural network

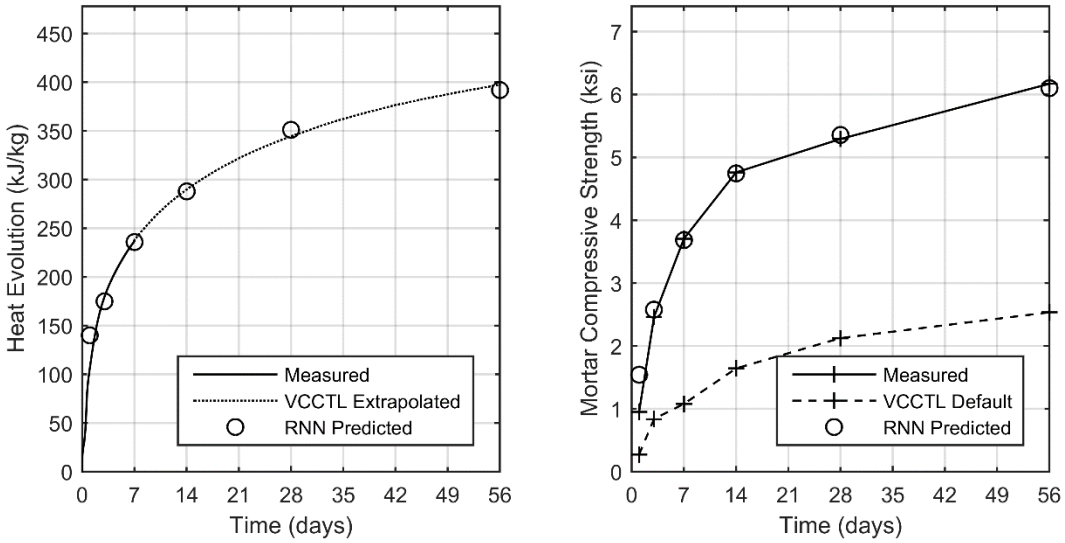

Figure 7-9. Measured heat of hydration and compressive strength for mortars with 50% class C fly ash, compared to the default VCCTL compressive strength prediction relationship as well as predictions from the implemented recurrent neural network

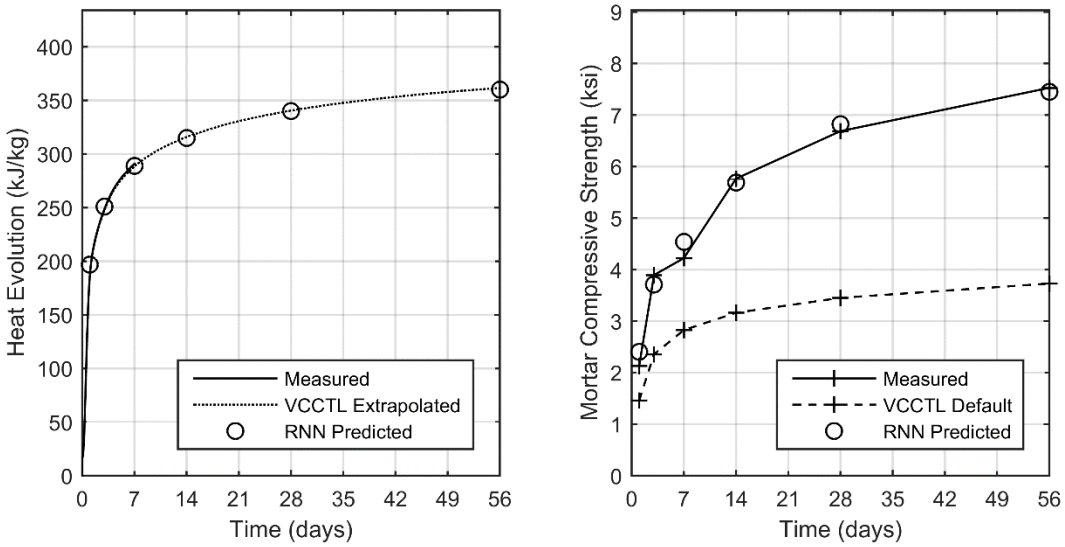

Figure 7-10. Measured heat of hydration and compressive strength for mortars with 20% class F fly ash, compared to the default VCCTL compressive strength prediction relationship as well as predictions from the implemented recurrent neural network

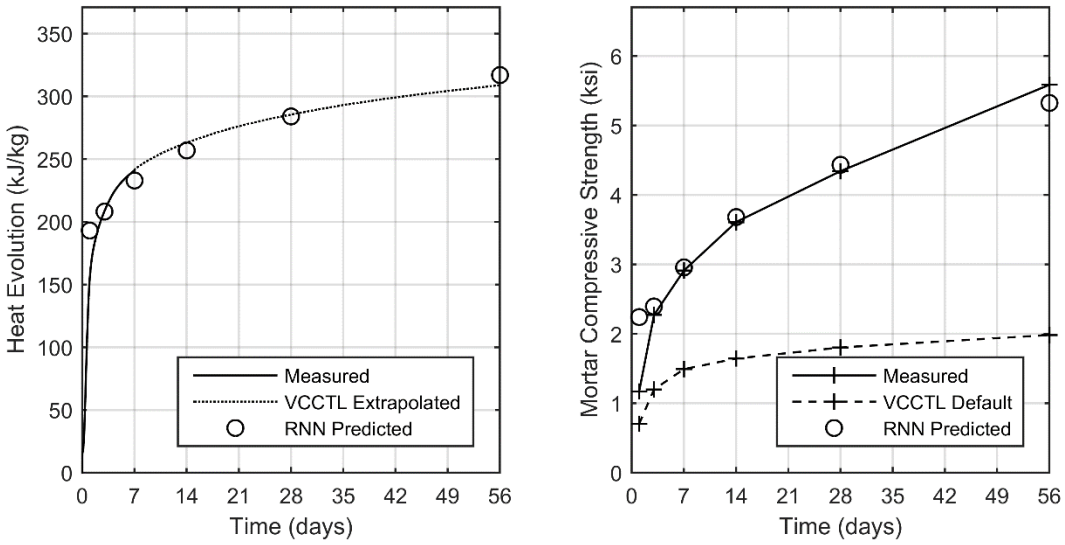

Figure 7-11. Measured heat of hydration and compressive strength for mortars with 40% class f fly ash, compared to the default VCCTL compressive strength prediction relationship as well as predictions from the implemented recurrent neural network

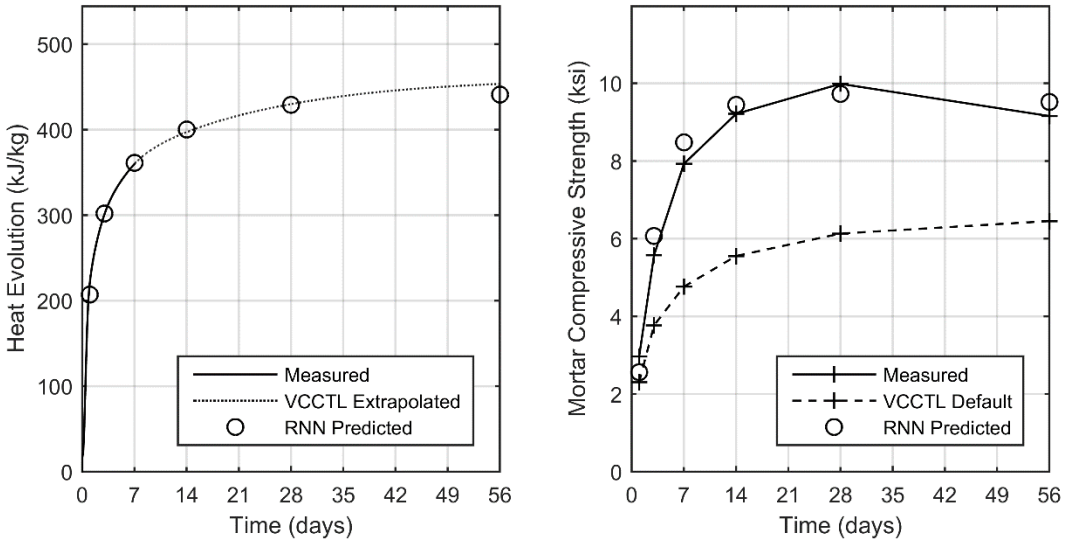

Figure 7-12. Measured heat of hydration and compressive strength for mortars with 5% metakaolin, compared to the default VCCTL compressive strength prediction relationship as well as predictions from the implemented recurrent neural network

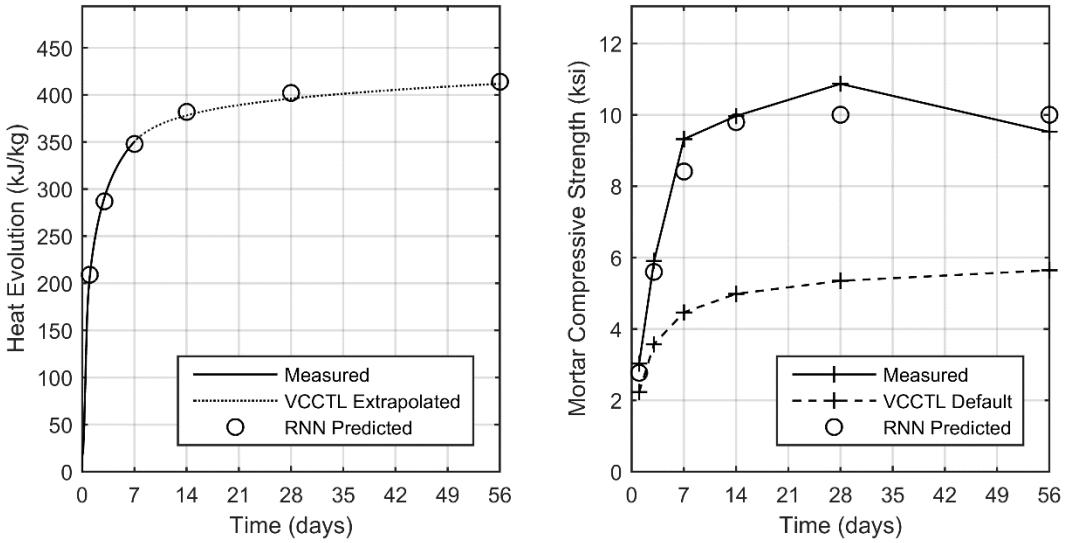

Figure 7-13. Measured heat of hydration and compressive strength for mortars with 10% metakaolin, compared to the default VCCTL compressive strength prediction relationship as well as predictions from the implemented recurrent neural network

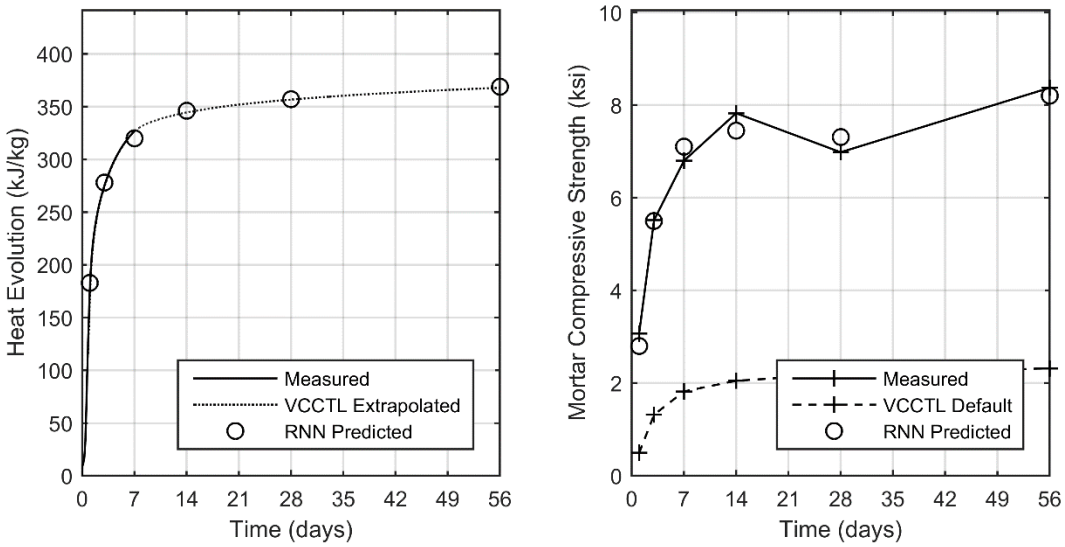

Figure 7-14. Measured heat of hydration and compressive strength for mortars with 5% rice husk ash, compared to the default VCCTL compressive strength prediction relationship as well as predictions from the implemented recurrent neural network

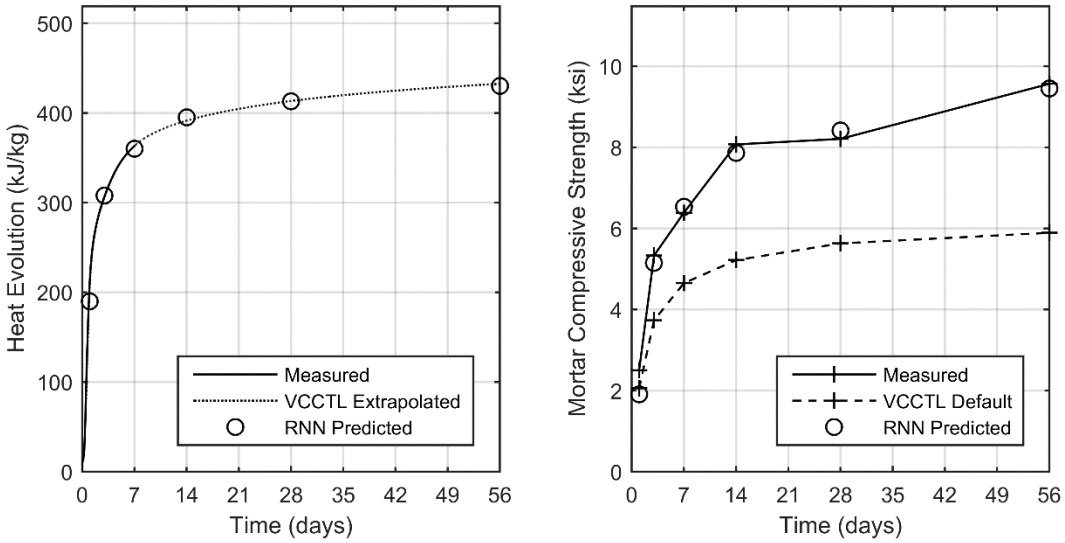

Figure 7-15. Measured heat of hydration and compressive strength for mortars with 10% rice husk ash, compared to the default VCCTL compressive strength prediction relationship as well as predictions from the implemented recurrent neural network

7.5. Discussion

This proof-of-concept exercise demonstrates that recurrent neural networks may be a viable option for the replacement of the VCCTL in the role of prediction of compressive strength and heat of hydration for cementitious mortars. This methodology has the advantages of being quick to train and quick to execute, with the training and implementation of this network

requiring approximately 15 minutes in total on standard hardware, while the equivalent VCCTL simulations required several hours to complete. Another advantage of this approach is its modularity, the same exercise could be quickly implemented if additional inputs were present or relevant, and if additional output data was available. Both a limitation and advantage of ANN are that they are only as good as the data available for training, and while using simulated data from the VCCTL for training prior to training on real experimental data alleviates this somewhat, more experimental data would be valuable to ensure robust predictions for materials outside those considered here. Further training may also be implemented as more data becomes available, concurrently with existing recurrent material testing and qualification programs.

8. APPLICATION OF VCCTL TO DURABILITY PREDICTIONS

8.1. Introduction

This chapter details an investigation of the capabilities of the Virtual Cement and Concrete Testing Laboratory (VCCTL) with regard to prediction of cementitious material properties related to long term durability under harsh exposure conditions. A brief overview of concrete properties related to durability is presented, followed by an explanation of the limitations and capabilities of the VCCTL in this context. Finally, a comparison of VCCTL predicted durability properties with measured properties obtained in collaboration with ongoing FDOT project BDV31-TWO-977-42 (Evaluation of Porometry, Permeability, and Transport of Structural Concrete) is presented, by evaluating the correlation of several different measured and predicted properties over a range of ages.

8.2. Background

The ingress of chloride ions through portland cement concrete and the subsequent corrosion of steel reinforcement is a major concern for many concrete mixtures in Florida where exposure to seawater is expected. An array of test methods exist to quantify the resistance of different concrete mixture designs to this phenomenon [101–104], all of which quantify the ability of solutions to move through the hydrated microstructure in some way. Properties of concrete that influence the ability of solutions to move through its structure are collectively referred to as transport properties; the most significant of these for durability is diffusion, driven by an ionic concentration gradient.

The Virtual Cement and Concrete Testing Laboratory is nominally capable of predicting several hydrated material properties that are related to diffusion of ions through a cementitious microstructure. A tool to accurately predict durability testing results through a few hours of simulations would be particularly valuable, as many of the test methods to quantify concrete transport properties require months to complete. There are limitations to the fundamental approach of VCCTL unique to the context of transport property prediction, however. These properties depend to a significant degree on physical characteristics of the cement pore structure that are orders of magnitude smaller than the 1 μm resolution of the VCCTL microstructure. While it is possible that VCCTL transport measurements may agree or correlate with real experimental data, this limitation of the VCCTL should be acknowledged.

The VCCTL is capable of estimating the formation factor and the transport factor (inverse of formation factor) for cement paste, mortar and concrete from snapshots of the virtual microstructure captured at critical ages using finite difference analysis [23]. Formation factor is defined as the ratio of a material's conductivity to the conductivity of its pore solution [105], and effectively characterizes the pore structure of porous materials [106]. A snapshot of the virtual microstructure is converted in to a real conductor network, [24], a simplified example of which is shown in Figure 8-1. When the real conductor network is initialized, the different voxels of the frozen microstructure are assigned relative conductivity values based on the mineral phase they represent [107]. Particles of unreacted cement and solid cement hydration products are assigned a conductivity of zero, while water filled porosity is assigned a conductivity of 1. The only

hydration products considered to be conductive by the model is CSH, which is assigned a relative conductivity value of 0.0025.

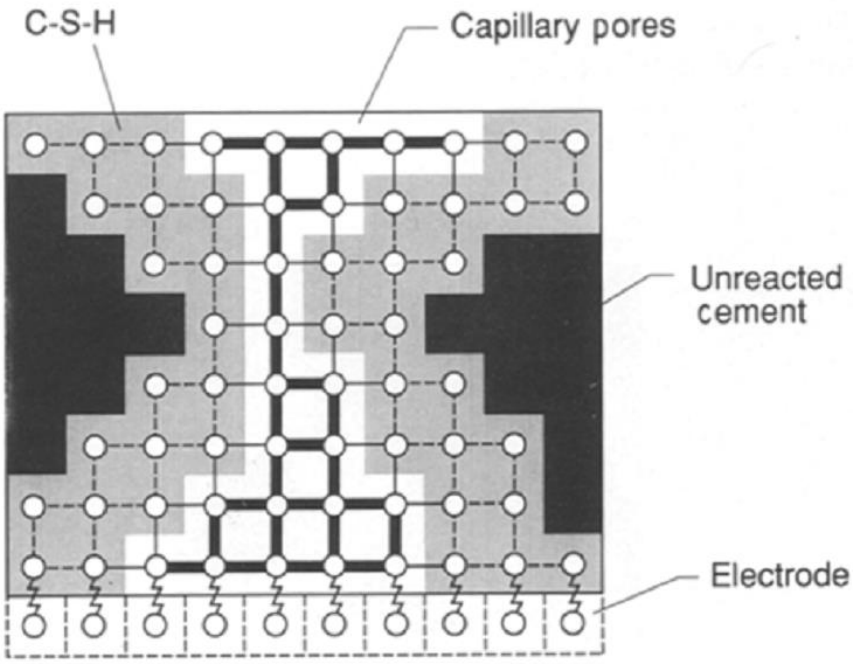

Figure 8-1. Simplified example of the conversion of the VCCTL digital image microstructure into a network or real conductors [108]

The algorithm operates by applying a constant current across the network of conductors in the x, y and z directions, then uses the conjugate gradient algorithm to minimize the equation:

$$C_{eff} = \frac{1}{2} uAu \qquad 8\text{-}1$$

where C_{eff} is the effective conductivity, A is generated from the conductivities between voxels, and u is a vector of voltages.

When the paste microstructure is generated for a mortar or concrete, an invisible barrier (Figure 8-2) is placed in the center of the microstructure along the yz plane. This simulates single-sided growth of hydration products against an aggregate surface and replicates the mechanisms responsible for the formation of the interfacial transition zone (ITZ) [25].

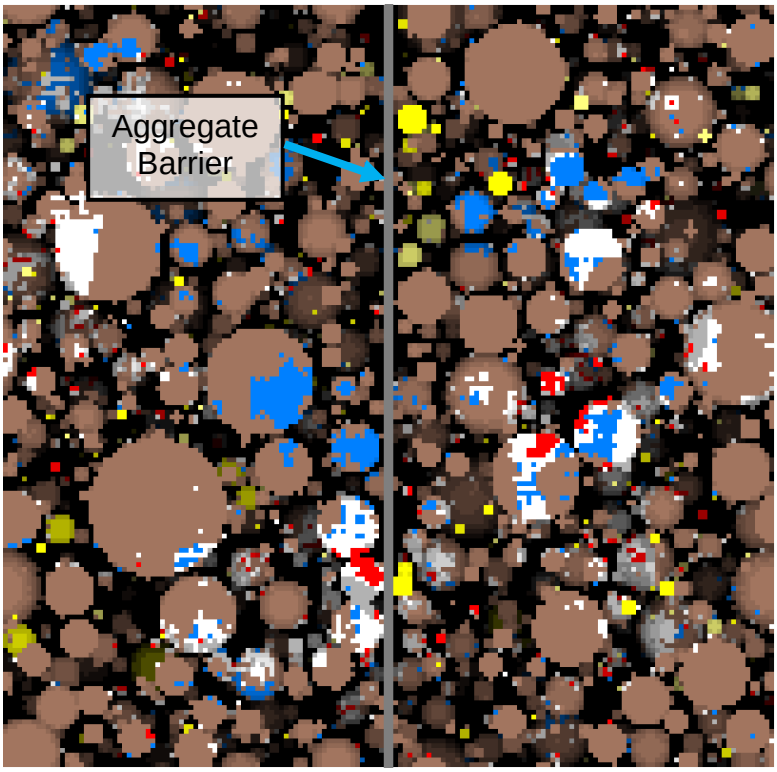

Figure 8-2. Example VCCTL microstructure with representation of aggregate barrier shown in gray

To calculate the effective conductivity of the ITZ, its width is first set as equal to the median cement particle size [26]. The conductivity of each slice of the hydrated microstructure within this distance of either side of the aggregate barrier is then averaged to determine the ITZ conductivity. The conductivity of the mortar or concrete is calculated as the mass weighted average of paste, ITZ, and aggregate conductivity defined by the user.

The authors would like to note that while the above documented functionality is described in the VCCTL manual [19] and detailed in the source code of the program that calculates transport properties [17], it currently does not appear to function as designed. Transport values calculated from mortars currently match those calculated from cement pastes with the same cement and w/c. The authors attempted to identify the reason for this by investigating the source code, in addition to standard troubleshooting steps such as reinstalling the software or running the program on a different workstation; however, this functionality appears to be dormant with the latest version of the VCCTL in the as delivered state.

8.3. Experiment

To investigate potential correlations between durability-related VCCTL predictions and actual experimental data, the VCCTL-computed transport factor and volume fraction porosity were compared to experimental measurements. Other VCCTL-computed parameters were also considered initially, including fraction interconnected porosity and solution conductivity; however, it was found that the former parameter dropped to zero at relatively early ages for

lower w/c mixtures, while the latter was discontinuous in all simulations performed, approximately doubling its value in a single simulation time-step. Surface and bulk resistivity [109,110] measurements were obtained in collaboration with ongoing project BDV31-TWO-977-42 for comparison to the VCCTL computed parameters. These two tests measure the electrical resistivity of porous materials across the surface or through the bulk cross section of the specimen respectively, and were chosen due to the number of measurements available for comparisons. Generally speaking, the electrical resistivity of a porous material increases as the conductivity of the material decreases. The experimental data for paste, mortar, and concrete was obtained from two mixtures having water to cement ratios of 0.37 and 0.50. The cement used for these mixtures was obtained from the same source as the cement detailed in Project Deliverable 4, and the same characterized cement properties were used for simulations. Because the VCCTL currently will not calculate transport properties for cementitious mortars or concrete, simulation results for paste at the two different w/c's were used for comparison with all experimental data. Simulations were executed out to 182 days to encompass the oldest available experimental data. To evaluate potential correlations between simulated properties and experimental measurements predictions at all ages were plotted against their respective measurements. A simple linear regression was performed for each comparison to provide a qualitative indicator correlation.

8.4. Paste Results

The results of bulk resistivity for the two portland cement pastes are compared with VCCTL predictions of volume fraction porosity and transport factor in Figures 8-3 and 8-4. Bulk resistivity measurements for 7, 28, 56, and 91 days generally appear to be nonlinear with respect to simulated measurements at both 0.5 and 0.37 w/c. The effect of w/c is apparent for both simulated properties and bulk resistivity measurements; volume fraction porosity and transport factor both increase significantly at higher w/c, to such a degree that no overlap exists between simulated values for the two mixtures. Maximum values for bulk resistivity measurements increase as w/c decreases. Changes in w/c also produce linear regressions with significantly different slope and intercept values, indicating that a correlation independent of w/c is unlikely.

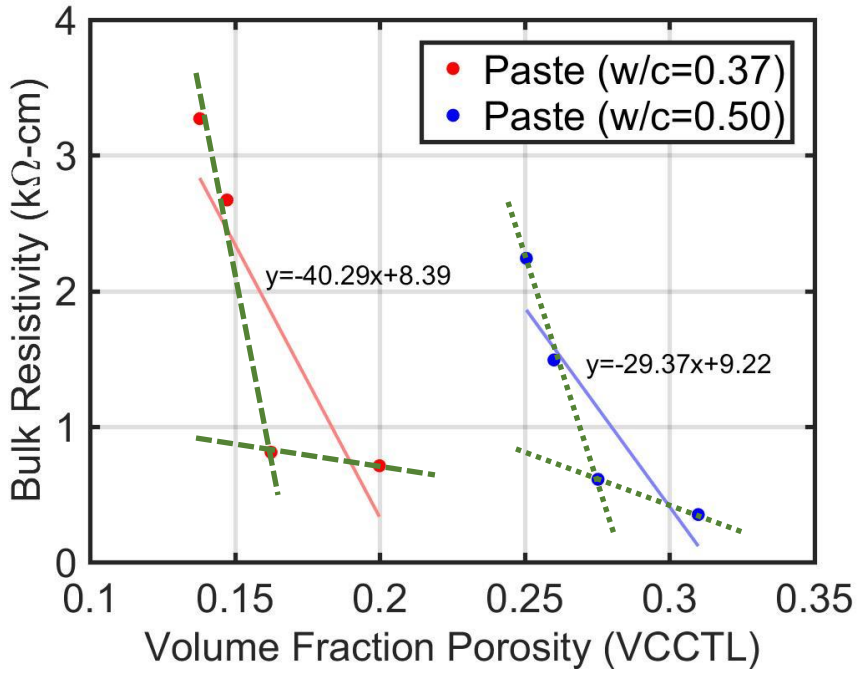

Figure 8-3. Comparison of VCCTL calculated paste porosity volume fraction with bulk resistivity measurements for paste

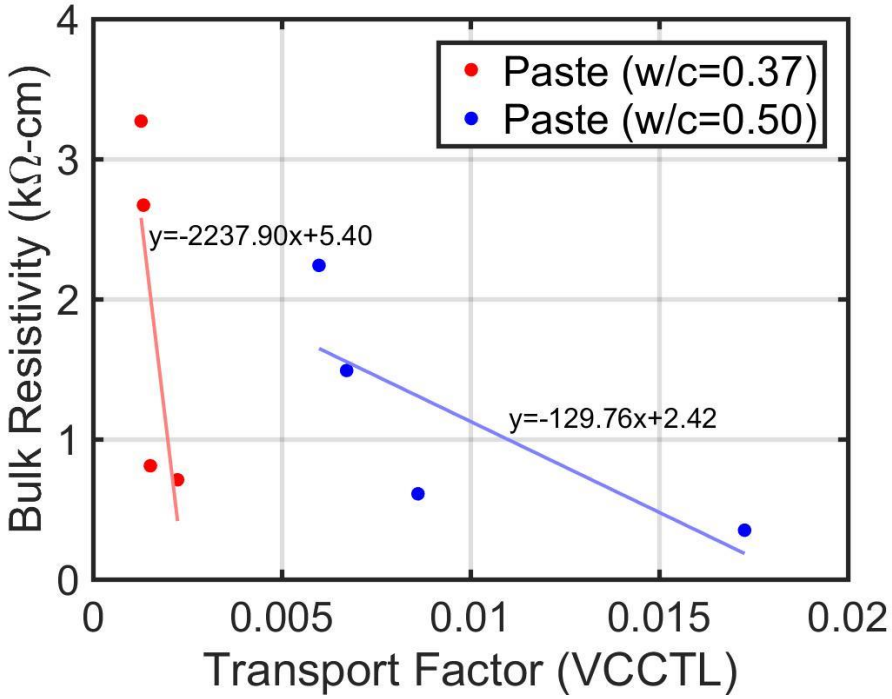

Figure 8-4. Comparison of VCCTL calculated paste transport factor with bulk resistivity measurements for paste

Surface resistivity measurements for paste appear to correlate more strongly with VCCTL-predicted values for transport factor and volume fraction porosity as shown in Figures 8-5 and 8-6. The same trends exist with w/c for surface resistivity as do with bulk; however, the dependency of surface resistivity measurements on w/c is more pronounced. Unlike the bulk resistivity measurements, the lowest measurements of surface resistivity at a w/c of 0.37 are higher than the highest measurements of surface resistivity at a w/c of 0.5. As with the VCCTL comparisons against bulk resistivity, the slope and intercept parameters of the linear regressions are significantly different at different w/c, indicating that a linear correlation of VCCTL and resistivity measurements independent of w/c is unlikely.

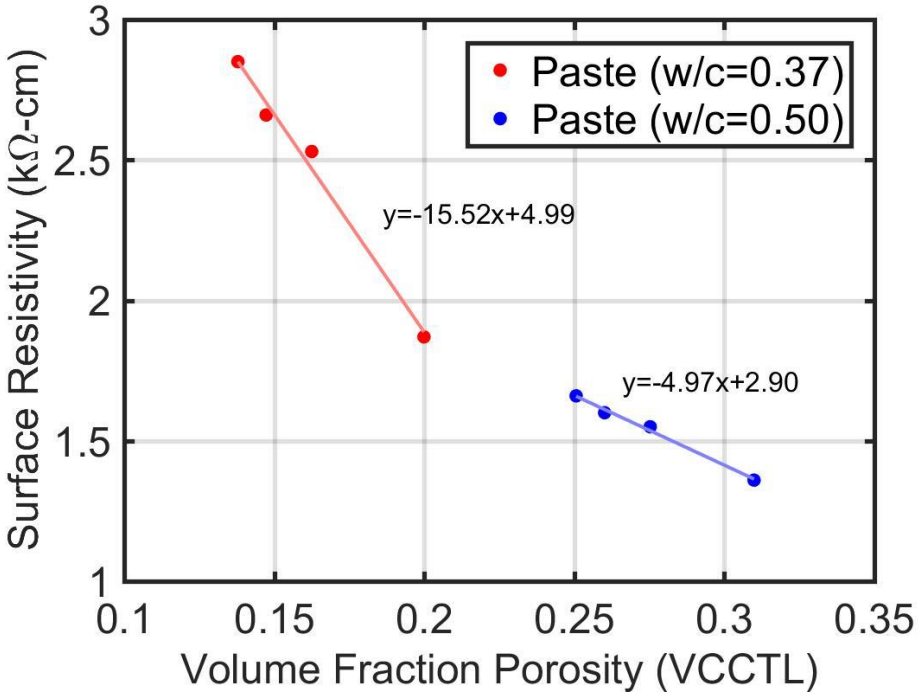

Figure 8-5. Comparison of VCCTL calculated paste transport factor with surface resistivity measurements for paste

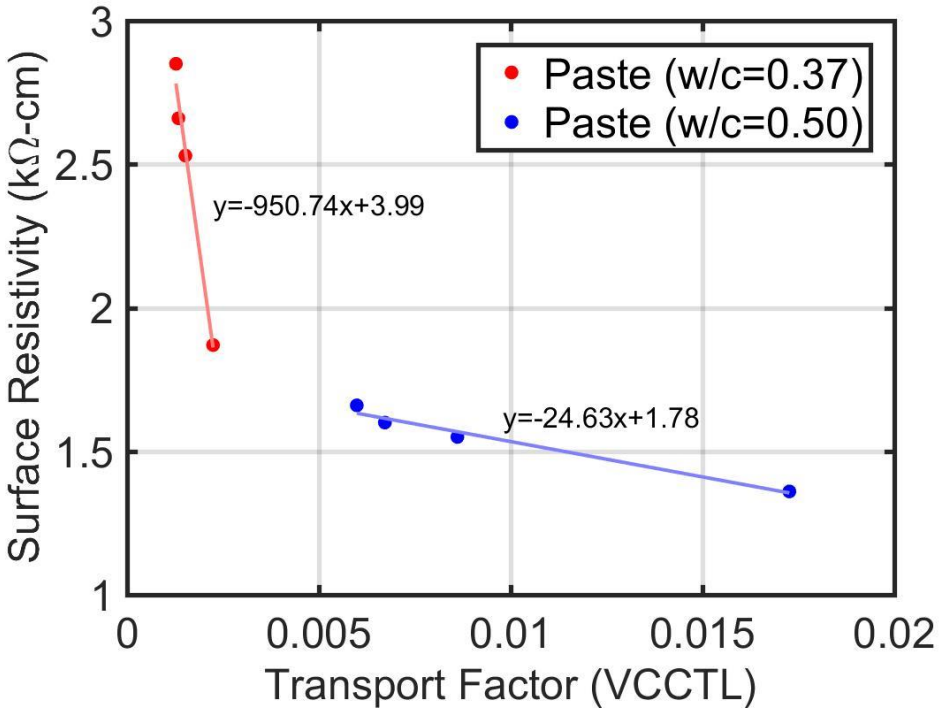

Figure 8-6. Comparison of VCCTL calculated paste transport factor with surface resistivity measurements for paste

8.5. Mortar and Concrete Results

Comparison of VCCTL values for volume fraction porosity and transport factor to surface and bulk resistivity measurements from mortar and concrete are shown in Figures 8-7 to 8-10 and Figures 8-11 to 8-14 respectively. The results are very similar to the comparisons with measured values for paste, only differing in the magnitude of the experimental measurements. Both surface and bulk resistivity measurements are higher for mortar than for paste, while concrete results are higher still.

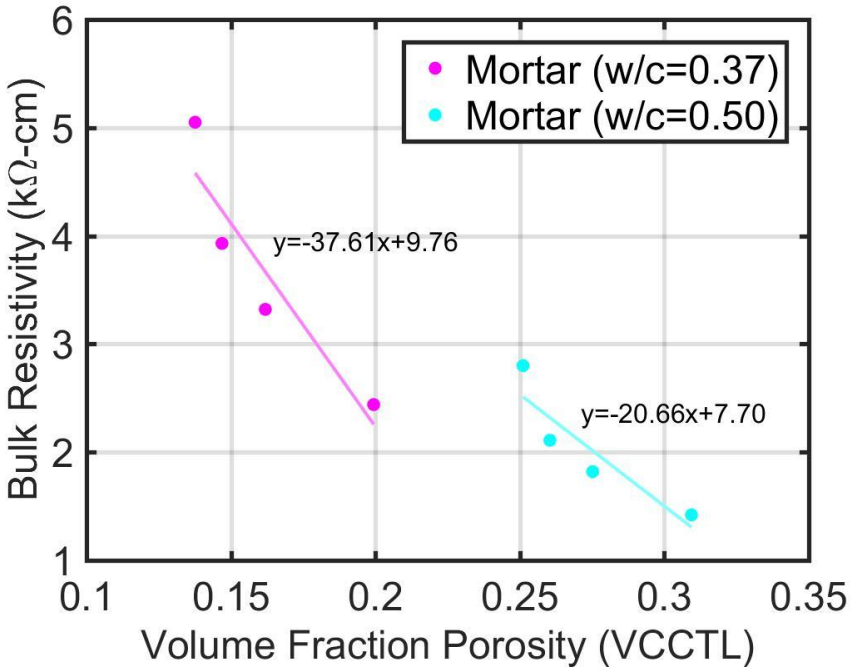

Figure 8-7. Comparison of VCCTL calculated paste porosity volume fraction with bulk resistivity measurements for mortar

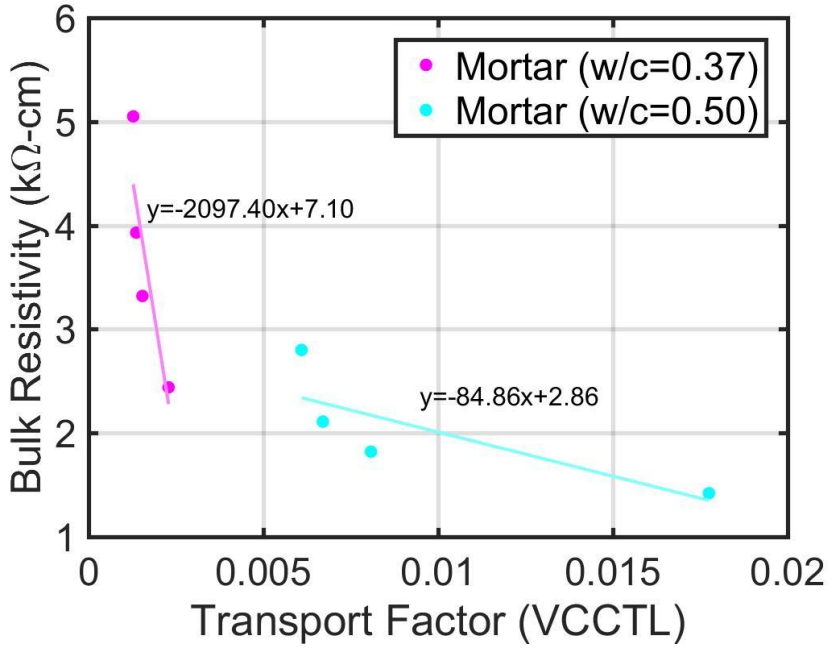

Figure 8-8. Comparison of VCCTL calculated paste transport facto with bulk resistivity measurements for mortar

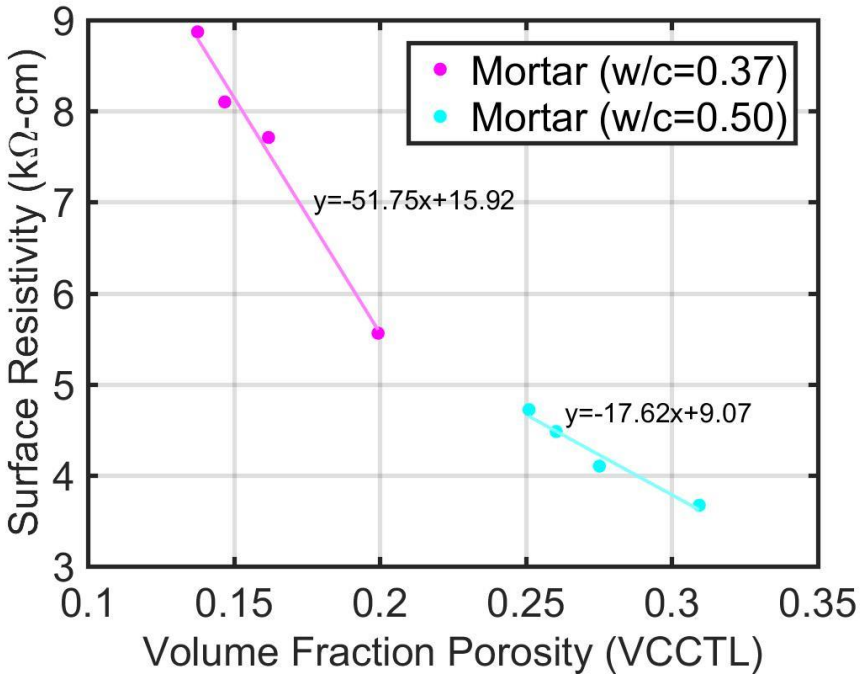

Figure 8-9. Comparison of VCCTL calculated paste porosity volume fraction with surface resistivity measurements for mortar

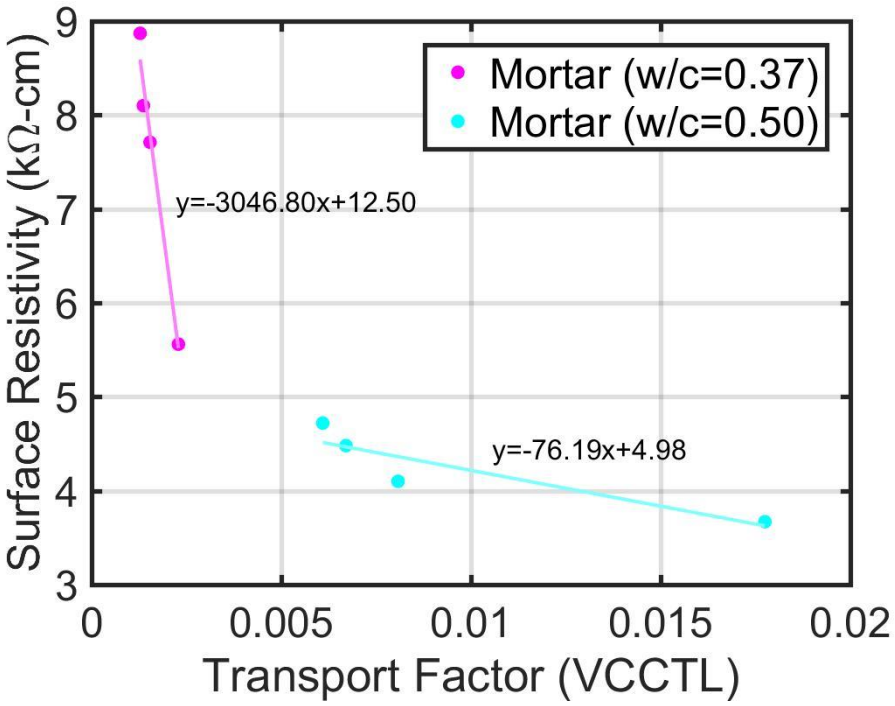

Figure 8-10. Comparison of VCCTL calculated paste transport factor with surface resistivity measurements for mortar

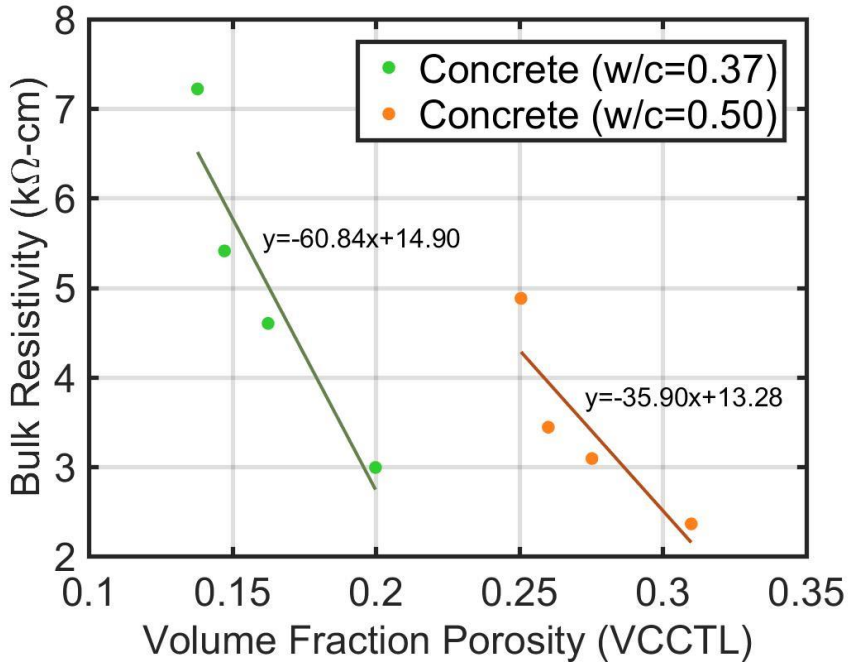

Figure 8-11. Comparison of VCCTL calculated paste porosity volume fraction with bulk resistivity measurements for concrete

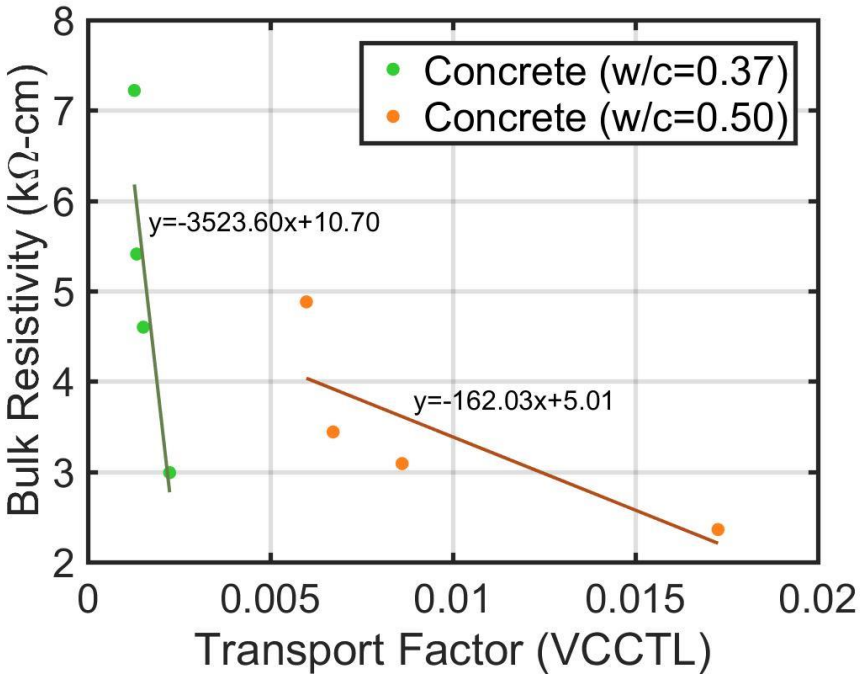

Figure 8-12. Comparison of VCCTL calculated paste transport factor with bulk resistivity measurements for concrete

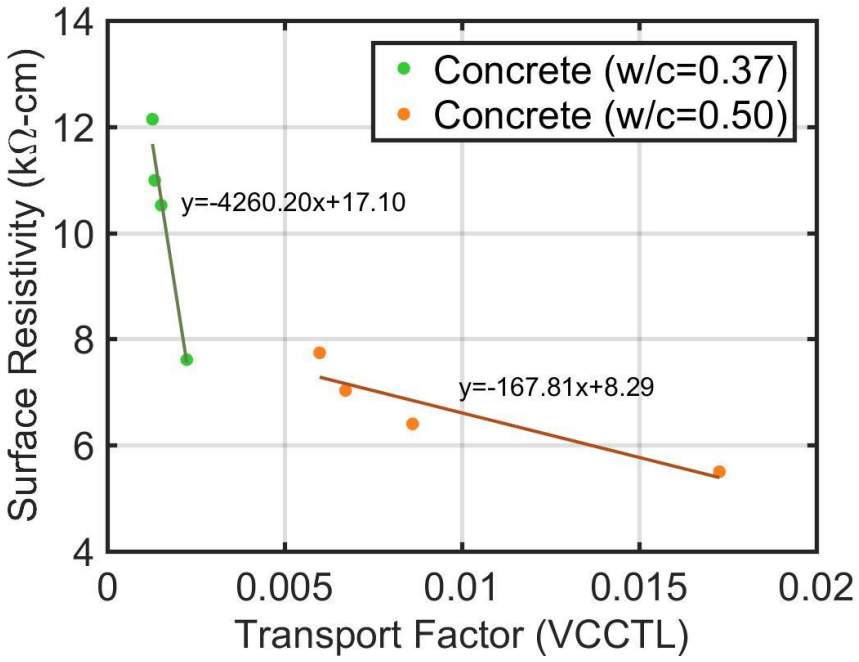

Figure 8-13. Comparison of VCCTL calculated paste transport factor with surface resistivity measurements for concrete

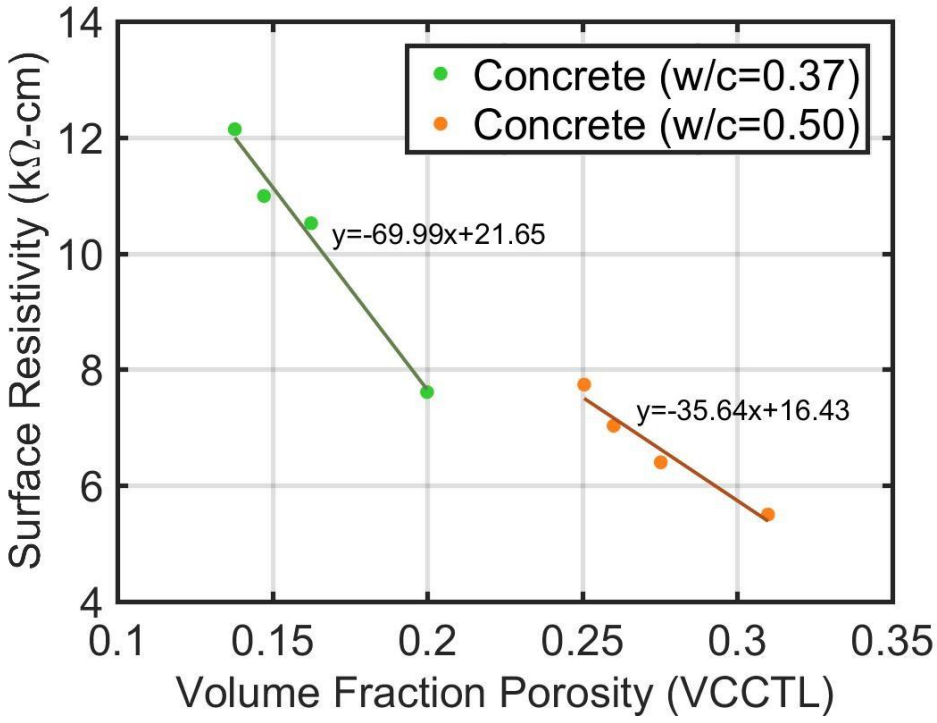

Figure 8-14. Comparison of VCCTL calculated paste porosity volume fraction with surface resistivity measurements for concrete

8.6. Discussion

The results presented in this report provide a basic assesment of the ability of the VCCTL to provide relative information about durability properties and its potential value as a comparative tool. The values predicted by the VCCTL generally trend in a predictable manner, with lower porosity, lower w/c mixtures having lower values for volume fraction porosity and transport factor. These values correlate to varying degrees with measurements of bulk and surface resistivity; however, in all cases as measurements of resistivity increase the VCCTL-predicted values decrease, and the differences between chemically identical mixtures with different w/c are very pronounced. This indicates that while the VCCTL may not be ideal for direct prediction of durability properties, it may have value as a tool for preliminary comparative assesment between mixtures of varying composition.

9. MULTI-OBJECTIVE OPTIMIZATION OF VCCTL SIMULATIONS

9.1. Background

This chapter details efforts to develop optimization tools for mixture proportions and composition of cement to meet a number of performance criteria simultaneously. For instance, optimization of the cement and concrete mixture design is a process of searching for a mixture for which the sum of the costs of the ingredients is lowest, yet satisfying the required performance of cement, such as strength, durability and sustainability. As the number of material variables increases, the problem of identifying optimal mixtures becomes more difficult. Statistical methods have been conducted to optimize cement and concrete mixture design [111–121]. These methods include fitting empirical models to the data for each performance criterion with a set of trial batches. Among these methods, each response is expressed as an algebraic function of factors. Considering that cement and concrete mixtures consist of multiple components, the optimization should be able to take into account several attributes at the same time. However, statistical methods become inefficient due to the prohibitive number of trial batches required to find optimal proportions.

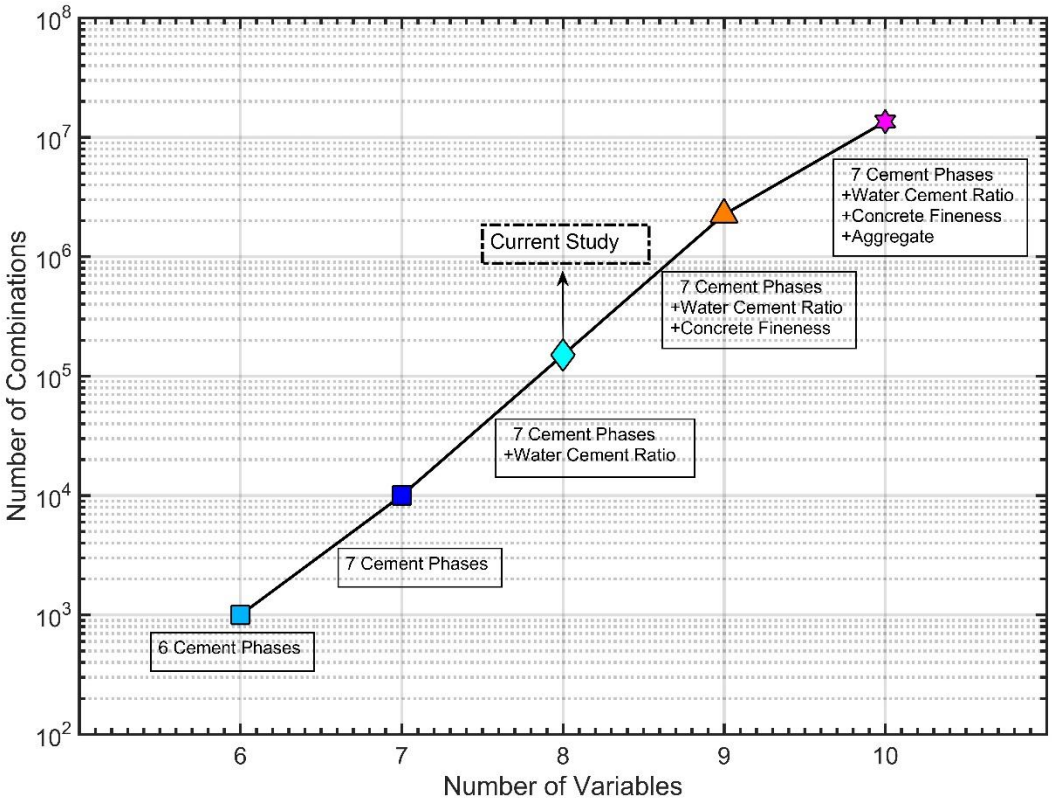

Figure 9-1. Potential combinations of cement and concrete with different number of variables from VCCTL

Figure 9-1 shows the potential combinations of cement and concrete with different number of variables from VCCTL. The number of simulations in VCCTL increases by 10 times with one more variables considered. It takes about an hour to conduct one simulation process in the University of Florida High Performance Computing (HPC) cluster of University of Florida. For concrete, there're 10^7 combinations for the total inputs. Therefore, a blind search with 10^7 simulations in VCCTL for specified performance criteria is not practical. Alternatively, metaheuristic techniques provide a reasonable direction for searching through a large feasible domain, which is efficient and suitable for the inputs and outputs from VCCTL. A metaheuristic is formally defined as an iterative generation process which guides a subordinate heuristic by combining intelligently different concepts for exploring and exploiting the search space, learning strategies are used to structure information [122] in order to find efficiently near-optimal solutions efficiently. During last two decades, metaheuristics optimization methods have had widespread success in solving difficult combinational optimization problems [123–130]. Examples include particle swarm optimization (PSO) [131–134], genetic algorithms [135–137], harmony search [138], simulated annealing [139,140], and TABU search [141].

Among these metaheuristic methods, one of most important and popular computational methods that deal with the engineering optimization problems is the PSO [131–134]. They do not need the optimization problem to be differentiable as is required by classic optimization method such as the gradient descent and quasi-Newton methods [142,143]. In this way, the computational methods are suitable for discrete problems matching the discrete input data required by VCCTL. In this paper, PSO is used to solve multi-objective optimization problems in cement modeling.

For current study, 7 cement phases and water cement ratio are considered as inputs, which gives about 150,000 combinations to run in VCCTL. The paper first presents an overview of virtual testing software VCCTL and two metaheuristic algorithms. Subsequently, different optimization cases with metaheuristic algorithms are demonstrated to optimize virtual testing of cement models. Third the converging analysis of the optimization methods is introduced. Finally, the application of optimization results is discussed.

9.2. VCCTL Dataset Enumeration

The core executables are compiled and VCCTL is run in a UNIX operating system with the UF HPC Cluster, which possesses more than 21,000 computing cores. The simulations are run on the HPC because a typical simulation run in the VCCTL on a PC computer requires one compute core and between 45 to 90 minutes to complete. Therefore, it is not feasible to employ blind searches within VCCTL. The use of the HPC cluster requires high computational effort, which is better suited for the use of an intelligent search algorithm to optimize the search.

In order to demonstrate the optimization tool, a set of input data is created and run into VCCTL. The database consisting of inputs and outputs of VCCTL for approximately 150,000 different portland cement compositions is sample data for metaheuristic optimization introduced in the following section. Table 9-1 shows the range of each parameter. Once VCCTL finishes simulating all input data, a set of output data is created. Among the input and output data, three parameters are selected as the objectives in the following optimization process. Figure 9-2 shows

the shape of the three objectives in space. Different colors represent different water cement ratios.

Table 9-1. Parameter variation of inputs

Input	Mass fraction		
	Lower Bound	Increments	Upper Bound
Water to Cement Ratio	0.20	0.02	0.53
Alite	0.50	0.0001	0.70
Belite	0.15	0.0001	0.37
Ferrite	0.05	0.0001	0.20
Aluminate	0.03	0.0001	0.10
Gypsum	0.00	0.0001	0.06
Anhydrite	0.00	0.0001	0.04
Hemihydrate	0.00	0.0001	0.04

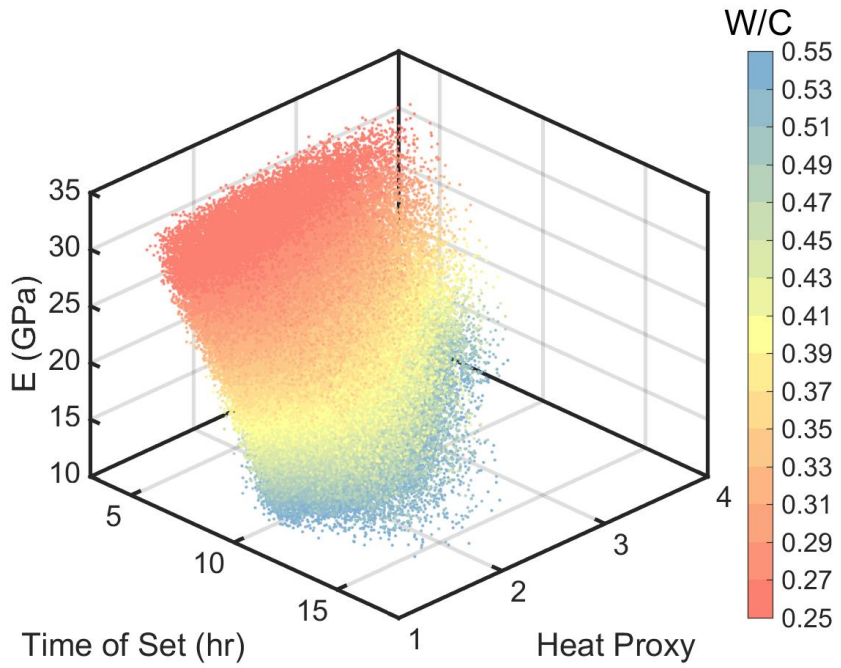

Figure 9-2. The shape of database with respect to three objectives from VCCTL. Different colors mean different water-cement ratios.

9.3. Multi-objective Optimization with Metaheuristic Algorithms based on VCCTL

9.3.1. Overview of Particle Swarm Optimization

Particle Swarm Optimization is a population-based metaheuristic originally developed by Kennedy and Eberhart in 1995 [144]. This metaheuristic was inspired by computing models to simulate bird flocking and fish schooling. A PSO algorithm maintains a population of particles

(the swarm) as it moves through a search space from random locations to locate the minimum (or maximum) of a given objective function.

Each particle in PSO is associated with a velocity. Particles move through the search space with dynamically adjusted velocities based on historical behaviors. Thus, the particles have the tendency to "fly" towards the better search area throughout the search process [145]. In order to add a social component, a neighborhood is defined for each individual particle. It is defined as comprising the target individual and the two individuals immediately adjacent in the array. Therefore, for each individual *i*, the neighborhood is composed of individuals *i*-1, *i*, and *i*+1. Each individual is treated as a volume-less particle (a point) in the D-dimensional search space. The i^{th} particle is represented as $X_i = (x_{i1}, x_{i2}, \ldots, x_{iD})$. The position of the best fitness value of the i^{th} particle is represented by $P_i = (p_{i1}, p_{i2}, \ldots, p_{iD})$. For each iteration, each particle is updated by the following two current 'best' values. The first is the best value achieved from a previous location giving the best fitness value. This value is called *pbest*. For each iteration, the *P* vector of the particle with the best fitness in the neighborhood, and the *P* vector of the current particle are combined to adjust the velocity along each dimension. This velocity is then used to compute a new position for the particle. The second best value is the best individual found in the entire swarm, which is called *gbest*.

General PSO procedure is as follows [145]:

1. Initialize a population (matrix) of particles, with positions and velocities in a space problem of *n* dimensional, randomly with uniform distribution.
2. Evaluate the objective function *f(x)* (also known as fitness function) for each particle.
3. Compare the evaluation of the particle aptitude function with the *pbest* of the particle. If the average value is better than the *pbest*, then the *pbest* value becomes the value of the aptitude function and the *pbest* location becomes the same of the current location in the *n* dimensional space.
4. Compare the aptitude function evaluation with the best previous value of the population aptitude. If the current value is better than the *gbest*, update the *gbest* value for the index and current particle value.
5. Update the new velocity of each particle *i* with
   a. $$V_i^{k+1} = wV_i^k + c_1 r_1 (P_i^k - x_i^k) + c_2 r_2 (P_g^k - x_i^k) \qquad (9\text{-}1)$$

Where P_i^k is *pbest* and P_g^k is *gbest*; *w* is called the *inertia weight*, which determines the influence of the old velocity. The higher *w* value, the more the individuals tend to search new areas. Typical values for *w* are slightly smaller than 1.0; c_1 and c_2 are the *acceleration coefficients*, which are also called the cognitive and the social parameter respectively; r_1 and r_2 are random values uniformly drawn from [0,1]. The second part of the Equation (9-1) consists of the "cognitive" part, representing the private thinking or independent knowledge of the particle itself. The third part is the "social" part, which represents the collaboration among the particles.

6. After velocity updates the new position of particle *i* is determined by
   a. $$x_i^{k+1} = x_i^k + V_i^{k+1} \qquad (9\text{-}2)$$

b. The position of particle *i* for next iteration is updated by adding velocity from Equation (9-2) to current position of particle *i*. The velocity guides the metaheuristic search to the positions where optimal solutions exist. If there is a maximum range for the location, the particle is reflected by the boundary.

7. Go back to step 2) until a stop criterion is found. It is usually a pre-defined error or a maximum number of iterations. In this research, convergence analysis is set as a post processing so that the computational cost could also be estimated.
8. Add constraints according to the property of the variable set.

9.3.2. Overview of Multi-objective Optimization

A multi-objective optimization problem (MOOP) deals with more than one objective function. In most practical decision-making problems, multiple objectives or multiple criteria are evident. A set of trade-off optimal solutions (known as Pareto-optimal solutions) instead of a single optimum solution, is obtained in such problems [146]. In this research, multi-objective optimization is applied because several performance criteria of cement need to be considered at the same time. Different from the single-objective optimization problem, the multi-objective optimization problem does not result in a single optimum solution. Instead, it results in a set of optimum solutions that represent different trade-offs among the objectives. These solutions are known as Pareto optimal solutions or constitute the Pareto optimal solution set. A Pareto front is obtained by plotting multiple objective functions of all the Pareto optimal solutions. For a bi-objective optimization case, Pareto front is an envelope curve covering the feasible domain in the plane. For a tri-objective optimization, it is a surface covering the feasible domain in space.

Based on the concept of dominance [146], Pareto optimal fronts are used in most multi-objective optimization algorithms. Two solutions are compared on the basis of whether one dominates the other or not. The concept of domination is defined as a solution $x^{(1)}$ is as follows.

A solution $x^{(1)}$ is said to dominate the other solution $x^{(2)}$ if both conditions below are true:

1. The solution $x^{(1)}$ is no worse than $x^{(2)}$ in all objectives.
2. The solution $x^{(1)}$ is strictly better than $x^{(2)}$ in at least one objective.

Pareto optimal set is a set of solutions that are not dominated by any member of the entire search space. For a minimization problem with *m* objective functions, a design variable vector x^* is the Pareto optimal if and only if there is no vector $\vec{x}$ in the feasible space with the characteristics: $f_i(x) \leq f_i(x^*)$ for all $i=1,2,\ldots,m$ and $f_i(x) < f_i(x^*)$ for at least one *i*. In this way, fitness values of solutions are evaluated by comparing the dominance of objective functions. Non-dominated solutions are stored in an external archive and updated for each generation. If any solution *i* dominates any member of the archive, then that dominated member is removed from the archive. Otherwise, if the solution *i* is dominated by any member of the archive, the solution *i* is ignored. If solution i is not dominated by any member of the archive, it is entered in the archive. This is how the archive grows with non-dominated solutions. When all solutions of the population are checked, the remaining members of the archive constitute the non-dominated set, which is called Pareto-optimal set or Pareto front. The Pareto-optimal set always consists of solutions from a particular edge of the feasible search region.

9.4. Bi-objective Optimization of VCCTL Modeling

To serve as a point of reference, bi-objective optimization problem without constraint is conducted. Two objective functions, 7-day elastic modulus and time of set, are optimized simultaneously. Based on the concept of domination, Pareto front consists of all the non-dominated solutions where no better solution is found outside the Pareto front. Figure 9-3 (a) presents the performance envelope for the full simulation outputs, with the Pareto fronts superimposed for four cases:

1. Min-Min: min(time of set) & min(E)
2. Min-Max: min(time of set) & max(E)
3. Max-Min: max(time of set) & min(E)
4. Max-Max: max(time of set) & max(E)

The Pareto fronts obtained from the PSO were generated using 30% of the simulations of required to fully enumerate the sample space, which results in a substantial reduction in computational expense without a significant tradeoff in accuracy. The Pareto fronts coincide for the majority of the data envelope, varying by less than one hour and 5 GPa on the horizontal and vertical scales, respectively, in the absolute worst case.

This example, while simple, demonstrates the potential of the PSO generated Pareto front as a substitute for bulk analysis to define infeasibility. For example, Figure 9-3(b) shows the Pareto front for w/c = 0.29. The graph shows that a modulus of elasticity of 28 GPa and a time of set > 8.5 hours are incompatible (in this numerical simulation).

Further, it sets a framework to understand how variations in the phase distribution affect performance. Consider the Min-Max and Max-Max Pareto fronts shown for each w/c in Figure 9-4 Examination of primary phase mass fractions for cements from the Min-Max and Max-Max fronts (Figure 9-5) show that the optimal cements for the Min-Max case have higher median amounts of C_3S and lower median amounts of C_2S and C_4AF compared to the full dataset. Distributions of mass fractions in the Min-Max case are also narrower than those of the full dataset or the Max-Max case, indicating that tighter limits on cement composition would be required to achieve optimal performance for fast setting and high-early modulus.

After the above four scenarios are verified by PSO bi-objective optimization, constraint problem is introduced to demonstrate the application of these methods. Figure 9-6 shows the optimal solutions for minimizing both time of set and C_3S/C_2S with the specified modulus (E>15GPa and E>30GPa). From Figure 9-6, optimal solutions are affected by the constraint because of the different range of feasible domain. These results offer a set of trade-off solutions under different requirements of strength for cement, which make the cement design more efficient without using large amount of trial batch.

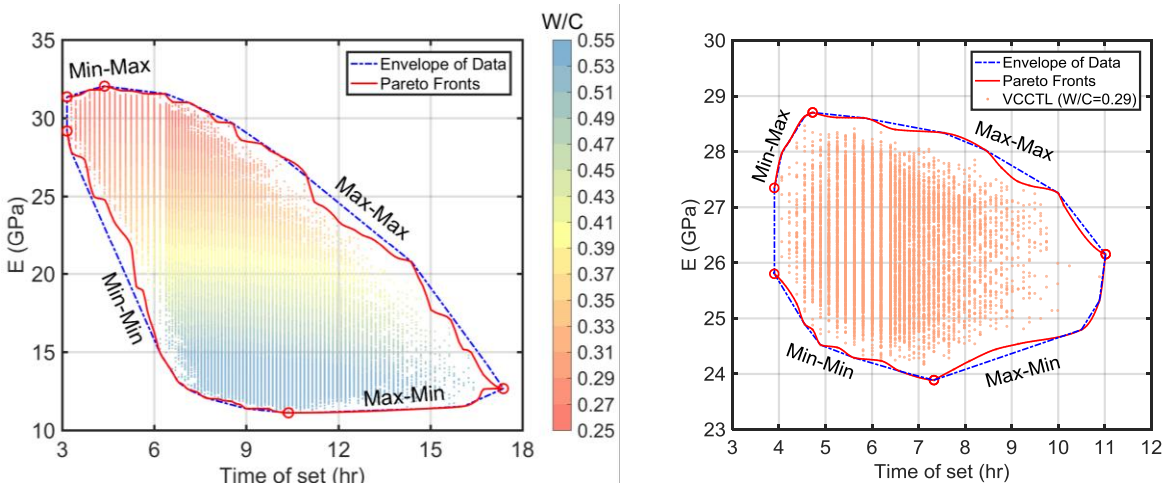

(a) Full dataset (b) Dataset corresponding to w/c = 0.29

Figure 9-3. Pareto fronts of four different bi-objective optimization scenarios without constraint compared with the envelope of data. Exploring Pareto fronts with PSO decreases the computational cost by more than 70% compared with blind search for data.

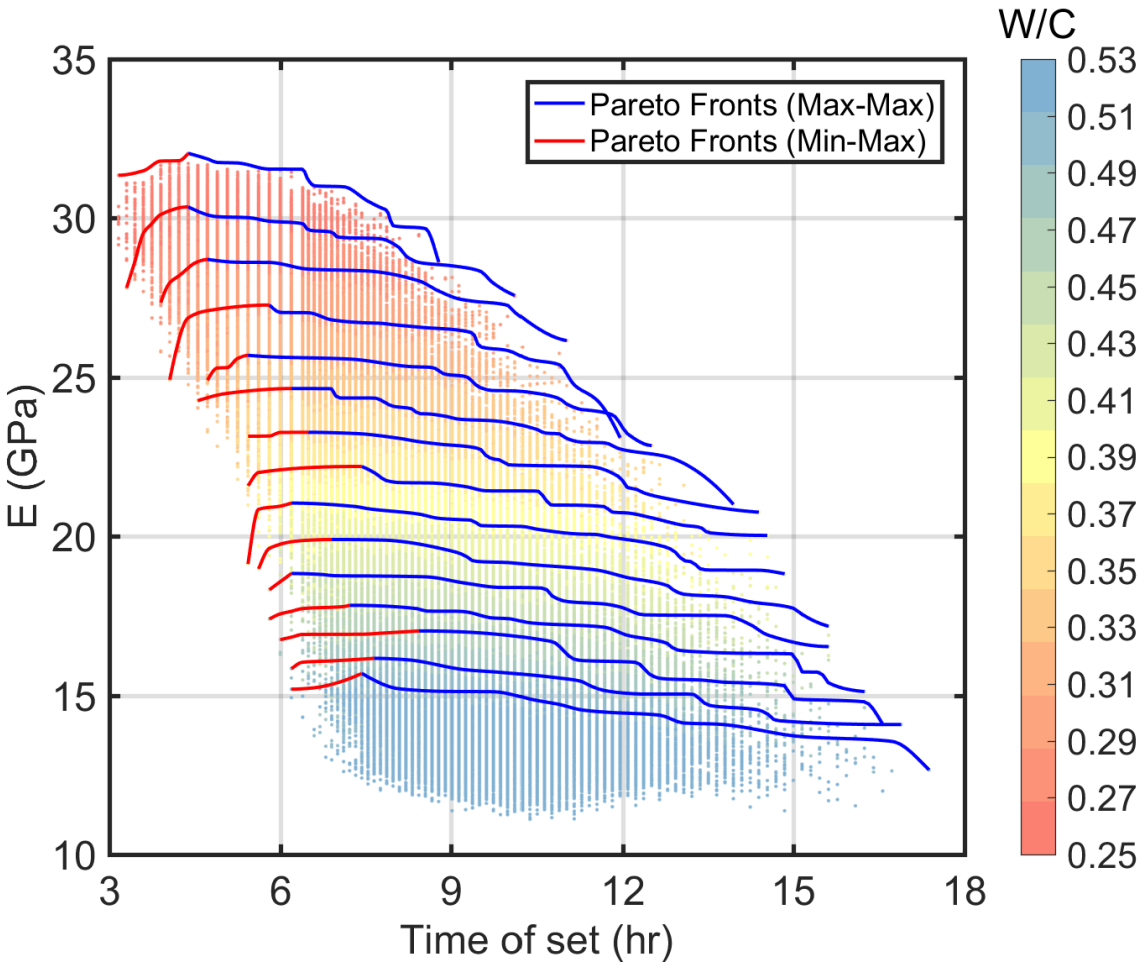

Figure 9-4. Min-Max and Max-Max Pareto fronts for elastic modulus and time of set at each water-to-cement ratio

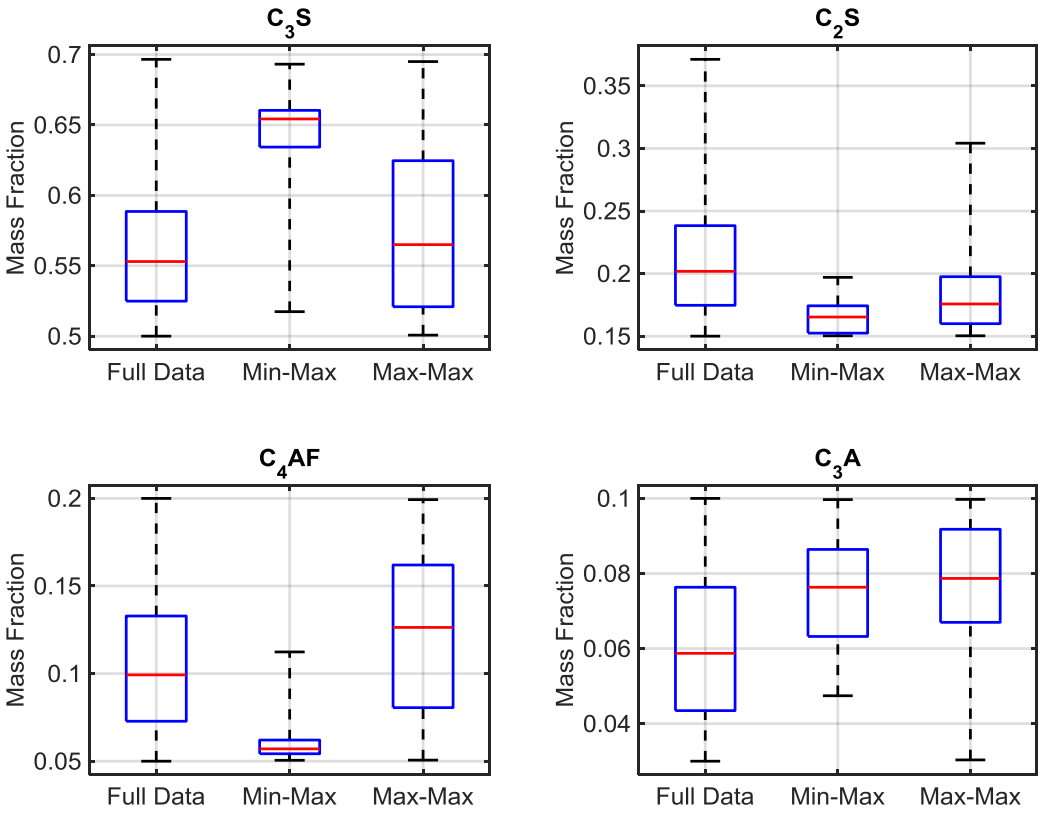

Figure 9-5. Primary cement phase composition for cements from the pareto fronts in Figure 9-4, compared with the compositions of the entire cement dataset. The boxes encompass the 25th to 75th percentile range of mass fractions

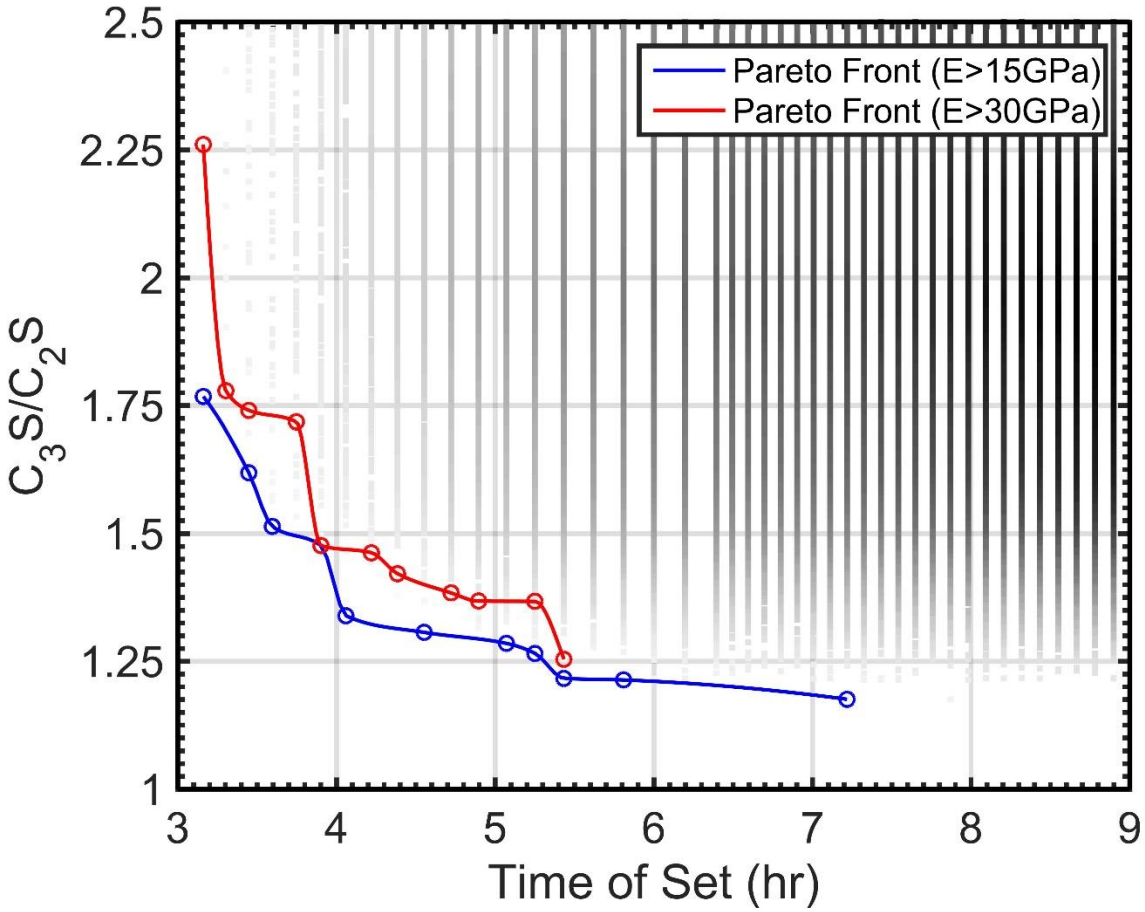

Figure 9-6 Pareto fronts of constrained bi-objective optimization under different constraints with elastic modulus.

9.5. Tri-objective Optimization of VCCTL Modeling

9.5.1. *Pareto Front for Different Optimization Cases*

For tri-objective optimization problems, Pareto fronts are continuous surfaces interpolated by discrete non-dominated solutions instead of continuous curves. Three objective functions are taken into consideration simultaneously using PSO, which are proxy for kiln temperature C_3S/C_2S (f_1), time of set (f_2), and 7-day elastic modulus (f_3). Three cases are conducted to get the Pareto fronts, which are min-min-max, min-min-min, and max-max-max cases.

Based on the concept of dominance mentioned earlier in multi-objective optimization algorithms, non-dominated solutions are selected by simultaneously comparing the three objective functions. For a design variable vector $\boldsymbol{x}^*$ for one generation, it is a non-dominated

solution set for the generation, if and only if, there is no vector $\boldsymbol{x}$ in that generation with one of the three characteristics below for min-min-max case:

1) $f_1(\boldsymbol{x}) \leq f_1(\boldsymbol{x}^*)$ and $f_2(\boldsymbol{x}) \leq f_2(\boldsymbol{x}^*)$ and $f_3(\boldsymbol{x}) > f_3(\boldsymbol{x}^*)$;
2) $f_1(\boldsymbol{x}) \leq f_1(\boldsymbol{x}^*)$ and $f_2(\boldsymbol{x}) < f_2(\boldsymbol{x}^*)$ and $f_3(\boldsymbol{x}) \geq f_3(\boldsymbol{x}^*)$;
3) $f_1(\boldsymbol{x}) < f_1(\boldsymbol{x}^*)$ and $f_2(\boldsymbol{x}) \leq f_2(\boldsymbol{x}^*)$ and $f_3(\boldsymbol{x}) \geq f_3(\boldsymbol{x}^*)$.

In this way, *pbest* and *gbest* used to update the velocity of each particle are selected from the non-dominated solution set of each generation. Also, for each generation, non-dominated solutions are stored into an external archive and updated by comparing the dominance with old solutions inside the archive. The solutions in the old archive that are dominated by the new evolved solutions are removed; thus, adding the new, non-dominated solutions. Similar process is conducted for maximizing case. Once all the non-dominated solutions are obtained, the scatter points of discrete solutions are interpolated to obtain a continuous surface.

Figure 9-7 shows the Pareto fronts for different water cement ratios when minimizing time of set, minimizing proxy for kiln temperature and maximizing 7-day elastic modulus. From the Figure 9-7, it shows that increasing the water cement ratio leads to the decreasing of the 7-day elastic modulus and increasing of setting time. Although, C_3S/C_2S is not affected by water cement ratio because C_3S, C_2S and water cement ratio are all inputs of cement and independent from one another. The different Pareto fronts provide the non-dominated solutions for different water cement ratios which could be used as a guidance for design. As an example, the optimization results with a specified water cement ratio (0.25) are taken. There are 88 non-dominated solutions found by the PSO optimization techniques. Inputs of those optimal solutions are obtained accordingly. Table 9-2 lists the inputs and outputs of the first 30 non-dominated solutions out of 88. This allows Figure 9-7 to provide a feasible guidance for cement designers. From all the trade-off optimal solutions, the selection of different combinations for inputs for cement design is based on the requirement of the cement paste performance.

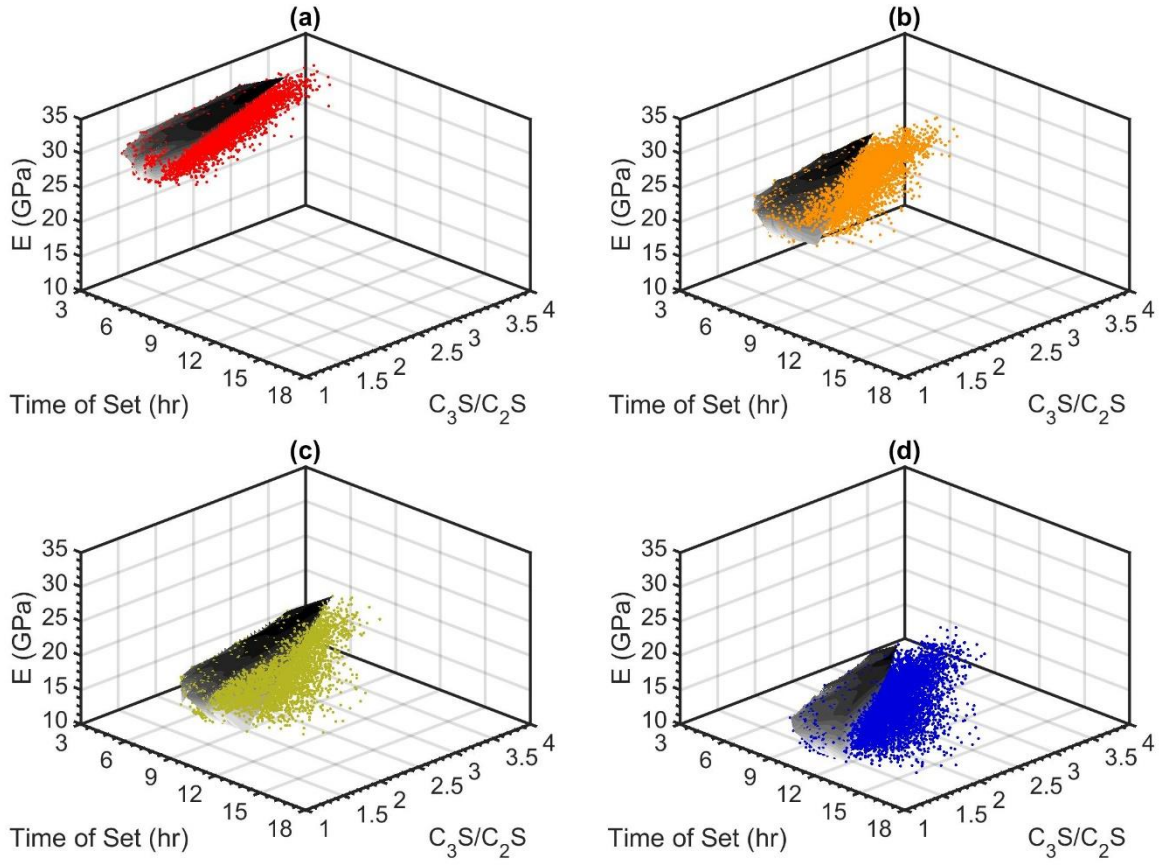

Figure 9-7. Pareto Fronts for Min (Time of set) – Min (C_3S/C_2S) – Max (E) with different water cement ratios. (a) w/c=0.25; (b) w/c=0.33; (c) w/c=0.43; (d) w/c=0.53.

Figure 9-8(a)(b) show the two Pareto fronts (gray meshes) from non-dominated solutions (red dots) for max (Time of set) – max (C_3S/C_2S) – max (E) and min (Time of set) – min (C_3S/C_2S) – min (E) cases. Figure 9-8(c) shows the two Pareto fronts with all the cement data. The colorbar on the left shows the change with water cement ratio from 0.25 (red) to 0.53 (blue) for cement data and the colorbar on the right shows the change with modulus on the Pareto front surfaces.

Table 9-2. First 30 non-dominated solutions for min-min-max case (w/c=0.25)

Inputs							Outputs			
Alite Mass fraction	Belite Mass fraction	Ferrite Mass fraction	Aluminate Mass fraction	Gypsum Mass fraction	Anhydrite Mass fraction	Hemihydrate Mass fraction	7-day Heat (kJ/kg)	Time of Set (hours)	Degree of hydration (%)	7-day Elastic Modulus (GPa)
0.54	0.27	0.07	0.07	0.01	0.03	0.00	264	4.55	0.03	31.1
0.69	0.17	0.06	0.05	0.01	0.01	0.01	288	4.39	0.03	32.0
0.57	0.19	0.07	0.09	0.00	0.04	0.04	275	3.30	0.04	30.7
0.51	0.24	0.08	0.09	0.02	0.04	0.02	257	3.60	0.04	29.8
0.61	0.15	0.06	0.10	0.00	0.04	0.03	285	3.16	0.03	31.4
0.50	0.28	0.07	0.09	0.01	0.03	0.01	248	4.55	0.03	29.9
0.65	0.19	0.05	0.06	0.00	0.03	0.01	275	3.60	0.03	31.1
0.53	0.24	0.07	0.09	0.01	0.03	0.03	262	3.45	0.03	30.4
0.52	0.26	0.07	0.10	0.02	0.03	0.01	269	4.55	0.03	30.7
0.50	0.30	0.10	0.05	0.01	0.03	0.00	242	4.90	0.03	29.8
0.54	0.28	0.05	0.09	0.00	0.03	0.01	271	4.90	0.03	31.0
0.61	0.16	0.11	0.07	0.00	0.03	0.01	280	3.90	0.03	31.8
0.59	0.21	0.11	0.05	0.00	0.02	0.02	267	4.39	0.03	31.3
0.58	0.19	0.11	0.08	0.00	0.03	0.00	277	4.90	0.03	31.8
0.65	0.20	0.07	0.04	0.00	0.02	0.02	274	4.22	0.03	31.7
0.60	0.20	0.12	0.04	0.00	0.03	0.00	268	4.39	0.03	31.4
0.52	0.29	0.07	0.08	0.00	0.03	0.01	259	4.90	0.03	30.8
0.52	0.18	0.14	0.10	0.00	0.03	0.02	273	4.06	0.04	30.9
0.52	0.29	0.10	0.05	0.00	0.03	0.01	249	4.72	0.03	30.5
0.53	0.27	0.09	0.06	0.00	0.03	0.01	252	4.39	0.03	30.7
0.54	0.27	0.07	0.07	0.01	0.03	0.00	264	4.55	0.03	31.1
0.69	0.17	0.06	0.05	0.01	0.01	0.01	288	4.39	0.03	32.0
0.57	0.19	0.07	0.09	0.00	0.04	0.04	275	3.30	0.04	30.7
0.51	0.24	0.08	0.09	0.02	0.04	0.02	257	3.60	0.04	29.8
0.61	0.15	0.06	0.10	0.00	0.04	0.03	285	3.16	0.03	31.4
0.50	0.28	0.07	0.09	0.01	0.03	0.01	248	4.55	0.03	29.9
0.65	0.19	0.05	0.06	0.00	0.03	0.01	275	3.60	0.03	31.1
0.53	0.24	0.07	0.09	0.01	0.03	0.03	262	3.45	0.03	30.4
0.52	0.26	0.07	0.10	0.02	0.03	0.01	269	4.55	0.03	30.7
0.50	0.30	0.10	0.05	0.01	0.03	0.00	242	4.90	0.03	29.8

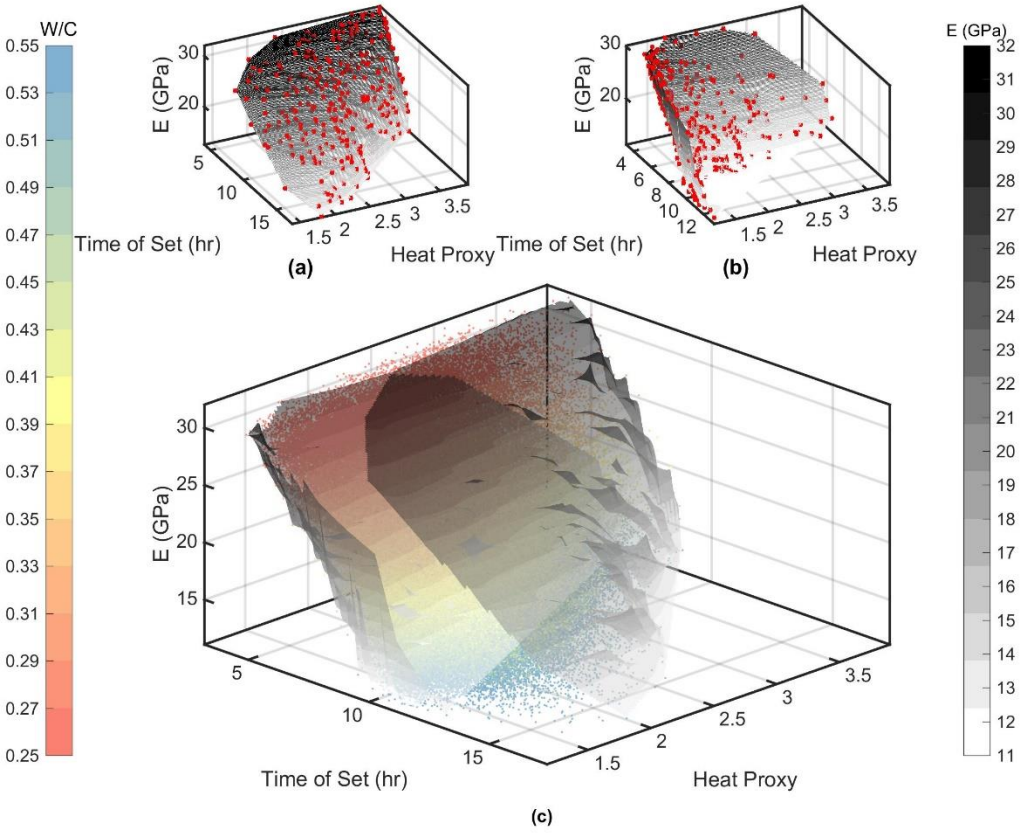

Figure 9-8 (a) 3D surface mesh of Pareto front from non-dominated solution (red markers) for the Max-Max-Max case (b) 3D surface mesh of Pareto front from non-dominated solution (red markers) for the Min-Min-Min case, and (c) 3D surface of Pareto fronts for the combined cases

9.5.2. *Convergence Test*

To minimize the computational expense, metaheuristic search algorithms should be terminated once the estimated value is within a defined tolerance with respect to the target value. Multiple types of stopping criteria for metaheuristic algorithms have been suggested [147–150]. In this paper, we applied a Pareto dominance-based convergence metric to multi-objective evolutionary algorithms similar to that of Goel and Stander [151]. This metric tracks the change of the archive based on a non-dominated criterion to generate a convergence curve, using two terms referred to as the improvement ratio and consolidation ratio.

The improvement ratio is the scaled number of dominated solutions, and the consolidation ratio is the scaled number of non-dominated solutions. Here we adopted the consolidation ratio as the convergence metric because to the variations observed in the improvement ratio were deemed unacceptable. Goel's method [151] was applied to the Min-Min-Min case above to test the convergence with different population sizes. In this study, convergence for the algorithm occurred with a consolidation ratio exceeding 0.85, greater than the proposed value of 0.66. In this case, the number of generations for convergence is 600 when the population size is 300 (shown in Figure 9-9).

The performance of the PSO search algorithm was found to vary by population size; larger population sizes converge in fewer generations (Figure 9-10a), but have a greater computational cost overall (Figure 9-10b). This trend matches that observed by Alander [152] for genetic algorithms.

As the population size increases, the number of non-dominated solutions generations captured by the algorithm increases (Figure 9-10c). To reduce computational cost while maintaining convergence, the population size was optimized for the PSO search algorithm. The lowest feasible population size is 10, which captures 80% (70/87) of the non-dominated solutions relative to larger population sizes. When the population size is less than 10, the consolidation ratio does not exceed the pre-determined cut-off value (0.85) and convergence does not occur. Thus, the minimum number of simulations with PSO is 13,821 out of a total of 149,572 VCCTL simulations, a reduction of 90% compared to a blind search of the full dataset.

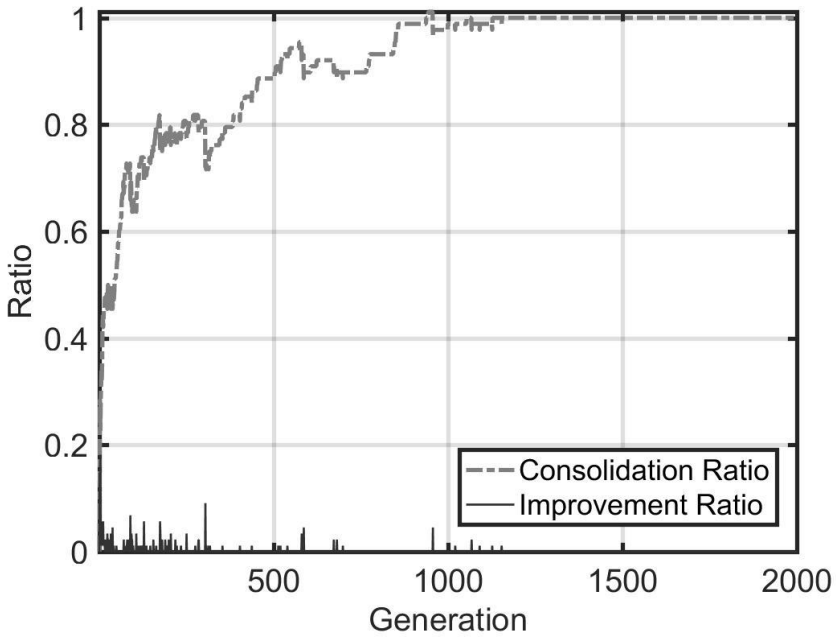

Figure 9-9. Consolidation ratio and Improvement ratio for population size = 300

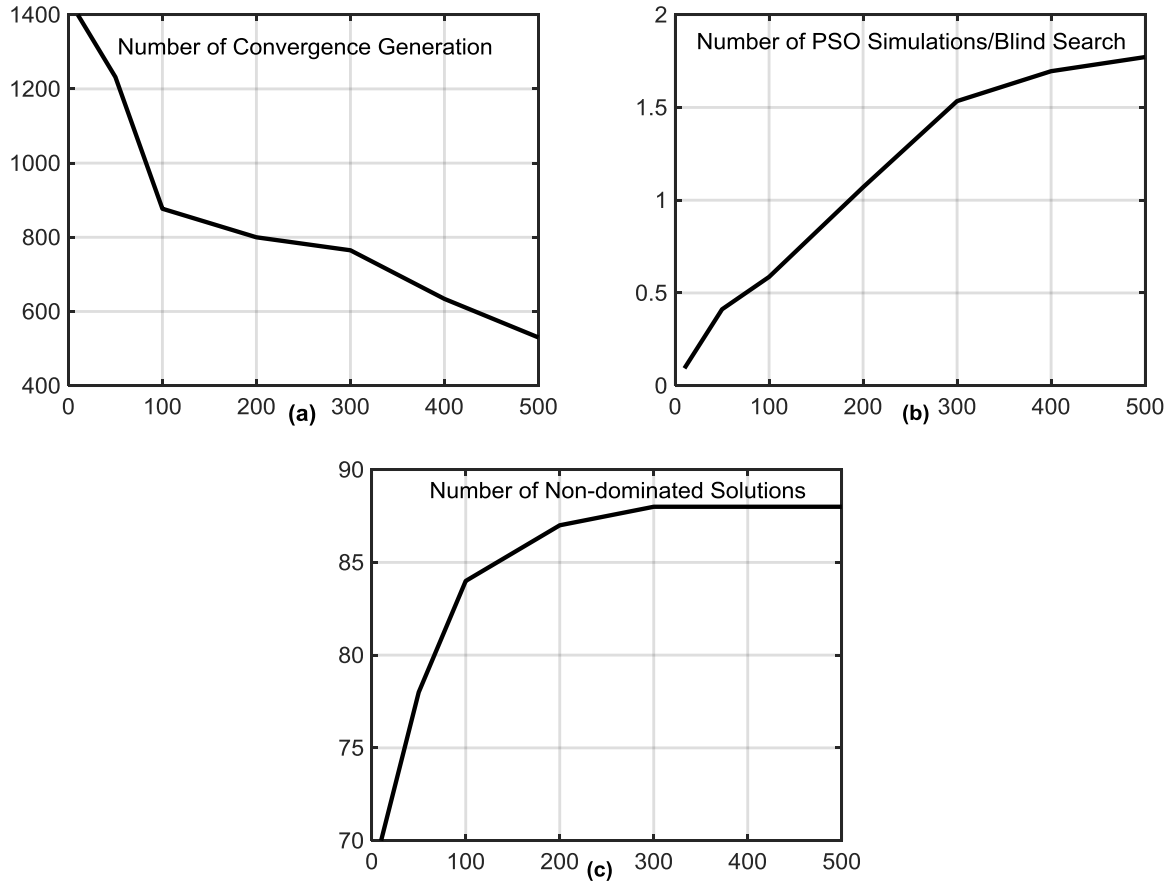

Figure 9-10. (a) Convergence generations, (b) number of simulations vs. population size, (c) number of non-dominated solutions

9.5.3. *Objectively Rating Cement Quality*

A numerical system to objectively rate cement quality does not exist in contemporary practice. As is the practice for other civil engineering materials such as timber and steel (ASTM D245, ASTM A322), portland cements are stratified into discrete types or classes based on physical testing results and intended service applications (ASTM C150), which can be perceived to tacitly imply that all cements of a given type will perform the same. Cement hydration modeling improves this characterization by providing a tool to compare the performance of an individual cement to other cements that share similar properties. Further it can give objective guidance to modify the cement to achieve optimal performance.

This section gives one such example, using a random sample of the full dataset to reduce computational expense. The cumulative distribution function (CDF) was fitted by a four-parameter beta distribution using maximum likelihood estimation [153] and compared to analysis of the full dataset (Figure 9-11). Through trial and error purposes, it was determined that a random sample of 10% of the values gives a reasonable baseline.

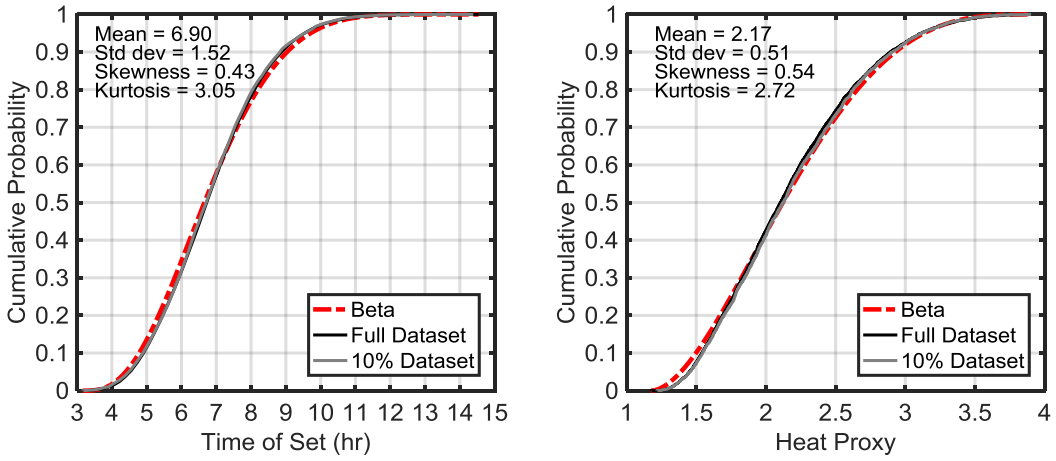

Figure 9-11. Beta distribution fitting of the full enumerated dataset with 10% of the full dataset

The proposed objective characterization system is based on the CDF of the data given a user-specified constraint such as $E \geq E_0$:

$$P_c\,(X, Y \mid E \geq E_0) \tag{9-3}$$

where P_c is the joint CDF within time of set (X) and heat proxy (Y), and E_0 is the minimum allowable modulus of elasticity. The procedure follows:

1. Project cements with $E \geq E_0$ to the surface $E = E_0$
2. If independently assessing time of set (x), or heat proxy (y), evaluate $P_c\,(X \leq x \mid E \geq E_0)$ or $P_c\,(Y \leq y \mid E \geq E_0)$
3. If assessing both time of set and heat proxy, calculate the joint cumulative probability as $P_c\,(X \leq x, Y \leq y \mid E \geq E_0)$
4. Given that a lower time of set and heat proxy are desirable, calculate the score as $S_c = 1 - P_c$. Thus the score corresponds to the probability of exceedance; i.e. scores of zero and unity represent the worst and best possible outcomes respectively

Examples of the proposed performance characterization system are provided in Figure 9-12 which illustrates the assignment of scores. The score for an example paste with a w/c of 0.35 (shown as the black marker) with regard to time of set and heat proxy are $S_{c,time\ ofset} = 1 - P_c\,(X \leq 7.98\ hr \mid E \geq E_0) = 0.22$ and $S_{c,heat\ proxy} = 1 - P_c\,(Y \leq 1.51 \mid E \geq E_0) = 0.92$.

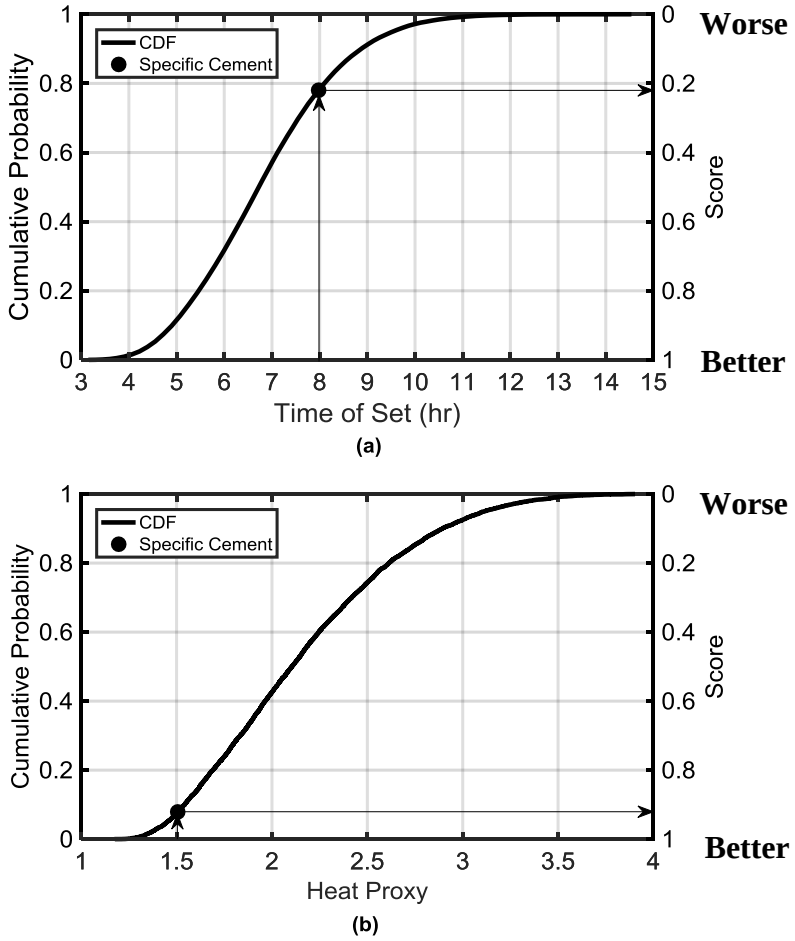

Figure 9-12. Marginal CDF with regard to time of set and heat proxy for a specific cement meeting the constraint E>20 GPa

This cement paste requires far less energy to produce but takes much longer to set that its counterparts in its unmodified form. Using the same database, it is observed this tradeoff can be overcome by lowering the w/c (Figure 9-13). As the w/c of the paste decreases from 0.35 to 0.25, the score increases from 0.22 to 0.88. Each incremental reduction in w/c results in an incremental increase in the score. The result is consistent with the expected behavior of cement paste, as a lower w/c reduces the interparticle spacing and the associated time required for hydration products to bridge particles and form a rigid matrix [154].

Multiple performance objectives are characterized simultaneously in Figure 9-14, which shows a spectrum of joint scores $S_c\,(X, Y|\,E \geq E_0)$ for all cements with the user-specified constraint. The arrow overlays on Figure 9-14 demonstrate how performance data can be applied to modify paste w/c and cement chemistry (Table 9-3) to improve performance, while adhering to the ASTM C150 chemical specifications for a Type I portland cement.

Consider Paste A, which has a relatively poor joint score of 0.3 with a time of set of 10 hours and heat proxy value of 2.63 at a w/c of 0.39. Modifying Paste A by reducing alite and increasing belite to convert it Paste B results in a significantly better joint score because of the associated reduction of the heat proxy value, with minimal changes to setting time, aluminate content, or ferrite content. The joint score is improved further by reducing the w/c of Paste B to produce Paste C, resulting in a 40% decrease in setting time.

This example, while simple, demonstrates a methodology for improving the quantitative performance of cement through small changes to chemistry and mixture design, with a significant reduction in computational expense compared to the full enumerated dataset.

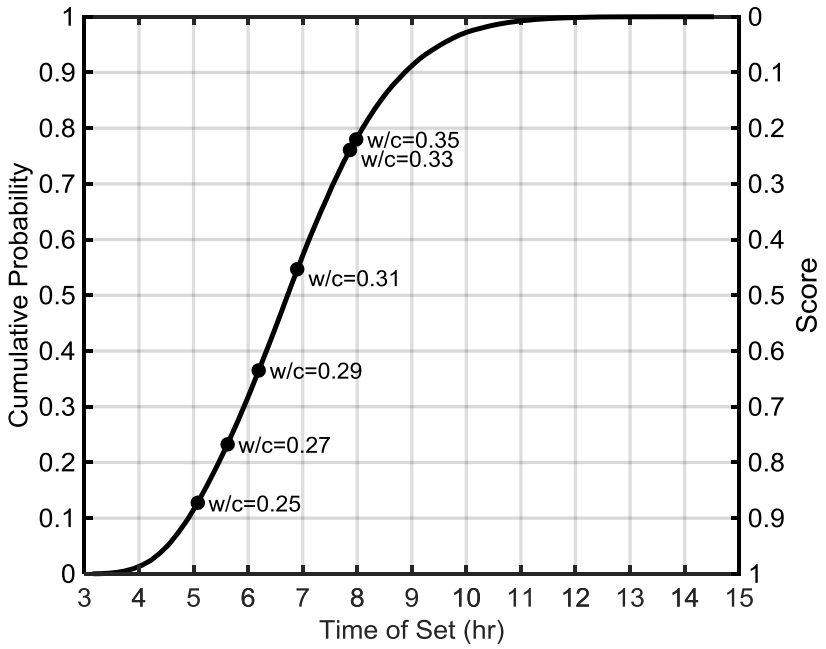

Figure 9-13. Effect of water to cement ratio on the score of the same cement chemistry used in Figure 9-129-12. As the w/c of a paste is decreased the time of set also decreases, and the resulting score increases

Table 9-3. Joint scores, compositions, and performance metrics for cements shown in Figure 9-14

Cement Paste	A		B		C
Joint Score	0.30		0.85		0.99
W/C	0.39	-	0.39	↓	0.25
Alite (%)	59.09	↓	50.05	-	50.05
Belite (%)	18.12	↑	24.67	-	24.67
Ferrite (%)	11.44	↑	12.93	-	12.93
Aluminate (%)	6.88	-	6.37	-	6.37
Gypsum (%)	0.71	↑	3.38	-	3.38
Hemihydrate (%)	0.19	↑	1.15	-	1.15
Anhydrite (%)	3.56	↓	1.46	-	1.46
Time of Set (hr)	9.74	-	10.12	↓	5.81
Heat Proxy	2.52	↓	1.52	-	1.52
Modulus (GPa)	20.90	-	20.05	↑	28.82

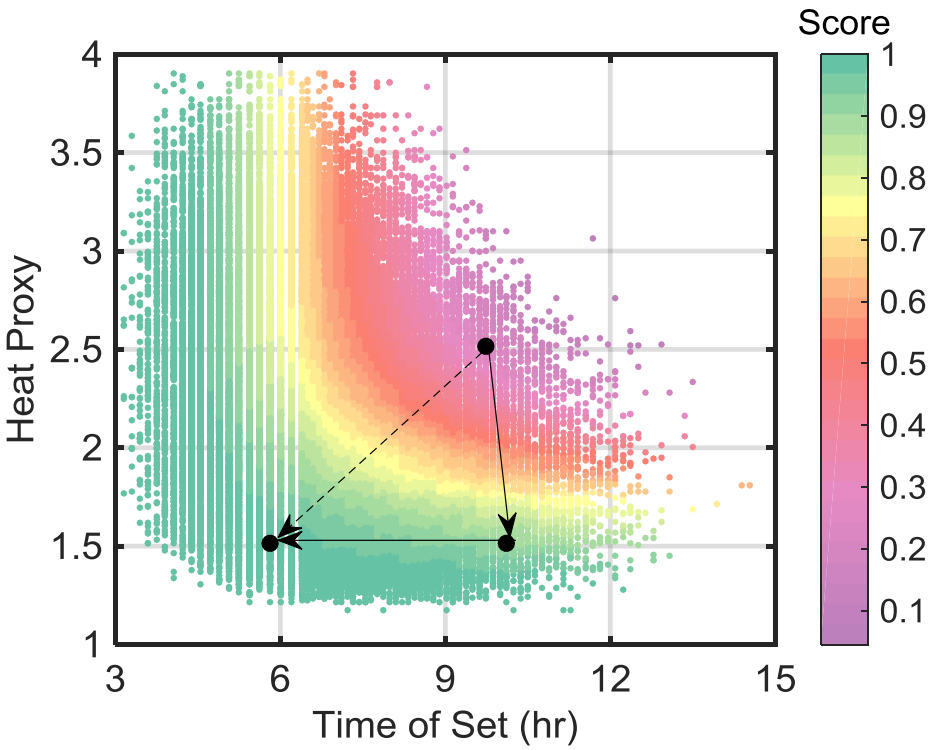

Figure 9-14. Joint scores for cement pastes meeting the constraint E>20 GPa with respect to heat proxy and time of set

9.6. Implications of Cement Optimization Tool

The PSO optimization technique used in this paper as applied to the VCCTL has some implications in practice. The technique can be applied to select and create cements based on performance criterion. The portland cement industry is moving toward the implementation and use of performance specifications [155]. It is often the case that to ensure durability cement and concrete producers specify concrete mixtures to be stronger than required, even when overdesign is specified. Concrete made with the use of performance specifications must address the needs of the industry which includes the assurance of strength, durability, economy, and sustainability. This technique allows for the rapid assessment of solutions through constraints on critical parameters, while providing relative performance values for secondary parameters of interest, which enables immediate visualization of possibilities, as well as rapid selection of solutions.

Second, this optimization technique objectively assesses different cements for any measurable performance parameter. It could be used for the exploration of new mixtures and forecast possible responses to changes in material supply or market demand without physical testing. By adaptive scoring of different criterial based on the scale of possible results, it responds to all changes in composition and physical parameter. It is developed for cement and could be directly applicable to concrete simulations.

Additionally, the optimization technique has the ability to improve performances of ordinary portland cement (OPC) systems more economically than to attempt to supplement performance with other materials. Modern Type I/II portland cements are empirically optimized for fast construction and low cost [156]. Current cement compositions require supplementary materials to improve longevity and increase sustainability [157]. Quantification of the tradeoffs between rapid strength developments, cost of production, and long-term durability for portland cement could motivate changes in production.

9.7. Conclusions

This paper presents the application of a metaheuristic algorithm applied to cement modeling using the VCCTL. Multi-objective optimizations with PSO were used to find a set of optimal solutions from a cement database created from 150,000 VCCTL simulations. Pareto fronts are explored for different problems including constrained bi-objective or non-constrained tri-objective. The non-dominated solutions provide information in terms of specified objective functions. Then by evaluating the Pareto front using the convergence test, the computational cost for optimization techniques is calculated. Compared to VCCTL blind search, metaheuristic algorithm search decreases the cost by nearly 90%. Based on the Pareto fronts, cement data provide a technique for the evaluation of cement for the purposed of optimization and design. Ultimately, this technique provides an approach to increase the efficiency of cement and concrete modeling with intelligent metaheuristic search.

10. CONCLUSIONS, OBSERVATIONS, AND RECOMMENDATIONS FOR FUTURE WORK

10.1. Background

Traditional predictive relationships between the behavior of portland cement concrete and the properties of its constituent materials are largely derived from physical, empirical testing programs. Physical testing of concrete for quality assurance or experimental research requires substantial time and labor, and empirical relationships derived from the resulting data become less precise when applied to materials not included in the original experiment. Models which simulate the hydration of portland cement aim to provide a direct link between measured material characteristics and concrete performance metrics without resource intensive testing programs. A number of models exist [1]; however, the Virtual Cement and Concrete Testing Laboratory (VCCTL) possesses the ability to predict the results of common quality control tests for cement, mortar, and concrete, making it readily applicable to real problems in concrete mixture design.

The VCCTL is capable of simulating the physical properties of cementitious materials, including early-age properties such as heat of hydration, temperature rise, and time of setting. Additionally, the model simulates the physical and mechanical properties such as compressive strength and modulus of elasticity, and values of bulk diffusion and conductivity to estimate durability. Virtual simulations of 28-day properties typically require less than two hours to complete. The VCCTL requires different input properties for the material constituents of cement paste, mortar, and concrete. Chemical and physical properties are required for cementitious binders, mechanical properties for aggregate, and the relative proportions of each determined based on the mixture design. The ability to quickly and accurately predict properties of concrete that would normally require significant labor and extended periods of time to obtain has a number of potential benefits. The cost and risk associated with development of new mixture designs would fall, incentivizing performance based mixture design. Increased confidence in the performance of concrete would allow for a reduction in overdesign, while potentially a reduction in the amount of cement required for a given mix, improving the sustainability of the mixture by minimizing the CO_2 emissions.

10.2. Research Objectives

The objectives of the research detailed in this report were diverse; however, the overall goals of the project related to investigation of the capabilities and limitations of the model with respect to practical implementation, as well as implementation of new computational techniques to improve or expand the capabilities of the VCCTL. These goals included the following specific initiatives

- Validate the VCCTL in the context of Cement and Concrete Reference Laboratory (CCRL) proficiency testing
- Investigate performance when modeling chemical and mineral admixtures
- Develop improvements for modeling chemical and mineral admixtures

- Develop applications integrating the VCCTL with high performance computing resources at UF
- Apply advanced optimization techniques to analyze the behavior of the VCCTL and select optimal cement chemistries and mixture proportions
- Investigate applications of machine learning for partial replacement of VCCTL functionality
- Investigate the applications of the VCCTL to prediction of durability parameters

10.3. Conclusions

The main conclusions of this study are summarized as follows:

- It is feasible for FDOT to use the VCCTL to participate in the CCRL proficiency sample program without performing heat of hydration testing or mortar compressive strength testing. The results of this research indicate that if this was implemented, virtual laboratory scores would exceed those of a majority of participating labs. This can be accomplished without the extensive SEM/EDS acquisition and analysis procedures proscribed by NIST, using only XRF Bogue Composition results and a cement particle size distribution obtained using LPA
- The accelerating or retarding effects of admixtures can be simulated to a limited degree with the VCCTL by calibrating the time scale of simulations using heat of hydration curves obtained from pastes incorporating those admixtures
- VCCTL predictions of properties related to durability correlate well with measured results of surface resistivity, and generally obey trends expected based on observations reported in literature
- The implementation of VCCTL in a high performance computing environment enabled comprehensive evaluation of the behavior of the model with respect to ordinary portland cements and binary mixtures through enumeration of more than 500,000 unique simulations
- Multi-objective optimization techniques developed using enumerated simulation data enable rapid determination of ideal cement chemistries when user specified constraints on elastic modulus, time of set, and CO_2 emissions are provided
- The default capabilities of the VCCTL with respect to pozzolanic materials do not accurately predict compressive strength for binary mortars; however, by implementing and training machine learning algorithms using enumerated data it is possible to predict compressive strength with high accuracy

10.4. Observations

- The VCCTL predicts initial and final set of plain portland cement paste to within an accuracy of 5 minutes when calibrated with a heat of hydration curve.
- Using a simplified set of virtual material properties, it is possible to emulate a physical laboratory using the VCCTL and retroactively participate in the CCRL proficiency sample program, while producing virtual test results that fall within the limits of acceptability specified by CCRL.

- The VCCTL is capable of virtually measuring the compressive strength for ASTM C109 mortars made with 20 different cements to within 1.5 standard deviations of the experimental values.
- The VCCTL can virtually measure the heat of hydration for a set of 20 different cements, and produce results that are within an average of two standard deviations away from the experimental mean.
- For ASTM C109 mortars, empirical predictions of compressive strength are more accurate when based on simulated heat of hydration than when based on simulated elastic modulus.
- It is not necessary to calibrate the VCCTL time/cycle^2 factor for individual cements. The results obtained in this study used the default value of 0.00035 time/cycle^2 for each of the cements used in this study.
- Generally speaking, the VCCTL qualitatively replicates commonly observed trends associated with changes in pozzolan fineness and replacement percentage
- Artificial neural networks are capable of predicting mortar compressive strength for binary pozzolans using the same inputs as the VCCTL, with a much higher degree of accuracy
-

10.5. Recommendations for future work

Based upon the findings from this study, the following recommendations are suggested:

- Implement a virtual cement proficiency testing program side by side with existing physical testing programs
- Develop Virtual Testing Specifications for virtual ASTM C109 mortar testing and virtual ASTM C1702 heat of hydration testing based on the procedures detailed in Chapter 3
- Conduct Virtual Testing in parallel with FDOT mixture qualification testing, using only X-ray Fluorescence and Laser Particle Size Analysis data for cementitious material inputs
- Conduct research program applying machine learning to performance prediction of concrete containing mineral admixtures, using FDOT database of mixtures and hardened performance
- Apply the multi-objective optimization routines developed in this project to FDOT materials, to inform the development of performance based specifications

REFERENCES

[1] J.J. Thomas, J.J. Biernacki, J.W. Bullard, S. Bishnoi, J.S. Dolado, G.W. Scherer, A. Luttge, Modeling and Simulation of Cement Hydration Kinetics and Microstructure Development, Cem. Concr. Res. 41 (2011) 1257–1278. doi:10.1016/j.cemconres.2010.10.004.

[2] S. Mindess, J. Young, Concrete. Englewood, (1981).

[3] M.S. Mamlouk, J.P. Zaniewski, Materials for civil and construction engineers, Addison-Wesley Reading, Mass, USA, 1999.

[4] B.V. Reddy, K. Jagadish, Embodied energy of common and alternative building materials and technologies, Energy Build. 35 (2003) 129–137.

[5] B.V. Reddy, G. Leuzinger, V. Sreeram, Low embodied energy cement stabilised rammed earth building—A case study, Energy Build. 68 (2014) 541–546.

[6] J.W. Bullard, C. Ferraris, E.J. Garboczi, N. Martys, P. Stutzman, Virtual cement, Chapt. 10 (2004) 1311–1331.

[7] B.E. Watts, Analysis of the Sensitivity of a Concrete Virtual Model to Different Material Input Parameters, (2013).

[8] D.P. Bentz, CEMHYD3D: A Three-Dimensional Cement Hydration and Microstructure Development Modeling Package: Version 3.0, (2005).

[9] J.W. Bullard, MicroChar: An Application for Quantitative Analysis of Cement and Clinker Microstructure Images, NIST Tech. Note. (2015).

[10] ASTM B822, Standard Test Method for Particle Size Distribution of Metal Powders and Related Compounds by Light Scattering, (2010).

[11] H. Taylor, Cement Chemistry, 2nd ed., Thomas Telford Publishing, London, 2004.

[12] ASTM C1365-06, Standard Test Method for Determination of the Proportion of Phases in Portland Cement and Portland-Cement Clinker Using X-Ray Powder Diffraction Analysis, ASTM International, West Conshohocken, PA, 2011.

[13] E.J. Garboczi, Three-dimensional mathematical analysis of particle shape using X-ray tomography and spherical harmonics: Application to aggregates used in concrete, Cem. Concr. Res. 32 (2002) 1621–1638.

[14] J.W. Bullard, E.J. Garboczi, A model investigation of the influence of particle shape on portland cement hydration, Cem. Concr. Res. 36 (2006) 1007–1015. doi:10.1016/j.cemconres.2006.01.003.

[15] M.S. Mamlouk, J.P. Zaniewski, Materials for Civil and Construction Engineers, 3 edition, Prentice Hall, Upper Saddle River, 2010.

[16] A. Neville, Properties of Concrete, 5th ed., Prentice Hall, 2011.

[17] E.J. Garboczi, D.P. Bentz, J.W. Bullard, VCCTL Source Code: Transport.c, NIST, Gaithersburg, MD, 2014.

[18] D.P. Bentz, Three-Dimensional Computer Simulation of Portland Cement Hydration and Microstructure Development, J. Am. Ceram. Soc. 80 (1997) 3–21. doi:10.1111/j.1151-2916.1997.tb02785.x.

[19] J.W. Bullard, VCCTL Version 9.5 User Guide, NIST, 2014.

[20] J.J. Thomas, J.J. Biernacki, J.W. Bullard, S. Bishnoi, J.S. Dolado, G.W. Scherer, A. Luttge, Modeling and simulation of cement hydration kinetics and microstructure

development, Cem. Concr. Res. 41 (2011) 1257–1278. doi:10.1016/j.cemconres.2010.10.004.
[21] G. Sant, M. Dehadrai, D. Bentz, P. Lura, C.F. Ferraris, J.W. Bullard, J. Weiss, Detecting the Fluid-to-Solid Transition in Cement Pastes, Concr. Int. 31 (2009) 53–58.
[22] B.E. Watts, C.C. Ferraro, Prediction of setting for admixture modified mortars using the VCCTL, Cem. Concr. Compos. 78 (2017) 63–72. doi:10.1016/j.cemconcomp.2016.11.002.
[23] E.J. Garboczi, Finite Element and Finite Difference Programs for Computing the Linear Electric and Elastic Properties of Digital Images of Random Materials, NIST, Gaithersburg, MD, 1998.
[24] E.J. Garboczi, J.W. Bullard, D.P. Bentz, VCCTL Source Code: Elastic.c, NIST, Gaithersburg, MD, 2013.
[25] E.J. Garboczi, D.P. Bentz, Digital Simulation of the Aggregate–Cement Paste Interfacial Zone in Concrete, J. Mater. Res. 6 (1991) 196–201.
[26] D.P. Bentz, E.J. Garboczi, Computer modelling of interfacial transition zone: microstructure and properties, RILEM Rep. (1999) 349–385.
[27] E.J. Garboczi, J.G. Berryman, Elastic moduli of a material containing composite inclusions: effective medium theory and finite element computations, Mech. Mater. 33 (2001) 455–470. doi:10.1016/S0167-6636(01)00067-9.
[28] J.F. Douglas, E.J. Garboczi, Intrinsic viscosity and the polarizability of particles having a wide range of shapes, Adv. Chem. Phys. 91 (1995) 85–154.
[29] K. Wang, Z. Ge, J. Grove, J.M. Ruiz, R. Rasmussen, T. Ferragut, Developing a simple and rapid test for monitoring the heat evolution of concrete mixtures for both laboratory and field applications, 2007.
[30] D.P. Bentz, C.F. Ferraris, Rheology and setting of high volume fly ash mixtures, Cem. Concr. Compos. 32 (2010) 265–270. doi:10.1016/j.cemconcomp.2010.01.008.
[31] D.P. Bentz, C.J. Haecker, X.P. Feng, P.E. Stutzman, Prediction of Cement Physical Properties by Virtual Testing, in: Fifth Int. VDZ Congr. Proc., Dusseldorf, Germany, 2002: pp. 53–63.
[32] A. Princigallo, P. Lura, K. van Breugel, G. Levita, Early development of properties in a cement paste: A numerical and experimental study, Cem. Concr. Res. 33 (2003) 1013–1020. doi:10.1016/S0008-8846(03)00002-4.
[33] D.P. Bentz, E.J. Garboczi, J.W. Bullard, C.F. Ferraris, N.S. Martys, P.E. Stutzman, Virtual Testing of Cement and Concrete, in: J. Lamond, J. Pielert (Eds.), Significance Tests Prop. Concr. Concr.-Mak. Mater., ASTM International, 100 Barr Harbor Drive, PO Box C700, West Conshohocken, PA 19428-2959, 2006. http://www.astm.org/doiLink.cgi?STP169D-EB (accessed November 18, 2015).
[34] J.W. Bullard, P.E. Stutzman, Analysis of CCRL proficiency cements 151 and 152 using the Virtual Cement and Concrete Testing Laboratory, Cem. Concr. Res. 36 (2006) 1548–1555. doi:10.1016/j.cemconres.2006.05.024.
[35] S. Mindess, F. Young, D. Darwin, Concrete, Prentice-Hall, Inc, Upper Saddle River, NJ, 2003.
[36] A. Neville, Properties of Concrete, 5th ed., Prentice Hall, San Francisco, CA, 2011.
[37] H. Taylor, Cement Chemistry, 2nd ed., Thomas Telford Publishing, London, 2004.

[38] J.W. Bullard, H.M. Jennings, R.A. Livingston, A. Nonat, G.W. Scherer, J.S. Schweitzer, K.L. Scrivener, J.J. Thomas, Mechanisms of cement hydration, Cem. Concr. Res. 41 (2011) 1208–1223. doi:10.1016/j.cemconres.2010.09.011.
[39] P. Hewlett, Lea's Chemistry of Cement and Concrete, 4th ed., Elsevier Ltd, 2006.
[40] J. Cheung, A. Jeknavorian, L. Roberts, D. Silva, Impact of admixtures on the hydration kinetics of Portland cement, Cem. Concr. Res. 41 (2011) 1289–1309. doi:10.1016/j.cemconres.2011.03.005.
[41] V.K. Peterson, M.C.G. Juenger, Time-resolved quasielastic neutron scattering study of the hydration of tricalcium silicate: Effects of CaCl2 and sucrose, Phys. B Condens. Matter. 385–386, Part 1 (2006) 222–224. doi:10.1016/j.physb.2006.05.194.
[42] ASTM C494, Standard Specification for Chemical Admixtures for Concrete, ASTM International, West Conshohocken, PA, 2014. http://www.astm.org/Standards/C494.htm (accessed August 23, 2014).
[43] ASTM C1582, Standard Specification for Admixtures to Inhibit Chloride-Induced Corrosion of Reinforcing Steel in Concrete, ASTM International, West Conshohocken, PA, 2011. http://www.astm.org/Standards/C1582.htm (accessed August 23, 2014).
[44] ASTM C191, Standard Test Methods for Time of Setting of Hydraulic Cement by Vicat Needle, ASTM International, West Conshohocken, PA, 2013.
[45] R.G. Burg, The Influence of Casting and Curing Temperature on the Properties of Fresh and Hardened Concrete, Portland Cement Association, Skokie, IL, 1996.
[46] S.H. Kosmatka, M.L. Wilson, Design and Control of Concrete Mixtures, Portland Cement Association, Skokie, IL, 2015.
[47] K. De Weerdt, Combining Plasticizers/Retarders and Accelerators, Katholieke Universiteit Leuven, 2006.
[48] P. Sandberg, C. Porteneuve, F. Serafin, J. Boomer, N. LoConte, V. Gupta, B. Dragovic, F. Doncaster, L. Alioto, T. Vogt, Effect of Admixture on Cement Hydration Kinetics by Synchrotron XRD and Isothermal Calorimetry, in: Int. Congr. Chem. Cem., 2008.
[49] S.A. Farrington, Evaluating the Effect of Mixing Method on Cement Hydration in the Prescence of a Polycarboxylate High-Range Water Reducing Admixture by Isothermal Calorimetry, in: Proc. Twelfth Int. Congr. Chem. Cem., Montreal, Canada, 2007.
[50] D.P. Bentz, X.P. Feng, C.J. Haecker, P.E. Stutzman, Analysis of CCRL Proficiency Cements 135 and 136 Using CEMHYD3D, NIST, Gaithersburg, MD, 2000.
[51] W.J. Youden, Statistical Aspects of the Cement Testing Program, Proc. Am. Soc. Test. Matierals. 59 (1959) 1120–1128.
[52] J.R. Crandall, R.L. Blaine, Statistical Evaluation of Interlaboratory Cement Tests, Proc. Am. Soc. Test. Mater. 59 (1959) 1129.
[53] M. Balonis, F.P. Glasser, The density of cement phases, Cem. Concr. Res. 39 (2009) 733–739. doi:10.1016/j.cemconres.2009.06.005.
[54] D.P. Bentz, P.E. Stutzman, SEM Analysis and Computer Modeling of Hydration of Portland Cement Particles, in: S.M. Dehayes, D. Stark (Eds.), Petrogr. Cem. Mater., American Society for Testing and Materials, 1994: pp. 60–73.
[55] D.P. Bentz, P.E. Stutzman, C.J. Haecker, S. Remond, SEM/X-ray Imaging of Cement-Based Materials, in: Proc. 7th Euroseminar Microsc. Appl. Build. Mater., Delft University of Technology, 1999.

[56] T.C. Powers, T.L. Brownyard, Studies of the PHysical Properties of Hardened Portland Cement Paste, J. Am. Concr. Inst. 18 (1947) 845–880.
[57] D.P. Bentz, J.T. Conway, Computer modeling of the replacement of ``coarse'' cement particles by inert fillers in low w/c ratio concretes Hydration and strength, Cem. Concr. Res. 31 (2001) 503–506. doi:10.1016/S0008-8846(01)00456-2.
[58] Y. Kosaka, Y. Tanigawa, M. Kawakami, Effect of coarse aggregate on fracture of concrete (part 1), J. AIJ. 228 (1975) 1–11.
[59] L. Valentini, M. Parisatto, V. Russo, G. Ferrari, J.W. Bullard, R.J. Angel, M.C. Dalconi, G. Artioli, Simulation of the hydration kinetics and elastic moduli of cement mortars by microstructural modelling, Cem. Concr. Compos. 52 (2014) 54–63. doi:10.1016/j.cemconcomp.2014.05.005.
[60] D.P. Bentz, T. Barrett, I.D. la Varga, W.J. Weiss, Relating Compressive Strength to Heat Release in Mortars, Adv. Civ. Eng. Mater. 1 (2012) 1–14. doi:10.1520/acem20120002.
[61] G. Sant, P. Lura, J. Weiss, Measurement of volume change in cementitious materials at early ages: review of testing protocols and interpretation of results, Transp. Res. Rec. J. Transp. Res. Board. (2006) 21–29.
[62] D.P. Bentz, Three-Dimensional Computer Simulation of Portland Cement Hydration and Microstructure Development, J. Am. Ceram. Soc. 80 (1997) 3–21. doi:10.1111/j.1151-2916.1997.tb02785.x.
[63] B.E. Watts, C.C. Ferraro, Prediction of setting for admixture modified mortars using the VCCTL, Cem. Concr. Compos. (2016).
[64] D.P. Bentz, CEMHYD3D: A Three-Dimensional Cement Hydration and Microstructure Development Modeling Package: Version 3.0, (2005).
[65] R.D. Hooton, M.D. Thomas, Pore Solution Analysis as a Tool for Studying Early–Age Hydration & Predicting Future Durability, Cem. Hydration Summit. (2009).
[66] J.W. Bullard, P.E. Stutzman, Analysis of CCRL proficiency cements 151 and 152 using the Virtual Cement and Concrete Testing Laboratory, Cem. Concr. Res. 36 (2006) 1548–1555. doi:10.1016/j.cemconres.2006.05.024.
[67] C.C. Ferraro, J.M. Paris, T.G. Townsend, M. Tia, Evaluation of Alternative Pozzolanic Materials for Partial Replacement of Portland Cement in Concrete, (2016).
[68] D.P. Bentz, S. Remond, Incorporation of fly ash into a 3-D cement hydration microstructure model, US Department of Commerce, Technology Administration, National Institute of Standards and Technology, 1997.
[69] D.P. Bentz, Calculation of slag characteristics, (https://ciks.cbt.nist.gov/~bentz/slagcalc.html (accessed March 15, 2017).
[70] D.P. Bentz, CEMHYD3D: A Three-Dimensional Cement Hydration and Microstructure Development Modeling Package: Version 3.0, (2005).
[71] F. Zhu, M. Takaoka, K. Shiota, K. Oshita, Y. Kitajima, Chloride chemical form in various types of fly ash, Environ. Sci. Technol. 42 (2008) 3932–3937.
[72] J.E. Renew, K.M. Ellison, K. Hendershot, J. Rajterowski, C.-H. Huang, Impact of Salt on Metal Leaching from Coal Fly Ash, in: Nashville, TN, 2015.
[73] J.M. Paris, J.G. Roessler, C.C. Ferraro, H.D. DeFord, T.G. Townsend, A review of waste products utilized as supplements to Portland cement in concrete, J. Clean. Prod. 121 (2016) 1–18.

[74] R. Walker, S. Pavía, Physical properties and reactivity of pozzolans, and their influence on the properties of lime–pozzolan pastes, Mater. Struct. 44 (2011) 1139–1150. doi:10.1617/s11527-010-9689-2.
[75] R. Siddique, M.I. Khan, Supplementary Cementing Materials, Springer, 2011.
[76] N.M. Al-Akhras, Durability of metakaolin concrete to sulfate attack, Cem. Concr. Res. 36 (2006) 1727–1734. doi:10.1016/j.cemconres.2006.03.026.
[77] P.J.P. Gleize, M. Cyr, G. Escadeillas, Effects of metakaolin on autogenous shrinkage of cement pastes, Cem. Concr. Compos. 29 (2007) 80–87. doi:10.1016/j.cemconcomp.2006.09.005.
[78] B.B. Sabir, S. Wild, J. Bai, Metakaolin and calcined clays as pozzolans for concrete: a review, Cem. Concr. Compos. 23 (2001) 441–454. doi:10.1016/S0958-9465(00)00092-5.
[79] R. Siddique, M.I. Khan, Supplementary Cementing Materials, Springer, 2011.
[80] V.M. Malhotra, P.K. Mehta, Pozzolanic and Cementitious Materials, Taylor & Francis, 1996.
[81] S. Diamond, S. Sahu, Densified silica fume: particle sizes and dispersion in concrete, Mater. Struct. 39 (2006) 849–859. doi:10.1617/s11527-006-9087-y.
[82] ASTM C109/109M, Standard Test Method for Compressive Strength of Hydraulic Cement Mortars (Using 2-in. or [50-mm] Cube Specimens), ASTM International, West Conshohocken, PA, 2013. http://enterprise.astm.org/filtrexx40.cgi?+REDLINE_PAGES/C109C109M.htm#_ga=1.170198176.1262400023.1389650879 (accessed August 23, 2014).
[83] E.J. Garboczi, D.P. Bentz, J.W. Bullard, Elastic.c, National Institute of Standards and Technology, 2014.
[84] R. Siddique, M.I. Khan, Supplementary Cementing Materials, Springer, 2011.
[85] P. Flach, Machine learning: the art and science of algorithms that make sense of data, Cambridge University Press, 2012.
[86] Y. Wu, M. Schuster, Z. Chen, Q.V. Le, M. Norouzi, W. Macherey, M. Krikun, Y. Cao, Q. Gao, K. Macherey, J. Klingner, A. Shah, M. Johnson, X. Liu, Ł. Kaiser, S. Gouws, Y. Kato, T. Kudo, H. Kazawa, K. Stevens, G. Kurian, N. Patil, W. Wang, C. Young, J. Smith, J. Riesa, A. Rudnick, O. Vinyals, G. Corrado, M. Hughes, J. Dean, Google's Neural Machine Translation System: Bridging the Gap between Human and Machine Translation, ArXiv160908144 Cs. (2016). http://arxiv.org/abs/1609.08144 (accessed January 24, 2017).
[87] J. Mao, W. Xu, Y. Yang, J. Wang, Z. Huang, A. Yuille, Deep captioning with multimodal recurrent neural networks (m-rnn), ArXiv Prepr. ArXiv14126632. (2014).
[88] W. Zaremba, I. Sutskever, Learning to Execute, ArXiv14104615 Cs. (2014). http://arxiv.org/abs/1410.4615 (accessed January 24, 2017).
[89] M.H. Hassoun, Fundamentals of artificial neural networks, MIT press, 1995.
[90] Z.C. Lipton, J. Berkowitz, C. Elkan, A critical review of recurrent neural networks for sequence learning, ArXiv Prepr. ArXiv150600019. (2015).
[91] D.E. Rumelhart, G.E. Hinton, R.J. Williams, Learning representations by back-propagating errors, Nature. 323 (1986) 533–536.
[92] H.T. Siegelmann, E.D. Sontag, Turing computability with neural nets, Appl. Math. Lett. 4 (1991) 77–80.

[93] A.M. Turing, On computable numbers, with an application to the Entscheidungsproblem, Proc. Lond. Math. Soc. 2 (1937) 230–265.
[94] S. Hochreiter, J. Schmidhuber, Long short-term memory, Neural Comput. 9 (1997) 1735–1780.
[95] A. Graves, Supervised sequence labelling, in: Supervised Seq. Label. Recurr. Neural Netw., Springer, 2012: pp. 5–13.
[96] R. Caruana, S. Lawrence, C.L. Giles, Overfitting in neural nets: Backpropagation, conjugate gradient, and early stopping, in: Adv. Neural Inf. Process. Syst., 2001: pp. 402–408.
[97] ASTM C109/109M, Standard Test Method for Compressive Strength of Hydraulic Cement Mortars (Using 2-in. or [50-mm] Cube Specimens), ASTM International, West Conshohocken, PA, 2013. http://enterprise.astm.org/filtrexx40.cgi?+REDLINE_PAGES/C109C109M.htm#_ga=1.170198176.1262400023.1389650879 (accessed August 23, 2014).
[98] A.A. Rusu, M. Vecerik, T. Rothörl, N. Heess, R. Pascanu, R. Hadsell, Sim-to-Real Robot Learning from Pixels with Progressive Nets, ArXiv161004286 Cs. (2016). http://arxiv.org/abs/1610.04286 (accessed May 7, 2017).
[99] Z. Tang, D. Wang, Z. Zhang, Recurrent Neural Network Training with Dark Knowledge Transfer, ArXiv150504630 Cs Stat. (2016) 5900–5904. doi:10.1109/ICASSP.2016.7472809.
[100] S. Shin, K. Hwang, W. Sung, Generative Knowledge Transfer for Neural Language Models, ArXiv160804077 Cs. (2016). http://arxiv.org/abs/1608.04077 (accessed May 7, 2017).
[101] ASTM C1202, Standard Test Method for Electrical Indication of Concretes Ability to Resist Chloride Ion Penetration, ASTM International, West Conshohocken, PA, 2012. http://www.astm.org/Standards/C1202.htm (accessed August 23, 2014).
[102] ASTM C1760, Standard Test Method for Bulk Electrical Conductivity of Hardened Concrete, West Conshohocken, PA, 2012.
[103] ASTM C1556, Standard Test Method for Determining the Apparent Chloride Diffusion Coefficient of Cementitious Mixtures by Bulk Diffusion, West Conshohocken, PA, 2016.
[104] ASTM C1543, Standard Test Method for Determining the Penetration of Chloride Ion into Concrete by Ponding, West Conshohocken, PA, 2012.
[105] G.E. Archie, The Electrical Resistivity Log as an Aid in Determining Some Reservoir Characteristics, Trans. AIME. 146 (1942) 54–62. doi:10.2118/942054-G.
[106] K.A. Snyder, The relationship between the formation factor and the diffusion coefficient of porous materials saturated with concentrated electrolytes: theoretical and experimental considerations, Concr. Sci. Eng. 3 (2001) 216–224.
[107] J.W. Bullard, D.P. Bentz, VCCTL Source Code: Disrealnew.c, NIST, Gaithersburg, MD, 2014.
[108] E.J. Garboczi, D.P. Bentz, Computer simulation of the diffusivity of cement-based materials, J. Mater. Sci. 27 (1992) 2083–2092. doi:10.1007/BF01117921.
[109] T. AASHTO, 95-11 “Standard Method of Test for Surface Resistivity Indication of Concrete’s Ability to Resist Chloride Ion Penetration.,” AASHTO Provisional Stand. 2011 Ed. (2011).

[110] R.P. Spragg, J. Castro, T. Nantung, M. Paredes, J. Weiss, Variability analysis of the bulk resistivity measured using concrete cylinders, Adv. Civ. Eng. Mater. 1 (2012) 1–17.
[111] O. Tan, A.S. Zaimoglu, S. Hinislioglu, S. Altun, Taguchi approach for optimization of the bleeding on cement-based grouts, Tunn. Undergr. Space Technol. 20 (2005) 167–173.
[112] M. Simon, K. Snyder, G. Frohnsdorff, Advances in concrete mixture optimization, in: 1999: pp. 21–32.
[113] E.S. Lagergren, K.A. Snyder, M.J. Simon, Concrete Mixture Optimization Using Statistical Mixture Design Methods, (1997).
[114] M. Simon, Concrete mixture optimization using statistical methods: final report, US Department of Transportation, Federal Highway Administration, Research, Development and Technology, Turner-Fairbank Highway Research Center, 2003.
[115] S. Ahmad, S.A. Alghamdi, A statistical approach to optimizing concrete mixture design, Sci. World J. 2014 (2014).
[116] K. Soudki, E. El-Salakawy, N. Elkum, Full factorial optimization of concrete mix design for hot climates, J. Mater. Civ. Eng. 13 (2001) 427–433.
[117] A. Ghezal, K.H. Khayat, Optimizing self-consolidating concrete with limestone filler by using statistical factorial design methods, ACI Mater. J. 99 (2002) 264–272.
[118] R. Patel, K. Hossain, M. Shehata, N. Bouzoubaa, M. Lachemi, Development of statistical models for mixture design of high-volume fly ash self-consolidating concrete, Mater. J. 101 (2004) 294–302.
[119] M. Muthukumar, D. Mohan, Optimization of mechanical properties of polymer concrete and mix design recommendation based on design of experiments, J. Appl. Polym. Sci. 94 (2004) 1107–1116.
[120] L. Xiaoyong, M. Wendi, Optimization for mix design of high-performance concrete using orthogonal test, Innov. Comput. Inf. (2011) 364–372.
[121] M. Sonebi, M. Bassuoni, Investigating the effect of mixture design parameters on pervious concrete by statistical modelling, Constr. Build. Mater. 38 (2013) 147–154.
[122] I.H. Osman, G. Laporte, Metaheuristics: A bibliography, (1996).
[123] N. Collins, R. Eglese, B. Golden, Simulated annealing–an annotated bibliography, Am. J. Math. Manag. Sci. 8 (1988) 209–307.
[124] B. Jaumard, P.S. OW, B. Simeone, A selected artificial intelligence bibliography for operations researchers, Ann. Oper. Res. 12 (1988) 1–50.
[125] J.P. Kelly, I.H. Osman, Meta-Heuristics: Theory and Applications, (1996).
[126] V. Nissen, Evolutionary algorithms in management science: An overview and list of references, European Study Group for Evolutionary Economics, 1993.
[127] I.H. Osman, An introduction to meta-heuristics, Oper. Res. Tutor. Pap. (1995) 92–122.
[128] M. Pirlot, General local search heuristics in combinatorial optimization: a tutorial, Belg. J. Oper. Res. Stat. Comput. Sci. 32 (1992) 7–69.
[129] V.J. Rayward-Smith, C. Osman, C.R. Reeves, G.D. Smith, Modern heuristic search methods, John Wiley, 1996.
[130] B.S. Stewart, C.-F. Liaw, C.C. White, A bibliography of heuristic search research through 1992, IEEE Trans. Syst. Man Cybern. 24 (1994) 268–293.
[131] Y. Shi, Particle swarm optimization: developments, applications and resources, in: IEEE, 2001: pp. 81–86.

[132] L. Li, Z. Huang, F. Liu, Q. Wu, A heuristic particle swarm optimizer for optimization of pin connected structures, Comput. Struct. 85 (2007) 340–349.
[133] L. Li, Z. Huang, F. Liu, A heuristic particle swarm optimization method for truss structures with discrete variables, Comput. Struct. 87 (2009) 435–443.
[134] X. Hu, R.C. Eberhart, Y. Shi, Engineering optimization with particle swarm, in: IEEE, 2003: pp. 53–57.
[135] D.E. Goldberg, M.P. Samtani, Engineering optimization via genetic algorithm, in: ASCE, 1986: pp. 471–482.
[136] S. Rajeev, C. Krishnamoorthy, Discrete optimization of structures using genetic algorithms, J. Struct. Eng. 118 (1992) 1233–1250.
[137] S.-J. Wu, P.-T. Chow, Steady-state genetic algorithms for discrete optimization of trusses, Comput. Struct. 56 (1995) 979–991.
[138] Z.W. Geem, J.H. Kim, G. Loganathan, A new heuristic optimization algorithm: harmony search, Simulation. 76 (2001) 60–68.
[139] E.H. Aarts, J.H. Korst, Simulated annealing, ISSUES. 1 (1988) 16.
[140] S. Kirkpatrick, Optimization by simulated annealing: Quantitative studies, J. Stat. Phys. 34 (1984) 975–986.
[141] F. Glover, M. Laguna, Tabu Search∗, Springer, 2013.
[142] J. F. Bonnans, J.C. Gilbert, C. Lemaréchal, C.A. Sagastizábal, Numerical optimization: theoretical and practical aspects, Springer Science & Business Media, 2006.
[143] W.H. Press, S.A. Teukolsky, W.T. Vetterling, B.P. Flannery, Numerical recipes: the art of scientific computing, (2007).
[144] R. Eberhart, J. Kennedy, A new optimizer using particle swarm theory, in: IEEE, 1995: pp. 39–43.
[145] C. Grosan, A. Abraham, M. Chis, Swarm intelligence in data mining, Swarm Intell. Data Min. (2006) 1–20.
[146] E.K. Burke, G. Kendall, Search methodologies, Springer, 2005.
[147] G. Li, T. Goel, N. Stander, Assessing the convergence properties of NSGA-II for direct crashworthiness optimization, in: 2008.
[148] L. Martí, J. García, A. Berlanga, J.M. Molina, A cumulative evidential stopping criterion for multiobjective optimization evolutionary algorithms, in: ACM, 2007: pp. 2835–2842.
[149] O. Roudenko, M. Schoenauer, A steady performance stopping criterion for Pareto-based evolutionary algorithms, (2004).
[150] H. Trautmann, U. Ligges, J. Mehnen, M. Preuss, A convergence criterion for multiobjective evolutionary algorithms based on systematic statistical testing, in: Springer, 2008: pp. 825–836.
[151] T. Goel, N. Stander, A Study of the Convergence Characteristics of Multiobjective Evolutionary Algorithms, in: 2010: p. 9233.
[152] J.T. Alander, On optimal population size of genetic algorithms, in: IEEE, 1992: pp. 65–70.
[153] F. Scholz, Maximum likelihood estimation, Encycl. Stat. Sci. (1985).
[154] A.M. Neville, Properties of concrete, 1995.
[155] J.A. Bickley, R.D. Hooton, K.C. Hover, Performance specifications for durable concrete, Concr. Int. 28 (2006) 51–57.
[156] M. Shetty, Concrete technology, publisher not identified, 2005.

[157] J.S. Damtoft, J. Lukasik, D. Herfort, D. Sorrentino, E.M. Gartner, Sustainable development and climate change initiatives, Cem. Concr. Res. 38 (2008) 115–127.
[158] B.E. Watts, C. Ferraro, A. Snyder, H.D. Deford, Automated and Manual Characterization of Input Parameters for the VCCTL, (2013).
[159] E.J. Garboczi, D.P. Bentz, Virtual Testing of Cement and Concrete−USA 2004, Concr. Int. 26 (2004) 33–37.
[160] David H. Campbell, Microscopical Examination and Interpretation of Portland Cement and Clinker, (1986).
[161] F. Hofmanner, Microstructure of Portland Cement Clinker, Holderbank Management & Consulting, 1973.
[162] P. Mehta, P. Stutzman, Cement Clinker Characterization by Scanning Electron Microscopy, Cem. Concr. Aggreg. 13 (1991) 109. doi:10.1520/CCA10126J.
[163] D.P. Bentz, Three-Dimensional Computer Simulation of Portland Cement Hydration and Microstructure Development, J. Am. Ceram. Soc. 80 (1997) 3–21. doi:10.1111/j.1151-2916.1997.tb02785.x.
[164] Lee, J. S., Digital image smoothing and the sigma filter, Comput. Visiont Graph. Image Process. 24 (1983) 255–269.
[165] P. Stutzman, J.R. Clifton, Sample Preparation for Scanning Electron Micrsocopy, in: Proc. Twenty-First Int. Conf. Cem. Micrsocopy, Las Vegas, Nevada, 1999: pp. 10–22.

A. APPENDIX A: VALIDATION OF AN AUTOMATED SCANNING ELECTRON MICROSCOPY (SEM) TECHNIQUE FOR THE CHARACTERIZATION OF CEMENTS

Abstract

The computer modeling of hydration of portland cement-based materials using the virtual cement and concrete testing laboratory (VCCTL) requires detailed characterization of the cement of interest, a process that involves a combination of backscatter Scanning Electron Microscopy (SEM) and Energy Dispersive X-Ray spectroscopy (EDX). The data obtained via these methods are merged to produce a segmented phase map from which phase specific volume and surface area fractions are measured. Typically, one dozen image fields are acquired to obtain representative measurements for an individual cement. The use of a thermal emission, manually controlled scanning electron microscope to implement this process is time intensive, and the manual combination of backscatter images and EDX elemental maps is laborious and can be imprecise. An automated method to characterize cements based on these procedures has been developed, using a computer controlled SEM (CCSEM) in conjunction with automated image segmentation routines. The robustness of this automated method has already been demonstrated [158], but a direct comparison to the original method using standard reference materials has yet to be performed. This paper presents an evaluation of the accuracy and repeatability of the automated method compared to the original manual method using a standardized reference cement, combined with analysis of the same image fields on the same sample using the two techniques.

Introduction

Quantitative characterization of portland cement using microscopy can yield compositional information beyond what can be obtained via bulk techniques such as X-Ray Diffraction (XRD) or X-Ray fluorescence (XRF) [159]. Certain parameters, such as the relative surface area fractions of the different phases present in ground cement, can only be obtained through quantitative scanning electron microanalysis of polished sections of the cement particles themselves. The surface area fractions along with the volume fractions of the constituent cement phases are useful as inputs for behavioral hydration models such as the VCCTL. Proper acquisition and analysis using traditional methods requires substantial expertise and labor. Techniques have been developed to apply automation to the acquisition and quantitative analysis in the interests of reducing the time and expertise required, and producing more consistent analysis results.

Background

The techniques used to perform compositional analysis of cement through scanning electron microscopy are adapted from those used for petrographic analysis, specifically the staining of polished clinker sections to distinguish phases and the point counting procedure used to quantify their relative abundance [160][161]. The application of scanning electron microscopy and energy dispersive x-ray spectroscopy (EDS) combined with computer-based image analysis [162] to clinker quantification replaced manual point counting and allowed for the quantification of characteristics beyond phase volume fractions. Parameters such as the specific surface area fraction for cement phases have been incorporated into behavioral hydration models such as CemHyd3D [163].

The fundamental technique for the measurement surface area fractions for cement phases relies on two different imaging modes of a scanning electron microscope (SEM). Backscattered electron (BSE) imaging, in which contrast is a result of the differences in average atomic number (z-contrast), is used to distinguish the four primary cement phases due to their differing compositions. Typically ferrite (C_4AF) is the brightest phase due to the presence of iron, followed by alite (C_3S), and the slightly darker belite (C_2S) and the aluminate (C_3A) phase. The differences in grey level are subtle; typically additional information is required to distinguish cement phases for use in computerized analysis.

EDS provides the additional information necessary to properly distinguish the different phases present. Elemental maps showing relative concentrations can be obtained due to the characteristic x-rays produced by beam-specimen interactions. The energy of the x-ray photons emitted determines the element present, and the number of photons detected determines the relative brightness at each location in the map. Maps are typically collected for calcium, silicon, aluminum, iron, and sulfur; maps for potassium and sodium may also be collected if the alkali sulfate phases are to be measured in addition to the major cement phases.

Image segmentation techniques

Image segmentation is a process that combines the information obtained from the backscattered and x-ray image fields into a single false color image. Each phase within the image is represented by a specific color, enabling the total area and perimeter of each phase to be measured. The transition from area and perimeter measurement to volume and surface area values relies on the fundamental assumption that the cement particles being measured do not exhibit preferential orientation [31]. This paper details two independent methods for the combination of images from backscattered and elemental SEM, one of which is based on a manual procedure developed at NIST (National Institute of Standards and Technology) [34], and a new automated procedure [158].

Manual segmentation

The manual image segmentation process begins with the raw backscatter and elemental image maps acquired using the SEM. The backscattered image and elemental maps are first converted to 8-bit greyscale images. The brightness and contrast of each image is then adjusted to maximize contrast without removing any of the brightest or darkest portions of the image.

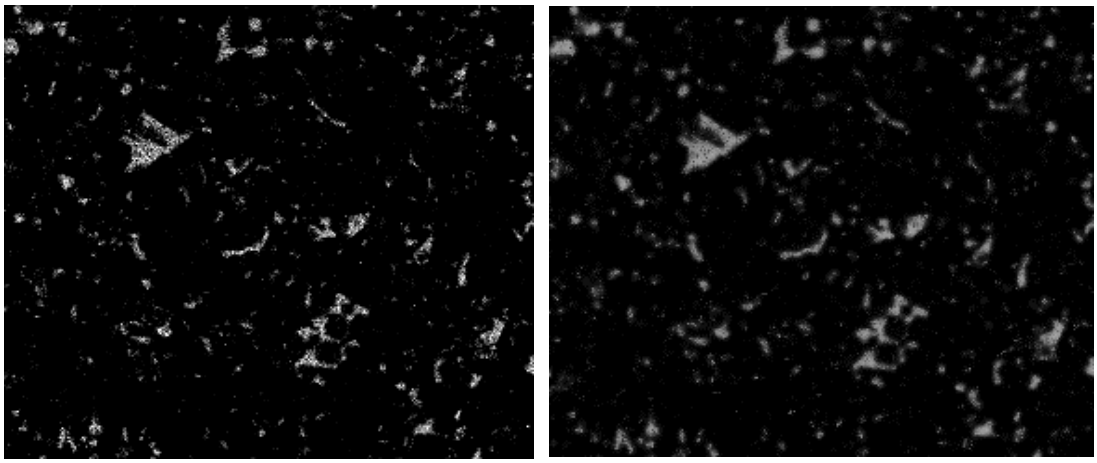

Figure A-1. Elemental Map before and after application of sigma filter.

A sigma filter [164], which operates by averaging the values of the surrounding pixels within a user-specified range is then applied (Figure A-1). The advantage of this type of filter is that it reduces noise without blurring particle edges. The brightness and contrast of the image is then optimized for a second time to maximize contrast between the bright particles and dark background. The images are then brought into a multispectral analysis program known as Multispec to perform the actual segmentation.

Multispec is a general purpose research tool developed by Purdue University for the purpose of processing and analyzing multispectral and hyperspectral image data. For the purposes of this research, Multispec was used to combine the x-ray images for calcium, silicon, iron, aluminum, potassium and sulfur into a single, 6-channel multispectral image. The user can

then select any combination of three of the six image channels to tint red, green, and blue. When the elemental maps are tinted red, green or blue and overlaid, the different brightness levels in each image combine to form distinct shades, allowing phases to be distinguished. The assignment of the calcium map to the blue channel, silicon to green, and aluminum to red enables the alite and belite phases to be identified (Figure A-2).

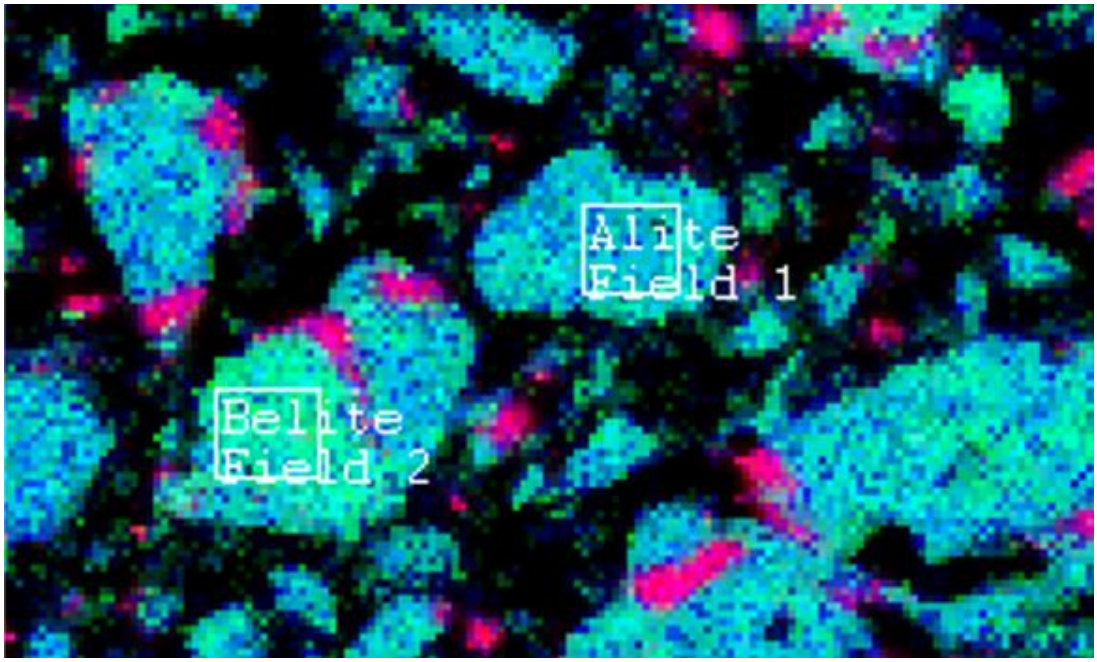

Figure A-2. Calcium, silicon, and aluminum assigned to blue, green and red channels.

Because of the different ratios of calcium to silicon in alite and belite, alite shows up as a darker/blue-green, while belite appears as lighter/greener phase. The user identifies known regions of the image as training fields, which are intended to be representative of a specific phase. These training fields provide information to Multispec on the selected that allows for the segmentation of the image into distinct phases at a later stage.

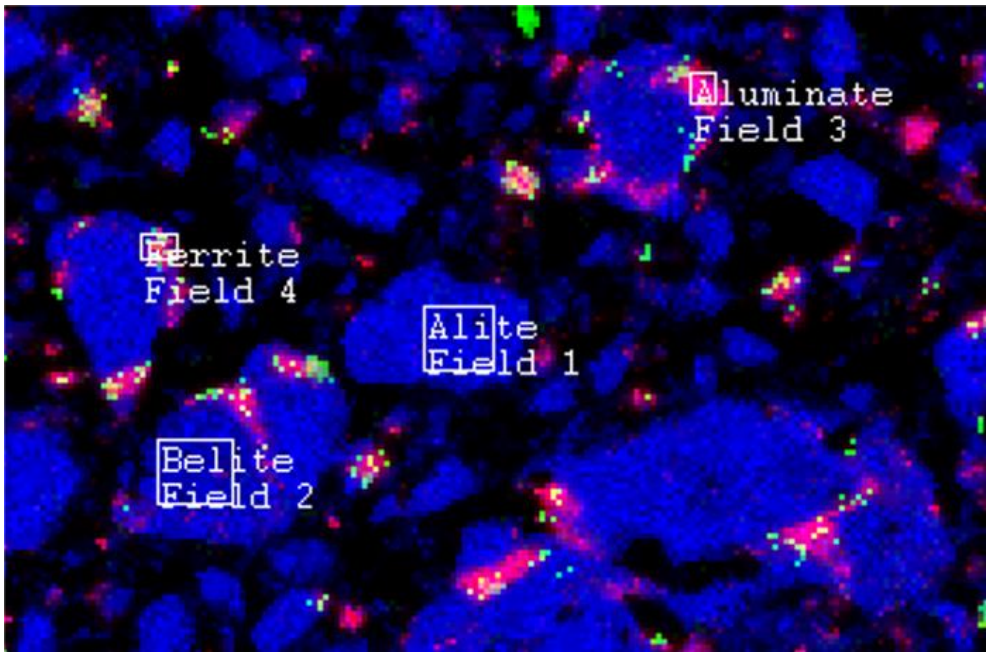

Figure A-3. Calcium, iron, and aluminum assigned to blue, green and red channels

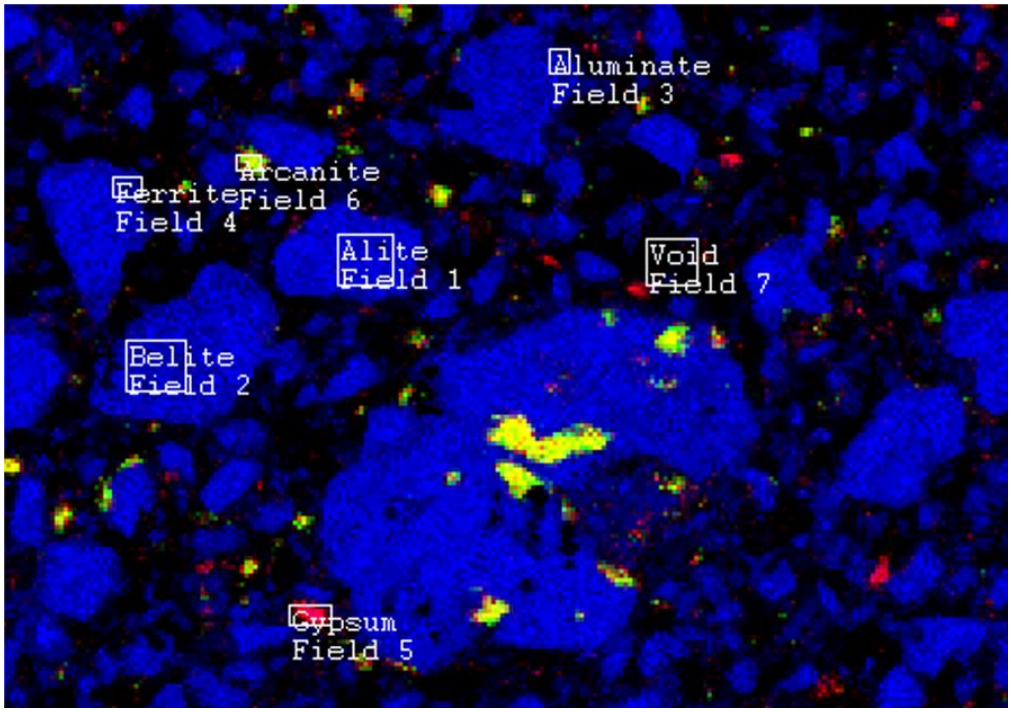

Figure A-4. Calcium, potassium and sulfur assigned to blue, green and red channels.

The aluminate and ferrite phases are identified by substituting iron for silicon in the green channel. The ferrite and aluminate phases then show up as either a yellow-pink phase or a purple phase respectively (Figure A-3). As before, training fields are selected based on user identified areas of known composition. While the training fields used for alite and belite still appear in images that no longer distinguish those phases, the specific maps that are associated with the

training fields are retained; the maps used when training fields are selected are the maps used to classify those phases, regardless of the current image. The final combination of maps enables the distinction of the Arcanite (K_2SO_4) alkali sulfate phase and gypsum by assigning those phases to red and green respectively (Figure A-4).

Typically, several training fields are selected for each identified phase as well as the void phase, to provide a robust representation of the pixel colors associated with each. The regions defined within each of these training fields are used to segment the image into the defined phases using a minimum Euclidian distance algorithm. In the resulting segmented image (Figure A-5) each phase is assigned a specific color: alite is brown, belite is blue, aluminate is grey, ferrite is white, gypsum is yellow, and arcanite is red. The resulting image frequently contains significant fine-grained noise, particularly between the alite and belite phases. To rectify this, a thresholded blur filter is applied (Figure A-6), which operates by comparing the value of a specific pixel to all the pixels within a user defined radius. This filter results in the removal of fine noise without distorting or blurring the boundaries between different regions. This step is critical, as the perimeter of each phase is measured by counting the number of edges for a particular phase that are adjacent to the void phase. Fine-grained, single pixel noise has an artificially high number of void-adjacent edges which can skew the resulting measurement.

This technique is referred to as “manual” in spite of the use of several tools to perform the analysis due to the large number of steps involved and the presence of several operations which require user experience to perform correctly. With practice, the entire process of processing raw x-ray maps into a segmented image can executed in less than 30 minutes.

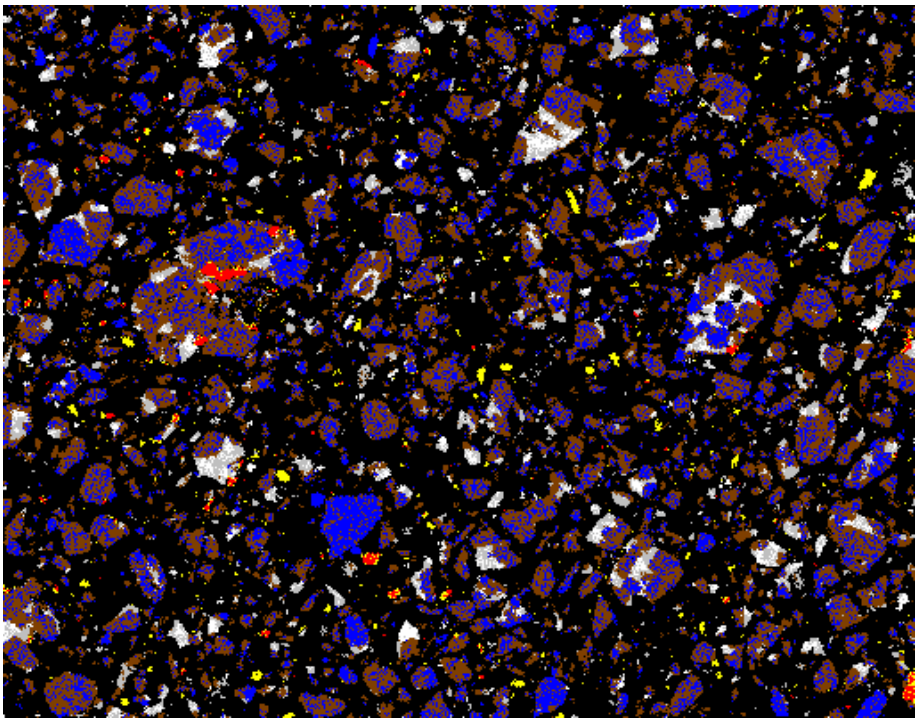

Figure A-5. Segmented image from Multispec.

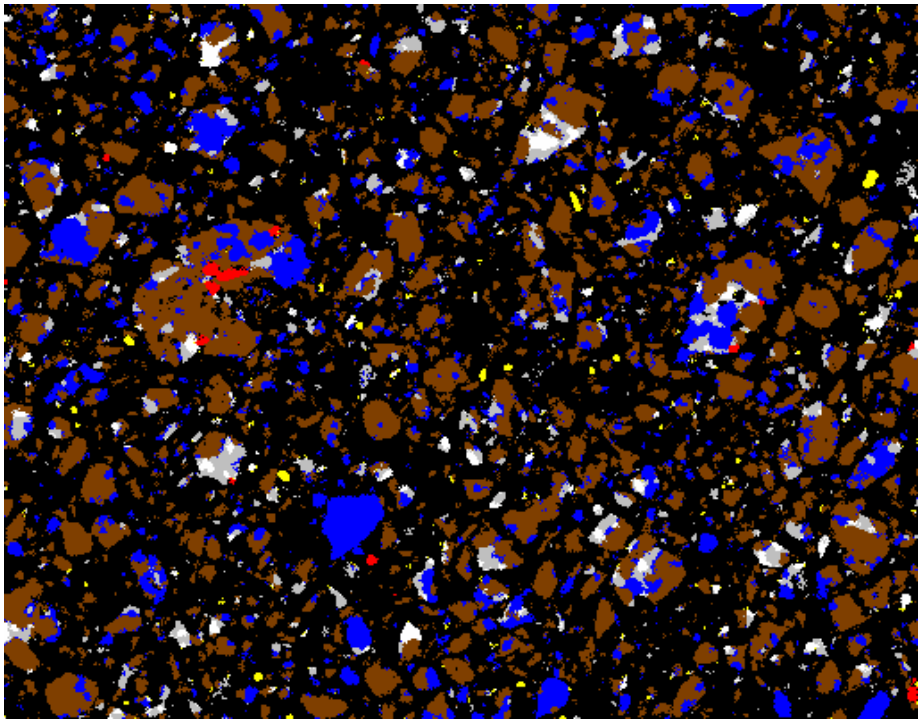

Figure A-6. Segmented image after thresholded blur filter.

Automated Segmentation Technique

The automation segmentation technique is an analysis method in which an algorithm was developed to automatically perform cement phase segmentation on elemental x-ray maps of petrographic sections. The segmentation is performed in a two pass routine, where the first pass partitions a composite X-ray map into multiple phases based upon the color dimensions of a pixel in the L*a*b* color space. Briefly, L*a*b* space is a color-opponent space consisting of two color parameters (a*,b*) and a lightness parameter (L*). A second pass, which is a clean-up procedure us used to correct the mis-assignments from the first pass partition with *ab initio* segmentation. . These correction address two types of errors: assignment of the epoxy filler to the aggregate phases and assignment of an incorrect phase to particle perimeters.

The coloring is implemented in L*a*b* space due to difficulty in phase separation in the traditional red-green-blue (RGB) space. Specifically, L*a*b* space takes advantage of the backscatter signal (brightness), which allows for better separation between alite and belite. Here, both phases are composed of the same elements, but differ in their unit cell composition and consequently, produce differing backscatter intensities. Phase segmentation in L*a*b* space is performed through the tabulation of an average color vector for each phase. Pixels are then assigned a phase, based upon the minimum distance between the pixel's (a*,b*) value and the phase averaged values. Six phases are identified during this procedure, which include a background (epoxy) phase, alite, belite, lime, sulfate, and aluminate/ferrite. In a final step, aluminate and ferrite are distinguished by evaluating pixels within this phase assignment with an appreciable iron L-$\alpha_1$signal.While the segmentation procedure is able to provide adequate estimation of areal coverage among these six phases, it does not consistently classify perimeter

pixels of aggregate as aggregate. This can be attributed to signal degradation due to interaction volume discrepancies at the edges of particles. As a result, reduced backscatter signals lead to problems with aggregate/background distinction and phase assignment.

To correct for challenges at the aggregate/background interface, a two-step procedure is used (Figure A-7). First, the background/aggregate mis-assignment is remedied through evaluation of the L* component of pixels assigned as background. Large L* values suggest appreciable backscatter signal and therefore a high probability of being from the aggregate. Through the process of thresholding at a fixed L* value, background assigned aggregate pixels can be identified. These pixels are subjected to a routine similar to the original phase assignment described above, but with the background phase option eliminated. The second correction, involving incorrect phase assignment at the perimeter of aggregate, is accomplished through the evaluation of the phase-centered coordinates in L*a*b* space. This mis-assignment is manifested as a "rings" of a second phase around primary phase particles and is a consequence of L*a*b* space partitioning. Specifically, if a line is drawn in (a*,b*) space between the background average coordinate and an aggregate phase coordinate, it is possible a second phase has a small projection distance onto this line. As a result, the second phase can appear as a ring phase on the particle. For example, in the petrographs evaluated in this study, sulfate frequently appeared as the ring phase to aluminate/ferrite particles.

Corrections for these ring artifacts are accomplished by producing two binary maps; one for the ring phase and one for the correct (internal) phase. These maps are combined with a union operation and compact objects containing at least one pixel from the internal phase are noted. Pixels that were associated with the ring phase in these identified objects have their phase assignment changed to the internal phase value. This process removes the artificial assignment of different phases to the perimeter of certain phases of aggregate.

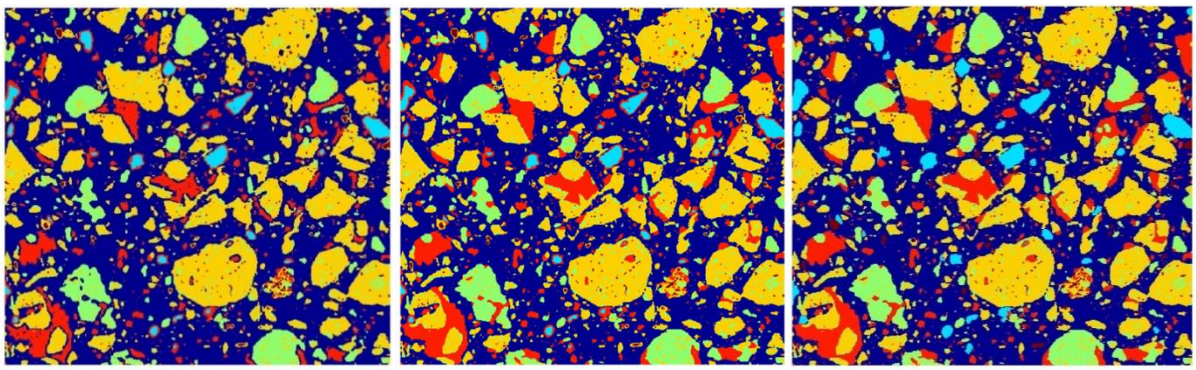

Figure A-7. Segmented images from left to right – after Step 1, after Step 2, and after ring artifact correction.

The phase analysis concludes with the production of a composite image where each pixel has been assigned to one of seven phases (six cement phases listed above, plus the background phase). Perimeters and areas covered by each phase can be trivially tabulated and as a result, area fractions and perimeter fractions calculated. Using a dual core processor, each segmentation procedure took on the order of 5 seconds per image in the Matlab environment.

Experiment

Sample Preparation

A cement specimen used for this study was prepared based on techniques developed at NIST [165], using the following procedure. The cement was first mixed with an optical grade epoxy resin in proportions that result in a stiff paste, then pressed into a specimen mold. The specimen was tapped firmly against the lab bench several times, then placed in a vacuum degassing chamber for approximately one hour to promote the removal of air bubbles. The epoxy was oven cured to achieve maximum hardness as recommended by manufacturer.

Polishing was performed using a semi-automated grinder polisher with user programmable powerhead and working wheel speeds, automatic lubricant and diamond abrasive dispensing, and variable hold down pressure for individual samples. The initial grinding step was performed using silicon carbide papers of several different grits. It was found that the best initial grind was obtained when the papers were used without any lubricant. The specimen is polished using progressively finer grit diamond abrasive and silk polishing cloths at each stage the specimen was polished until the imperfections left from the preceding abrasive were removed. Ethanol-based lubricants were used throughout the polishing process in order to prevent hydration of the cement grains or paste. The specimen was cleaned with ethanol between each grinding and polishing step to remove debris and residual abrasive. After the final polishing step, the specimen was coated with a thin layer of carbon using an evaporative coater. Specific details of the specimen preparation procedure are summarized in Table A-1.

Table A-1. Specimen Preparation Procedure

Step	Time	Abrasive	Abrasive Type	Media	Force	Head Speed (rpm)	Wheel Speed (rpm)	Lubricant Interval	Abrasive Interval
1	1:00	600 grit	Silicon Carbide	Grinding Paper	20 N	150	149	-	-
2	1:00	1200 grit	Silicon Carbide	Grinding Paper	20 N	150	149	-	-
3	1:00	4000 grit	Silicon Carbide	Grinding Paper	20 N	150	149	-	-
4	1:00	6 µm	Diamond Suspension	Silk Cloth	15 N	150	149	0:10	0:15
5	1:00	3 µm	Diamond Suspension	Silk Cloth	15 N	150	149	0:10	0:15
6	1:00	1 µm	Diamond Suspension	Silk Cloth	15 N	150	149	0:10	0:15
7	0:45	0.25 µm	Diamond Suspension	Silk Cloth	10 N	150	149	0:10	0:15

Experimental Design

To provide a robust comparison of the traditional and automated techniques, two independent analyses reference cement CCRL 168 were implemented. Elemental maps were first obtained for 10 specific image fields at the University of Florida, then the sample was sent to RJ Lee Group where the same 10 fields were relocated and acquired. Acquisition settings for the two different sets of fields are summarized in Table A-2. The same fields were acquired for the two analyses in an attempt to eliminate potential sampling error; even if the 10 fields together did not capture a sample representative of the bulk composition of the cement, the areas to be analyzed are known to be identical and the comparison between analysis techniques would remain valid.

Table A-2. Scanning Electron Microscope and EDS X-ray Acquisition Settings

	University of Florida	RJ Lee Group
EDS Detector	Silicon Drift Detector	Silicon Drift Detector
Accelerating Voltage	18 keV	10 KeV
EDS Acquisition Time	30 minutes	30 minutes

The SEM used to image the sample at the University of Florida utilized a motorized stage that was positioned manually prior to the acquisition of each field. The required acquisition time for each field was approximately 30 minutes, with 10-15 minutes of transition time required to move to the next field and begin the next round of acquisition. The total analyst time required for acquisition of a single field with this microscope was approximately 45 minutes.

Sample imaging at RJ Lee Group required significantly less analyst time due to the use of a computer controlled SEM (CCSEM). The fields for analysis were located and the stage coordinates were saved into the program. BSE images were collected at each field. The automated program is started and goes to each preselected field to acquire and save a position tagged spectrometry (PTS) EDS x-ray map at each field. The program allowed for input of 30 minute x-ray acquisition at each field. After acquisition of all fields, an analyst is needed to then save individual colored x-ray images for each field. The process takes approximately 20 minutes of an analyst's time per field.

Table A-3. Cement Phase Mass and Volume Fractions Obtained via XRD

Phase	Mass %	Volume %
Alite (C_3S)	60.4	60.4
Belite (C_2S)	17.2	16.8
Aluminate (C_3A-Cubic)	7.1	7.5
Ferrite (C_4AF)	8.3	7.2

Mg/Ca	3.0	2.6
Arcanite (K_2SO_4)	1.25	1.5
Hemihydrate	2.6	3.1
$CaCO_3$	0.8	1.0

Following acquisition, the two sets of fields were analyzed using the two techniques described previously; those acquired at UF were analyzed using the traditional, manual technique, while those acquired at RJ Lee Group were analyzed using the new automated technique. Both analysis techniques are more effective if compositional data from another source is available for benchmarking their accuracy. The results of the two analyses of CCRL 168 were compared against quantitative phase mass compositional XRD data provided by NIST. Mass fraction data was converted to volume fraction data using density values in literature [53] for a more direct comparison of the different phases. Both the mass fractions and volume fractions obtained via XRD are presented in Table A-3.

Results

Validation Study

The measured volume fractions for the four primary cement phases (alite, belite, aluminate, and ferrite) were averaged for both sets of the ten fields, and are presented in Figure A-8, along with the computed volume fractions from XRD.. Error bars are computed as the 95% confidence interval for the analyses performed at the University of Florida and RJ Lee Group.

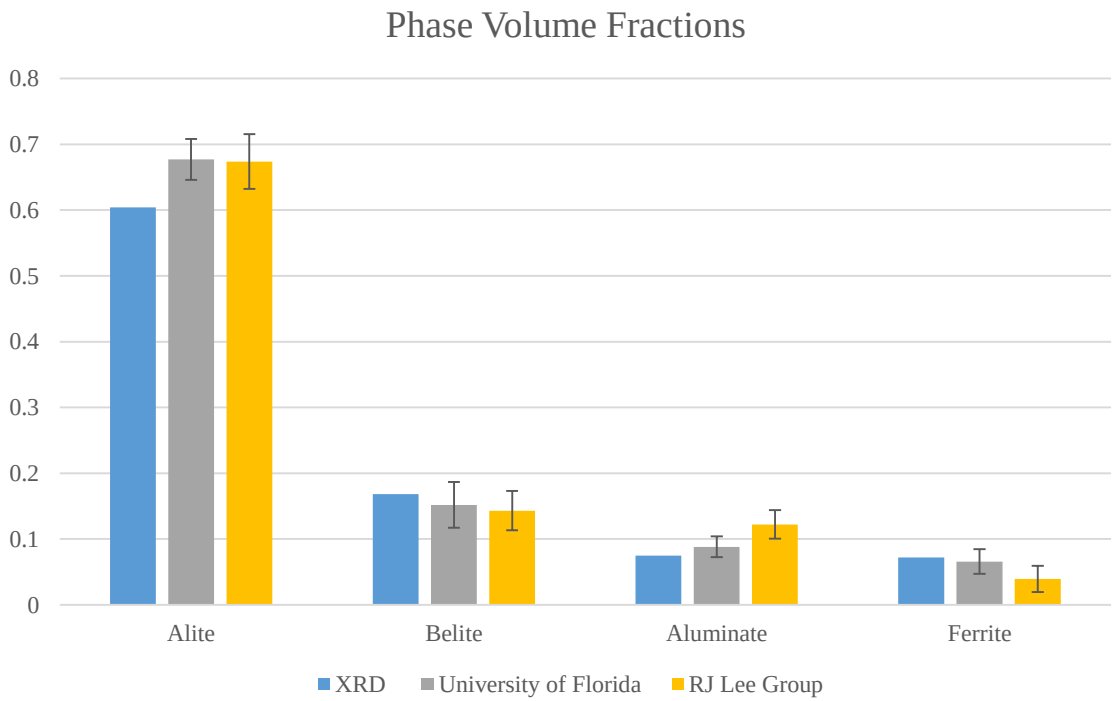

Figure A-8. Volume fraction analysis techniques.

The volume fraction results from the two analyses performed match closely, particularly for alite and belite. The results for ferrite and aluminate agree to within the 95% confidence interval calculated for each set. When compared to the volume fractions calculated from the XRD data provided by NIST, there is a slight discrepancy in the fraction of alite; the measured values from the microanalyses are approximately 7-8% larger. The size of the 95% confidence intervals for both analyses are comparable.

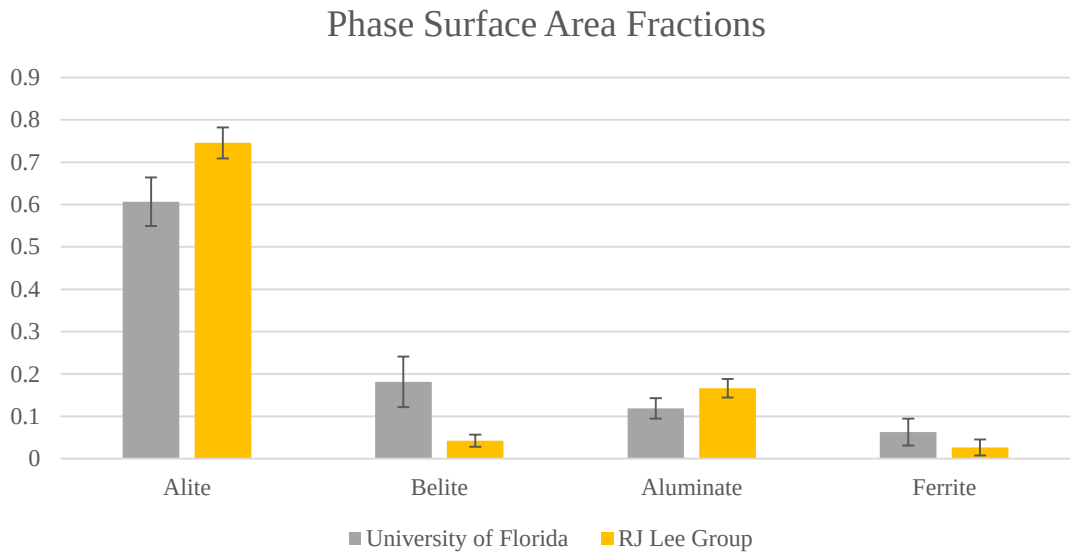

Figure A-9. Perimeter fraction analysis techniques.

The surface area fraction results of the study are exhibited in Figure A-9, with error bars again expressed as the 95% confidence interval for the sample set of each analysis. A comparison of the surface area fraction results reveals discrepancies that are more significant than those present in the volume fraction results. The largest difference is in the relative fractions of alite and belite; a higher value for alite and a lower value for belite was calculated by the automated segmentation routine. The error bars for aluminate and ferrite appear to have a slight degree of overlap, however their size relative to the actual values for those phases, particularly in the case of ferrite, nullify the significance of that overlap. Notably, the size of the error bars for the automated analysis performed by RJ Lee Group are smaller than those of the manual analysis for all surface area fraction measurements.

The discrepancies between the surface area results for the two data sets make conclusions about the accuracy of either difficult, particularly when considering the fairly close agreement of the volume fraction results both between the two analyses and the XRD benchmark. It is unlikely that the discrepancy is due to sampling error, simply because the same areas of the cement sample were analyzed in both cases.

Analysis and Acquisition Time

The total analyst time required to image 10 sample fields at the University of Florida was approximately 7.5 hours, followed by 6 hours of analyst time for manual image segmentation for a total of about 13.5 hours. The same analysis at RJ Lee Group required 1 hour of analyst time to set up the acquisition of fields, while analysis of the fields using the automated routine took about 5 seconds per field. The total time required to perform the analysis using the automated routine was under one minute, and effectively eliminates the labor required by the manual technique. Using the automated technique the time required to measure the volume and surface area fractions for a given cement is only limited by the amount of microscope time available for the acquisition of sample fields.

Conclusions

1. Through the application of automated image analysis routines the amount of time and labor required to perform a volume and surface area fraction analysis for raw cement is dramatically reduced.
2. The accuracy of the automated analysis routing with regard to volume fractions is comparable to that of the traditional manual technique.
3. Accuracy of the volume fraction results for a given technique does necessarily indicate that the surface area fraction results with also be accurate.